N73 28445

GEOTECHNICAL ENGINEERING

STATIC PENETRATION RESISTANCE OF SOILS

CASE FILE COPY

by

H. TURAN DURGUNOGLU

JAMES K. MITCHELL

PREPARED FOR NASA HEADQUARTERS, WASHINGTON, D.C.
UNDER NASA GRANT NGR 05-003-406, "LUNAR SOIL PROPERTIES AND SOIL MECHANICS"

APRIL 1973

SPACE SCIENCES LABORATORY

UNIVERSITY OF CALIFORNIA • BERKELEY

GEOTECHNICAL ENGINEERING

STATIC PENETRATION RESISTANCE OF SOILS

by

H. Turan Durgunoglu

James K. Mitchell

Prepared for NASA Headquarters, Washington, D. C. under NASA Grant NGR 05-003-406, "Lunar Soil Properties and Soil Mechanics"

April, 1973

SPACE SCIENCES LABORATORY

SERIES 14 ISSUE 24

UNIVERSITY OF CALIFORNIA · BERKELEY

ABSTRACT

Model test results were used to define the failure mechanism associated with the static penetration resistance of cohesionless and low-cohesion soils. Knowledge of this mechanism has permitted the development of a new analytical method for calculating the ultimate penetration resistance which explicitly accounts for penetrometer base apex angle and roughness, soil friction angle, and the ratio of penetration depth to base width. Curves relating the bearing capacity factors N_c and $N_{\gamma q}$ to the soil friction angle are presented for failure in general shear.

Strength parameters and penetrometer interaction properties of a fine sand were determined and used as the basis for prediction of the penetration resistance encountered by wedge, cone, and flat-ended penetrometers of different surface roughness using the proposed analytical method. Because of the close agreement between predicted values and values measured in laboratory tests, it appears possible to deduce in-situ soil strength parameters and their variation with depth from the results of static penetration tests.

A procedure for determining the soil cohesion and friction angle from the results of static penetration tests is proposed. This procedure is illustrated by application to model test results, to penetration data presented by other investigators, and to penetration data obtained for the lunar surface by the Apollo 15 self-recording penetrometer and the Soviet Lunar Rover Lunokhod-1.

PREFACE

This report presents the results of one phase of the research undertaken as a part of National Aeronautics and Space Administration Grant NGR-05-003-406, "Lunar Soil Properties and Soil Mechanics." The in-depth study of the static penetration resistance of soils described herein was made as a background study in support of the Apollo Soil Mechanics Experiment (S-200) to aid in the analysis and interpretation of penetration data obtained on the lunar surface.

The major part of the material presented in this report was developed by H. T. Durgunoglu for a dissertation in partial fulfillment of the requirements of the degree, Doctor of Philosophy in Geotechnical Engineering at the University of California, Berkeley.

ACKNOWLEDGEMENTS

Appreciation is expressed to Professors W. N. Houston and S. A. Schaaf who critically reviewed the research results. Mr. D. D. Treadwell reviewed the manuscript and provided valuable suggestions, and Dr. R. E. Nobari and Messrs. W. A. Lacerda and P. Lade contributed helpful discussions and suggestions.

Mr. C. K. Chan assisted in the development of techniques and equipment used in the experimental phases of this study. The equipment was carefully constructed in the Institute of Transportation and Traffic Engineering shop under the supervision of Mr. R. Newcomb and Mr. T. W. Pickrell.

TABLE OF CONTENTS

LIST OF FIGURES

LIST OF TABLES

LIST OF SYMBOLS

English Letters

a, b	dimensionless parameters
B, B_o	diameter of penetrometer base and shaft
c	cohesion
c_a	adhesion
D, D_{cr}, D_R	depth, critical depth, and relative density of soil
d_c, d_γ, d_q	depth factors for cohesion, friction and surcharge
D/B	relative depth
$(D/B)_{cr}$	critical relative depth
e, e_c	void ratio, pre-shear void ratio
E, E_{1-D}	elastic modulus, one-dimensional compression modulus
f_c	roughness factor for cohesive soils, = c_a/c
f_o, f_o^*	unit skin friction, average unit skin friction
I, I_i, I_r	iteration number, i^{th} integral, rigidity index
K	lateral earth pressure coefficient
K_{zz}	vertical stress factor
L	moment arm of a force
L	length of foundation or length of vane
m	relative depth, = D/B
$m(e_c)$	reduction in ϕ per log-cycle change in confining pressure
n	number of blades
N	blow count in Standard Penetration Test
N_c, N_γ, N_q	bearing capacity factors for cohesion, friction and surcharge
$N_{\gamma q}$	bearing capacity friction-surcharge factor
p, q	stress invariants
P. Q	load
p_a	atmospheric pressure
q	surcharge
q_c	penetration resistance of Dutch Cone
q_f	ultimate bearing capacity or penetration resistance
Q_s	skin load
r	radius of vane, radius of logarithmic spiral
r_c	maximum extend of shear surface in lateral direction

r_γ	roughness factor
s_o	shear strength of c - ϕ soil
T	torque
w	water content of soil
X, Y	body forces per unit volume in the x and y directions
z	vertical distance to ground surface

LIST OF SYMBOLS

Greek Letters

α	base semiapex angle
β, ψ, θ, θ_o	angles which determine the shear surface associated with penetration of a wedge
β_c, β_o, β_n	correct, old and new values of β
γ	the topmost angle of plane shear zone
γ_s	unit weight of soil
δ	penetrometer to soil friction angle or shear displacement
δ/ϕ	roughness
η	angle used in determination of β, = 180° - (γ+ψ)
ξ_c, ξ_γ, ξ_q	shape factors for cohesion, friction, and surcharge
$\varepsilon_{\gamma q}$	shape factor for friction-surcharge term
ε_a	axial strain
ν	correction factor for bearing capacity of shallow foundations or Poisson ratio
σ	normal stress
σ_x, σ_y, τ_{xy}	stress components in x-y plane
σ_m, $\sigma_{g,M}$, σ_{mf}	mean normal stress, mean value of mean normal stress along a failure surface, normal stress on failure surface
σ_1, σ_3	major, minor principal stress
σ_1/σ_3, $(\sigma_1/\sigma_3)_f$	principal stress ratio, principal stress ratio at failure
ϕ, ϕ_p, ϕ_1	angle of internal friction, peak value of friction angle, angle of internal friction at confining pressure of p_a
ϕ_r, ϕ_{ult}	residual or ultimate friction angle
τ	shear stress
τ_f	shear strength

CHAPTER ONE

INTRODUCTION

It has been recognized since early in the lunar exploration program that a knowledge of lunar soil properties is essential for satisfactory solution of a number of scientific and engineering problems. As examples are questions related to (1) formation and compaction of surface layers, (2) characterization of different materials, (3) slope stability and downslope movement of soil and rock, (4) prediction of seismic velocities and analysis of seismic data, (5) estimation of thermal behavior, (6) characterization of dielectric properties for use in radar and electrical studies, (7) gas diffusion through the lunar surface, (8) strength and deformation properties for use in engineering studies, and (9) definition of conditions for terrestrial simulation studies.

To help in the development of this knowledge a soil mechanics investigation was included as a part of Apollo missions 11 and 12, and a formal Soil Mechanics Experiment was assigned to missions 14 through 17. As a part of this experiment it was desired that quantitative data be obtained to the extent possible within the constraints of lead time for apparatus development, spacecraft payload, and astronaut time and capability on the lunar surface. A self-recording penetration test device was selected for this purpose and included as a part of the Apollo 15 and Apollo 16 missions. A penetration test was selected because (1) it is simple, (2) it can be done by hand, (3) conditions can be explored to depths of several tens of centimeters, and (4) there is much available terrestrial experience with this type of test.

At the same time a number of limitations in the understanding of penetration resistance of soils in relation to soil strength and compressibility properties were recognized. Thus a basic investigation of penetrometer-soil interaction was undertaken for the development of a suitable analytical technique for expression of the static penetration resistance of soils in terms of penetrometer base apex angle, base roughness, depth of penetration, and soil cohesion and friction angle. The specific objectives were:

(1) To develop an improved understanding of the soil failure mode during a static penetration test,

(2) To determine the influence on penetration resistance of penetrometer base apex angle, size, and roughness, relative depth of base, and angle of internal friction and compressibility of soil,

(3) To develop an analytical technique which will allow prediction of static penetration resistance of soils in terms of physical properties of the penetrometer and basic soil properties or, alternatively, determination of in-situ soil properties from the results of penetration tests,

(4) To explain previous test results, many of which cannot be adequately accounted for in terms of existing theories.

This report presents the results of these studies. Initially, the state-of-the-art was critically reviewed (Chapter Two). The failure mechanism associated with deep static penetration in soils was determined using model tests (Chapter Three). Knowledge of this mechanism permitted development of a new theory for determining the ultimate base resistance of a penetrometer in terms of factors that depend on soil friction angle, penetrometer base apex angle, depth to base width ratio, and penetrometer to soil friction (Chapter Four). The strength and penetrometer interaction properties of a fine sand were then studied (Chapter Five) and the results were used as a basis for prediction of resistance to penetration by wedges, cones and flat-ended penetrometers of different surface roughness. Laboratory penetration tests were conducted to provide a basis for comparison with predictions. The effects of each variable, (base apex angle, base roughness, relative depth, soil friction angle, and soil compressibility) were further investigated both experimentally and theoretically (Chapter Six).

Finally, a procedure for deduction of in-situ soil properties from the results of static cone penetration tests is outlined. This procedure is illustrated by application to model tests, to penetration data obtained from the literature, and to penetration resistance data for the lunar surface obtained during the Apollo 15 and Siviet Rover Lunokhod-1 missions (Chapter Seven).

CHAPTER TWO

BEARING CAPACITY AND PENETRATION RESISTANCE THEORIES

THEORETICAL CONSIDERATIONS

General

Most theories for ultimate bearing capacity are based on the fundamental formula of Prandtl, which is valid for the case of a rigid-plastic, incompressible, weightless material whose shear strength characteristics are given by the Mohr-Coulomb failure criteria:

$$\tau_f = c + \sigma\tan\phi \tag{2.1}$$

where τ_f = shear strength
c = soil cohesion
σ = normal stress
ϕ = angle of internal friction of soil

The solution of Prandtl (1921) for the bearing capacity under a strip load on a rigid-plastic, incompressible and weightless material is:

$$q = cN_c \tag{2.2}$$

where

$$N_c = \cot\phi\ [e^{\pi\tan\phi}\ \tan^2(\tfrac{\pi}{4} + \tfrac{\phi}{2})\ - 1] \tag{2.3}$$

Reissner (1924) considered the effect of a surcharge, q, and concluded that the bearing capacity was increased by an amount qN_q where:

$$N_q = e^{\pi\tan\phi}\ \tan^2(\tfrac{\pi}{4} + \tfrac{\phi}{2}) \tag{2.4}$$

It can be seen that the bearing capacity factors N_c and N_q are related by the following equation:

$$N_c = (N_q - 1)\ \cot\phi \tag{2.5}$$

A widely used bearing capacity equation which considers soil cohesion, friction, and surcharge was first presented by Terzaghi (1943) by combining Equations 2.3 and 2.4 and adding a friction term $(1/2 \cdot \gamma_s B N_\gamma)$, giving:

$$q_f = cN_c + 1/2 \cdot \gamma_s B N_\gamma + qN_q \qquad (2.6)$$

where q_f = ultimate bearing capacity or unit resistance under an infinitely long foundation of width, B

c = soil cohesion

γ_s = unit weight of soil

q = surcharge

N_c, N_γ, N_q = primary bearing capacity factors, $f(\phi)$.

Inclusion of soil weight considerably complicates the mathematical solution. To handle this difficulty, many approximate methods have been proposed.

Numerical Techniques

The finite difference approximation based on the method of characteristics is widely used in the numerical analysis of differential equations of the type applicable to the bearing capacity problem. Lundgren and Mortensen (1953) used this method to obtain a solution of the strip footing bearing capacity problem. The same method was used for the axially symmetric circular footing problem by Cox et al (1961), Cox (1962), and Larkin (1968).

In recent years, the same technique has been applied to deep foundations. Strip loading conditions were analyzed by Graham (1968) and solutions were provided for axisymmetric circular foundations by Nowatzki (1971) and Nowatzki and Karafiath (1972).

Numerical methods have both advantages and disadvantages when compared to other methods for the calculation of bearing capacity. They may be summarized as follows:

Advantages:

(1) Soil weight can be considered easily and properly.

(2) Dependence of soil friction angle on mean normal stress along a failure surface can be considered in the solution.

Disadvantages:

(1) The angle of internal friction and the unit weight of the soil are usually considered as independent variables, although, in fact, they may be interdependent.

(2) They are not conducive to development of simple graphs or formulations.

(3) The Haar and von Karman hypotheses used in the analysis of axi-symmetric problems is not a good assumption (see Chapter Four).

(4) For deep foundations, the extensions of slip lines are arbitrary, e.g. Nowatzki (1971) has assumed that slip surface reverts to the penetrometer shaft as was assumed by Meyerhof (1951) (Fig. 2.1b); however, Nowatzki and Karafiath (1972) in the analysis of the same problem assumed that slip surface ends at the base level, which is equivalent to neglecting the shear strength of overburden, as was assumed by Terzaghi (1943) (Fig. 2.1a).

(5) Statically correct solutions found by the method of characteristics are kinematically inadmissible.

Consequently kinematically more acceptable slip surfaces were introduced, e.g. Jumikis (1961), Balla (1962), Hu (1964), and Gorbunov-Possadov (1965).

As yet, however, there is no completely correct theoretical solution for the friction (N_γ) factor for the simple shallow footing problem. In view of this, Meyerhof (1955) and Brinch Hansen (1961) suggested the use of following empirical formulas for the calculation of the bearing capacity factor N_γ:

Meyerhof $$N_\gamma = (N_q - 1)\tan(1.4\phi) \quad (2.7)$$

Brinch Hansen $$N_\gamma = 1.8(N_q - 1)\tan\phi \quad (2.8)$$

Slip Surface Assumptions for Shallow Foundations

The bearing capacity equation (Equation 2.6) generally includes three bearing capacity factors (N_c, N_γ and N_q). Commonly, the values of N_c and N_q are those corresponding to the slip surface valid for weightless soil (i.e., $q/(\gamma_s B)=\infty$). Further, the value of N_γ used is that corresponding to a slip surface valid for $q/(\gamma_s B) = 0$ (footing at the surface).

This situation leads to calculated ultimate bearing capacity values (in which N_γ and N_q are supposed to be determined independently) which are somewhat on the conservative side. This is due to the linear superposition of two terms, each of which is determined from a statically admissible rupture surface which is different from the surface which actually applies for values of $q/(\gamma_s B)$ other than zero or infinity.

If there is no surcharge other than the overburden, $q/(\gamma_s B)$ becomes equal to D/B. In fact, when $q/(\gamma_s B)$ is greater than zero and less than infinity,

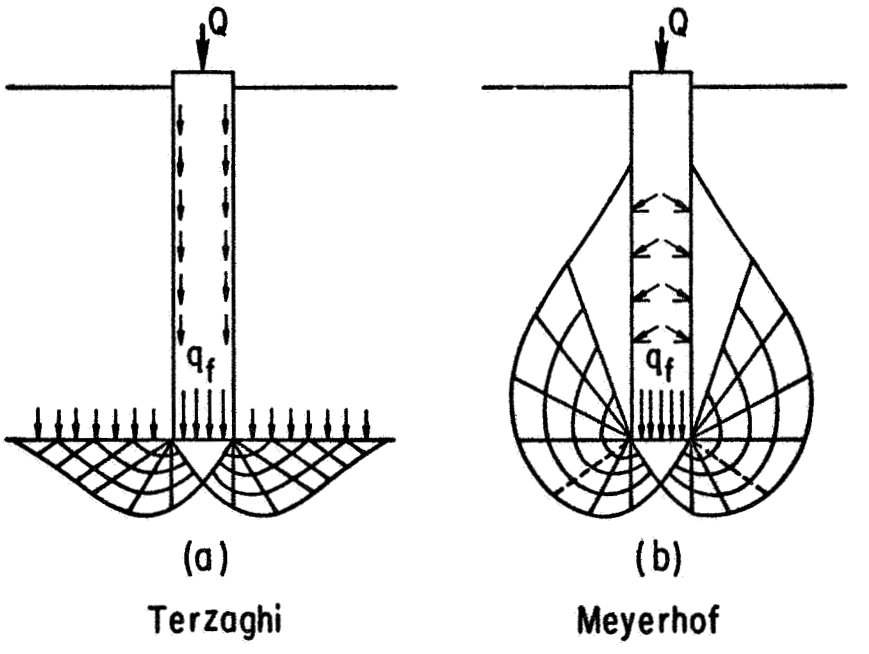

FIG. 2.1 DIFFERENT FAILURE SURFACE ASSUMPTIONS FOR DEEP FOUNDATIONS

the slip surface is unique and intermediate to the two limiting slip surfaces shown at the top and bottom of Fig. 2.2.

DeBeer (1967) has suggested the following correction formula for the bearing capacity calculated assuming two different slip surfaces:

$$q_f = \nu(1/2\gamma_s B N_\gamma + qN_q) \tag{2.9}$$

where N_γ and N_q are bearing capacity factors calculated for two different slip surfaces and ν is a correction factor that depends on ϕ and D/B. The correction factor for $\phi = 30°$ is shown in Fig. 2.3a. Its maximum value is 1.17 and occurs for $q/(\gamma_s B)$ or D/B equal to 0.4. Hansen and Christensen (1969) calculated the same correction factor for a smooth strip footing, with the results shown in Fig. 2.3b.

General Bearing Capacity Equation

In Equation 2.6 the term ($q\ N_q$) represents the increase in bearing capacity caused by overburden pressure. This term does not consider the effect of the shear strength of soil above the foundation level if the primary bearing capacity factors (which are valid for D/B = 0) are used. Therefore, for deep foundations new bearing capacity factors should be calculated, Meyerhof (1951). However, Brinch Hansen (1961) has suggested that this effect can be taken into account by depth factors (d_c, d_γ, d_q). Also, because the general bearing capacity equation is formulated for strip foundations, shape factors (ξ_c, ξ_γ, ξ_q) must be employed when considering other foundation configurations. With these modifying factors Equation 2.6 can be written in the following form:

$$q_f = cN_c\xi_c d_c + 1/2\ \gamma_s B N_\gamma \xi_\gamma d_\gamma + \gamma_s D N_q \xi_q d_q \tag{2.10}$$

where ξ_c, ξ_γ, ξ_q = shape factors for the cohesion, friction, and surcharge terms.

d_c, d_γ, d_q = depth factors for the cohesion, friction, and surcharge terms.

Values of the primary bearing capacity factors, N_c, N_γ, and N_q are given in Fig. 2.4.

Depth Factors

Skempton (1951) proposed a depth factor for the cohesion term as follows:

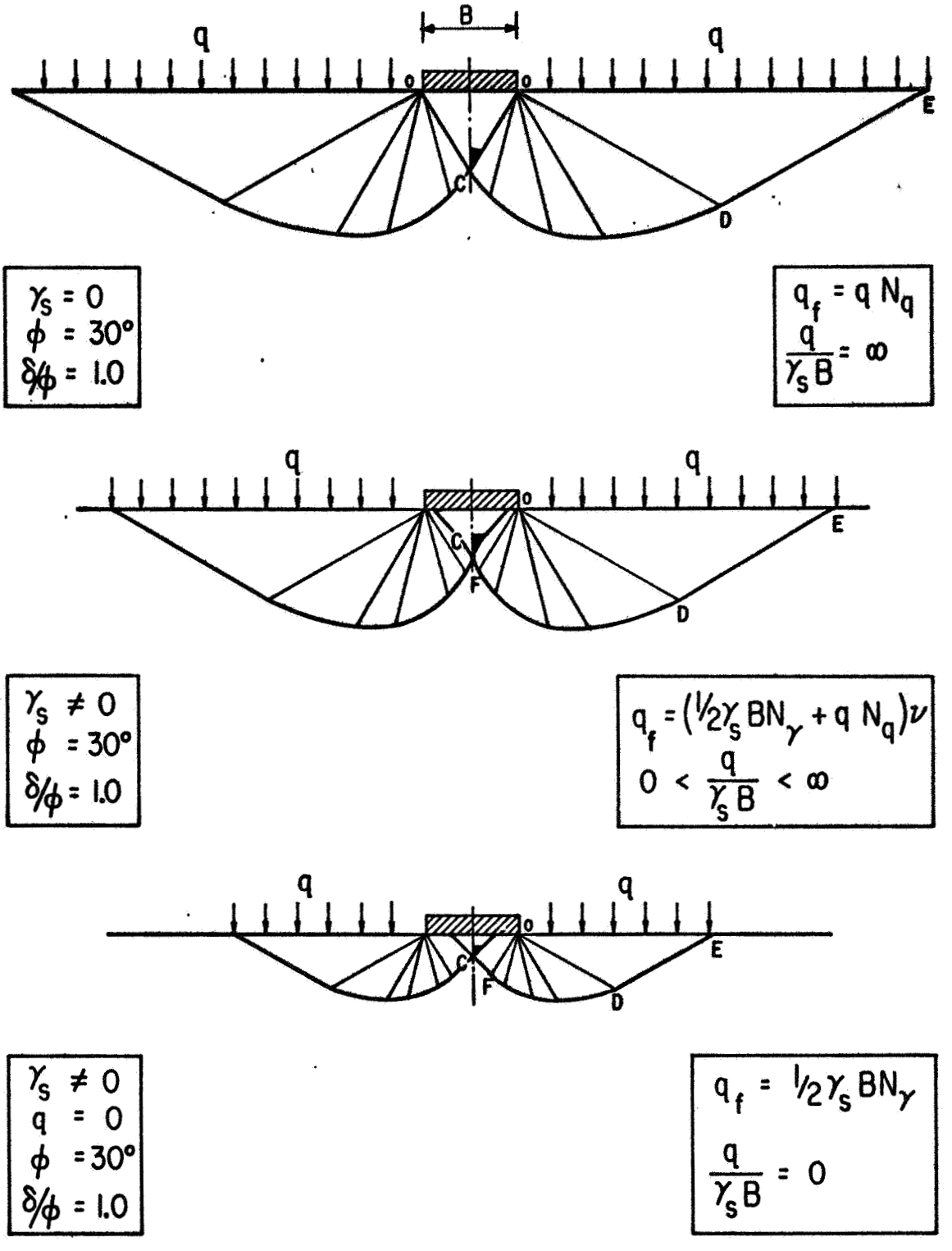

FIG. 2.2 FAILURE PATTERNS UNDER A SHALLOW FOUNDATION
(After De Beer, 1967)

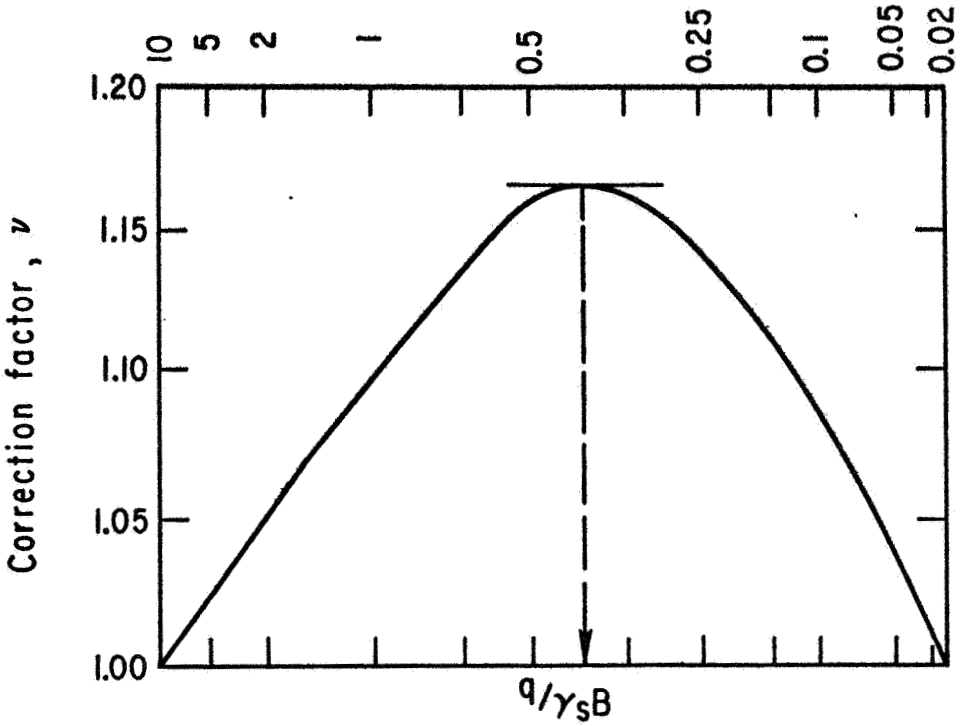

FIG. 2.3a CORRECTION FACTOR FOR BEARING CAPACITY OF A SHALLOW FOUNDATION (After De Beer, 1967)

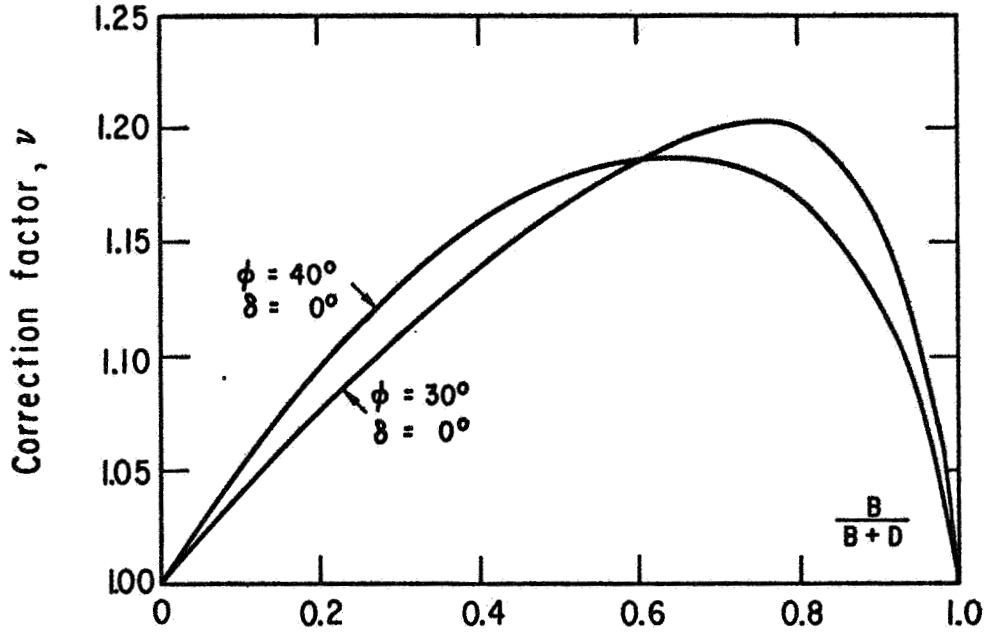

FIG. 2.3b CORRECTION FACTOR ν ON LINEAR SUPERPOSITION ASSUMED BY BEARING CAPACITY FORMULA AS FUNCTION OF B/(B+D) FOUND FOR SMOOTH STRIP FOOTINGS (After Hansen and Christensen, 1969)

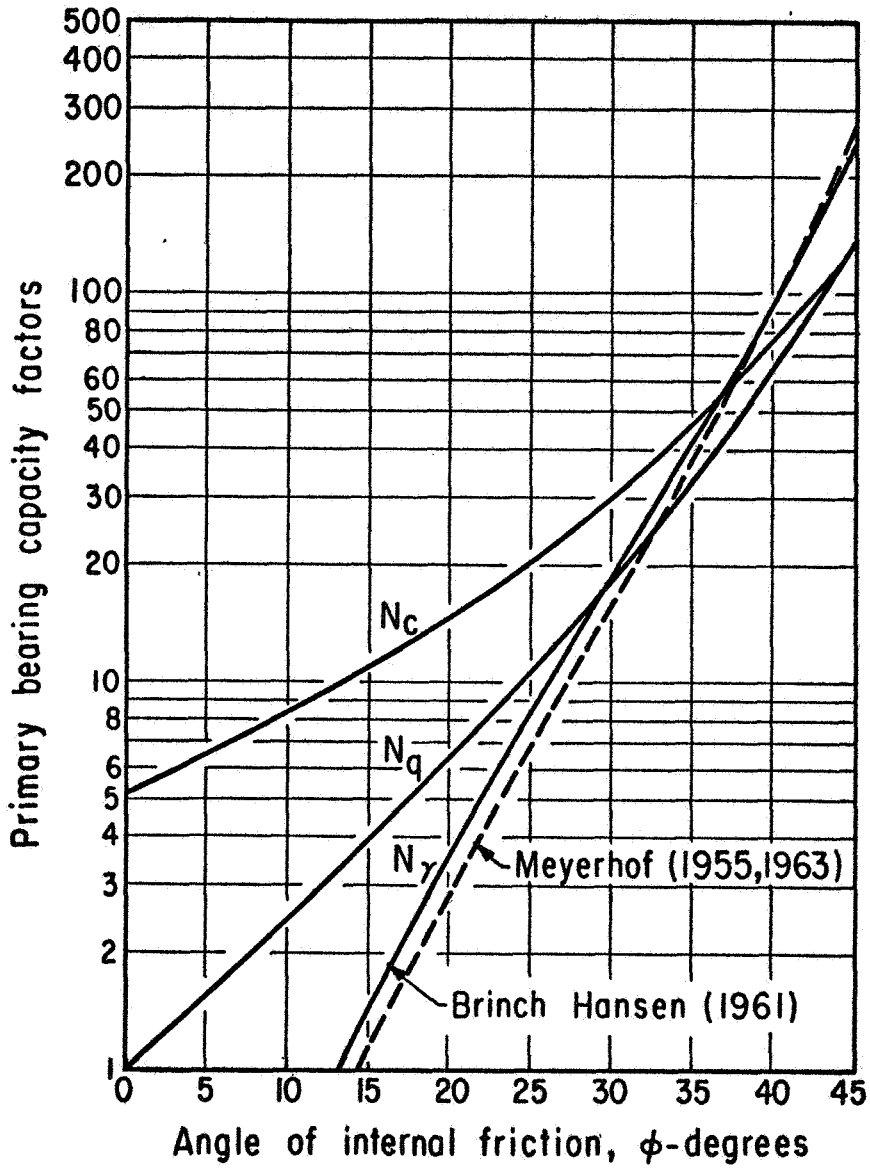

FIG. 2.4 PRIMARY BEARING CAPACITY FACTORS

$$d_c = 1.0 + 0.2\ (D/B) \tag{2.11}$$

for purely cohesive soils ($\phi = 0$) and values of D/B up to 2.5. A constant depth factor $d_c = 1.5$ was suggested for depths greater than D = 2.5B.

Brinch Hansen (1961, 1966) suggested the approximate relationship:

$$d_c = 1.0 + 0.35\ (D/B) \tag{2.12}$$

as an average value of d_c for D/B smaller than 1.0 and values of ϕ between 0 and 40 degrees. Brinch Hansen (1961) has also proposed the following generalized and semiempirical equations for the depth factors:

$$d_c = 1.0 + \frac{0.35}{(B/D) + [0.6/(1+7\tan^4\phi)]}$$

$$d_\gamma = 1.0 \tag{2.13}$$

$$d_q = d_c - \frac{d_c - 1}{N_q}$$

These relations are shown in Fig. 2.5. The factors d_c and d_q approach the indicated limiting values with increasing relative depth, D/B for a given value of ϕ.

Meyerhof (1963) proposed the following equations for the depth factors:

$$d_c = 1.0 + 0.2\ (D/B)\ \tan\left(\frac{\pi}{4} + \frac{\phi}{2}\right) \tag{2.14}$$

for $\phi = 0°$:

$$d_q = d_\gamma = 1.0$$

for $\phi > 10°$ and $D/B < 1.0$:

$$d_q = d_\gamma = 1.0 + 0.1(D/B)\tan\left(\frac{\pi}{4} + \frac{\phi}{2}\right) \tag{2.15}$$

The values of d_c are slightly larger, whereas those of d_q are smaller than the values proposed by Brinch Hansen.

DeBeer (1967) suggested the following depth factors:

$$d_q = 1 + \left[\tan^2\left(45° - \frac{\phi}{2}\right)e^{\pi\tan\phi} - 1\right] e^{-\pi\tan\ (B/D)}$$

$$d_\gamma = 1.0 \tag{2.16}$$

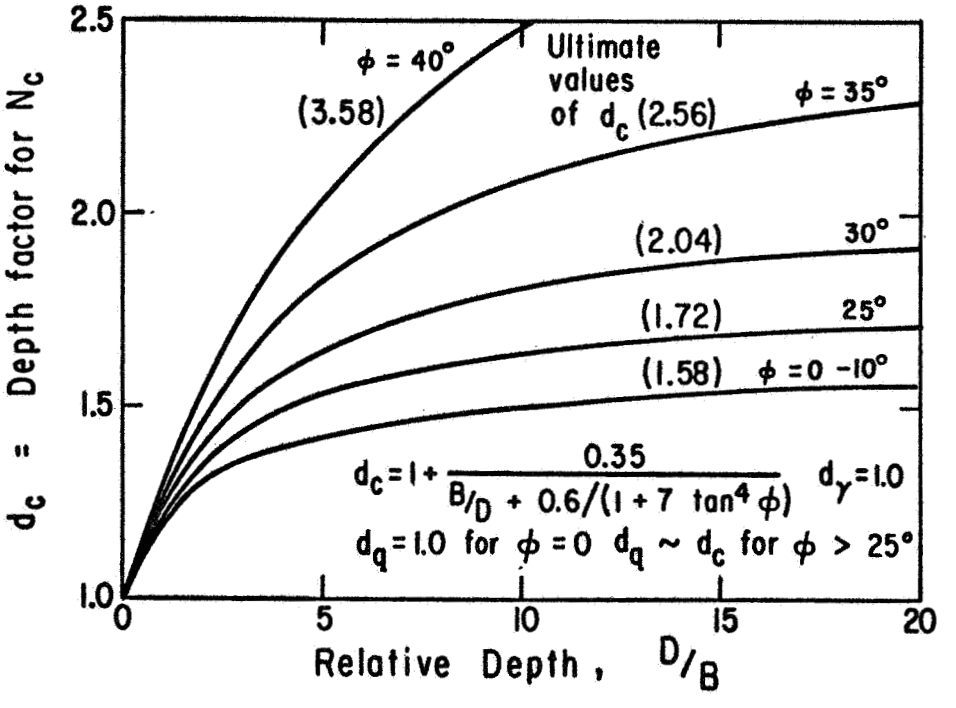

FIG. 2.5 DEPTH FACTORS AS A FUNCTION OF RELATIVE DEPTH

Ultimate depth factors are estimated using the bearing capacity factors given by Meyerhof (1951) for shallow and deep foundations. A comparison with Brinch Hansen's ultimate values is given in Table 2.1, where it can be seen that Meyerhof's values are much higher. This is due to the nature of the failure mechanism assumed by Meyerhof (1951) for deep foundations, (see Fig. 2.1b). It should be noted that Biarez et al (1961) showed, from the results of model tests, that the slip surface reaches vertical tangency provided that the relative depth is sufficiently large.

Table 2.1 ULTIMATE DEPTH FACTORS FOR COHESION TERM

Angle of internal friction, ϕ-degrees	Ultimate depth factor for cohesion term, $(d_c)_{ult.}$	
	Meyerhof	Brinch Hansen
20	3.3	1.6
25	4.8	1.7
30	6.3	2.0
35	8.7	2.6
40	14.4	3.5
45	23.4	5.7
50	36.2	9.9

Shape Factors

Early suggestions by Terzaghi (1943) and Skempton (1951) concerning the shape factors may be summarized as follows:

Circular Areas	Square and Rectangular Areas
$\xi_c = 1.3$	$\xi_c = 1 + 0.2(B/L)$
$\xi_\gamma = 0.6$	$\xi_\gamma = 1 - 0.2(B/L)$

where B is the width and L is the length of contact area.

Meyerhof (1951) presented a diagram for the determination of combined shape and depth factors that are functions of B/L, D/B, and ϕ. Based on Meyerhof's diagram Brinch Hansen (1961) developed the following semi-empirical

equations for the individual shape factors that are independent of depth:

$$\xi_c = 1 + (0.2+\tan^6\phi)\ (B/L)$$

$$\xi_q = \xi_c - \frac{\xi_c - 1}{N_q} \qquad (2.17)$$

$$\xi_\gamma = 1 - \frac{1}{2}\ (0.2+\tan^6\phi)\ (B/L)$$

Meyerhof (1961b, 1963) also proposed the following empirical expressions for the individual shape factors:

$$\xi_c = 1 + 0.2\ \tan^2(45° + \frac{\phi}{2})\ (B/L)$$

$$\xi_q = \xi_\gamma = 1.0 \qquad \text{for } \phi=0° \qquad (2.18)$$

$$\xi_q = \xi_\gamma = 1 + 0.1\ \tan^2(45° + \frac{\phi}{2})\ (B/L) \quad \text{for } \phi>10°$$

DeBeer (1967) presented the results of tests for determination of shape factor ξ_γ. From these test results it was concluded that the shape factor ξ_γ has a value of 0.6 independent of the soil density. In a recent study, DeBeer (1970) proposed the following empirical formula for the shape factor ξ_q:

$$\xi_q = 1 + (B/L)\ \sin\phi \qquad (2.19)$$

Further evaluation of the proposed shape factors is made in Chapter Six.

ADDITIONAL FACTORS INFLUENCING BEARING CAPACITY

Dependence of Angle of Internal Friction on Mean Normal Stress

According to Mohr-Coulomb yield criteria, soil strength may be characterized by Equation 2.1. However, Terzaghi (1925) and others have pointed out that the angle of internal friction (ϕ), for sand varies not only with density but also with the mean normal stress (σ_m), at a given density. Due to the fact that along a possible sliding surface underneath a foundation the values of normal stress are variable from point to point, the strength characteristics of a sand are not likely to conform to the simple linear function indicated by the Mohr-Coulomb yield criteria.

As listed under the advantages of numerical methods, it is more difficult to use a non-linear function than the linear Mohr-Coulomb equation. Yareshenko (1964) has suggested the following non-linear relationship be used instead of the Mohr-Coulomb criteria:

$$\tau = (k\sigma_m)^{1/n} \tag{2.20}$$

where k and n are constants and functions of the angle of internal friction. The yield function given by Equation 2.20 has been employed in the solution of a plane footing problem by Berezantsev and Kovalev (1968). Later, Kingston and Spencer (1970) presented a solution procedure for a general non-linear function.

An average value of mean normal stress along the slip surface is generally considered in analytical solutions. Meyerhof has shown that the average mean normal stress is approximately equal to one-tenth of the ultimate bearing capacity. The symbol $\sigma_{g,M}$ will be used to denote the mean value of mean normal stress along a slip surface. As shown in Fig. 2.6, the angle ϕ' corresponding to the secant connecting the origin to the point $\sigma_{g,M}$ was used (DeBeer, 1967) for the calculation of the ultimate bearing capacity. Thus the true curved strength envelope OMN shown in Fig. 2.6 is replaced by the straight line OPQ intersecting the true curve at point P with an abscissa value of:

$$\sigma_{g,M} = q_f/10 \tag{2.21}$$

DeBeer (1967) gave the following empirical expression for the average mean normal stress along the slip surface:

$$\sigma_{g,M} = (1-\sin\phi)\,\frac{q_f + 3q}{4} \tag{2.22}$$

The dependence of angle of internal friction on mean normal stress along a potential slip surface is of great importance in the interpretation of the results of model tests of shallow foundations. As the ultimate bearing capacity increases with the width of the footing for shallow foundations, so does the mean value of mean normal stress along the slip surface increase with the footing width, thus the secant angle ϕ' decreases in value as may be seen by inspection of Fig. 2.6. As a result of this influence, the results of laboratory tests on very small shallow footings may lead to

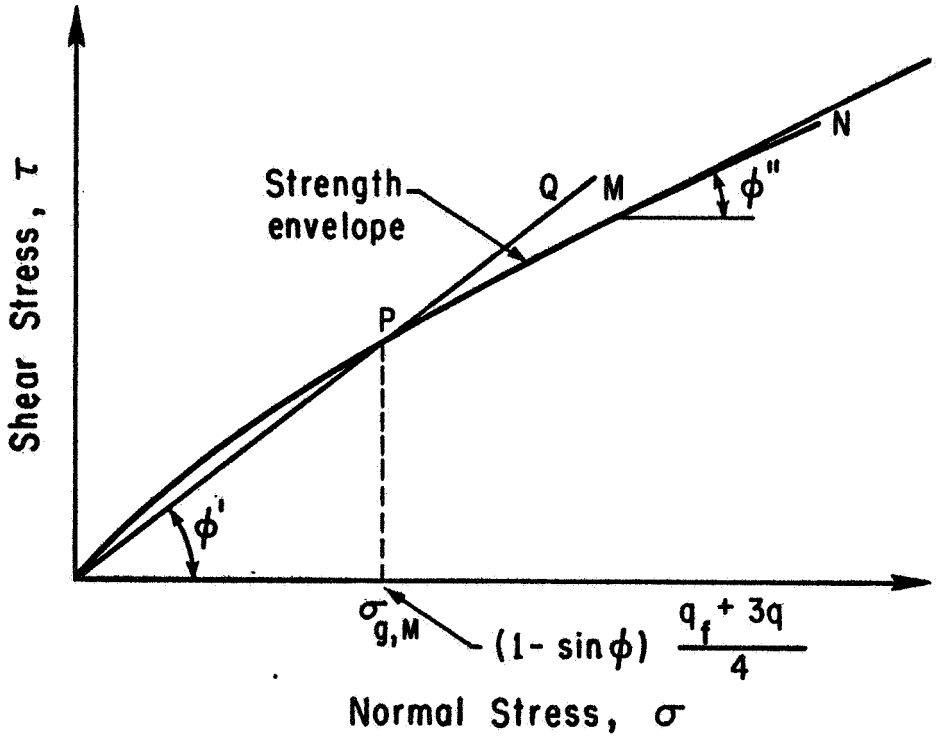

FIG. 2.6 DEPENDENCE OF ϕ ON NORMAL STRESS
(After De Beer, 1967)

an overestimation of the bearing capacity of much larger actual shallow footings.

Progressive Rupture

It may be inferred from the previous discussion of the influence of mean normal stress that it would be desirable to conduct loading tests on shallow footings with footings of actual full size. Such tests have been performed on a large scale by Muhs (1963). The values of N_γ determined from these tests are shown in Fig. 2.7. When comparing these values to those determined in small scale tests, DeBeer (1967) points out that the large scale tests give larger values of N_γ than the small scale tests at low densities, while at high densities the reverse is true. This occurrence can be explained by the phenomenon of progressive rupture.

The progressive rupture phenomenon is due to the fact that during the gradual increase of load on a soil, the shear strength is not immediately mobilized at all points on the potential slip surface, but initially only at the points where the shearing stresses are largest. From these points, the rupture gradually extends to other points along the slip surface. This gradual progression causes modifications and variations of the soil properties along the slip surface.

In loose soils, because of the compressional deformations which occur before the rupture load is reached, the density of the soil in the highly stressed zone is already increased before rupture, and the same is true for the shear strength, which increases with increased density. Therefore, at rupture, the shear strength corresponding to the initial density no longer governs, but there exists some variable shear strength along the rupture surface.

In dense soils, the reverse occurs. In the highly stressed zones, the dense soil begins to dilate, causing a decrease in density and thus a decrease in shear strength to take place. Therefore, when the state of rupture along a slip surface in a dense soil is reached, the shear strength corresponding to the original density is not available along the entire rupture surface.

DeBeer (1967) further states that the progressive rupture phenomenon is scale dependent for shallow footings because the relative settlement at

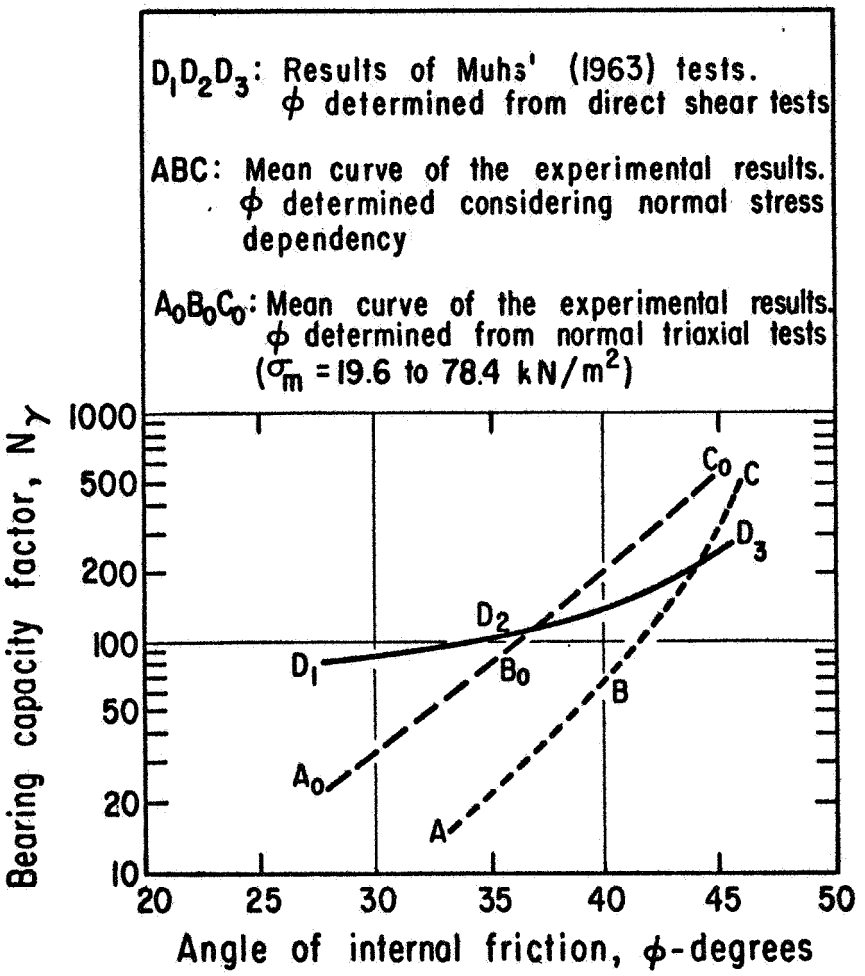

FIG. 2.7 BEARING CAPACITY FACTOR N_γ DETERMINED FROM EXPERIMENTS (After De Beer, 1967)

rupture increases with the width of the footing. This dependency may be inferred from Fig. 2.8, which relates relative settlement at failure to footing size.

Influence of Base Roughness

The primary bearing capacity factors shown in Fig. 2.4 apply only to perfectly rough bases ($\delta/\phi = 1$). Investigations by Meyerhof (1955) and others indicate that in cohesive soils the roughness has little influence on the bearing capacity. However, in cohesionless soils, the bearing capacity of a surface footing with a smooth base is significantly less than that for a footing with a rough base. To account for this difference, Meyerhof has suggested that the N_γ factor be multiplied by a roughness factor (r_γ), expressed as:

$$r_\gamma = n_r + \frac{1}{2}(1-n_r^2) \tag{2.23}$$

where n_r is the degree of roughness, defined by the ratio of the tangents of the angle of base friction (δ), and the angle of internal friction (ϕ):

$$n_r = \tan\delta/\tan\phi \tag{2.24}$$

Equation 2.23 applies only to plane, horizontal bases at the soil surface.

Hansen and Christensen (1969) calculated N_γ values for different values of base roughness and angle of internal friction. Their results are shown in Fig. 2.9, which indicates that the values of N_γ for perfectly smooth footings ($\delta=0$) are approximately one-half the values of N_γ for perfectly rough footings ($\delta=\phi$).

Recently, Graham and Stuart (1971) presented solutions showing the influence of base roughness and various assumptions as to the distribution of friction along the base upon N_γ factors. A graphical summary of their solutions compared to other theoretical solutions is given in Fig. 2.10.

Influence of Base Configuration

The influences of various non-planar base configurations (e.g., wedges and cones) on bearing capacity factors have been obtained, with certain assumptions and under certain conditions, by Meyerhof (1961a). As an example, the bearing capacity factors for shallow strip loading on smooth and rough wedges in a soil with $\phi=30°$ are shown in Fig. 2.11.

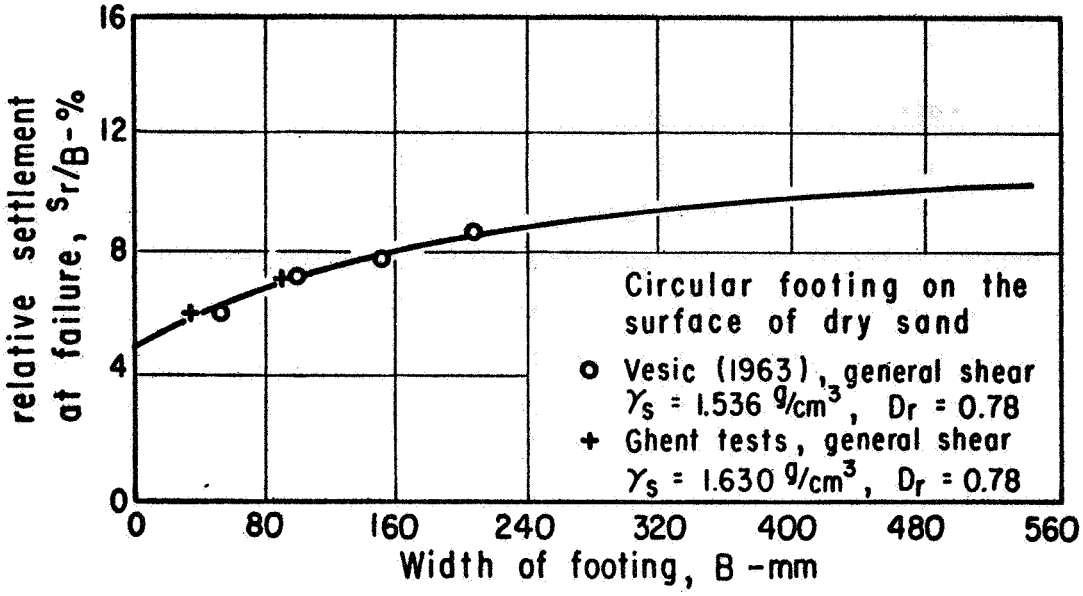

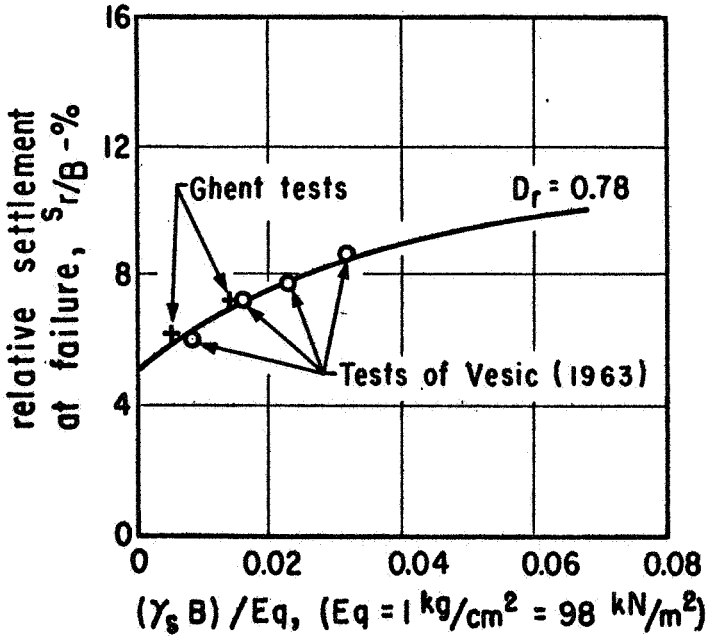

FIG. 2.8 RELATIVE SETTLEMENT AT FAILURE AS A FUNCTION OF FOUNDATION SIZE (After De Beer, 1967)

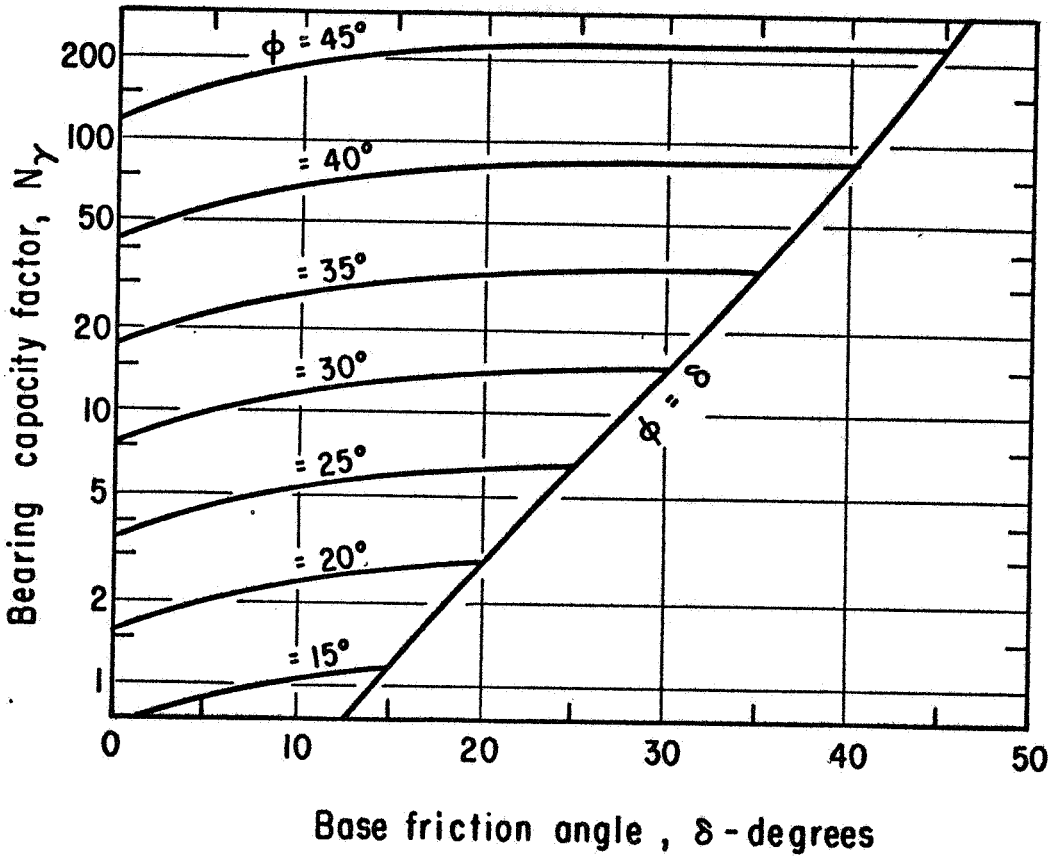

FIG. 2.9 BEARING CAPACITY FACTOR N_γ FOR STRIP FOOTINGS AS A FUNCTION OF ϕ AND δ (After Hansen and Christensen, 1969)

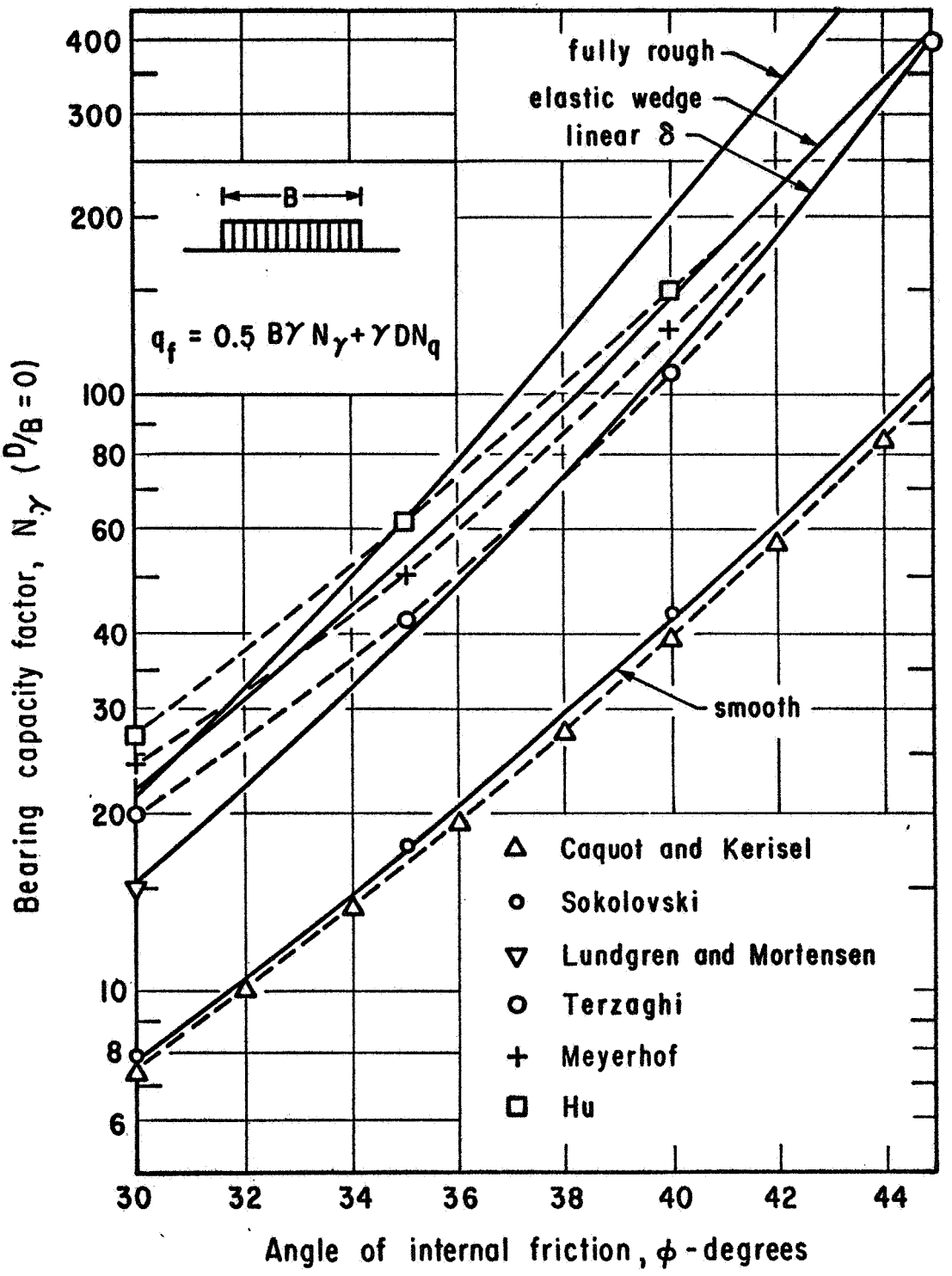

FIG. 2.10 COMPARISON OF THEORETICAL SOLUTIONS FOR N_γ FOR SURFACE FOOTINGS (Zero surcharge), (After Graham and Stuart, 1971)

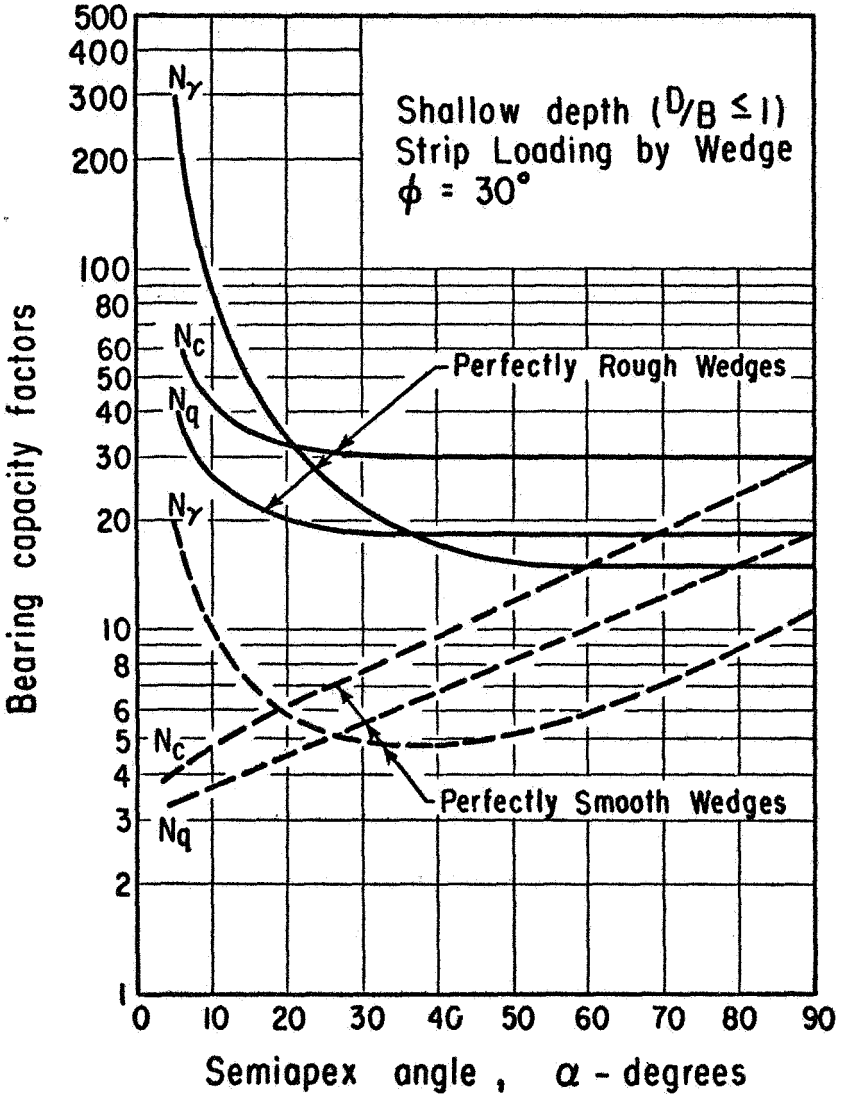

FIG. 2.11 BEARING CAPACITY FACTORS FOR WEDGES
(After Meyerhof, 1961a)

For perfectly rough wedges, there is little dependence of bearing capacity factors on the total apex angle (2α) for values of 2α greater than 90°. That is, for rough wedges and cones with obtuse apex angles, the bearing capacity factors are nearly equal to those for plane and horizontal contact areas. However, for perfectly smooth wedges, the values of N_c and N_q increase with increasing total apex angle.

Values of N_c as a function of apex angle for perfectly smooth and rough cones at shallow and great depths in purely cohesive (ϕ =0) soil as presented by Meyerhof (1961a) are shown in Fig. 2.12.

Influence of Soil Compressibility

Vesic (1967) has suggested that the relative compressibility of a sand mass may be expressed in terms of its rigidity index, I_r, defined as:

$$I_r = \frac{E}{(1+\nu)(c+q\tan\phi)} \tag{2.25}$$

where E = elastic modulus

c = soil cohesion

ϕ = soil friction angle

q = overburden pressure

ν = Poisson's ratio

Bearing capacity factors calculated by Vesic (1967) using the assumption that the ultimate pressure on the soil cone under a foundation is equal to the ultimate pressure needed to expand a spherical cavity inside the same soil mass are given in Fig. 2.13.

Vesic (1963) has also suggested that, for compressible soils, local (or punching) shear failure, rather than general shear failure, occurs. Based on the shear pattern shown in Fig. 2.14a, the following expression for N_q was developed:

$$N_q = e^{3.8\phi \tan\phi} \tan^2(45° + \frac{\phi}{2}) \tag{2.26}$$

This equation is plotted and compared to the classic Reissner equation for N_q for general shear in Fig. 2.14b. It may be seen in Figs. 2.13 and 2.14 that for compressible soils (local shear conditions), the bearing capacity factor N_q is much lower than for incompressible soils (general shear conditions).

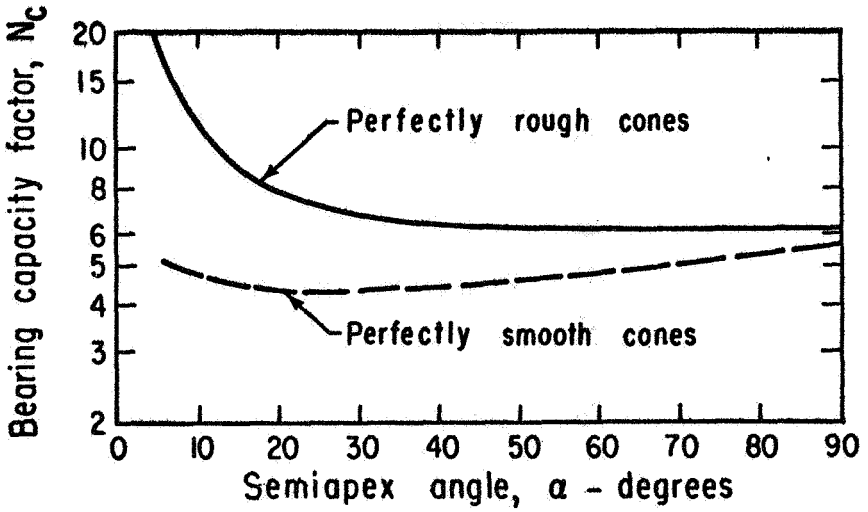

(a) SHALLOW DEPTHS

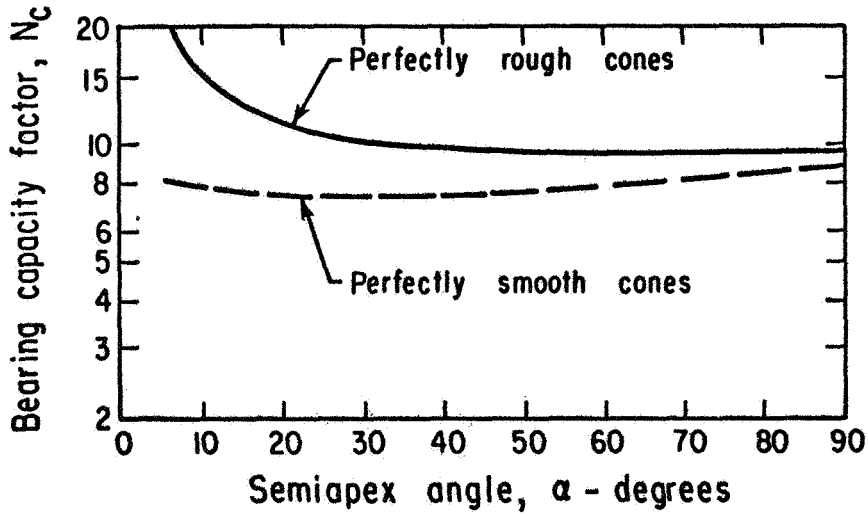

(b) GREAT DEPTHS

FIG. 2.12 BEARING CAPACITY FACTOR N_c FOR PURELY COHESIVE SOIL (After Meyerhof, 1961a)

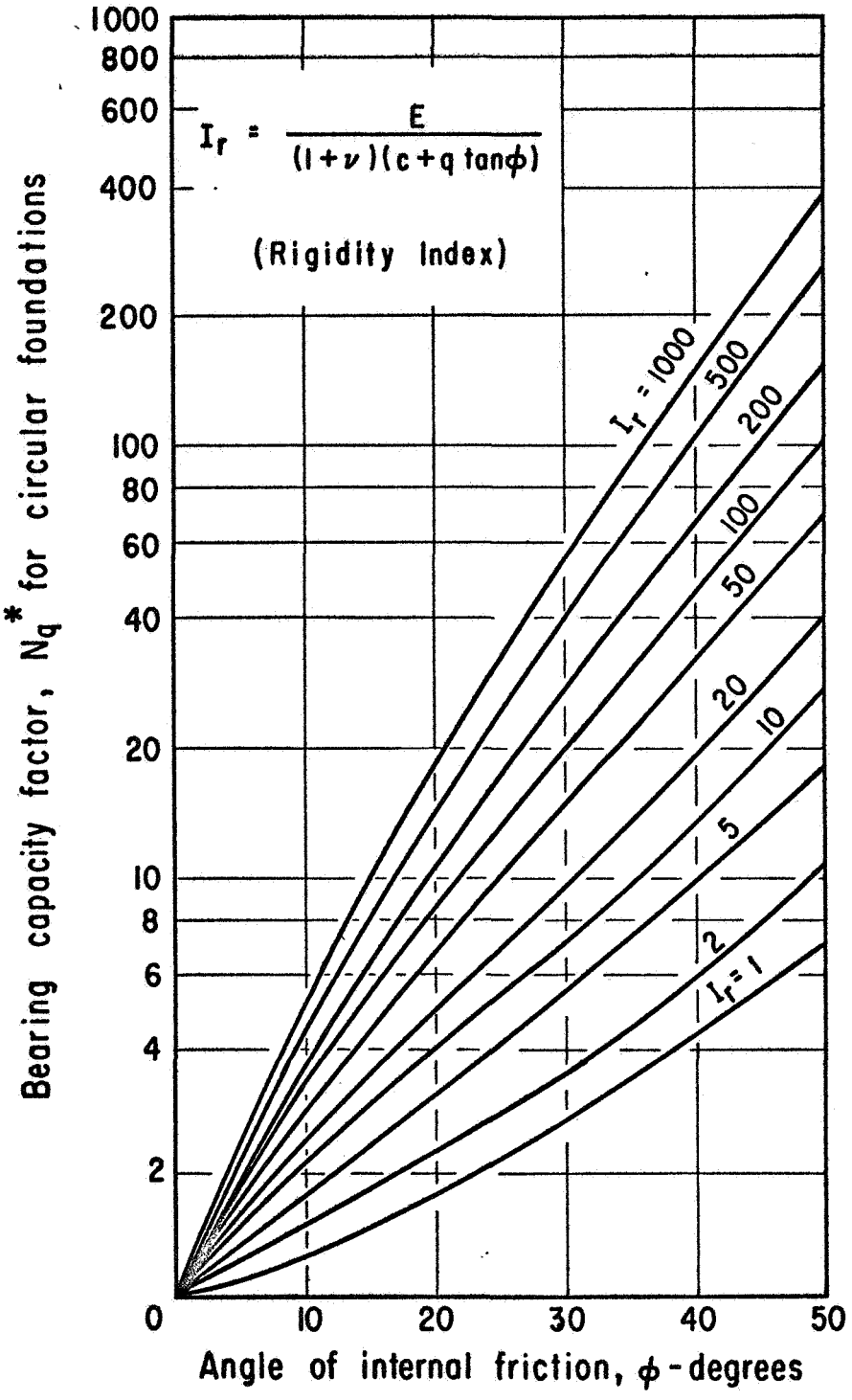

FIG. 2.13 BEARING CAPACITY FACTOR N_q FOR COMPRESSIBLE SOIL

(After Vesic, 1967)

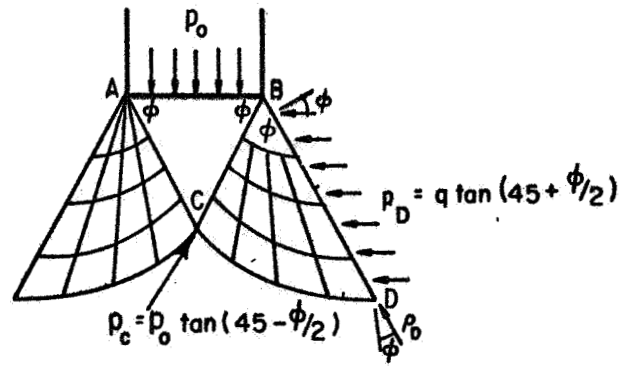

FIG. 2.14a FAILURE MODE FOR LOCAL SHEAR
(After Vesic, 1963)

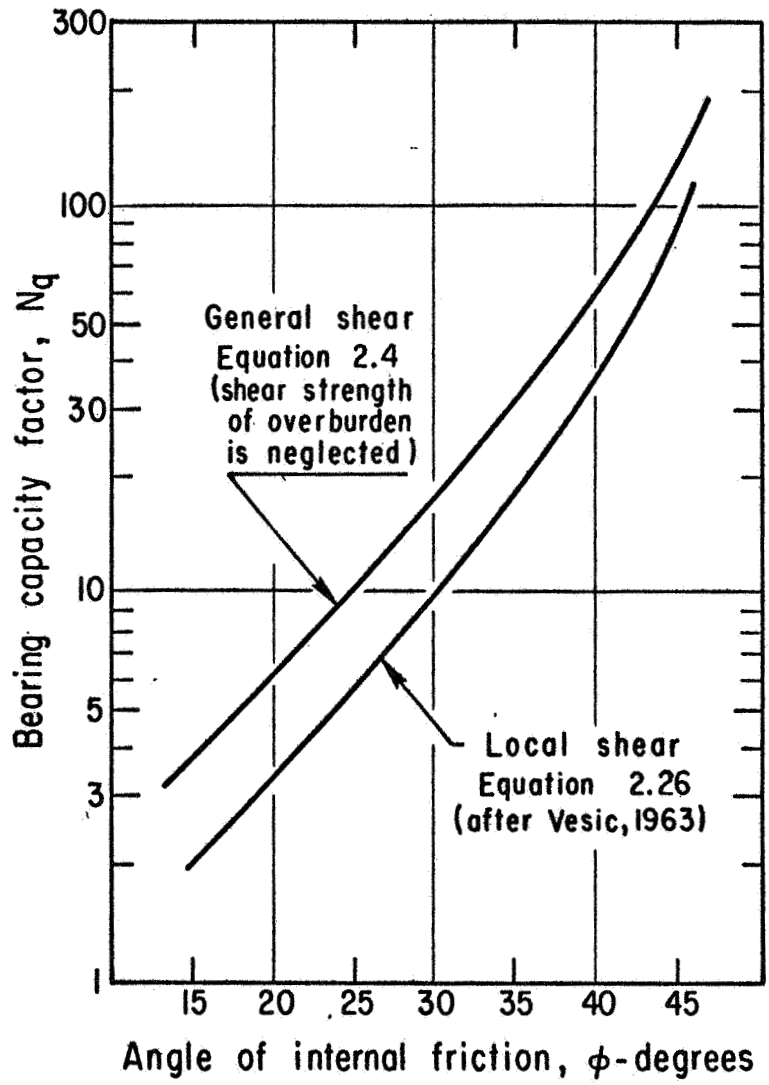

FIG. 2.14b COMPARISON OF BEARING FACTOR N_q
FOR LOCAL AND GENERAL SHEAR

APPLICATIONS OF DIMENSIONAL ANALYSIS TO STATIC PENETRATION

General

Many problems may be analyzed by considering model tests that are assumed to give a true representation of prototype phenomena, but at a reduced scale. In order to apply classical dimensional analysis geometric, dynamic, and kinematic similarity requirements must be satisfied.

The static penetration problem may include the following variables:

q_f = unit base resistance
γ_s = unit weight of soil
B = base width of the penetrometer
D = penetration depth
ϕ = soil friction angle
c = soil cohesion
δ = penetrometer to soil friction angle
2α = penetrometer base apex angle (wedges or cones)

Geometric similarity requires that

$$(D/B)_{model} = (D/B)_{prototype} \tag{2.27}$$

Dynamic similarity however, demands that:

$$q_f/(\gamma_s B)_{model} = q_f/(\gamma_s B)_{prototype} \tag{2.28}$$

Considerations of kinematic similarity may be ignored in the static penetration problem because the velocities involved are insignificant.

Lundgren (1957) states that, in order to represent the static penetration test in dimensionally correct form, the following relationship should be used:

$$D/B = f[q_f/(\gamma_s B)] \tag{2.29}$$

Hvorslev (1970) indicates that consideration of the dimensionless ratio $q_f/(\gamma_s B)$ from the general bearing capacity equation is convenient in the investigation of data for different penetrometer sizes and soil conditions.

Cohesive Soils (ϕ=0)

The bearing capacity equation for cohesive soils is normally expressed in the following form:

$$q_f = cN_c d_c + \gamma_s D N_q d_q \tag{2.30}$$

For purely cohesive soils (ϕ=0), N_q = 1.0 and d_q = 1.0. Also, for D $\leq$ 5B, and assuming that d_c is a linear function of relative depth (D/B), Equation 2.30 may be rewritten in dimensionless form:

$$q_f/c = N_c d_c + \frac{\gamma_s B}{c} (D/B) \qquad (2.31)$$

For γ_s and c constant, but variable B, Equation 2.31 will yield families of curves in terms of the parameters q_f/c and D/B. For shallow depths and small footing widths, the second term in Equation 2.31 is negligible and the equation may be written in the following form:

$$q_f/c = N_c d_c \qquad (2.32)$$

which, represents a single curve for different sizes as shown in Fig. 2.15a. However, Equation 2.32 should not be used for high values of D and B or very small values of cohesion without first estimating the relative influence of the second term in Equation 2.31.

Cohesionless Soils (c=0)

The bearing capacity equation for cohesionless soils is normally expressed in the following form:

$$q_f = \gamma_s D N_q d_q + \frac{1}{2} \gamma_s B N_\gamma d_\gamma \qquad (2.33)$$

As shown in the analysis of depth factors, d_γ = 1.0 and for small depths (D$\leq$5B) d_q is a linear function of relative depth (D/B). Then Equation 2.33 can be written in dimensionless form:

$$q_f/(\gamma_s B) = N_q d_q \frac{D}{B} + \frac{1}{2} N_\gamma \qquad (2.34)$$

Therefore, a plot of the parameters $q_f/\gamma_s B$ vs. (D/B) yields a single curve independent of the value of B, as shown in Fig. 2.15b. In recent years, various investigators have used these dimensionless parameters for graphical representation of the results of plate bearing tests on cohesionless soils. This equation does not, however, consider settlements that occur before the bearing capacity is developed.

Cohesion-Friction (c-ϕ) Soils

The bearing capacity equation for c-ϕ soils is normally expressed in the following form:

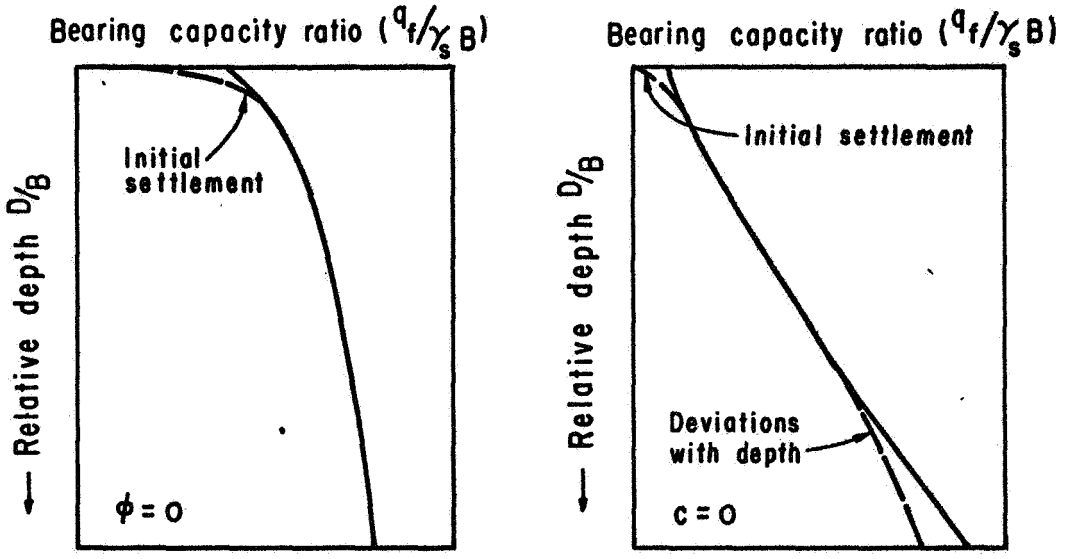

a. CLAY b. SAND

FIG. 2.15 BEARING CAPACITY RATIOS VERSUS RELATIVE DEPTH (After Hvorslev, 1970)

$$q_f = cN_c d_c + \gamma_s D N_q d_q + \frac{1}{2}\gamma_s B N_\gamma d_\gamma \qquad (2.35)$$

For small depths, d_c and d_q are linear functions of relative depth (D/B). The factor d_γ equals 1.0 for all depths. Therefore, Equation 2.35 may be written in dimensionless form as follows:

$$q_f/(\gamma_s B) = [c/(\gamma_s B)]N_c d_c + N_q d_q \frac{D}{B} + \frac{1}{2} N_\gamma \qquad (2.36)$$

For c-ϕ soils, the ratio $q_f/(\gamma_s B)$ is not independent of B, because c is a soil constant and the ratio $c/(\gamma_s B)$ decreases with increasing values of B. That is, results of bearing capacity or penetration tests with penetrometers of various sizes will form a family of curves, and the values of $q_f/(\gamma_s B)$ for a given value of D/B will decrease with increasing values of B. However, Equation 2.36 can be used to estimate c and ϕ separately by having penetration data with two different sizes of cone. A proposed procedure for this calculation is outlined in Chapter Seven.

STATIC PENETRATION TEST AND ITS APPLICATIONS

Description

Although static penetrometer equipment and procedures have not been standardized, some generally accepted practices have been developed. The Dutch Cone (Fig. 2.16a) is widely used. It has a base area of 10 sq cm and apex angle of 60°. The rate of penetration is from 15 to 20 mm/sec. The normal sounding test (early version) has the following procedure:

The tube is pushed together with rod and cone (see Fig. 2.16a) into soil for about 0.3 meters. Subsequently, only the inner rod is pushed downward while the tube is retained by the skin friction of the soil. The resistance to cone penetration is generally measured by a hydraulic gage. After penetration of the cone for about 125 mm, the tube is pushed down without pressure on the inner rod and cone. When the tubes are pressed further into the soil the cone moves down with the tube so that full frictional and cone resistance will be obtained. Tube and cone are advanced 75 mm after which the procedure is repeated thus giving measurements of total friction and cone resistance every 0.2 m.

The sounding equipment was improved by Vermeiden (1948), who developed the sleeve cone (see Fig. 2.16b) because of difficulties experienced with

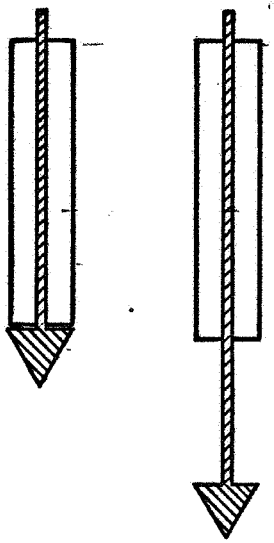

FIG. 2.16a
ORIGINAL MECHANICAL CONE
IN RETRACTED AND EXTENDED
POSITION

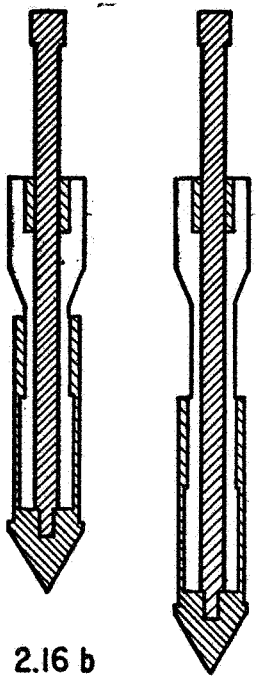

FIG. 2.16 b
MECHANICAL DELFT CONE (Sleeve Cone)
PENETROMETER IN RETRACTED AND
EXTENDED POSITION

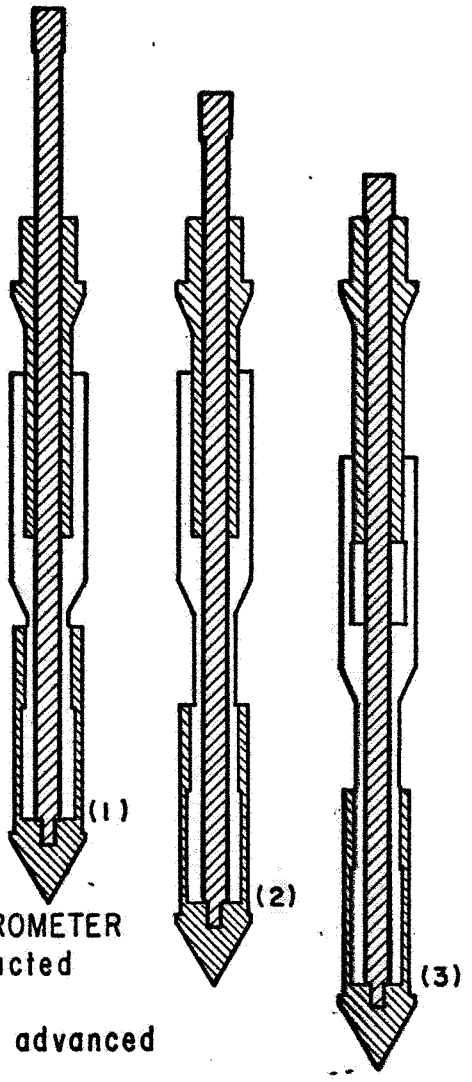

FIG. 2.16 c
BEGEMANN FRICTION CONE PENETROMETER
(1) Cone and friction sleeve retracted
(2) Cone in extended position
(3) Cone and friction sleeve both advanced

the original cone associated with friction between tube and rod due to sand particles. In the procedure used by the Department of Municipal Works of Rotterdam, tube and rod are advanced simultaneously while the forces on tube and rod are measured separately. The measurements are generally performed automatically at the top of the rods by means of an electric pressure-gauge.

Begemann (1965) reported the development of a friction cone (see Fig. 2.16c) enabling the measurement of local friction along a sleeve. The ratio of friction to cone resistance was found to be dependent on the type of soil, thus permitting an approximate determination of the soil profile. Later, electric strain gage penetrometers were developed, as described by De Ruiter (1971).

Determination of Soil Type

Begemann (1965, 1969) has shown that there is a definite relationship between the ratio of unit frictional resistance (f_s) to unit cone resistance (q_c) and the soil type as shown in Fig. 2.17. Schmertmann (1967) proposed the following ratios:

Soil Type	f_s/q_c (%)
soft rock or shells	0.0 - 0.5
sand	0.5 - 2.0
silt	2.0 - 5.0
clay	> 5.0

Determination of Soil Compressibility

There have been many attempts to relate compressibility of soils to the cone resistance. Bachelier and Parez (1965) gave the following relationship for oedometer modulus (E), and cone resistance for silty and clayey soils:

$$E = 2.3\ (q_c/\alpha) \qquad (2.37)$$

where α is a soil constant.

The values of α for different types of soil tested were in the range of 0.33 to 1.0.

Schmertmann (1970) proposed the following relationship between compressibility modulus of cohesionless soils and the cone resistance:

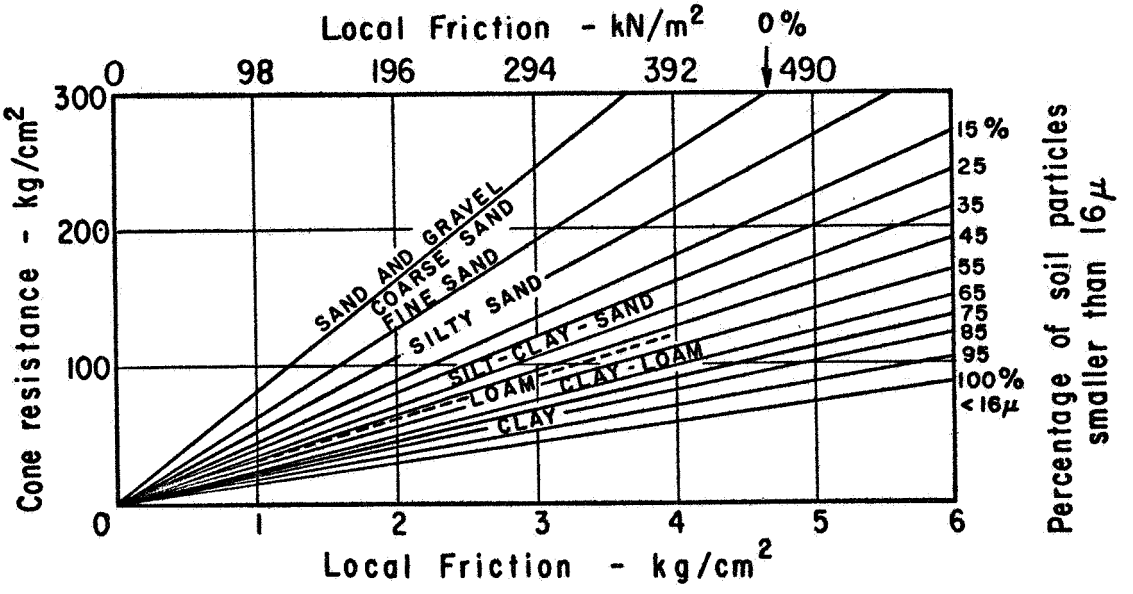

FIG. 2.17 RELATIONSHIP BETWEEN CONE RESISTANCE, LOCAL FRICTION AND SOIL TYPE
(After Begemann, 1969)

$$E_s = 2.0\ q_c \tag{2.38}$$

where E_s = Young's modulus for sand in kg/cm^2

q_c = Dutch cone bearing capacity in kg/cm^2

Determination of Shear Strength of Cohesive Soils

There have been many attempts to relate undrained shear strength of cohesive soils to cone penetration resistance. Gawith (1952) proposed the following relationships:

$$c = q_c/10 \quad \text{for soft clay} \tag{2.39}$$

$$c = q_c/14.8 \quad \text{for firm compact clay} \tag{2.40}$$

where c = cohesion in kg/cm^2

q_c = Dutch cone bearing capacity in kg/cm^2

Later, Begemann (1965) gave the following relationship based on friction cone data:

$$c = q_c/14 \tag{2.41}$$

where c = cohesion in kg/cm^2

q_c = Dutch cone bearing capacity in kg/cm^2

SUMMARY

Primary bearing capacity factors based on classical Prandtl-Reissner solutions are widely used in Equation 2.6 to compute the ultimate bearing capacity of shallow foundations. The utilization of two different slip surfaces for the determination of the different bearing capacity factors (N_c, N_q, and N_γ) has been shown to underestimate the bearing capacity, in some cases by as much as 17 percent.

The ultimate bearing capacity of deep foundations is generally determined using primary bearing capacity factors and ignoring the shear strength of the overburden as proposed by Terzaghi (1943). However, in general shear failure the shear strength of the overburden cannot be neglected. Brinch Hansen (1961) proposed modification of the primary bearing capacity factors with empirically determined depth factors for the determination of the unit bearing resistance of deep foundations.

Many slip line geometries have been assumed for determining the bearing capacity of deep foundations, and the range of bearing capacity

values obtained from the different assumed failure mechanisms is large. Experimental justification for a proposed slip line geometry at failure for deep foundations has been provided by Biarez et al (1961) who showed that the slip surface reaches vertical tangency provided that the relative depth of the foundation is sufficiently large. The validity of the slip line geometry proposed by Biarez should be further investigated for the continuous deep penetration of penetrometers with different base configurations. Further, because of the large deformations involved, the fundamentals of the progressive development of failure surfaces during continuous penetration must be investigated.

Meyerhof (1961a) investigated the influence of base configuration on the slip line geometry in the vicinity of the base. It was postulated that a soil cone (or wedge) forms under rough, blunt bases and that a plane shear zone forms adjacent to smooth, sharp bases. However, the validity of these assumptions needs experimental justification. Further, the influence of base configuration on slip line geometry in the vicinity of the base for intermediate base roughnesses ($0<\delta/\phi<1$) should be studied. The extent of the plane shear zone, if any, should be formulated in terms of soil friction angle (ϕ) and base roughness (δ/ϕ) and the validity of any theoretical considerations should be justified by observations.

The only analytical solution available for the determination of the bearing capacity of wedges (or cones) is given by Meyerhof (1961a). This solution is valid only for very shallow and very deep foundations and perfectly rough or smooth bases. In this solution bearing capacity factors are given as a function of base apex angle and soil friction angle. The shortcomings of this solution can be summarized as follows:

(1) Bearing capacity will be overestimated, even in general shear failure, due to the invalidity of the assumed failure mechanism for deep foundations (see Table 2.1).

(2) For a given relative depth (D/B) of foundation, the bearing capacity can only be determined by linear interpolation between solutions for shallow ($D/B<1$) and deep foundations. Such interpolation is later shown to be incorrect.

(3) For a given intermediate base roughness ($0<\delta/\phi<1$), the bearing capacity can only be determined by linear interpolation (later shown incorrect) between solutions corresponding to perfectly rough and perfectly smooth bases.

(4) No solutions are provided for determining N_c when the soil friction angle is larger than 30°.

Meyerhof (1955) and other investigators have indicated that for cohesive soils the roughness of a plane and horizontal contact area has little influence on bearing capacity. However, in cohesionless soils, the bearing capacity of a surface footing with a smooth base is only about half of that for a footing with a rough base.

Numerical solutions utilizing the Haar and von Karman hypothesis have been developed to determine the bearing capacity of circular shallow and deep foundations. However, these theoretical calculations are open to doubt, because the validity of Haar and von Karman hypothesis for soils is questionable. For this reason, it is concluded that theoretical calculations of bearing capacities developed for circular foundations are still so uncertain that the best estimates are made by the application of empirical shape factors to the bearing capacity factors for strip foundations. Many empirical relationships for shape factors have been proposed, however, resulting in great range of values. Therefore, it is concluded that the validity of these relations over the range of interest should be investigated experimentally.

Since general shear failure cannot reasonably be assumed for compressible soils, the influence of soil compressibility should be considered in determination of the bearing capacity (or unit penetration resistance) of foundations. There have been some empirical methods proposed which account for soil compressibility, but their general validity has not yet been established.

For cohesionless soils, stress-strain relationships are stress, strain and density dependent. Because of progressive rupture, the proper selection of soil friction angles in the determination of the penetration resistance should be investigated.

Many empirical relationships have been proposed to relate soil shear strength parameters, soil compressibility, and soil type to penetration resistance. However, no theory heretofore available has explicitly accounted for the influence of such important variables as base configuration, base roughness, and relative depth over the range of values of interest. The analytical procedures developed in this study which are presented in detail in the following chapters should provide a basis for overcoming some of these deficiencies.

CHAPTER THREE

FAILURE MECHANISM ASSOCIATED WITH STATIC PENETRATION

PREVIOUS STUDIES

The failure mechanism associated with static penetration has been previously investigated both theoretically and experimentally. Terzaghi (1943) and Meyerhof (1951) both proposed that the slip line of the radial shear zone under a strip foundation (see Fig. 2.1) may be approximated by a logarithmic spiral (theoretically correct for weightless soils). Meyerhof (1961a) reasoned theoretically that a plane shear zone exists adjacent to the penetrometer base. Biarez et al (1961) observed experimentally that a rigid wedge (or cone) develops under the base of rough flat-ended penetrometers for relative depths greater than one (D/B>1). The fact that for great relative depths the slip line of the radial shear zone reaches vertical tangency was experimentally shown by Biarez et al (1961) and applied to pile foundations (flat-ended) by Hu (1965). To date, no model studies have been reported which consider the effects of base configurations other than flat. Also, the effect of base roughness on the failure mechanism associated with wedge-shaped and conical penetrometers has not been studied.

MODEL STUDIES

General

Model tests were performed to establish a rational basis for theoretical developments and to improve the understanding of penetrometer-soil interaction. The effects of penetrometer configuration, penetrometer to soil friction, soil relative density, and relative depth on the failure mechanism were investigated.

Materials and Equipment

The models were constructed in a special lucite box with inside dimensions of 15"x15"x15" (0.38m x 0.38m x 0.38m). The box consisted of three sections, each 5.0 inches (0.13m) wide, held together with tie bars and made watertight by a sealant tape. The box was so designed that the

tie bars can be removed and a section of box can be separated. A steel plate and electrical vibrator were used to densify samples. To prepare loose samples, the sand was deposited above a screen which was then slowly raised. In order to level the successive sand layers during placement a special leveling plate (screed) was used. During trimming, the sample box was placed on a tilted platform in order to safely trim the desired sections. A spatula and a sharpened trowel were used to trim the sample.

The soil used in all the tests described herein was a fine air-dried sand, Monterey Sand No. 0 (engineering properties are given in Chapter Five). In order to facilitate observation of the failure mechanism, alternate horizontal layers of clean and colored sand were placed. The sand was colored using dye and carbon tetrachloride, a technique which minimizes the change in the characteristics of the sand.

Model Preparation and Testing Procedure

The models were prepared and tested as follows:

(1) A filter paper was placed inside the box on top of the water exit, to serve as a drain and to prevent piping during later saturation and drainage of the samples.

(2) The initial and subsequent alternate layers of clean and colored sand were placed and leveled carefully with the leveling plate. Changes in soil density due to placement of additional layers of sand were found to be insignificant.

(3) The elevation of soil was measured and the average density was calculated.

(4) Various penetrometers were pushed into the sand at a constant rate, 0.2 in./min. (5 mm/min.) and the resistance was measured with a load cell and recorded using an electronic recorder print-out system. Penetration was measured by movement of a marker on a ruler. The test was stopped upon reaching the desired base elevation.

(5) The penetrometer was disconnected from the load cell without disturbing the soil and left in the model.

(6) The sand was then water-saturated slowly from the bottom under a very low hydraulic gradient. About four hours were required. The settlement due to saturation was negligible.

(7) The model was then allowed to drain overnight. The capillary tension remaining in the wet sand after drainage allowed the sand to be safely trimmed when the box was clamped to a wooden platform inclined approximately 35° to the horizontal.

(8) The removable portion of the box was detached and the model trimmed along any desired section. Each section was photographed.

Results and Observations

More than 15 model tests were performed. The results of some of them are analyzed in the following paragraphs and summarized in Table 3.1. Photographs of the center sections of the models are given in Figs. 3.1 through 3.8. Observations based on studies of the center sections may be summarized as follows:

(1) For the tested range of relative depths (D/B) and relative densities, only general shear type failures were observed for tests using wedges. These test points are plotted on Fig. 3.9 which also shows the boundaries proposed by Vesic (1963) for different failure modes at various relative depths and relative densities. It may be seen that the limits of the general shear zone indicated by this research are wider than those proposed by Vesic for another sand. This difference is apparently due to the fact that the two sands do not have the same compressibility characteristics.

(2) A plane shear zone exists adjacent to the penetrometer base and the topmost angle of this zone varies with the roughness of the base as may be seen in Figs. 3.4, 3.5, and 3.6.

(3) Figs. 3.4, 3.5, and 3.6 also show a radial shear zone adjacent to the plane shear zone. It may be seen that the radial shear zone extends to the surface of the sand. Fig. 3.10 indicates that the slip surface of this zone may be closely approximated by a logarithmic spiral.

(4) Figs. 3.4 shows that, for penetrometers whose base dimension exceeds the shaft dimension, a zone of loose soil is created along the shaft.

(5) The approximate volume change of the soil during shear was calculated by studying the cross-section photographs. It appears that the soil dilated during shear in each case. The dilation zones

Table 3.1 SUMMARY OF MODEL TESTS

Model No.	Strain Conditions	Base Semi-Apex Angle α - Degrees	Roughness (δ/ϕ)	Relative Depth (D/B)	Relative Density, D_r (%)
1	Plane strain (wedge)	90	0.5	1.0	56.0
2	"	90	0.5	2.5	44.0
3	"	90	0.5	4.0	66.0
4	"	15	0.5	4.0	58.0
5	"	30	0.5	5.0	66.0
6	"	30	0.9	4.0	41.0
7	Axisymmetric (cone)	90	0.9	5.0	60.0
8	"	15	0.9	5.0	60.0
9	"	90	0.5	1.0	55.0
10	"	90	0.5	0.5	70.0

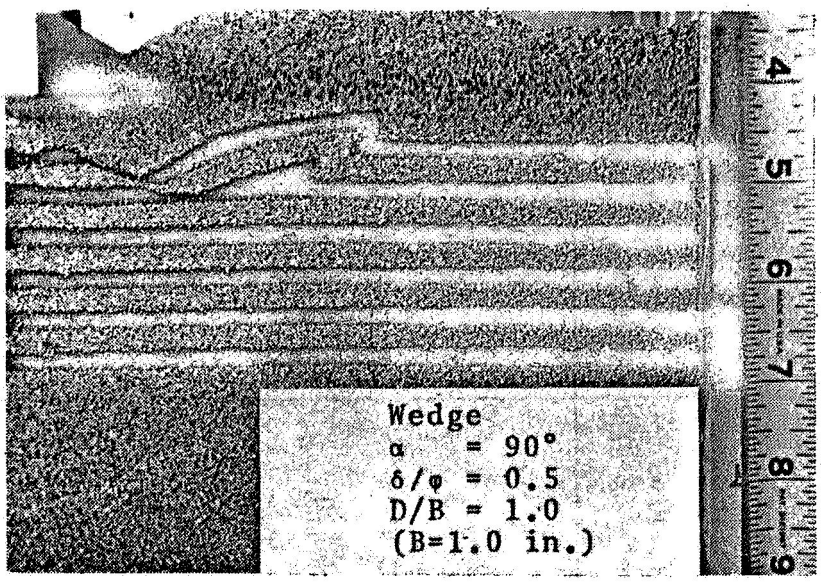

FIG. 3.1 a CENTER SECTION PHOTOGRAPH OF MODEL NO. 1

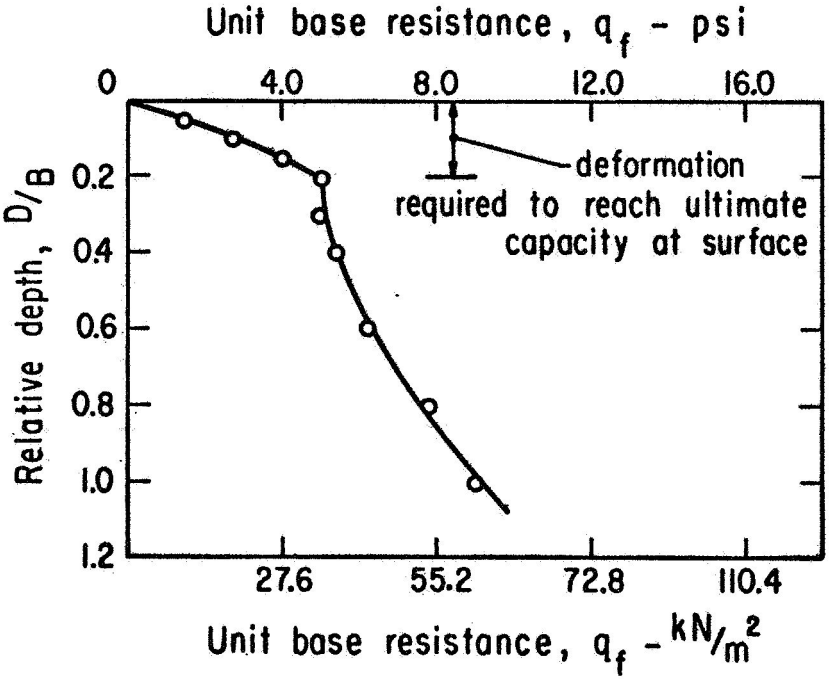

FIG. 3.1 b PENETRATION RESISTANCE CURVE FOR MODEL NO. 1

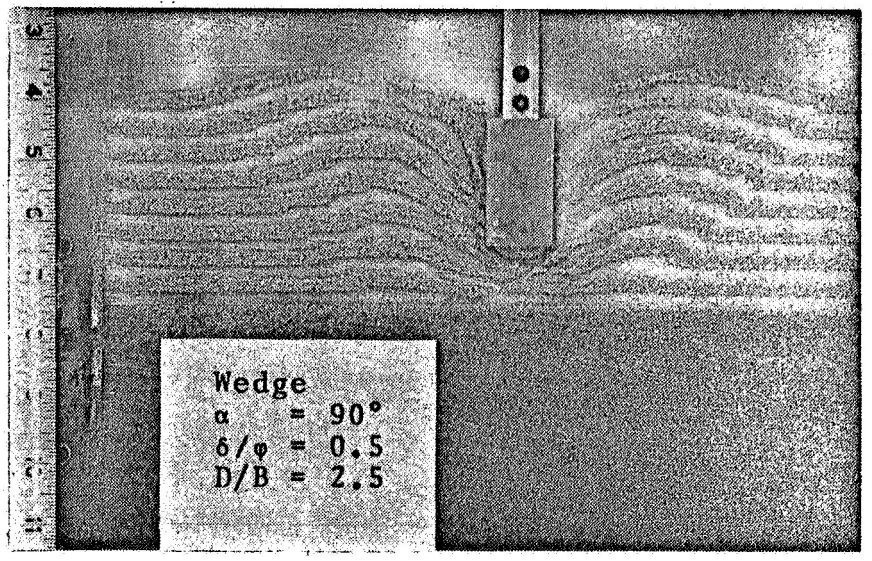

(a) OVERALL VIEW

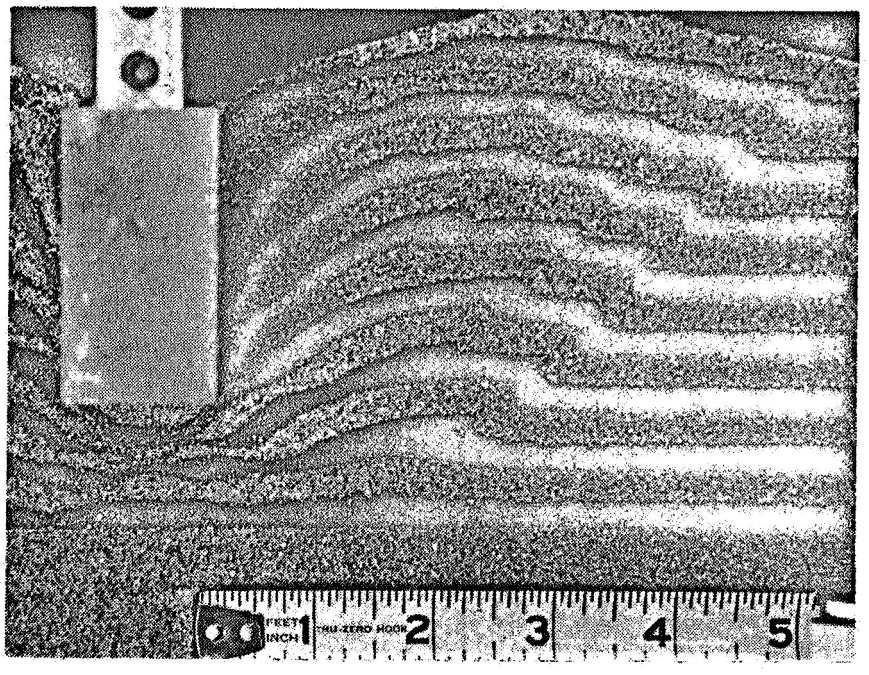

(b) CLOSE-UP VIEW

FIG. 3.2 CENTER SECTION PHOTOGRAPHS OF MODEL NO. 2

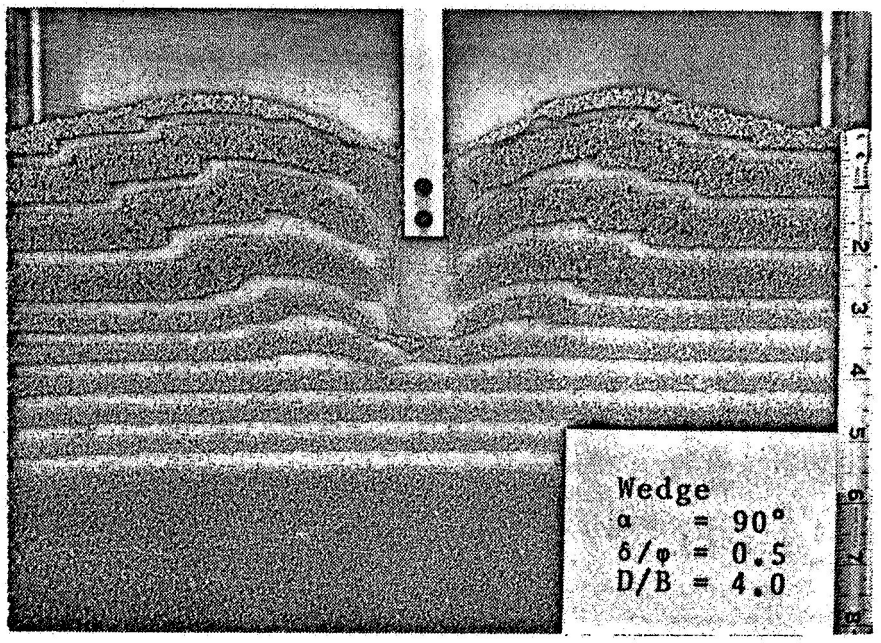

(a) OVERALL VIEW

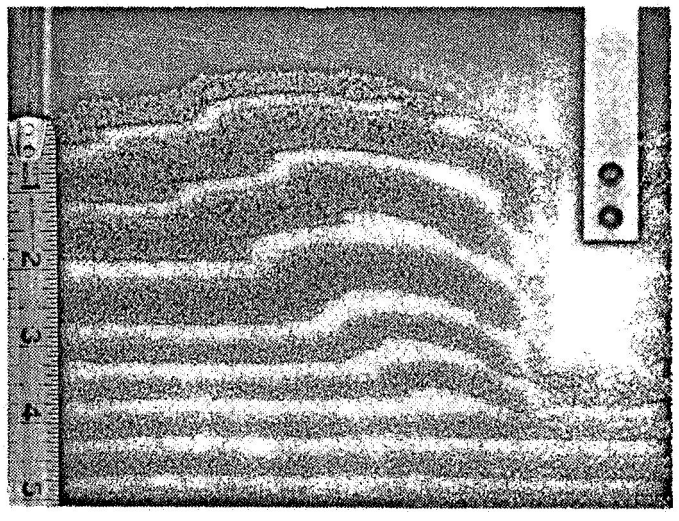

(b) CLOSE-UP VIEW

FIG. 3.3 CENTER SECTION PHOTOGRAPHS OF MODEL NO. 3

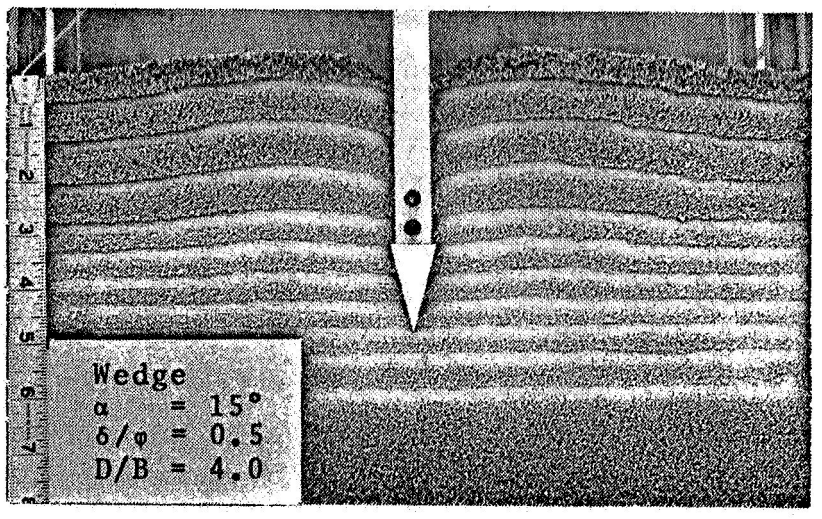

(a) OVERALL VIEW

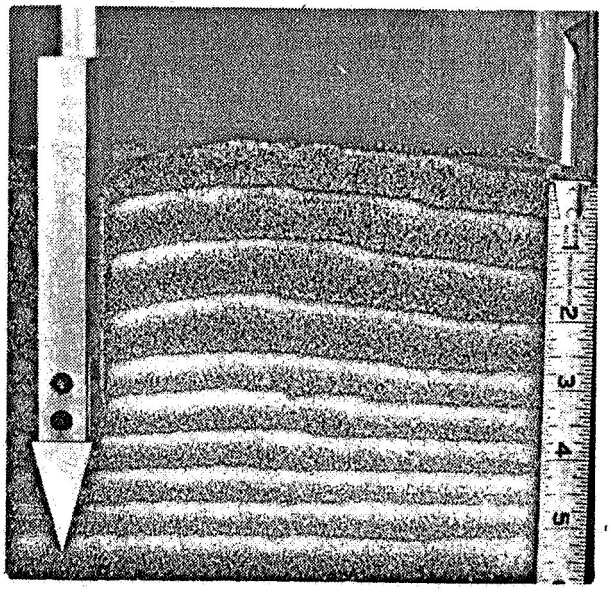

(b) CLOSE-UP VIEW

FIG. 3.4 CENTER SECTION PHOTOGRAPHS OF MODEL NO. 4

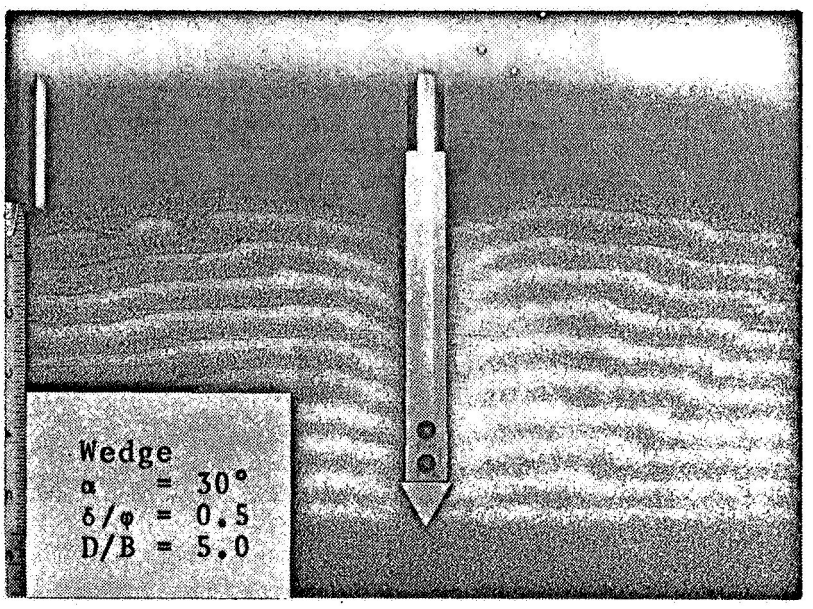

(a) OVERALL VIEW

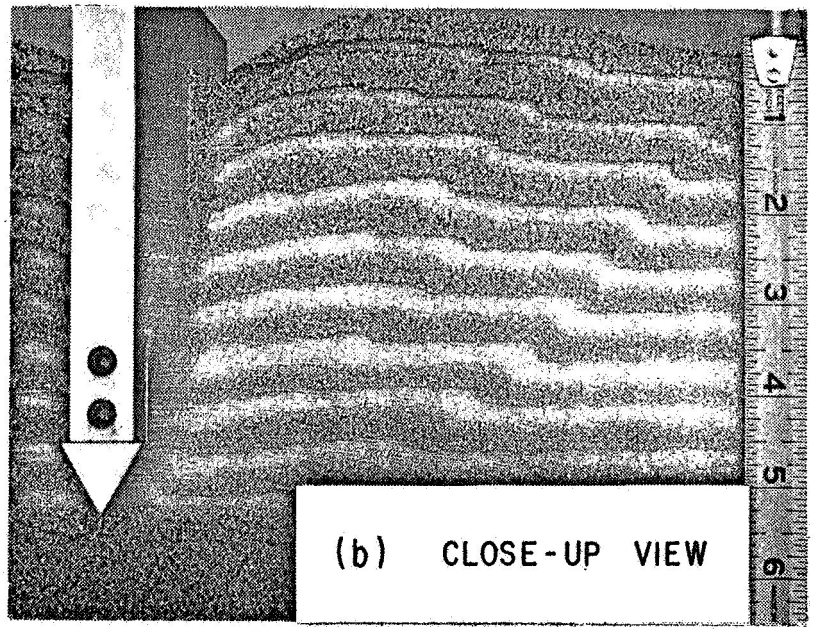

FIG. 3.5 CENTER SECTION PHOTOGRAPHS OF MODEL NO. 5

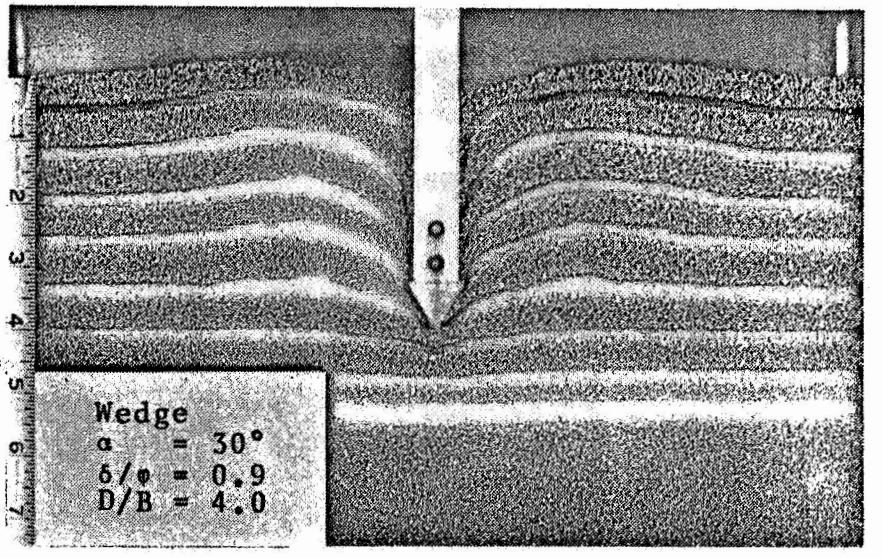

(a) OVERALL VIEW

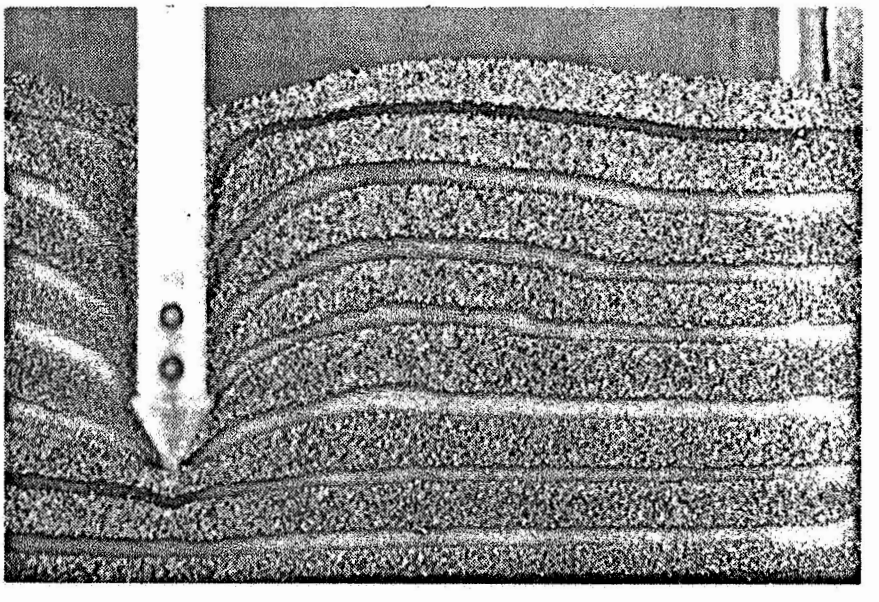

(b) CLOSE-UP VIEW

FIG. 3.6 CENTER SECTION PHOTOGRAPHS OF MODEL NO. 6

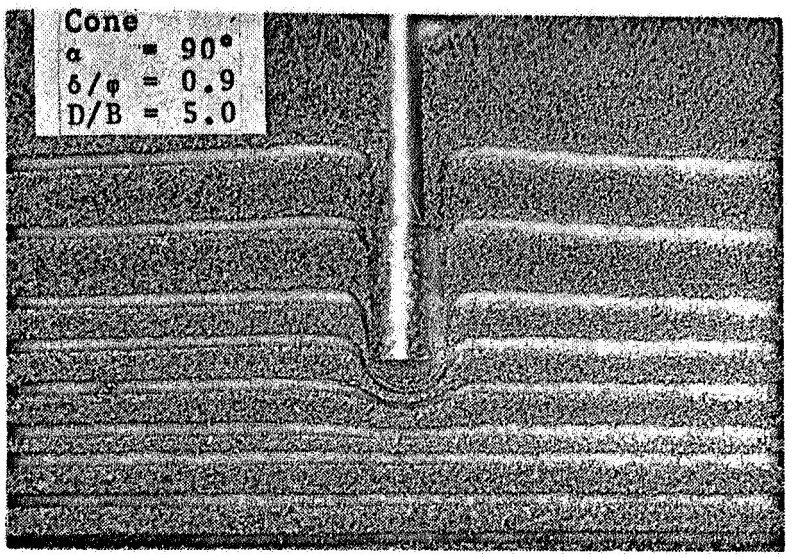

FIG. 3.7 a CENTER SECTION PHOTOGRAPH OF MODEL NO. 7

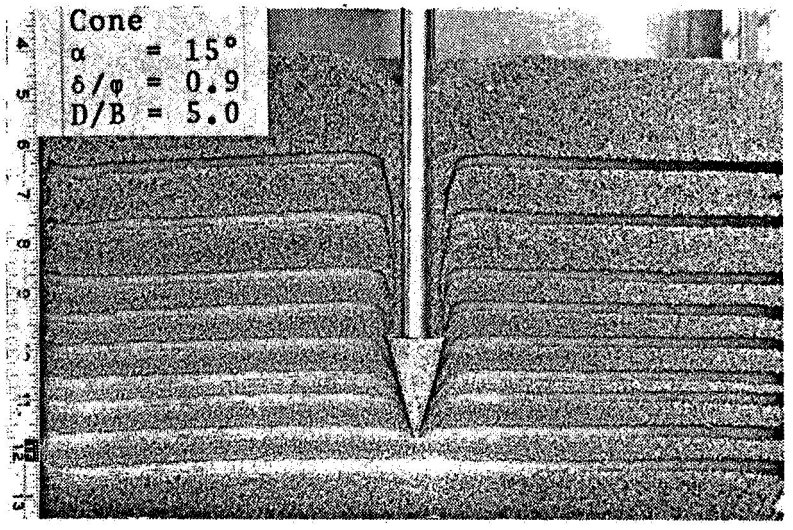

FIG. 3.7 b CENTER SECTION PHOTOGRAPH OF MODEL NO. 8

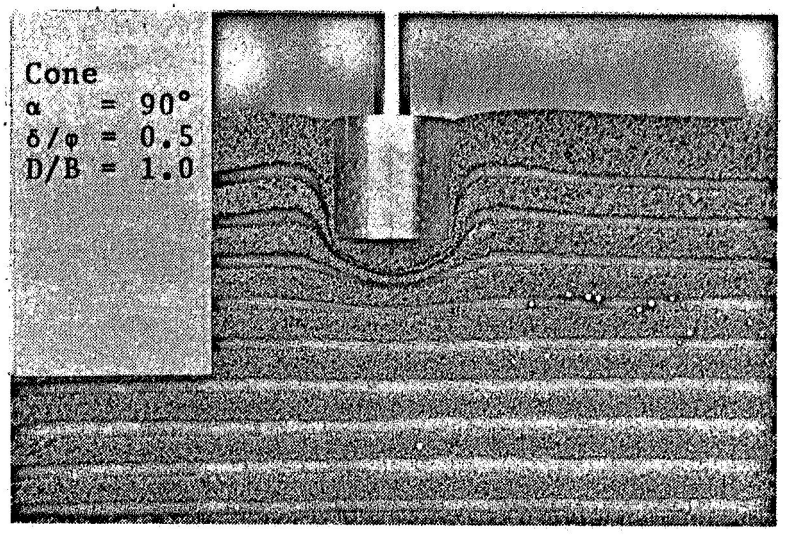

FIG. 3.8 a CENTER SECTION PHOTOGRAPH OF MODEL NO. 9

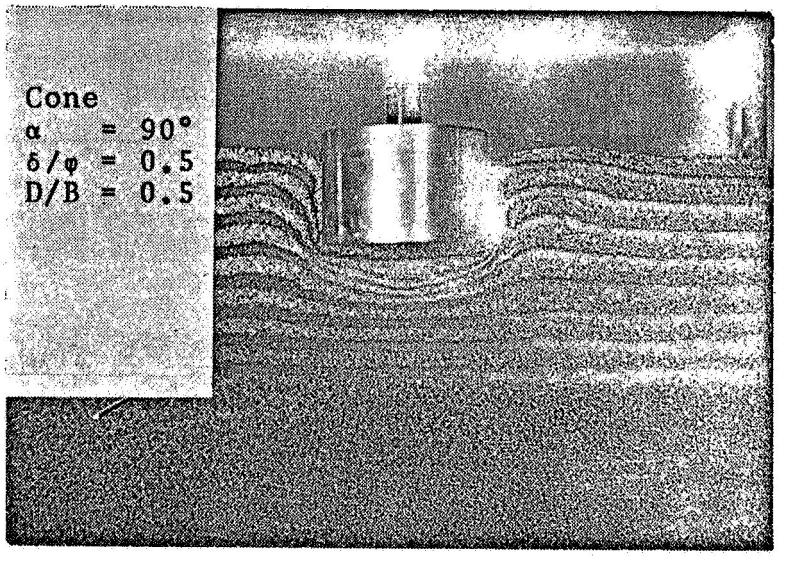

FIG. 3.8 b CENTER SECTION PHOTOGRAPH OF MODEL NO. 10

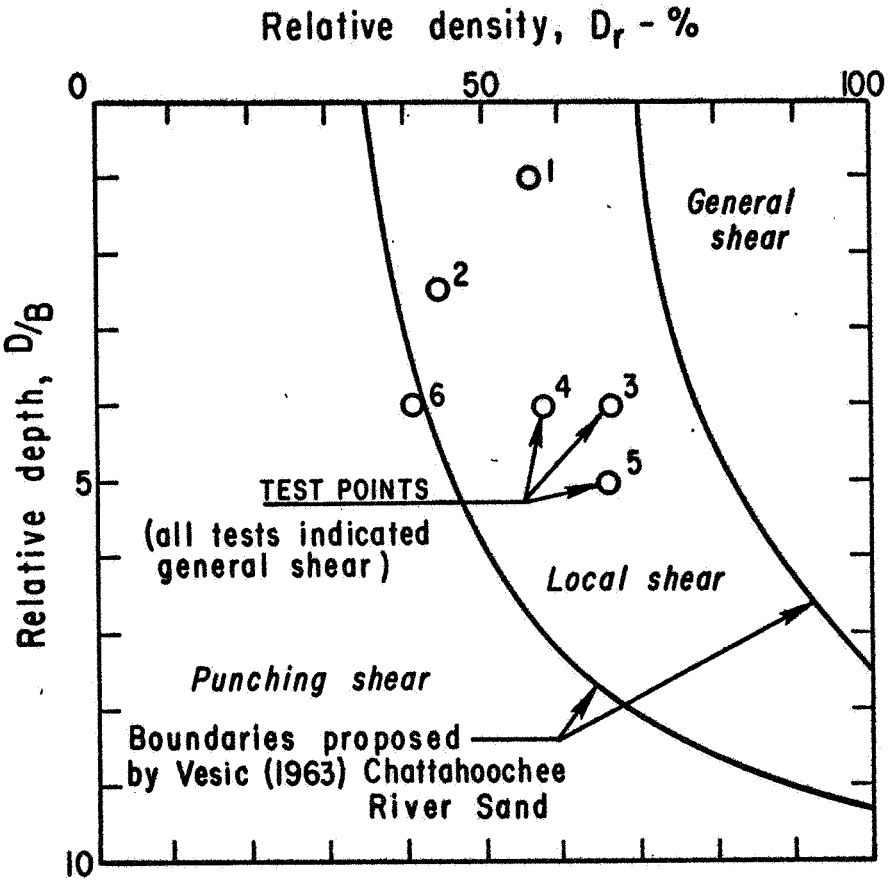

FIG. 3.9 TYPES OF FAILURE FOR FOUNDATIONS IN SAND AT DIFFERENT RELATIVE DEPTHS (D/B)

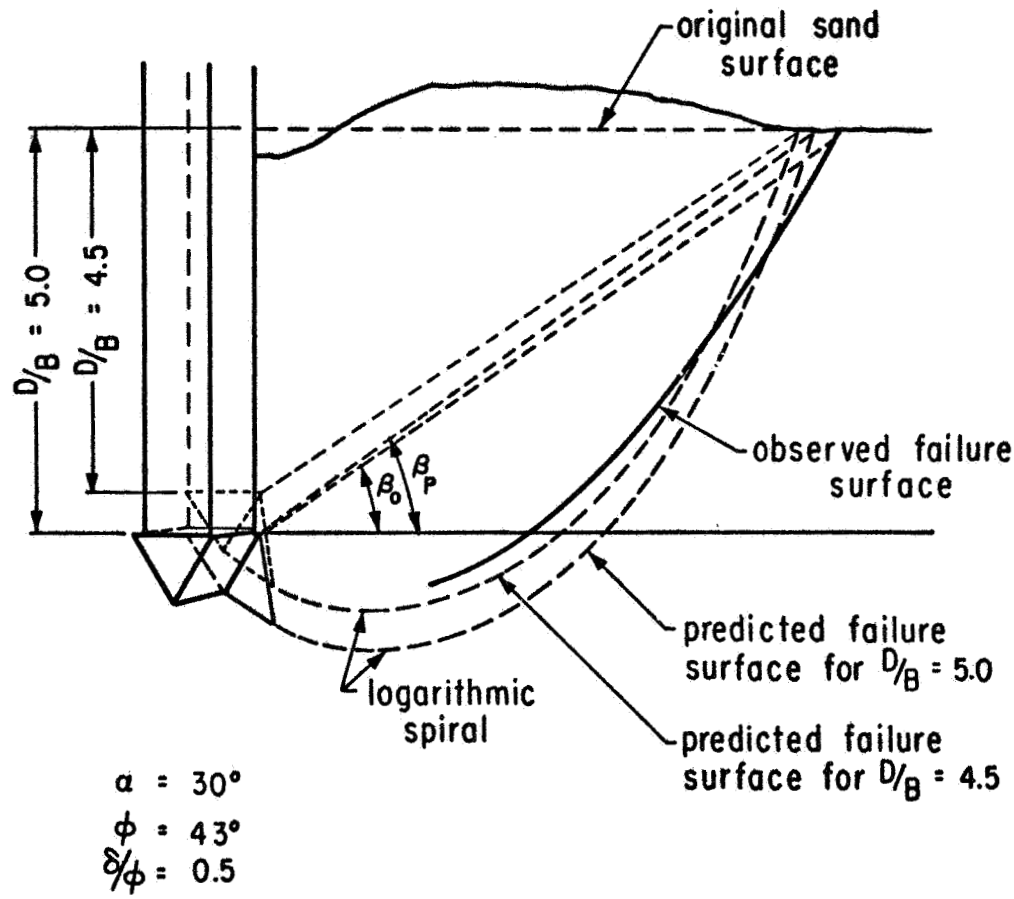

FIG. 3.10 A COMPARISON OF OBSERVED AND PREDICTED FAILURE SURFACES FOR MODEL No. 5

were determined by measuring the distance increases between the dark-colored interfaces.

(6) Very small rigid wedges were observed (Figs. 3.2 and 3.3) for the case of flat-ended penetrometers. This is believed (Abdul-Baki and Lewis, 1970) to be due to the fact that penetrometer to soil friction does not become fully developed for the flat-ended case. The low developed friction also causes the volume of the failed soil to be smaller than expected (see Table 3.2).

(7) All of the photographs show that there are many shear surfaces developed during penetration. Each failure surface corresponds to a certain relative depth. The discontinuous, step-wise development of the shear surfaces is due to the fact that further penetration is required in order to develop the full shear resistance of the soil along another shear surface.

(8) It may be seen from Figs. 3.7 and 3.8 that the soil zone undergoing shear is much smaller in the case of axisymmetric strain conditions than in plane strain. This is due to the fact that the deformations developed at any given section are much smaller than in plane strain. The three dimensional nature of axisymmetric strain conditions is also the probable cause of the fact that no distinct shear surfaces were observed for this case.

(9) The affected volume of soil increases with an increase in the roughness of the penetrometer base (see Table 3.2).

(10) The affected soil volume increases with a decrease in the base apex angle of the penetrometer (see Table 3.2 for Models 4 and 5).

PROPOSED FAILURE MECHANISM FOR WEDGE LOADING

A failure mechanism under strip loading by wedges which satisfies all of the observed features of the model tests as well as the knowledge obtained from previous studies for the range of relative depths considered is shown graphically in Figs. 3.11a and 3.11b. A plane shear zone exists adjacent to the base of the penetrometer (see Fig. 3.11b). A logarithmic spiral approximates the slip surface of the radial shear zone and either intersects the ground surface at point E (see Fig. 3.11a) or becomes vertically tangent to line EF (see Fig. 3.11b). A similar failure mechanism was proposed for flat-ended piles by Hu (1965) and by Abdul-Baki and Lewis (1970).

Table 3.2 COMPARISON OF OBSERVED AND PREDICTED GEOMETRIC CONFIGURATIONS OF FAILURE SURFACES

Model No.	Base Semi-Apex Angle α - degrees	Roughness (δ/ϕ)	r_c/B^*		β^*(deg.)	
			Measured	Predicted	Measured	Predicted
1	90	0.5	5.6	4.4 6.9	10.4	12.8 8.2
2	90	0.5	4.3	4.6 7.1	30.0	28.3 19.3
3	90	0.5	7.6	5.8 9.1	27.8	34.7 23.8
4	15	0.5	8.0	9.6	26.6	22.5
5	30	0.5	7.6	7.3	34.2	34.3
6	30	0.9	6.4	7.4	31.4	27.8

*see Fig. 3.11.

Note: Upper-predicted values for $(\delta/\phi)_{developed} = 0.0$
Lower-predicted values for $(\delta/\phi)_{developed} = 0.5$ for Model Nos. 1 to 3.

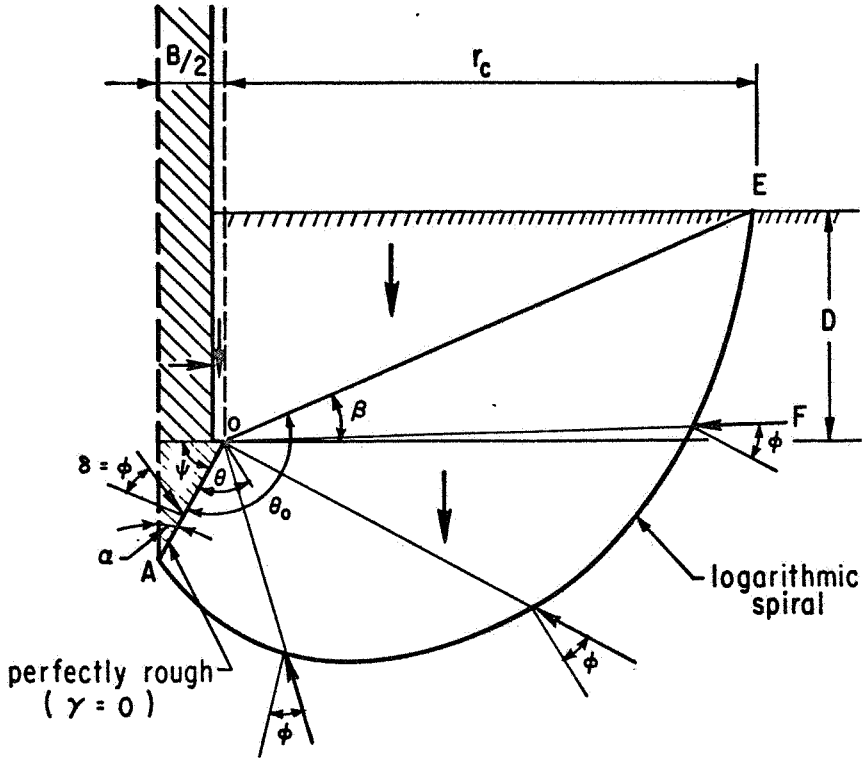

FIG. 3.11 a PROPOSED FAILURE MECHANISM ASSOCIATED WITH WEDGE PENETRATION INTO SOIL FOR SMALL RELATIVE DEPTHS

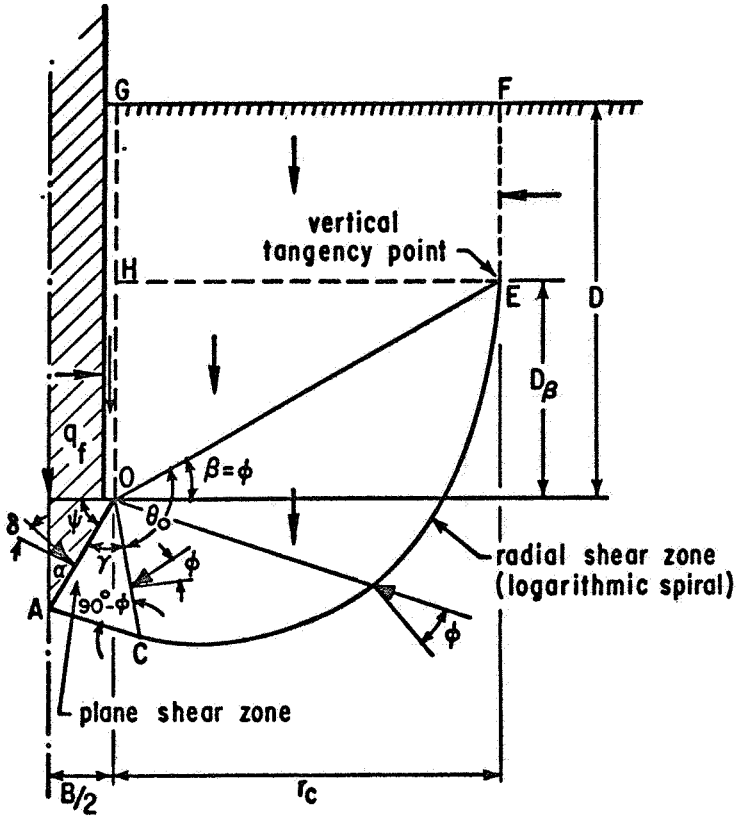

FIG. 3.11 b PROPOSED FAILURE MECHANISM ASSOCIATED WITH WEDGE PENETRATION INTO SOIL FOR LARGE RELATIVE DEPTHS

Referring to Fig. 3.11b for the more general deep penetration case, it has been shown by Abdul-Baki and Lewis (1970) that the point 0 is the center of the logarithmic spiral. The zone bounded by OCEFG is one in which the state of plastic equilibrium has been reached at every point. The earth pressures developed along vertical faces EF and OG are considered. It is assumed, as proposed by Hu (1970) that no shear stress develops along the vertical face EF. This implies that for penetration depths greater than D_β, all the soil deformation is accommodated below plane HE. The effects of the angle of internal friction and the penetrometer to soil friction on the magnitude of the topmost angle of the plane shear zone (γ) are considered in the following section. Further, for blunt, rough ($\delta=\phi$) bases, model tests show that a rigid soil wedge (or cone) will be developed in front of the tip having a base angle of $45°+\phi/2$.

A comparison of predicted and observed geometric features of the failure surfaces for the model tests is presented in Table 3.2.

THEORETICAL CONSIDERATIONS

Determination of the Topmost Angle (γ) of the Plane Shear Zone

The geometric configuration of the plane shear zone adjacent to the wedge (Fig. 3.11b) is determined by the known wedge semi-apex angle (α), the topmost angle (γ), and the included angle ACO which is equal to ($90° - \phi$). As the roughness (δ/ϕ) of the wedge increases, the angle γ at point 0 decreases and vanishes for a perfectly rough ($\delta=\phi$) wedge. Means for calculating this angle are given in the following paragraphs.

Cohesionless soils (c=0)

As shown in Fig. 3.11b, the logarithmic spiral starts from point C. According to plasticity theory OC should be a plane along which full mobilization of shear strength of soil takes place. In other words:

$$\tau_b = \sigma_b \tan\phi \qquad (3.1)$$

in which τ_b = shear stress on plane OC, σ_b = normal stress on plane OC, and ϕ = angle of internal friction of soil. It should also be noted that the stresses on plane OA should satisfy the following relationship:

$$\tau_a = \sigma_a \tan\delta \qquad (3.2)$$

in which τ_a = shear stress on plane OA, σ_a = normal stress on plane OA, and δ = penetrometer to soil friction angle.

It can be seen from Fig. 3.12a that the following relationships can be written:

$$\tau_a = \left(\frac{\sigma_{1f}-\sigma_{3f}}{2}\right) \cos(2\gamma-\phi) \tag{3.3}$$

and

$$\sigma_a = \left(\frac{\sigma_{1f}+\sigma_{3f}}{2}\right) + \left(\frac{\sigma_{1f}-\sigma_{3f}}{2}\right) \sin(2\gamma-\phi)$$

where σ_{1f} = major principal stress at failure, σ_{3f} = minor principal stress at failure and γ = the topmost angle of the plane shear zone. By substituting Equation 3.3 into Equation 3.2, the following relationship may be obtained.

$$\tan\delta = \frac{(\sigma_{1f}-\sigma_{3f}) \cos(2\gamma-\phi)}{(\sigma_{1f}+\sigma_{3f}) + (\sigma_{1f}-\sigma_{3f}) \sin(2\gamma-\phi)} \tag{3.4}$$

or

$$\tan\delta = \frac{[(\sigma_1/\sigma_3)_f-1] \cos(2\gamma-\phi)}{[(\sigma_1/\sigma_3)_f+1] + [(\sigma_1/\sigma_3)_f-1] \sin(2\gamma-\phi)} \tag{3.5}$$

By introducing $K = (\sigma_1/\sigma_3)_f$, Equation 3.5 becomes:

$$\tan\delta = \frac{\cos(2\gamma-\phi)}{[(K+1)/(K-1)] + \sin(2\gamma-\phi)} \tag{3.6}$$

From Fig. 3.12a, the ratio of major principal stress to minor principal stress at failure can be written as follows:

$$K = (\sigma_1/\sigma_3)_f = \frac{1 + \sin\phi}{1 - \sin\phi} \tag{3.7}$$

By substituting Equation 3.7 into Equation 3.6:

$$\tan\delta = \frac{\cos(2\gamma-\phi)}{(1/\sin\phi) + \sin(2\gamma-\phi)} \tag{3.8}$$

or

$$\tan\delta\,[1+\sin\phi \sin(2\gamma-\phi)] - \sin\phi \cos(2\gamma-\phi) = 0 \tag{3.9}$$

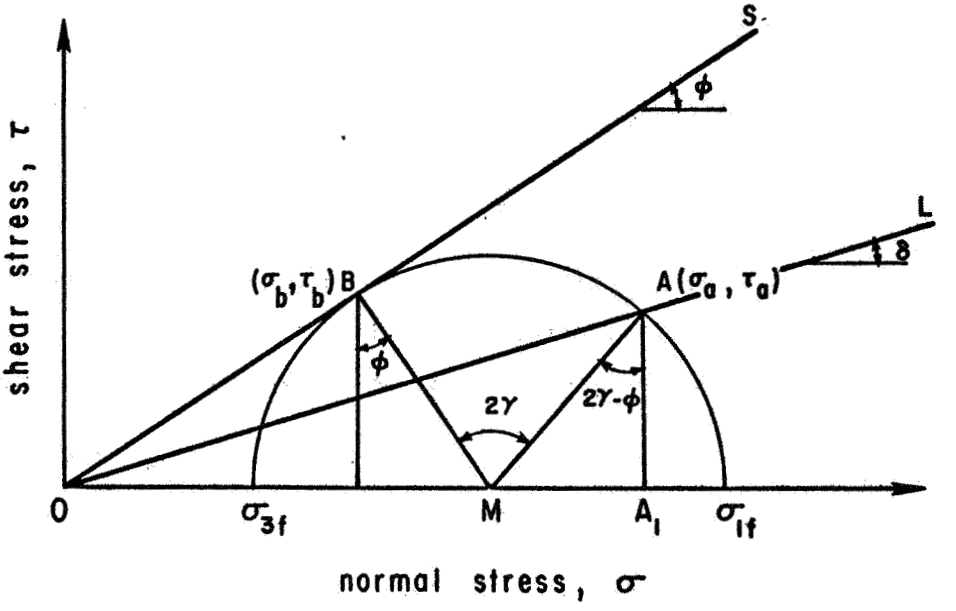

(a) Cohesionless Soils (c=0)

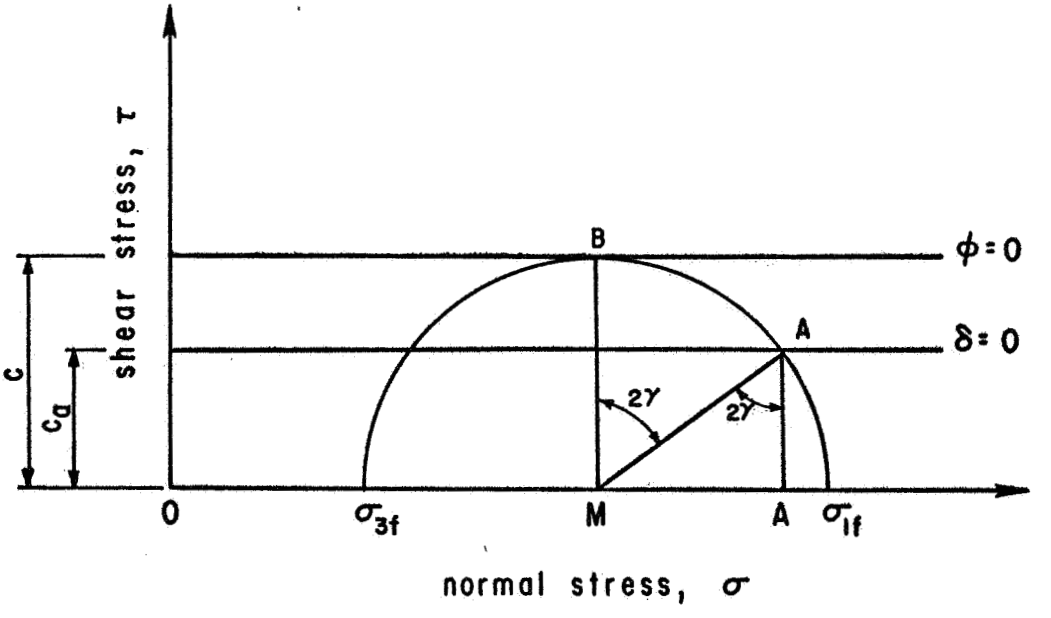

(b) Cohesive Soils ($\phi = 0$)

FIG. 3.12 DETERMINATION OF THE TOPMOST ANGLE (γ) OF THE PLANE SHEAR ZONE

Equation 3.9 indicates that for cohesionless soils, there is a unique value of angle γ, for given values of δ and ϕ.

For perfectly smooth wedge ($\delta=0$) in cohesionless soils, Equation 3.9 becomes:

$$\sin\phi \cdot \cos(2\gamma-\phi) = 0 \tag{3.10}$$

For $\phi\neq0$, $\cos(2\gamma-\phi) = 0$ or $2\gamma-\phi = (2n+1)\frac{\pi}{2}$ and consequently (for n=1);

$$\gamma = 45° + \frac{\phi}{2} \tag{3.11}$$

This may be seen directly from Fig. 3.12a. For $\delta=0$, the line OL coincides with the σ axis and 2γ becomes equal to $90°+\phi$.

For a perfectly rough wedge ($\delta=\phi$), Equation 3.9 becomes:

$$\tan\phi\,[1+\sin\phi\,\sin(2\gamma-\phi)] - \sin\phi\,\cos(2\gamma-\phi) = 0 \tag{3.12a}$$

or for $\phi\neq0$:

$$1 + \sin\phi\,\sin(2\gamma-\phi) - \cos\phi\,\cos(2\gamma-\phi) = 0 \tag{3.12b}$$

or

$$1 - \cos(2\gamma) = 0$$

and consequently;

$$\gamma = 0$$

This also can be seen from Fig. 3.12a. For $\delta=\phi$, lines OL and OS coincide and the angle γ vanishes.

Cohesive soils ($\phi=0$)

For cohesive soils ($\phi=0$), Equation 3.8 does not apply. In this case, the angle γ can be calculated as follows: The roughness of a wedge for $\phi=0$ soils is defined as:

$$f_c = c_a/c \tag{3.13}$$

where $0\leq f_c \leq 1$ is the roughness factor, c_a is the adhesion (cohesion between wedge and soil), and c is the cohesion. From Fig. 3.12b:

$$\sin\left(\frac{\pi}{2} - 2\gamma\right) = \frac{AA_1}{MA} = \frac{c_a}{c} \tag{3.14}$$

or

$$\gamma = \frac{\pi}{4} - \frac{1}{2} \sin^{-1} (f_c) \tag{3.15}$$

For perfectly smooth wedges, $f_c = 0$ and γ becomes equal to 45°, and for perfectly rough wedges, $f_c = 1$ and γ becomes equal to zero.

Cohesion-friction (c-ϕ) soils

Similar to cohesionless soils, the shear stresses on plane OC are given by (see Fig. 3.13):

$$\tau_b = c + \sigma_b \tan\phi \tag{3.16}$$

and the shear stresses on plane OA are given by:

$$\tau_a = c_a + \sigma_a \tan\delta \tag{3.17}$$

Also, from Fig. 3.13, τ_a and σ_a are given by Equation 3.3. By substituting Equation 3.3 into Equation 3.17:

$$(\sigma_{1f}-\sigma_{3f}) \cos(2\gamma-\phi) = 2c_a + [(\sigma_{1f}+\sigma_{3f})+(\sigma_{1f}-\sigma_{3f})\sin(2\gamma-\phi)]\tan\delta \tag{3.18}$$

The major principal stress at failure σ_{1f} is given by:

$$\sigma_{1f} = \frac{1 + \sin\phi}{1 - \sin\phi} + \frac{2c \cos\phi}{1 - \sin\phi} \tag{3.19}$$

By substituting σ_{1f} into Equation 3.18:

$$\underline{F} (c_a, c, \delta, \phi, \gamma, \sigma_{3f}) = 0 \tag{3.20}$$

which implies that for c-ϕ soils, the angle γ is a function of σ_{3f}. It can be seen, however, that for a perfectly rough wedge γ=0, and for a perfectly smooth wedge $\gamma = 45° + \frac{\phi}{2}$.

It can be shown that the dependency of the angle γ on σ_{3f} vanishes under the following assumption:

$$c_a/c = \tan\delta/\tan\phi \tag{3.21}$$

and that functional $\underline{F}$ becomes:

$$\underline{F} (c_a, c, \delta, \phi, \gamma) = 0 \tag{3.22}$$

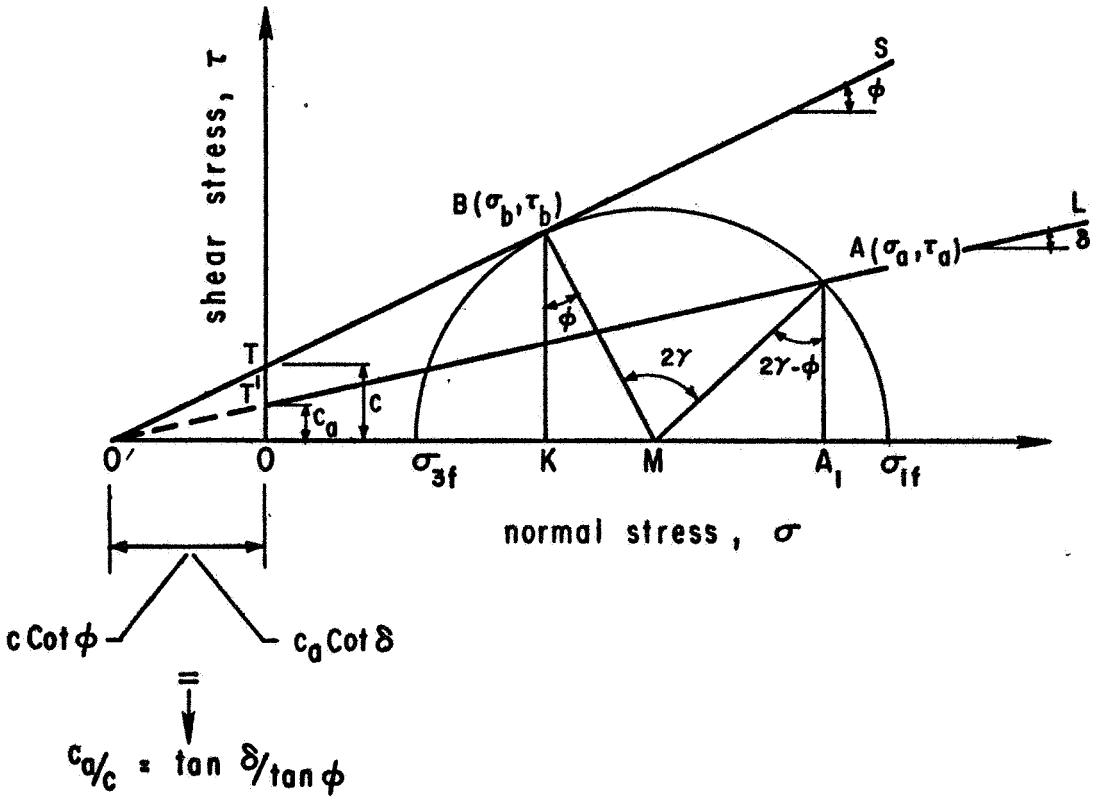

FIG. 3.13 DETERMINATION OF THE TOPMOST ANGLE (γ) OF THE PLANE SHEAR ZONE FOR COHESION - FRICTION ($c-\phi$) SOILS

Equation 3.21 implies that lines TS and T'L intersect at point 0' on the axis (see Fig. 3.13). It can thus be seen that functional $\underline{F}$ may be calculated.

Geometrically it can be seen that $00' = c\cot\phi = c_a\cot\delta$ or that $c_a/c = \tan\delta/\tan\phi$, which is a reasonable assumption for most c-ϕ soils. With this assumption, Fig. 3.13 yields the following:

$$MB = KB/\cos\phi$$

and $$AA_1 = MA\cos(2\gamma-\phi) \tag{3.23}$$

Since MA=MB=radius of Mohr's circle:

$$AA_1 = KB\,\frac{\cos(2\gamma-\phi)}{\cos\phi} \tag{3.24}$$

From Fig. 3.13:

$$\begin{aligned} O'K &= KB\cot\phi \\ KM &= KB\tan\phi \\ MA_1 &= AA_1\tan(2\gamma-\phi) \\ O'A_1 &= AA_1\cot\delta \end{aligned} \tag{3.25}$$

By substituting Equation 3.25 into $O'A = O'K + KM + MA_1$, the following relationship is obtained

$$AA_1\cot\delta = AA_1\tan(2\gamma-\phi) + KB(\cot\phi + \tan\phi) \tag{3.26}$$

By substituting Equation 3.24 into Equation 3.26:

$$\cot\delta = \tan(2\gamma-\phi) + \frac{\cos\phi}{\cos(2\gamma-\phi)}\ (\cot\phi + \tan\phi)$$

or,

$$\tan\delta\ [1 + \sin\phi\sin(2\gamma-\phi)] - \sin\phi\cos(2\gamma-\phi) = 0 \tag{3.27}$$

It can be seen that Equation 3.27 is exactly the same as Equation 3.9. In other words, the angle γ satisfies the same relationship in both cohesionless and cohesion-friction soils provided that Equation 3.21 is satisfied.

Values of the angle γ for different values of roughness and angle of internal friction may be calculated from Equation 3.9 using Subroutine ANG (See Appendix A). An iterative procedure was used to calculate values of

γ to an accuracy of 0.1°. These values are tabulated in Table 3.3. Fig. 3.14 shows the variation of angle γ with roughness for different values of angle of internal friction.

The following conclusions can be drawn from the analysis of Table 3.3 and Fig. 3.14:

(1) The effect of angle of internal friction on the angle γ is much more pronounced for low values of roughness than for high values.

(2) For high values of roughness, there is a considerable increase in γ values for a small decrease in δ/ϕ values.

(3) The theoretical curve for γ versus δ/ϕ is well above the linear variation curve, indicating that linear interpolation for γ values between 0° and $45°+\phi/2$ for different roughness values is not permissible.

Determination of Critical Relative Depth

The vertical tangency point of the shear surface coincides with the ground surface (see Fig. 3.11b) for a certain relative depth depending on base apex angle, base roughness, and angle of internal friction of the soil. This relative depth is defined as the critical relative depth, $(D/B)_{cr}$. If the relative depth of the penetrometer base is greater than the critical relative depth, the angle β (see Fig. 3.11b) will be equal to the angle of internal friction (ϕ); otherwise it will be smaller than the friction angle and must be calculated by iterative procedures. The iterative technique used is described in Chapter Four. A summary of calculated critical relative depth values is given in Table 3.4. The significance of these values can be summarized as follows:

(1) If the relative depth is greater than the critical relative depth:

  (a) For further penetration, there will be no change in the bearing capacity cohesion factor (N_c) values (see Chapter Four).

  (b) For further penetration, the increase in friction-surcharge bearing capacity factor ($N_{\gamma q}$) will be proportional to the increase in depth. In other words, $N_{\gamma q}$ values for larger depths can be calculated by linear extrapolation (see Chapter Four).

(2) They are used as the basis for the calculation of depth factors (see Chapter Four).

Table 3.3 VALUES OF ANGLE γ (DEG.), CALCULATED FROM EQUATION 3.9 FOR DIFFERENT VALUES OF ANGLE OF INTERNAL FRICTION AND ROUGHNESS

δ/ϕ ϕ(deg.)	0.1	0.2	0.3	0.4	0.5	0.6	0.7	0.8	0.9
5	44.4	41.2	38.0	34.7	31.2	27.5	23.5	18.9	13.2
10	46.6	43.2	39.7	36.2	32.4	28.5	24.2	19.4	13.4
15	48.8	45.2	41.4	37.6	33.6	29.4	24.9	19.8	13.5
20	51.1	47.1	43.1	39.0	34.7	30.3	25.5	20.2	13.7
25	53.3	49.0	44.7	40.4	35.8	31.1	26.1	20.5	13.8
30	55.5	51.0	46.4	41.7	36.9	31.9	26.6	20.8	13.9
35	57.7	52.9	48.0	43.0	37.9	32.7	27.1	21.0	13.9
40	59.9	54.7	49.6	44.3	38.9	33.4	27.5	21.2	13.9
45	62.1	56.6	51.1	45.5	39.9	34.0	27.9	21.4	13.9
50	64.2	58.4	52.6	46.7	40.8	34.6	28.3	21.5	13.8

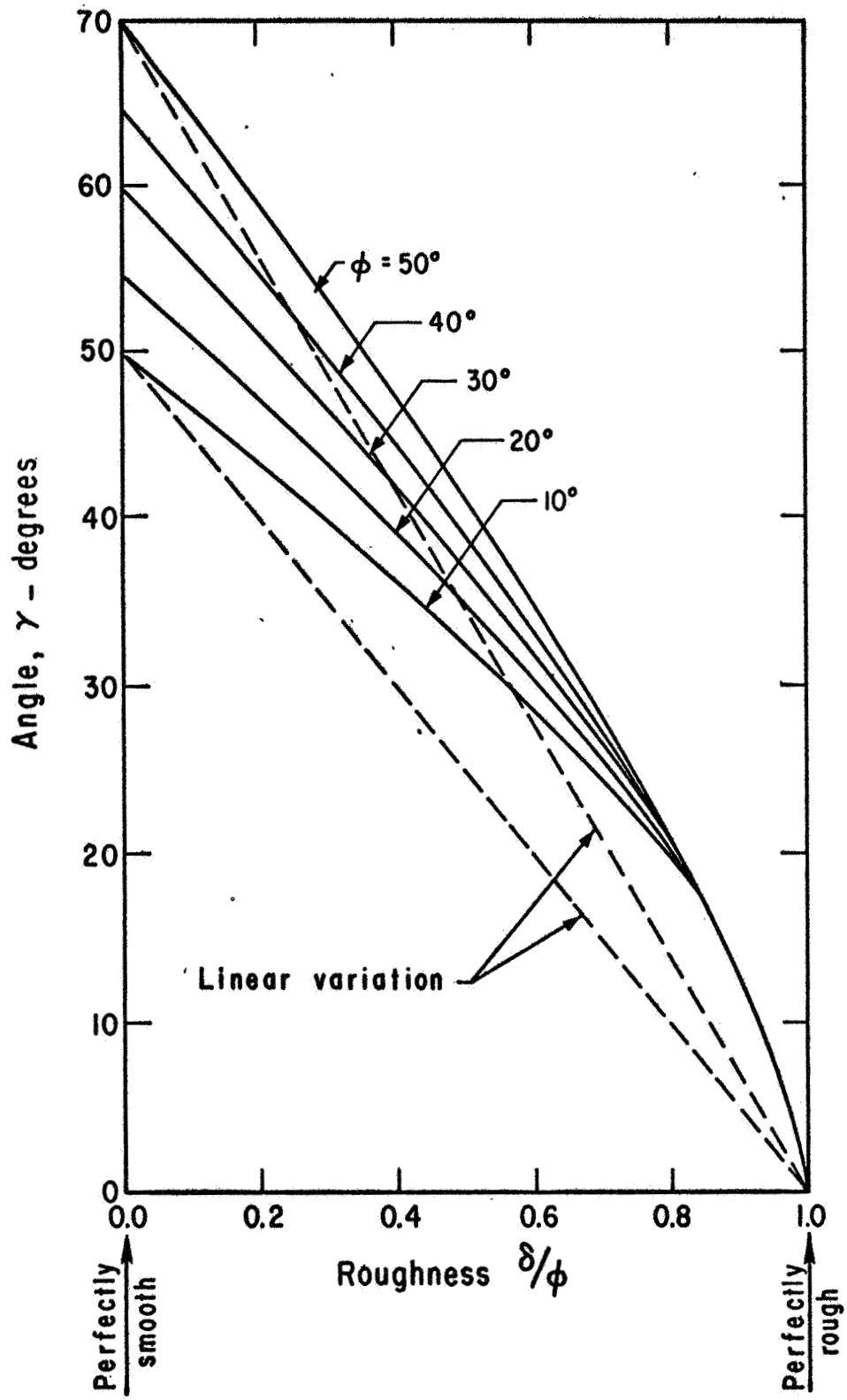

FIG. 3.14 EFFECT OF ROUGHNESS ON ANGLE γ, FOR GIVEN VALUES OF ANGLE OF INTERNAL FRICTION

Table 3.4 VALUES OF CRITICAL RELATIVE DEPTH, $(D/B)_{cr}$

$\alpha=15°$			
φ \ δ/φ	0.0	0.5	1.0
25	1.37	1.91	2.36
30	2.06	2.98	3.77
35	3.10	4.71	6.15
40	4.75	7.68	10.41
45	7.55	13.20	18.79
50	12.72	24.55	37.34

$\alpha=30°$			
φ \ δ/φ	0.0	0.5	1.0
25	0.80	1.12	1.38
30	1.24	1.79	2.27
35	1.93	2.93	4.01
40	3.06	4.95	7.38
45	5.08	8.86	14.48
50	8.99	17.34	31.34

$\alpha=45°$			
φ \ δ/φ	0.0	0.5	1.0
25	0.64	0.89	1.31
30	1.02	1.48	2.27
35	1.64	2.49	4.01
40	2.70	4.36	7.38
45	4.66	8.14	14.48
50	8.68	16.75	31.34

$\alpha=90°$	
φ \ δ/φ	1.0
25	1.31
30	2.27
35	4.01
40	7.38
45	14.48
50	31.34

Determination of Lateral Extent of the Radial Shear Zone

The lateral extent of the shear surface is a maximum for relative depths equal to or greater than the critical relative depth. The lateral distance from the pole of the logarithmic spiral to the shear surface at the point of vertical tangency is denoted by r_c (see Fig. 3.11b). Table 3.5 summarizes the maximum lateral extent of the slip surface, in terms of the dimensionless variable r_c/B, for various values of base semiapex angle (α), base roughness (δ/ϕ), and soil friction angle (ϕ).

The importance of considering the lateral extent of the failure surface has recently discussed by Nowatzki and Karafiath (1972). The soil volume affected in the two dimensional (plane strain) problem will be proportional to r_c and the volume affected in the three dimensional (axisymmetric) problem is proportional to r_c^2. Volumetric considerations are particularly important in compressible soils because to develop full frictional resistance along a larger failure surface larger soil volume must be compressed. Consequently, indices obtained with penetrometers whose configurations result in large affected soil volume are likely to be more representative of soil compressibility than of soil shear strength properties.

SUMMARY

Previous studies of the failure mechanism associated with static penetration have been reviewed. Model tests have been performed and the results used to further define the mechanism of failure. The effects of penetrometer configuration, penetrometer to soil friction, soil friction angle, and relative depth on the failure mechanism have been investigated. A proposed failure mechanism for wedge penetration based on the interpretation of features observed in the model tests and the results of previous studies is presented. The geometric features of the proposed failure mechanism have been formulated in terms of base semiapex angle, base roughness, soil friction angle, and relative depth of penetrometer base.

Table 3.5 SUMMARY OF r_c/B VALUES FOR $D/B \geq (D/B)_{cr}$

α=15°			
φ \ δ/φ	0.0	0.5	1.0
25	2.94	4.09	5.05
30	3.57	5.16	6.53
35	4.43	6.73	8.78
40	5.66	9.16	12.40
45	7.55	13.18	18.78
50	10.66	20.57	31.13

α=30°			
φ \ δ/φ	0.0	0.5	1.0
25	1.72	2.39	2.95
30	2.15	3.11	3.93
35	2.75	4.18	5.73
40	3.65	5.90	8.79
45	5.07	8.86	14.47
50	7.54	14.54	26.22

α=45°			
φ \ δ/φ	0.0	0.5	1.0
25	1.37	1.91	2.80
30	1.77	2.55	3.93
35	2.34	3.55	5.73
40	3.21	5.20	8.79
45	4.66	8.14	14.47
50	7.28	14.05	26.22

α=90°	
φ \ δ/φ	1.0
25	2.80
30	3.93
35	5.73
40	8.79
45	14.47
50	26.22

CHAPTER FOUR

THEORETICAL CALCULATION OF STATIC PENETRATION RESISTANCE

INTRODUCTION

Both the results of model tests (Chapter Three) and additional experimental results (Chapter Six) show that for wedge (or cone) penetrometers, the ultimate penetration resistance depends strongly on the base semiapex angle (α), base roughness (δ/ϕ), and relative depth (D/B). No theory available heretofore has considered these three parameters explicitly over the ranges of interest. Knowledge of the failure mechanism has now permitted development of new relationships for the ultimate base resistance which account explicitly for these parameters. The development of the these relationships is described in this chapter, and curves showing bearing capacity factors versus angle of internal friction for several values of the parameters α, δ/ϕ, and D/B are presented. The importance of various parameters is discussed.

GENERAL CONSIDERATIONS

The general bearing capacity equation for a plane, horizontal strip foundation is:

$$q_f = cN_c + \frac{1}{2}\gamma_s BN_\gamma + qN_q \tag{4.1}$$

where q_f = ultimate bearing capacity, q = surcharge, c = cohesion, γ_s = effective unit weight of soil, B = width of loaded area, and N_c, N_γ, and N_q are bearing capacity factors for cohesion, friction and surcharge respectively. When the general bearing capacity equation (Equation 4.1) is applied to square, circular or any other contact areas of limited extent, the primary bearing capacity factors must be modified by shape factors (ξ_c, ξ_γ, ξ_q) which are usually determined empirically. With these modifying factors, Equation 4.1 is expanded to:

$$q_f = cN_c\xi_c + \frac{1}{2}\gamma_s BN_\gamma\xi_\gamma + qN_q\xi_q \tag{4.2}$$

It is customary (Meyerhof, 1951) to calculate N_c and N_q for one assumed failure surface and N_γ for another. As discussed in Chapter Two, the use of factors determined in this manner may lead to a significant underestimation of the ultimate bearing capacity. As an alternative to the customary procedure, the factors N_q and N_γ may be combined ($N_{\gamma q}$) and a proper single failure surface may be considered for the calculation of N_c and $N_{\gamma q}$ (Meyerhof, 1951 and Hu, 1965). Consequently, Equation 4.2 may be rewritten as:

$$q_f = cN_c\xi_c + \gamma_s BN_{\gamma q}\xi_{\gamma q} \tag{4.3}$$

where $N_{\gamma q}$ is the bearing capacity factor for the friction-surcharge term and $\xi_{\gamma q}$ is the corresponding shape factor. As previously mentioned, for wedge or cone penetrometers, both N_c and $N_{\gamma q}$ are functions of the following variables:

(1) Soil friction angle (ϕ)

(2) Base semiapex angle (α)

(3) Base roughness (δ/ϕ)

(4) Relative depth of penetrometer base (D/B)

Thus:

$$N_c,\ N_{\gamma q} = f_1,\ f_2\ (\phi,\ \alpha,\ \delta/\phi,\ D/B) \tag{4.4}$$

DETERMINATION OF BEARING CAPACITY FACTORS

General

Fig. 4.1 shows the free body diagram for the calculation of the bearing capacity factor N_c. The following expression for N_c may be derived (see Appendix A for details):

$$N_c = \frac{[1+\sin\phi\ \sin(2\gamma-\phi)]}{\sin\phi\ \cos\phi}\ e^{2\theta_o\tan\phi} + \frac{\cos(2\gamma-\phi)\ \tan\psi}{\cos\phi}\ e^{2\theta_o\tan\phi}$$

$$+ \frac{[\sin(2\xi+\phi)-\sin\phi][1+\sin\phi\ \sin(2\gamma-\phi)]}{\cos^2\phi[\cos\phi-\tan\phi[\sin(2\xi+\phi)-\sin\phi]]}\ e^{2\theta_o\tan\phi} - \frac{1}{\tan\phi}$$

$$+ \frac{\tan\phi\ \tan\psi\ \cos(2\gamma-\phi)[\sin(2\xi+\phi)-\sin\phi]}{\cos\phi[\cos\phi-\tan\phi[\sin(2\xi+\phi)-\sin\phi]]}\ e^{2\theta_o\tan\phi} \tag{4.5}$$

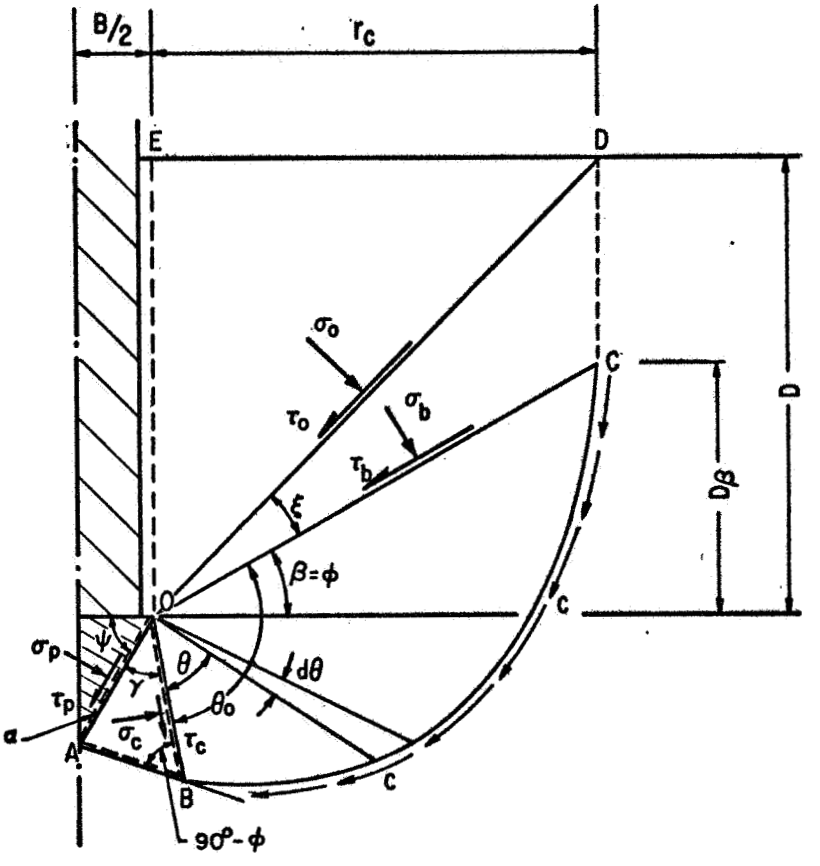

FIG. 4.1 FREE BODY DIAGRAM FOR DETERMINATION OF BEARING CAPACITY FACTOR N_c

Because it is assumed (Hu, 1970) that there is no shear stress developed on the vertical plane CD, the angle ξ vanishes, and Equation 4.5 simplifies to:

$$N_c = \frac{1+\sin\phi\ \sin(2\gamma-\phi)}{\sin\phi\ \cos\phi}\ e^{2\theta_o\tan\phi} - \frac{1}{\tan\phi} + \frac{\cos(2\gamma-\phi)\tan\psi}{\cos\phi}\ e^{2\theta_o\tan\phi} \qquad (4.6)$$

where N_c = bearing capacity factor for cohesion term,
ϕ = soil friction angle,
γ = the topmost angle of the plane shear zone,
ψ = $90°-\alpha$ (α = semiapex angle),
θ_o = $180°-(\psi+\gamma)+\beta$

Equation 4.6 can be written in functional form as:

$$N_c = F(\phi,\ \psi,\ \gamma,\ \beta) \qquad (4.7)$$

or because $\psi=90°-\alpha$, $\gamma=\underline{f}(\phi,\delta/\phi)$ and $\beta=\underline{f}_1(\phi,\ \delta/\phi,\ \alpha,\ D/B)$, Equation 4.7 can be restated as:

$$N_c = f_1\ (\phi,\ \alpha,\ \delta/\phi,\ D/B) \qquad (4.8)$$

Fig. 4.2 shows the free body diagram for the calculation of bearing capacity factor $N_{\gamma q}$. From static equilibrium of body OCEFG:

$$\Sigma M_o = 0 \qquad (4.9a)$$

or
$$F_b L_b + P_{s1} L_{s1} = P_{s2} L_{s2} + P_1 L_{p1} + P_2 L_{p2} + W_1 L_{w1} \qquad (4.9b)$$

The following expression for $N_{\gamma q}$ may be derived (see Appendix A for details):

$$N_{\gamma q} = \frac{\cos(\psi-\delta)}{\cos\delta}\ \frac{[1+\sin\phi\ \sin(2\gamma-\phi)]}{\cos\phi\ \cos(\gamma-\phi)} \left\{ \frac{\cos^2(\gamma-\phi)}{4\cos^2\psi\ \cos^2\phi}\ I_\theta + \right.$$

$$\frac{3\cos(\gamma-\phi)\ \cos^2\beta}{4\cos\psi\ \cos\phi}\ e^{2\theta_o\tan\phi}\left(m-\frac{2}{3}\,m'\right) - K_o\ \frac{\cos\psi\ \cos\phi}{\cos\ (\gamma-\phi)}$$

$$\left. \cdot(m-m')^2\cdot(m+2m') + K\ \frac{\cos\psi\ \cos\phi}{\cos(\gamma-\phi)}\ m^3 \right\} - \frac{\tan\psi}{4} \qquad (4.9)$$

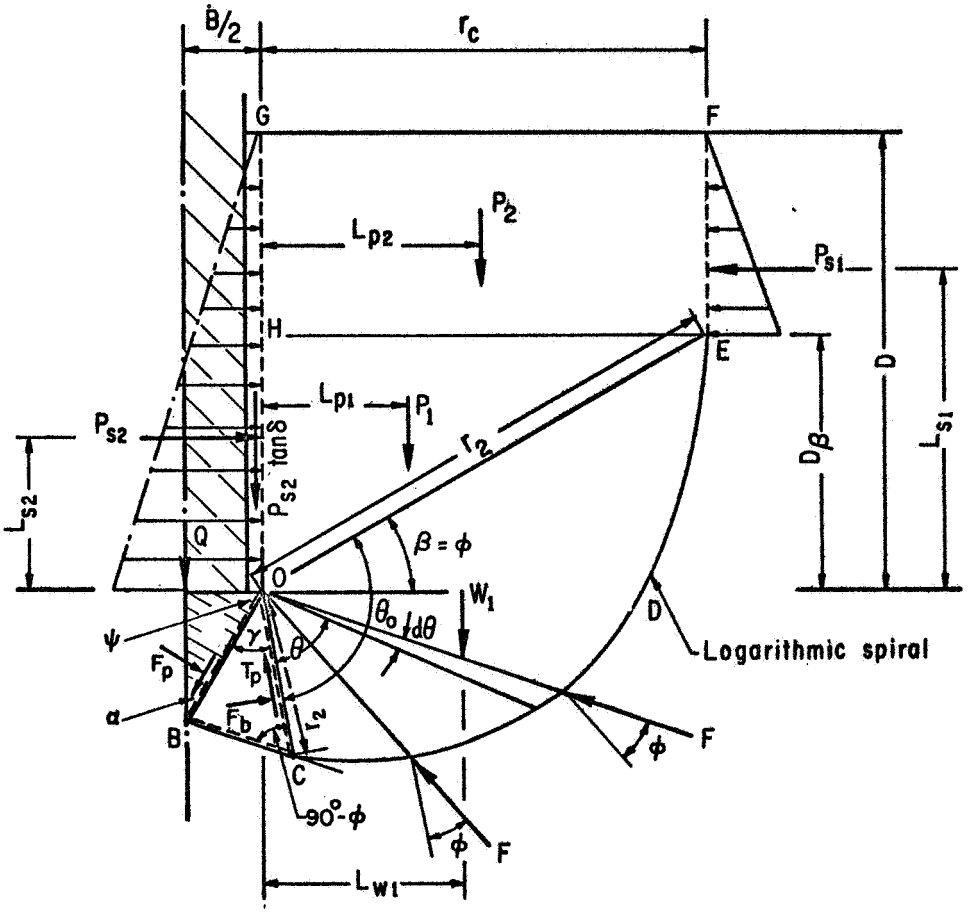

FIG. 4.2 FREE BODY DIAGRAM FOR DETERMINATION OF BEARING CAPACITY FACTOR $N_{\gamma q}$

where $N_{\gamma q}$ = bearing capacity factor for friction-surcharge,

ϕ = angle of internal friction of soil,

ψ = 90°-α (α=semiapex angle),

δ = base to soil friction angle,

γ = the topmost angle of the plane shear zone,

θ_o = 180°-(ψ+γ)+β,

K = lateral earth pressure coefficient (see the discussion later in this chapter for proper selection),

m = relative depth (D/B),

m' = D_β/B,

D_β = the vertical distance of point E on the failure surface above base level [a function of β (see Fig. 4.3)],

$$m' = \frac{1}{2} \frac{\sin\beta \cos(\gamma-\phi)}{\cos\psi \cos\phi} e^{\theta_o \tan\phi}$$

and I_θ is given by:

$$I_\theta = \frac{1}{1+9\tan^2\phi} \left\{ 3\tan\phi [e^{3\theta_o \tan\phi} \cos\beta - \cos(\theta_o-\beta)] + \right.$$

$$\left. + [e^{3\theta_o \tan\phi} \sin\beta + \sin(\theta_o-\beta)] \right\} \qquad (4.10)$$

Similarly to N_c, $N_{\gamma q}$ is a function of four parameters:

$$N_{\gamma q} = f_2 (\phi, \alpha, \delta/\phi, D/B) \qquad (4.11)$$

Determination of the Angle β

In order to calculate the bearing capacity factors N_c and $N_{\gamma q}$ from Equations 4.6 and 4.9, the value of the angle β (see Fig. 4.1) must be known. For relative depths equal or greater than the critical relative depth, the angle β is equal to the angle of internal friction (ϕ) of the soil. For relative depths less than the critical relative depth, the failure surface will intersect the ground surface before reaching vertical tangency. In this case, β will be smaller than ϕ and must be calculated by iterative procedures. The procedure used for the calcualtion of β is described in the following paragraphs.

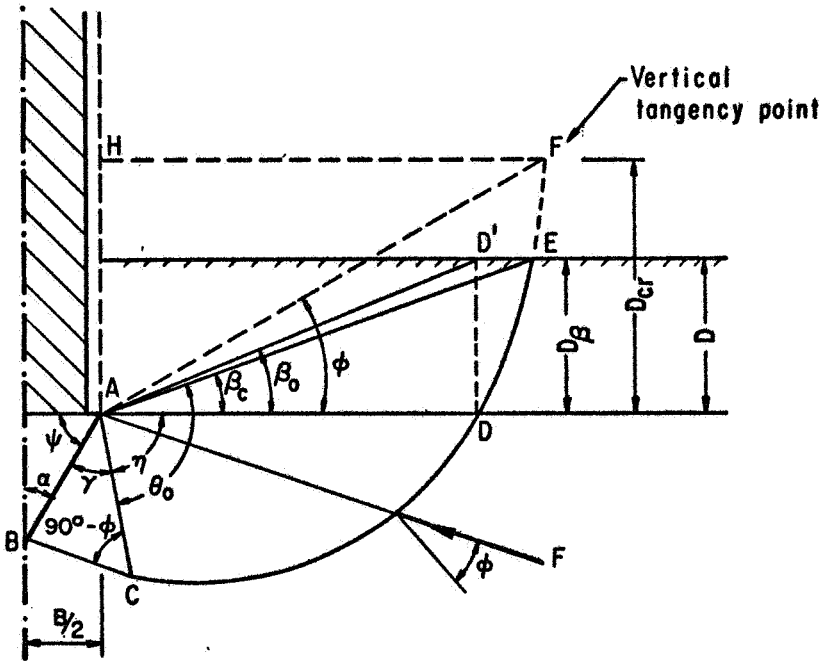

FIG. 4.3 ITERATIVE PROCEDURE USED FOR THE CALCULATION OF CORRECT VALUE OF ANGLE β (β_c)

From Fig. 4.3:

$$AB = B/(2\cos\psi) \quad \text{and} \quad AC = AB \cdot \frac{\cos(\gamma-\phi)}{\cos\phi} \tag{4.12a}$$

or

$$r_o = AC = \frac{B\cos(\gamma-\phi)}{2\cos\phi\ \cos\psi} \tag{4.12b}$$

Also from the same figure:

$$D = AE \cdot \sin\beta \tag{4.13a}$$

and from the property of a logarithmic spiral:

$$AE = AC \cdot e^{\theta_o \tan\phi} \tag{4.13b}$$

By substituting Equations 4.12b and 4.13b into Equation 4.13a:

$$D_\beta = \frac{B\cos(\gamma-\phi)\ \sin\beta}{2\cos\phi\ \cos\psi}\ e^{\theta_o \tan\phi} \tag{4.14a}$$

or

$$\frac{D_\beta}{B} = m' = \frac{\cos(\gamma-\phi)\ \sin\beta}{2\cos\phi\ \cos\psi}\ e^{\theta_o \tan\phi} \tag{4.14b}$$

The value of β is known if $m' \leq m$ ($m=D/B$) and is equal to the angle of internal friction. For $m' > m$, β will be smaller than ϕ. The following method is used to determine whether or not m' is smaller than m.

(1) $\beta_1 = \phi$ is assumed.

(2) This value is substituted into Equation 4.14b and the corresponding m' value is calculated.

(3) If $m' \leq m$ ($m=D/B$), the correct value of β is ϕ. If $m' > m$, the correct value of β is smaller than ϕ (see Fig. 4.3) and can be found by iterative procedures.

For $\beta=\beta_c$ (β_c=the correct value of β for the given variables), $m' = m$, or from Equation 4.14b:

$$\frac{\cos(\gamma-\phi)\cdot\sin\beta_c}{2\cos\phi\cdot\cos\psi}\ e^{\theta_o \tan\phi} = m \tag{4.15}$$

For given values of ϕ, δ/ϕ, α, and D/B, the angle β is the only unknown in Equation 4.15. Thus, the following iterative procedure can be used:

(1) From Fig. 4.3, $\eta = 180° - (\gamma+\psi)$ and $AD = AC \cdot e^{\eta \tan\phi}$ and by substituting Equation 4.12b for the value of AC:

$$AD = \frac{B\cos(\gamma-\phi)}{2\cos\phi\ \cos\psi}\, e^{\eta\tan\phi} \tag{4.16}$$

and as a first guess:

$$\tan\beta_o = DD'/AD$$

or

$$\beta_o = \tan^{-1}\left[\frac{2m\cos\phi\cdot\cos\psi}{\cos(\gamma-\phi)\cdot e^{\eta\tan\phi}}\right] \tag{4.17}$$

Thus, β_o can be calculated explicitly from Equation 4.17 because η is known.

(2) This value of $\beta = \beta_o$ is substituted into:

$$\sin\beta_n = \frac{2m\cos\phi\cdot\cos\psi}{\cos(\gamma-\phi)e^{\bar{\theta}_o\tan\phi}}$$

where $\bar{\theta}_o = 180° - (\gamma+\psi)+\beta_o$ and the new value of β, $(\beta=\beta_n)$ is calculated from:

$$\beta_n = \sin^{-1}\left[\frac{2m\cos\phi\cdot\cos\psi}{\cos(\gamma-\phi)e^{\bar{\theta}_o\tan\phi}}\right] \tag{4.18}$$

(3) Iteration is stopped after the first step if:

$$|\beta_n - \beta_o| \leq 0.1°$$

and the value of β_n is taken equal to β_c. If not, for the second iteration;

$$\beta_o = \frac{\beta_o + \beta_n}{2}$$

arithmetic average of first guess and first iteration values is used, and the same procedure is repeated until the error in β_c is equal or smaller than 0.1°.

In most cases only few iterations were necessary. Fig. 4.4 is an example of the convergence of this iterative procedure.

Procedure

Once β is known, the factors N_c and $N_{\gamma q}$ can be calculated from Equations 4.6 and 4.9, respectively, for given values of ϕ, α, δ/ϕ, and D/B. A computer program was written to calculate N_c and $N_{\gamma q}$ separately for different values of these four parameters. The complete program consist of Program NC Program NGQ and one subroutine, ANG which calculates angle γ (the topmost angle of the plane shear zone). The angle β_c is calculated in the main program. A flow diagram for the program is given in Fig. 4.5, and a listing is given in Appendix A.

Example curves showing N_c and $N_{\gamma q}$ versus ϕ for α=15° to 90°, δ/ϕ=0.0, 0.5, and 1.0, $K=K_o=1-\sin\phi$, and for D/B=10.0 are given in Figs. 4.6 and 4.7. It should be noted that the break points in Fig. 4.6 for N_c are a function of relative depth. The dashed lines indicate the N_c versus ϕ relationship for higher D/B values than indicated on the figure. For the relative depths indicated, solid lines should be used. A complete set of curves for several values of α, δ/ϕ, and D/B for general shear failure is presented in Appendix A.

Effect of Base Apex Angle

Theoretical and experimental (see Chapter Six) results both show that the ultimate penetration resistance of soil to wedge (or cone) shaped penetrometers depends strongly on the base apex angle (2α). Fig. 4.8 shows the effect of the base semiapex angle on the bearing capacity factors N_c and $N_{\gamma q}$ for various base roughnesses, for given values of soil friction angle (ϕ=30°) and relative depth (D/B=10.0).

For rough bases, Fig. 4.8 indicates that the bearing capacity factors do not change for semiapex angles larger than approximately 15°. This is due to the fact that a soil wedge (or cone) develops in front of blunt rough bases during penetration. However, the bearing capacity factors for rough bases do increase with decreasing values of α below 15°.

For smooth bases, the bearing capacity factors are strongly dependent on the value of the base semiapex angle. Fig. 4.8 indicates that the values

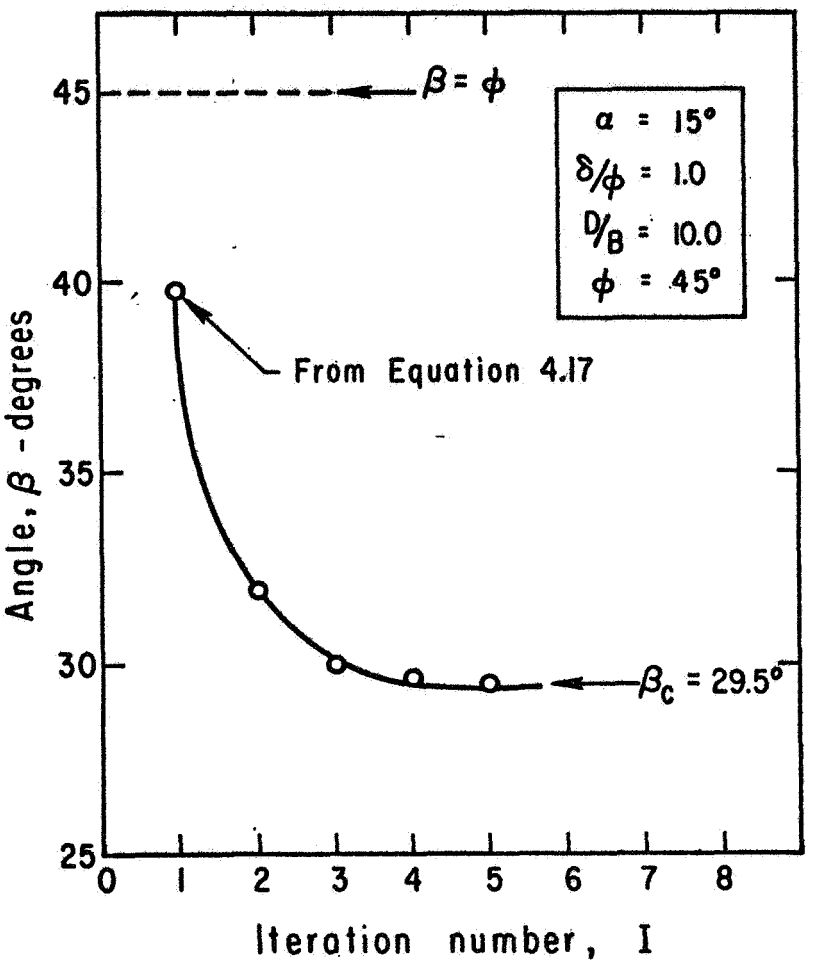

FIG. 4.4 AN EXAMPLE OF THE CONVERGENCE OF ITERATION PROCEDURE FOR THE CALCULATION OF ANGLE β_c

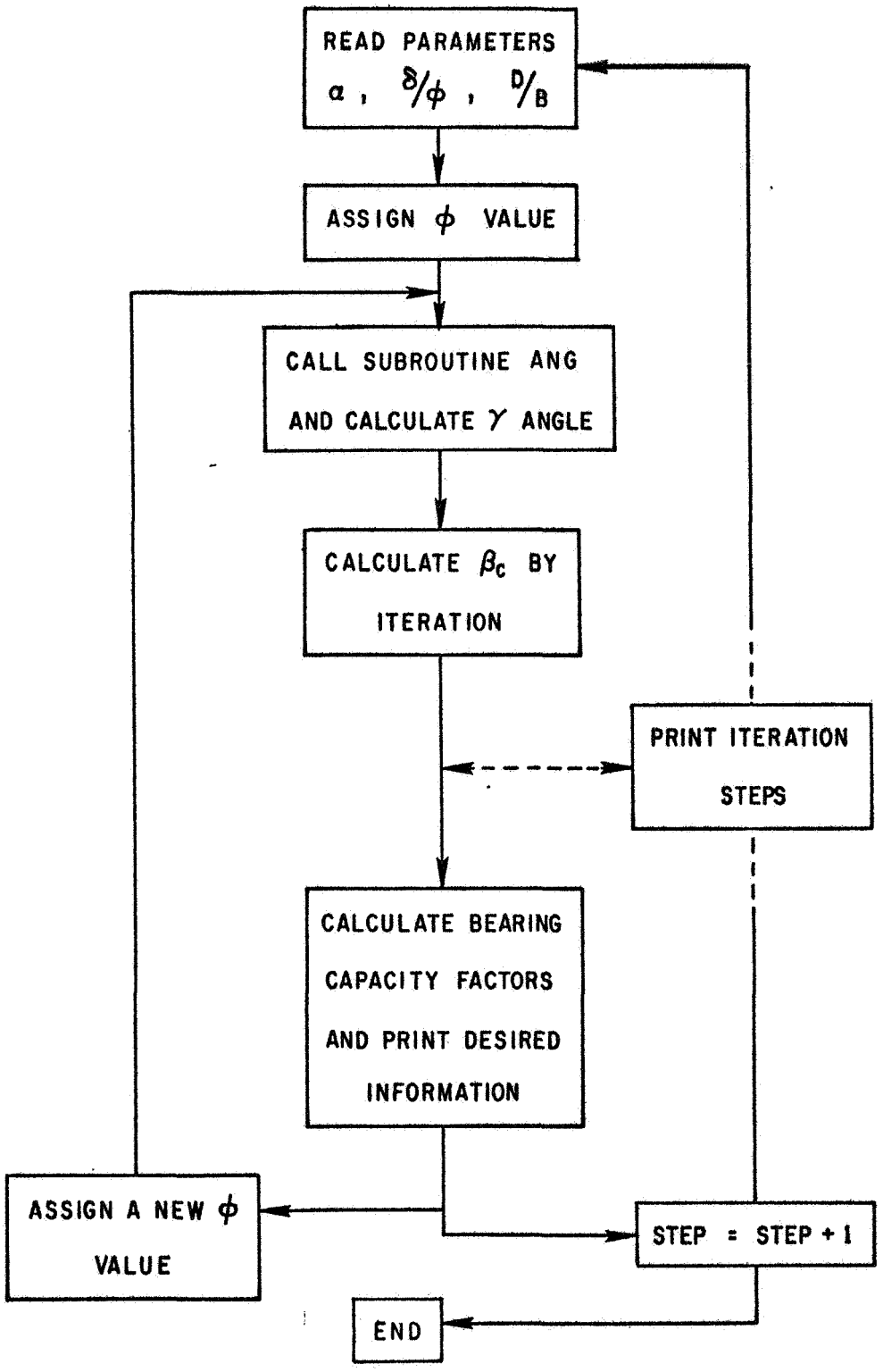

FIG. 4.5 FLOW DIAGRAM FOR DETERMINATION OF BEARING CAPACITY FACTORS

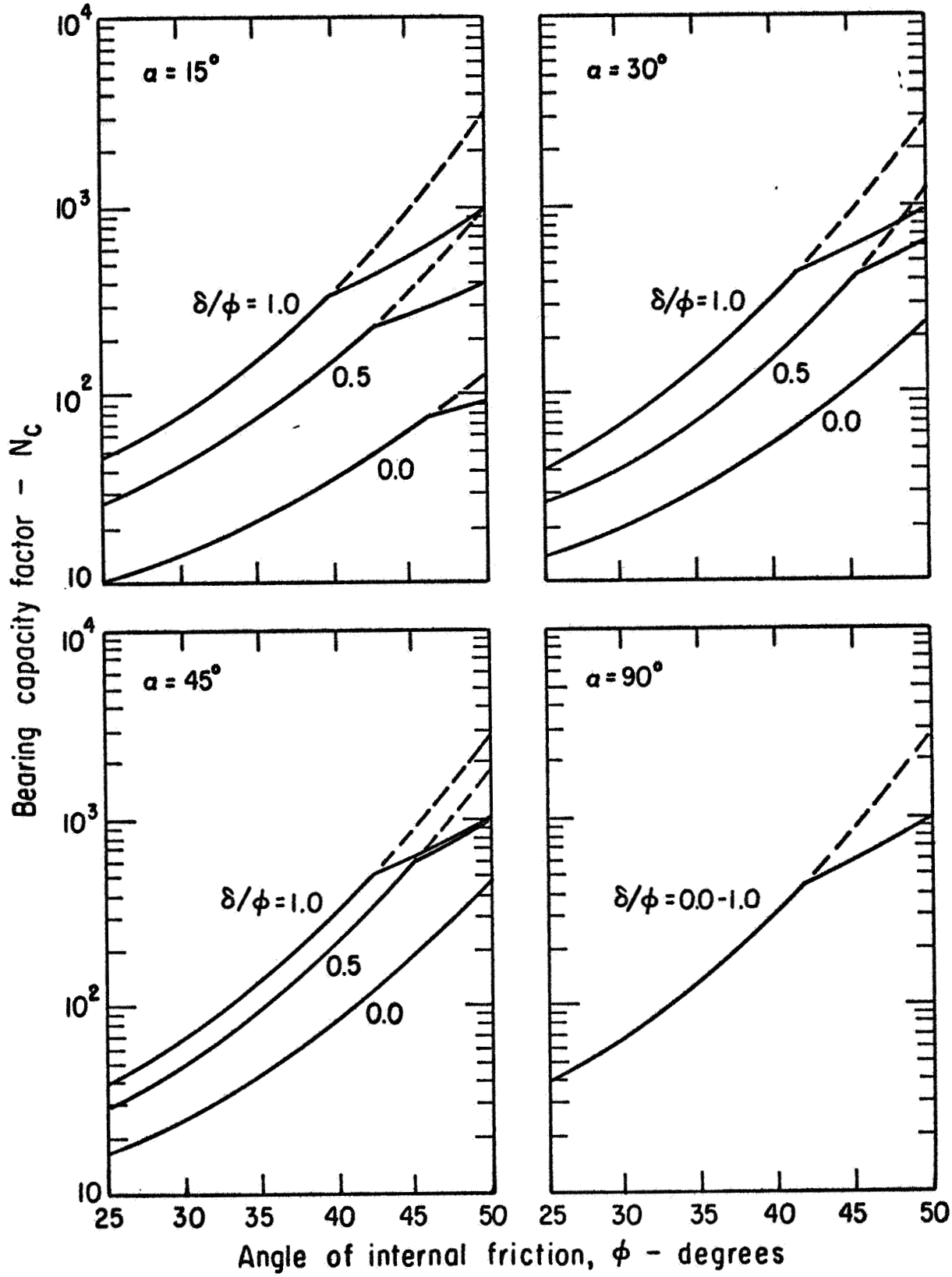

FIG. 4.6 N_c FACTORS FOR D/B = 10.0

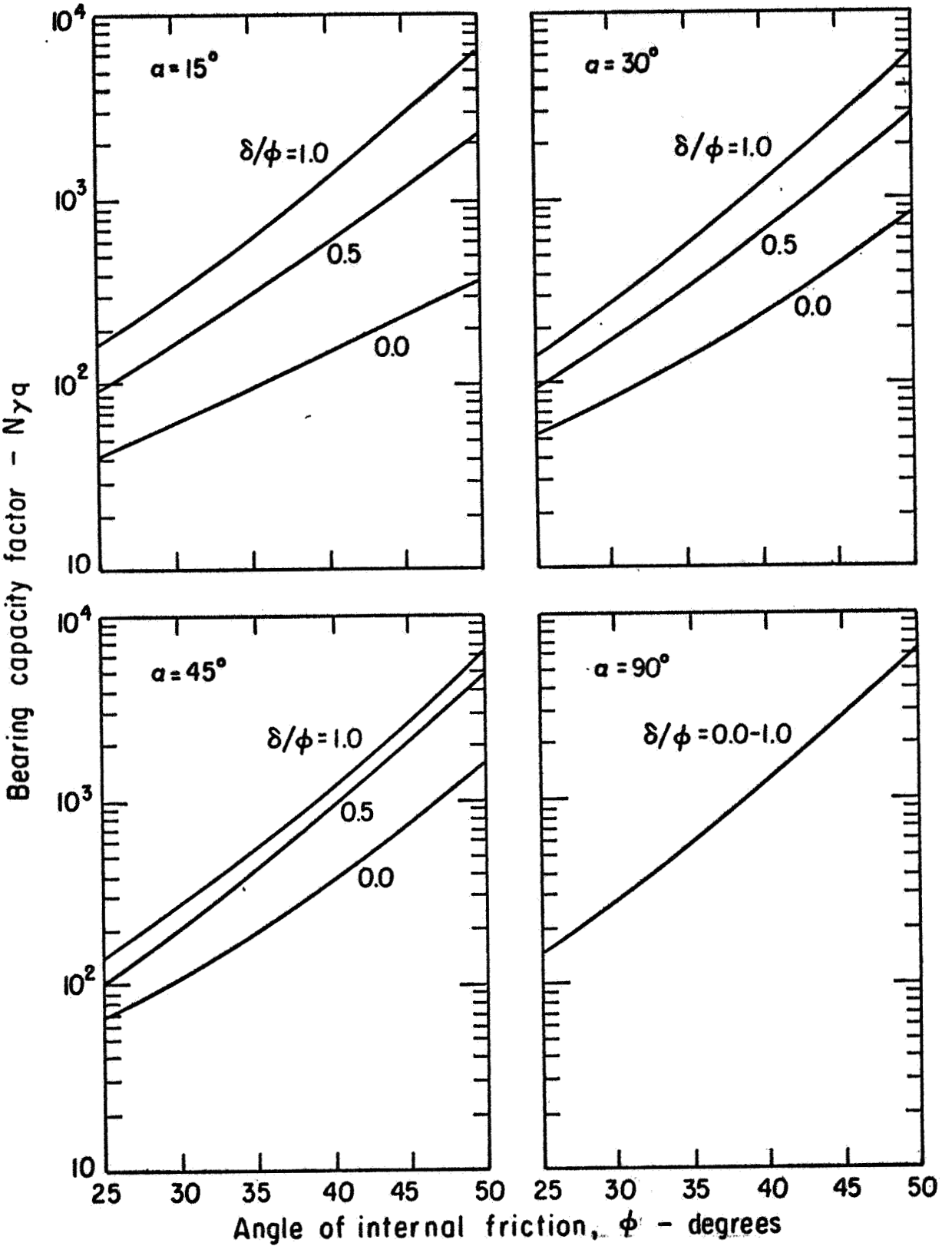

FIG. 4.7 $N_{\gamma q}$ FACTORS FOR D/B = 10.0

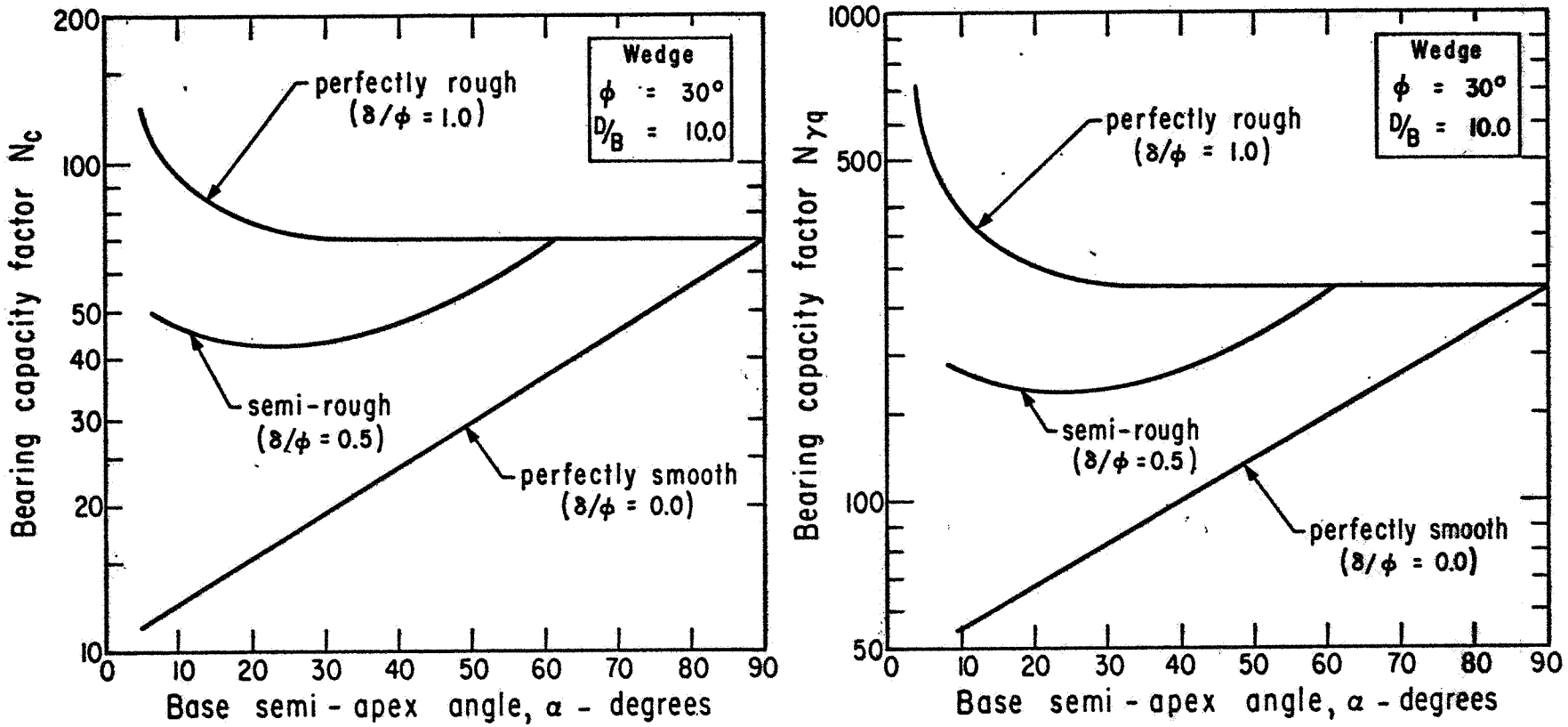

FIG. 4.8 VARIATION OF BEARING CAPACITY FACTORS WITH BASE SEMIAPEX ANGLE

of the factors increase sharply with increasing apex angles.

Effect of Base Roughness

The bearing capacity factors N_c and $N_{\gamma q}$ are dependent not only on α, but also on the base roughness (δ/ϕ). Therefore, knowledge of α alone is insufficient information from which to draw conclusions regarding penetration resistance.

As presented in Chapter Two, the base roughness has little influence on the penetration resistance encountered by a plane and horizontal contact area in cohesive (ϕ=0) soils. However, at the surface of a cohesionless soil, a smooth flat-ended penetrometer will encounter less penetration resistance than one having a rough base. The effect of roughness on the penetration resistance of flat-ended penetrometers in cohesionless soils diminishes for relative depths greater than 4.0 as can be seen from Figs. A.7 through A.10.

It can be seen from Fig. 4.8 that the effect of base roughness is specially important for sharp (small α) wedge or cone shaped penetrometers. However, this effect vanishes for larger values of base semiapex angle.

Fig. 4.9 shows the variation of the bearing capacity factors N_c and $N_{\gamma q}$ with base roughness for a base semiapex angle of 15°. It can be seen that the bearing capacity factors for a given intermediate roughness should not be estimated by linear interpolation between perfectly smooth and perfectly rough values. However, linear interpolation between δ/ϕ= 0.0 (perfectly smooth) and δ/ϕ= 0.5 (semi-rough) and between δ/ϕ= 0.5 and δ/ϕ= 1.0 (perfectly rough) yields a very good approximation to the correct values of N_c and $N_{\gamma q}$.

Effect of Initial Stresses

It can be seen from Equation 4.9 that the bearing capacity factor $N_{\gamma q}$ is dependent upon the value of lateral earth pressure coefficient (K). The value of K is determined by the penetrometer shape (relative sizes of penetrometer base and shaft), soil density, and initial stresses. An increase in the initial lateral stresses means an increase in the value of K. It has been shown that, for example, vibration of cohesionless soils will cause an increase in the value of K (D'Appolonia, et al., 1969). Therefore, the effect of initial lateral stresses on penetration resistance can implicitly be studied by assigning different values for K. As an example, Fig. 4.10 shows how the value of $N_{\gamma q}$ increases with increasing values of K.

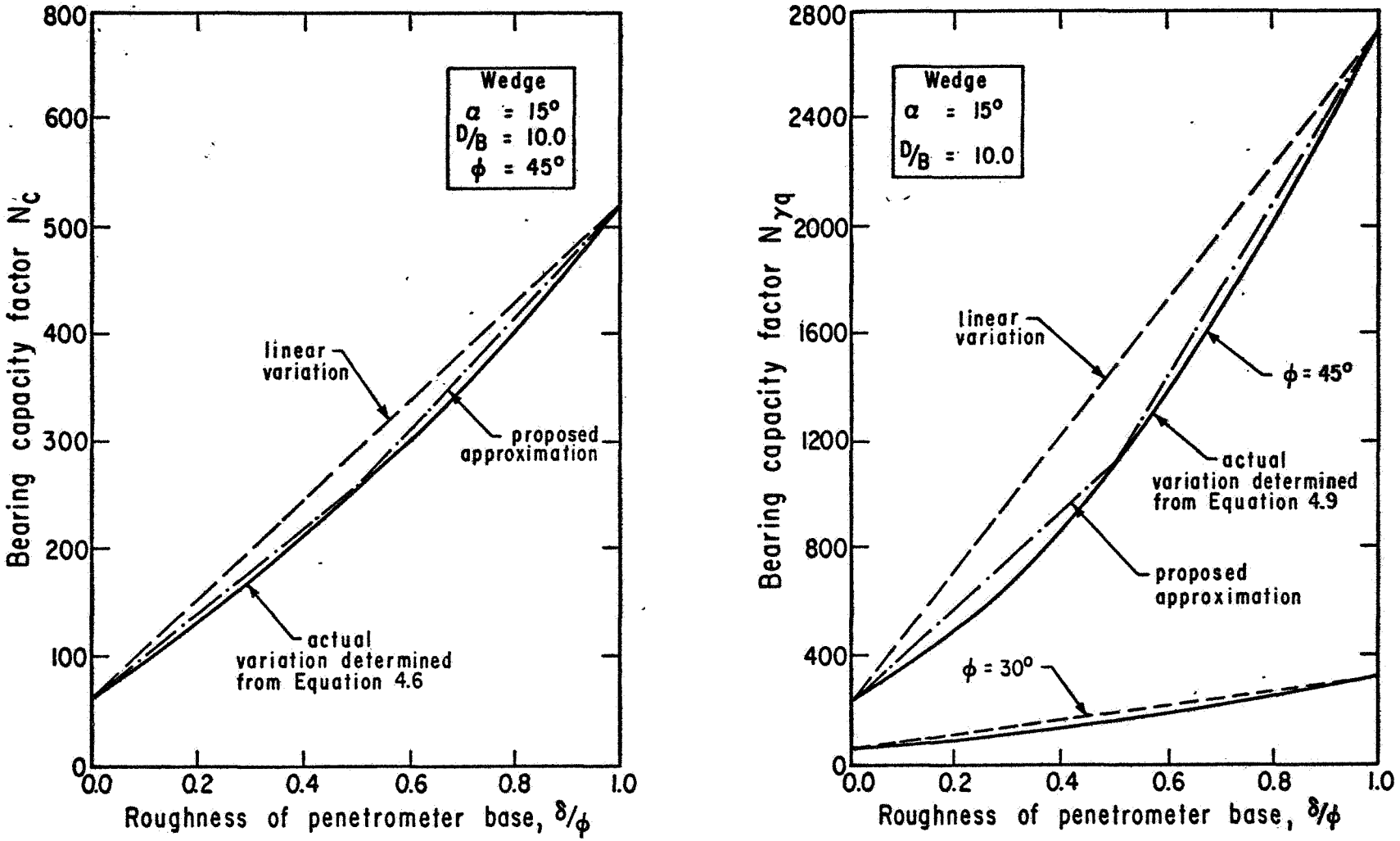

FIG. 4.9 VARIATION OF BEARING CAPACITY FACTORS WITH BASE ROUGHNESS

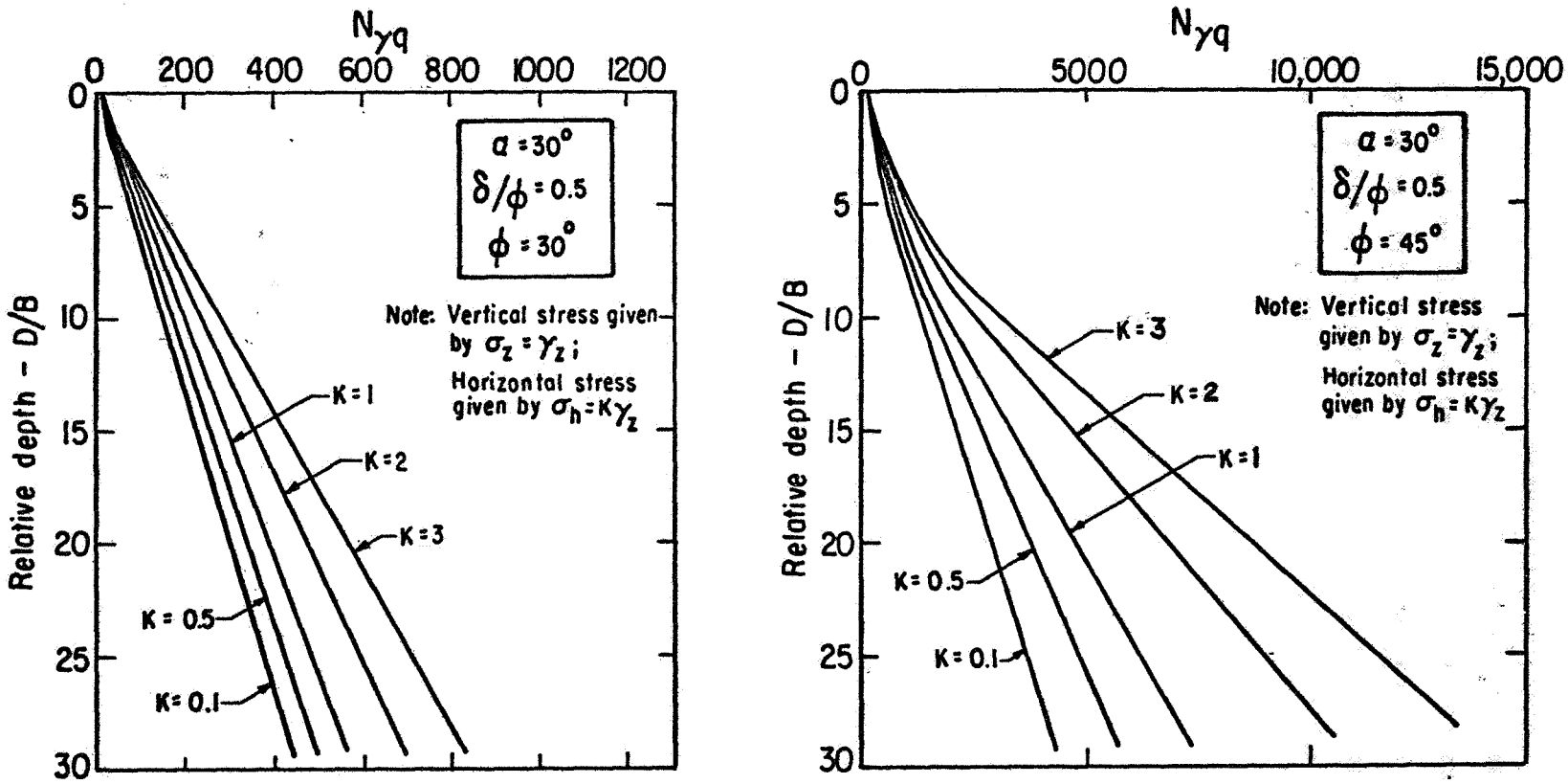

FIG. 4.10 EFFECT OF INITIAL STRESSES ON PENETRATION RESISTANCE

Comparison with Other Available Solutions

As discussed in Chapter Two, Brinch Hansen (1961) proposed that bearing capacity factors corresponding to D/B=0 be modified by depth factors in order to calculate bearing capacities corresponding to larger relative depths. Based on that study and investigations by Meyerhof (1951, 1955), Skempton (1951) and others, Brinch Hansen proposed the following generalized, semi-empirical depth factors:

$$d_c = 1.0 + \frac{0.35}{\frac{B}{D} + \frac{0.6}{(1+7\tan^4\phi)}} \tag{4.19a}$$

$$d_q = d_c - \frac{d_c - 1.0}{N_q} \tag{4.19b}$$

$$d_\gamma = 1.0 \tag{4.19c}$$

It is obvious that d_c and d_q approach limiting values with increasing relative depth for a given value of ϕ. Also, for $\phi>25°$, Brinch Hansen (1961) noted that the second term of Equation 4.19b approaches zero. Thus, for $\phi>25°$:

$$d_q = d_c \tag{4.20}$$

For high values of relative depth, the factor d_c approaches an ultimate value given by:

$$(d_c)_{ult.} = 1.0 + \frac{0.35}{0.6/(1+7\tan^4\phi)} \tag{4.21}$$

Ultimate depth factors may also be calculated theoretically from Meyerhof's (1961a) values of N_c corresponding to shallow and deep foundations by taking the following ratio:

$$(d_c)_{ult.} = \frac{N_c \text{ ("deep" foundations)}}{N_c \text{ ("shallow" foundations)}} \tag{4.22}$$

Further, the theory proposed in the current investigation may also be used to formulate ultimate depth factors as follows:

$$(d_c)_{ult.} = \frac{N_c \text{ (for } D/B \geq (D/B)_{cr})}{N_c \text{ (for } D/B = 0)} \qquad (4.23)$$

It should be noted that in Equation 4.23 the value of N_c remains constant for relative depths equal to or greater than the critical relative depth. Calculated values of the ultimate depth factors for the cohesion term obtained from Equations 4.21, 4.22, and 4.23 as a function of ϕ are compared in Fig. 4.11. It can be seen from Fig. 4.11 that there is a very close agreement between the values calculated from the theory developed in this investigation and the values proposed empirically by Brinch Hansen (1961).

The influence of base roughness and base apex angle on the ultimate depth factors were also investigated. It can be seen from Fig. 4.12 that the effect of roughness is relatively insignificant.

BEARING CAPACITY OF CIRCULAR PENETROMETERS

The calculated bearing capacities are applicable to strip foundations. In practice, however, most penetrometers are circular in shape. Further, as shown in Chapter Three, the deformations around a circular penetrometer are different than those observed for strip foundations. The failed soil zone was restricted to a smaller volume and no distinct failure surfaces were observed in the case of the circular penetrometers.

There have been some attempts (Larkin, 1968, Nowatzki, 1971, and Nowatzki and Karafiath, 1972) to treat this three-dimensional problem theoretically by assuming that the Haar and von Karman hypothesis is valid; i.e., by assuming that the circumferential stress is equal to the minor principal stress. However, according to Hansen and Christensen (1969), theoretical calculations of the bearing capacities of circular footings or penetrometers are open to doubt because the Haar and von Karman hypothesis is incompatible with the proportionality between the plastic strain and deviator stress tensors. Also, the assumed slip surface; i.e., convergence back upon the penetrometer shaft (Nowatzki, 1971) with a discontinity at base level (Nowatzki and Karafiath, 1972) is incompatible with that observed in model tests.

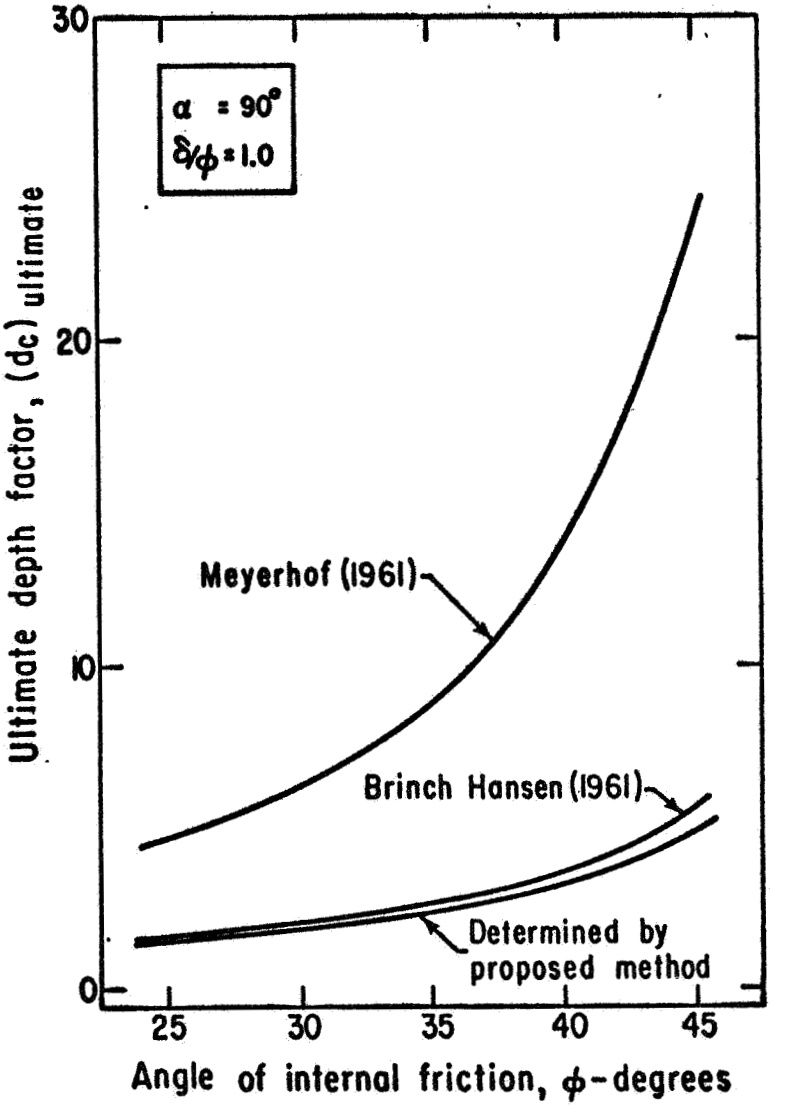

FIG. 4.11 COMPARISON OF ULTIMATE DEPTH FACTORS FOR COHESION TERM

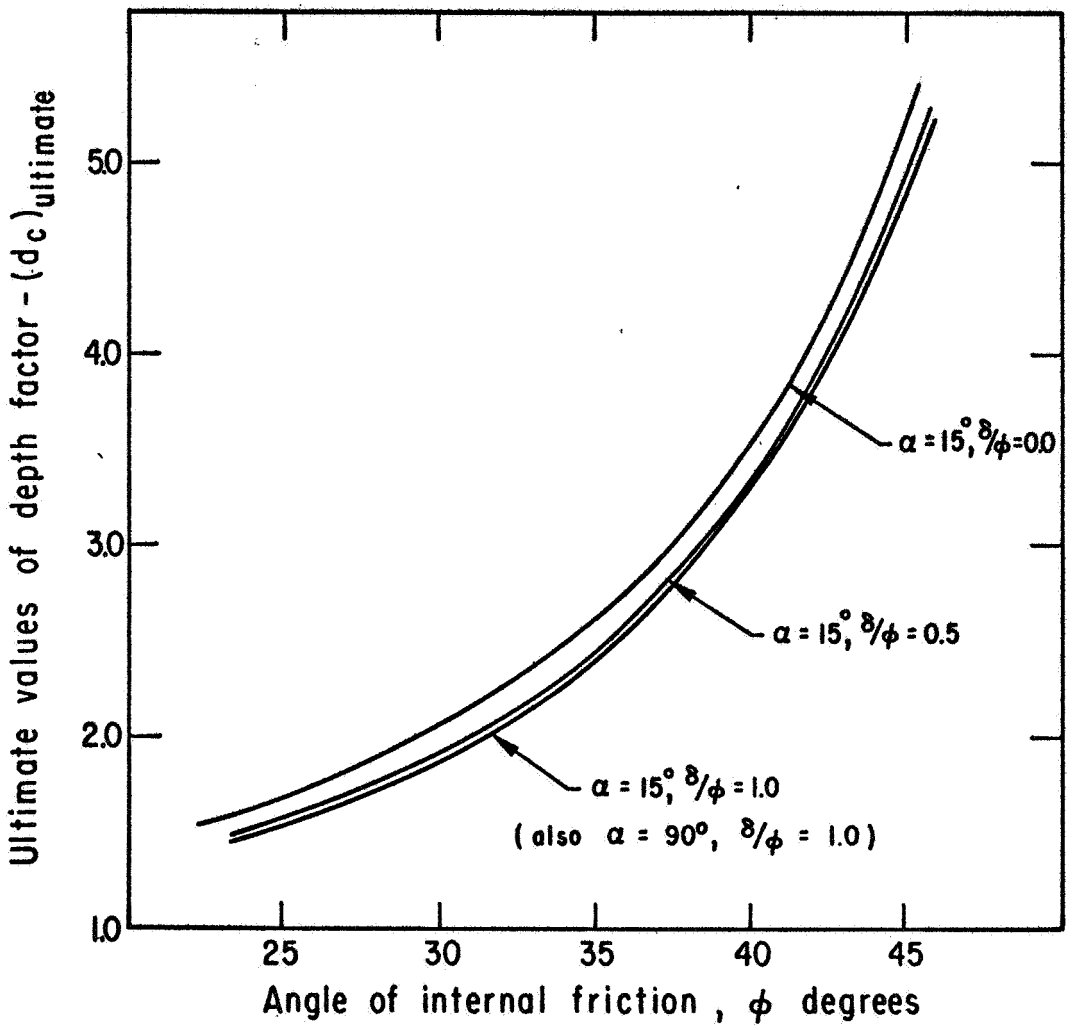

FIG. 4.12 INFLUENCE OF ROUGHNESS OF BASE ON ULTIMATE VALUES OF DEPTH FACTORS

For these reasons it was concluded that theoretical calculations of the bearing capacities of circular foundations are still so uncertain that best estimates are made by the application of shape factors, found empirically, to the bearing capacity factors for strip foundations.

Many empirical shape factors have been proposed. Those recommended by Brinch Hansen (1961) were adopted in this study, because they agreed very closely with the experimentally determined values (see Chapter Six). The following equations, determined semi-empirically, were presented by Brinch Hansen (1961) for the individual shape factors:

$$\xi_c = 1.0 + (0.2 + \tan^6\phi)\ (B/L) \tag{4.24a}$$

$$\xi_q = \xi_c - \frac{\xi_c - 1}{N_q} \tag{4.24b}$$

$$\xi_\gamma = 1.0 - \frac{1}{2}\ (0.2 + \tan^6\phi)\ (B/L) \tag{4.24c}$$

Brinch Hansen (1966) later suggested that ξ_γ be given by:

$$\xi_\gamma = 1.0 - 0.4\ (B/L) \tag{4.25}$$

Brinch Hansen also pointed out that for $\phi > 25°$:

$$\xi_q = \xi_c = 1.0 + [(0.2 + \tan^6\phi)(B/L)] \tag{4.26}$$

It may be seen from Equation 4.26 that the shape factor ξ_q is independent of relative depth. However, because the contributions of friction and surcharge were considered together in formulating the bearing capacity factor $N_{\gamma q}$, it may be shown that the corresponding shape factor $\xi_{\gamma q}$ is dependent on relative depth.

The procedure discussed below is used for the calculation of the shape factor $\xi_{\gamma q}$. As previously discussed, the unit resistance of strip and circular (or other than strip in shape) foundations may be expressed as:

$$(q_f)_{strip} = \frac{1}{2}\ \gamma_s B N_\gamma + \gamma_s D N_q \tag{4.27a}$$

$$(q_f)_{general} = \frac{1}{2}\gamma_s B N_\gamma \xi_\gamma + \gamma_s D N_q \xi_q \qquad (4.27b)$$

or

$$q_f/(\gamma_s B)_{strip} = \frac{1}{2} N_\gamma + \frac{D}{B} N_q \qquad (4.28a)$$

$$q_f/(\gamma_s B)_{general} = \frac{1}{2} N_\gamma \xi_\gamma + \frac{D}{B} N_q \xi_q \qquad (4.28b)$$

The ratio of $q_f/(\gamma_s B)_{general}$ to $q_f/(\gamma_s B)_{strip}$ is the shape factor $\xi_{\gamma q}$ and is given by:

$$\xi_{\gamma q} = \frac{\frac{1}{2} N_\gamma \xi_\gamma + m N_q \xi_q}{\frac{1}{2} N_\gamma + m N_q} \qquad (4.29)$$

where m = D/B.

At the surface (D/B=0) and the contribution of surcharge due to overburden will be zero, consequently;

$$\xi_{\gamma q} = \xi_\gamma = 1.0 - 0.4\ (B/L) \qquad (4.30)$$

or

$$\xi_{\gamma q} = 0.6 \text{ for circular penetrometers.}$$

For large values of relative depth, however, the contribution of the friction term can be neglected compared to the contribution of the surcharge (overburden) term, yielding the following expression from Equations 4.26 and 4.29:

$$\xi_{\gamma q} = \xi_q = 1.0 + (0.2 + \tan^6\phi)\ (B/L) \qquad (4.31)$$

Values of the shape factor $\xi_{\gamma q}$ may be calculated from Equation 4.29 for different values of ϕ and relative depth (m=D/B). The factors ξ_γ and ξ_q are determined from Equations 4.25 and 4.26, and the bearing capacity factors N_γ and N_q are taken from Fig. 2.4. The calculated values of $\xi_{\gamma q}$ are presented in Fig. 4.13.

However, in order to apply the procedure suggested in Chapter Seven

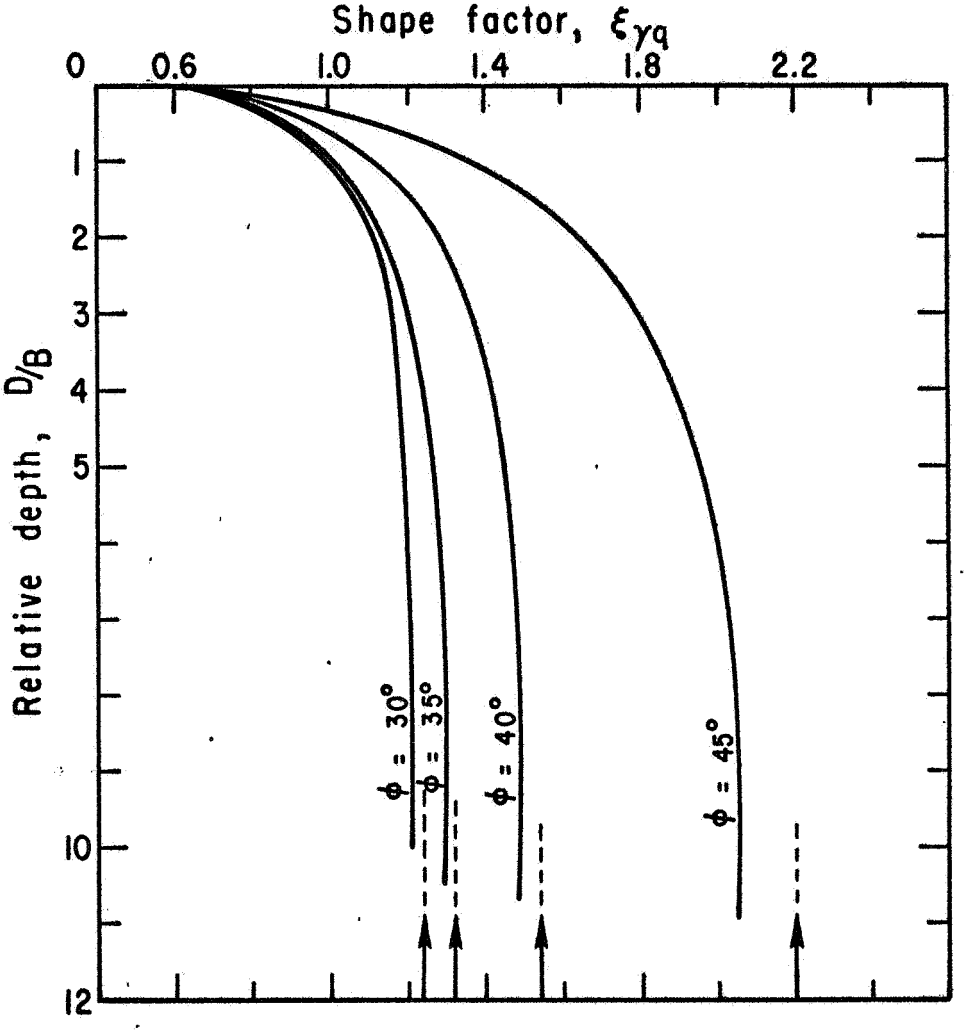

FIG. 4.13 VARIATION OF SHAPE FACTOR $\xi_{\gamma q}$ WITH DEPTH FOR GIVEN VALUES OF ANGLE OF INTERNAL FRICTION

for the determination of in-situ strength properties from the results of cone penetration tests, it is necessary to formulate the variation in $\xi_{\gamma q}$ analytically. The following empirical relationship has been obtained which agrees closely with the values calculated theoretically from Equation 4.29 for the range of interest:

$$\xi_{\gamma q} = 1.0 - 0.4(B/L) + \frac{1.5}{\frac{B}{D} + \frac{1.5}{(0.6+\tan^6\phi)(B/L)}} \tag{4.32}$$

where $\xi_{\gamma q}$ = shape factor for the friction-surcharge term
B = width of penetrometer base
D = depth of penetrometer base
L = length of penetrometer base (=B for circular penetrometers)
ϕ = angle of internal friction of soil

At the surface, (D/B=0), Equation 4.32 becomes:

$$\xi_{\gamma q} = \xi_{\gamma} = 1.0 - 0.4\ (B/L) \tag{4.33}$$

Further, it can be seen that, for large values of relative depth (D/B), Equation 4.32 becomes:

$$\xi_{\gamma q} = \xi_{q} = 1.0 + (0.2 + \tan^6\phi)\ (B/L) \tag{4.34}$$

Therefore, it can be seen that Equation 4.32 satisfies known relationships (Equations 4.25 and 4.26) at the limits (D/B = 0 and ∞).

Table 4.1 presents a comparison (over a wide range of values of ϕ and D/B) of values of $\xi_{\gamma q}$ by Equation 4.32 and by Equation 4.29. It can be seen that the agreement is quite good, and thus it may be concluded that Equation 4.32 may be satisfactorily utilized in the analysis of cone penetration data.

SUMMARY

Knowledge of the failure mechanism associated with static penetration (see Chapter Three) has permitted development of a new relationships for ultimate resistance to penetration of wedges which account explicitly for base apex angle, base roughness, soil friction angle, and relative depth. The derivation of

Table 4.1 COMPARISON OF SHAPE FACTORS ($\xi_{\gamma q}$) DETERMINED FROM EQUATIONS 4.29 AND 4.32

Relative Depth, D/B ϕ, (deg.)	0.0	0.05	0.5	1.0	2.0	5.0	10.0	∞
30	0.60	0.66	0.93	1.04	1.12	1.19	1.21	1.24
	0.60	0.67	0.96	1.05	1.13	1.19	1.21	1.24
35	0.60	0.66	0.93	1.06	1.16	1.25	1.28	1.34
	0.60	0.67	0.97	1.09	1.18	1.26	1.29	1.34
40	0.60	0.66	0.99	1.15	1.29	1.42	1.48	1.55
	0.60	0.67	1.02	1.18	1.32	1.44	1.49	1.55
45	0.60	0.68	1.14	1.40	1.67	1.93	2.06	2.20
	0.60	0.67	1.11	1.37	1.64	1.91	2.04	2.20

Note: Upper values are by Equation 4.29, lower values are by Equation 4.32.

the bearing capacity factors N_c and $N_{\gamma q}$ in terms of these parameters and curves relating these factors to the angle of internal friction of soil for several values of α, δ/ϕ, and D/B for strip foundations were presented. The values of ultimate depth factors calculated from these relationships agree closely with the empirical values given by Brinch Hansen (1961). The shape factor $\xi_{\gamma q}$ was calculated in terms of relative depth using the values of ξ_{γ} and ξ_{q} proposed by Brinch Hansen (1961). Based on the results of these calculations, an empirical relationship was proposed which relates $\xi_{\gamma q}$ to the angle of internal friction of soil and relative depth.

CHAPTER FIVE

EXPERIMENTAL INVESTIGATION - SOIL PROPERTIES

INTRODUCTION

In order to evaluate the proposed theory experimentally, accurate values of the angle of internal friction of the soil and the penetrometer to soil friction must be determined. Comprehensive series of drained triaxial and direct shear tests were performed to measure the strength properties of the test soil, and a series of direct shear tests was done in order to determine the penetrometer to soil friction. The results of these tests enabled the formulation of:

(1) The soil friction angle (ϕ) in terms of the pre-shear void ratio and mean normal stress (or confining pressure),

(2) The penetrometer to soil friction angle (δ) in terms of the pre-shear void ratio and normal stress for various penetrometer materials and,

(3) The variation of roughness (δ/ϕ) with pre-shear void ratio.

These results were used to predict the penetration resistance of the soil using the proposed theory, thus enabling a comparison between predicted and measured values (see Chapter Six).

SOIL CLASSIFICATION

A fine, clean, air-dried sand (Monterey Sand No. 0) was chosen for this study. Classification data for this sand are summarized below:

Mean diameter	0.36 mm
Coefficient of uniformity	1.45
Specific gravity of grains	2.648 g/cm^3
Maximum void ratio	0.825
Minimum void ratio	0.558

The gradation curve of Monterey Sand No. 0 is given in Fig. 5.1. Microscopic observation of the sand showed that the particles were sub-rounded and that quartz and feldspar were the predominant minerals with a trace of mica.

STRENGTH PROPERTIES FROM TRIAXIAL COMPRESSION TESTS

Test Procedure

Specimens were prepared in a triaxial cell to the desired uniform initial densities. The desired chamber pressure (pressures used were

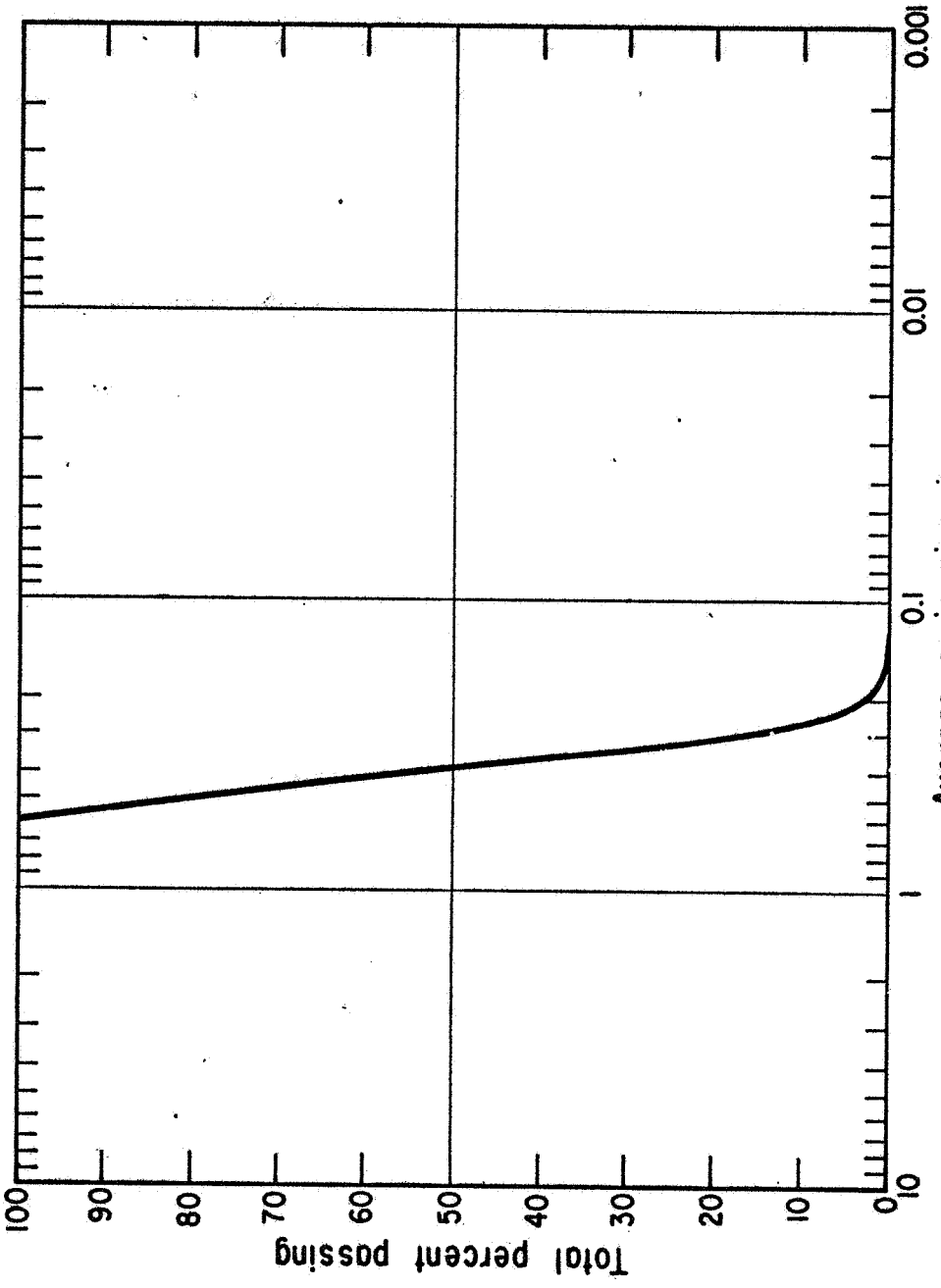

FIG. 5.1 GRADATION CURVE OF MONTEREY SAND No. 0

29.4, 58.8, 98, and 294 kN/m^2) was applied by air pressure on the chamber water and the specimen was tested 30 minutes later in a Wykeham-Farrance strain-controlled testing machine at a deformation rate of 0.006 inches per minute (0.152 mm/min). During the test, measurements were taken of the axial load with a load cell, axial deformation with a dial gage and change in volume of chamber water with a volume change device of the type developed by Chan and Duncan (1967).

Test Results

A total of 16 drained triaxial shear tests was conducted. The results of these tests are plotted in Figs. 5.2 and 5.3 which show the values of principal stress ratio (σ_1/σ_3) versus axial strain for the conditions investigated. The peak values of soil friction angles were calculated from the results of these tests using the equation:

$$\phi = \sin^{-1}\{[(\sigma_1/\sigma_3)_f - 1]/[(\sigma_1/\sigma_3)_f + 1]\} \qquad (5.1)$$

The triaxial shear tests were carried to axial strain values of 10 to 15 percent. In the determination of residual triaxial friction angles, principal stress ratios corresponding to axial strains of from 8 to 12 percent were used. The change in principal stress ratio beyond these axial strain values was negligible for the range of confining pressures and soil densities used.

Peak and ultimate triaxial friction angles are presented in Table 5.1 and are plotted against pre-shear void ratio (e_c) for the various confining pressures in Fig. 5.4. Values of the peak friction angles determined from plane strain tests by Lade (1972) for the same sand are also plotted on Fig. 5.4 for comparison.

It can be seen that the difference between peak and ultimate values of friction angles obtained from triaxial shear tests is not great, with almost no difference for loose soil conditions.

Peak principal stress ratios were found to decrease with increasing confining pressures (or mean normal stress) for a given pre-shear void ratio. As a result, the failure envelopes shown in Fig. 5.5 are slightly curved, indicating that an increase in mean normal stress causes a reduction in soil friction angle values.

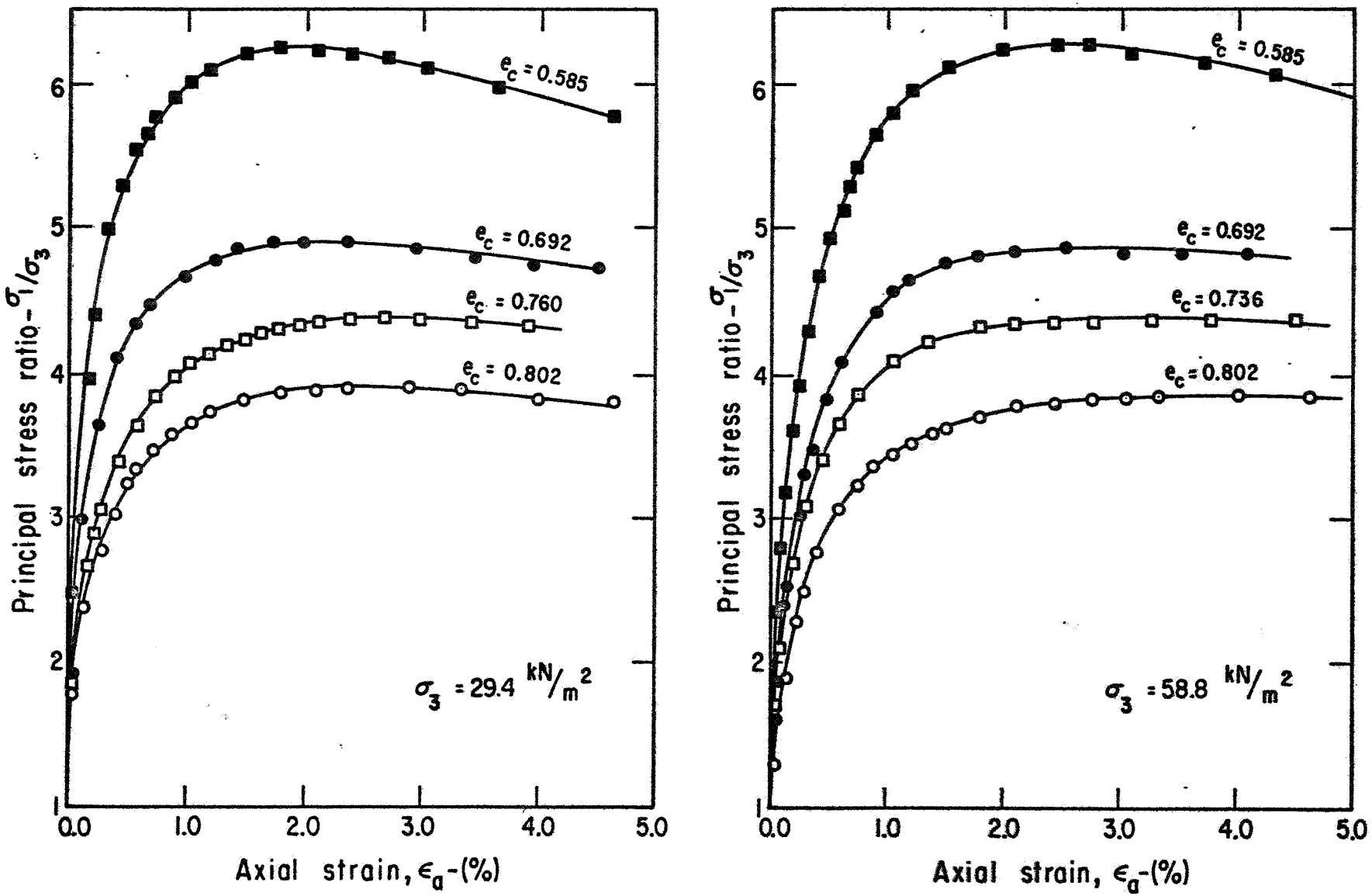

FIG. 5.2 STRESS-STRAIN RELATIONSHIPS OF AIR-DRY MONTEREY SAND No. 0 DETERMINED FROM TRIAXIAL SHEAR TESTS

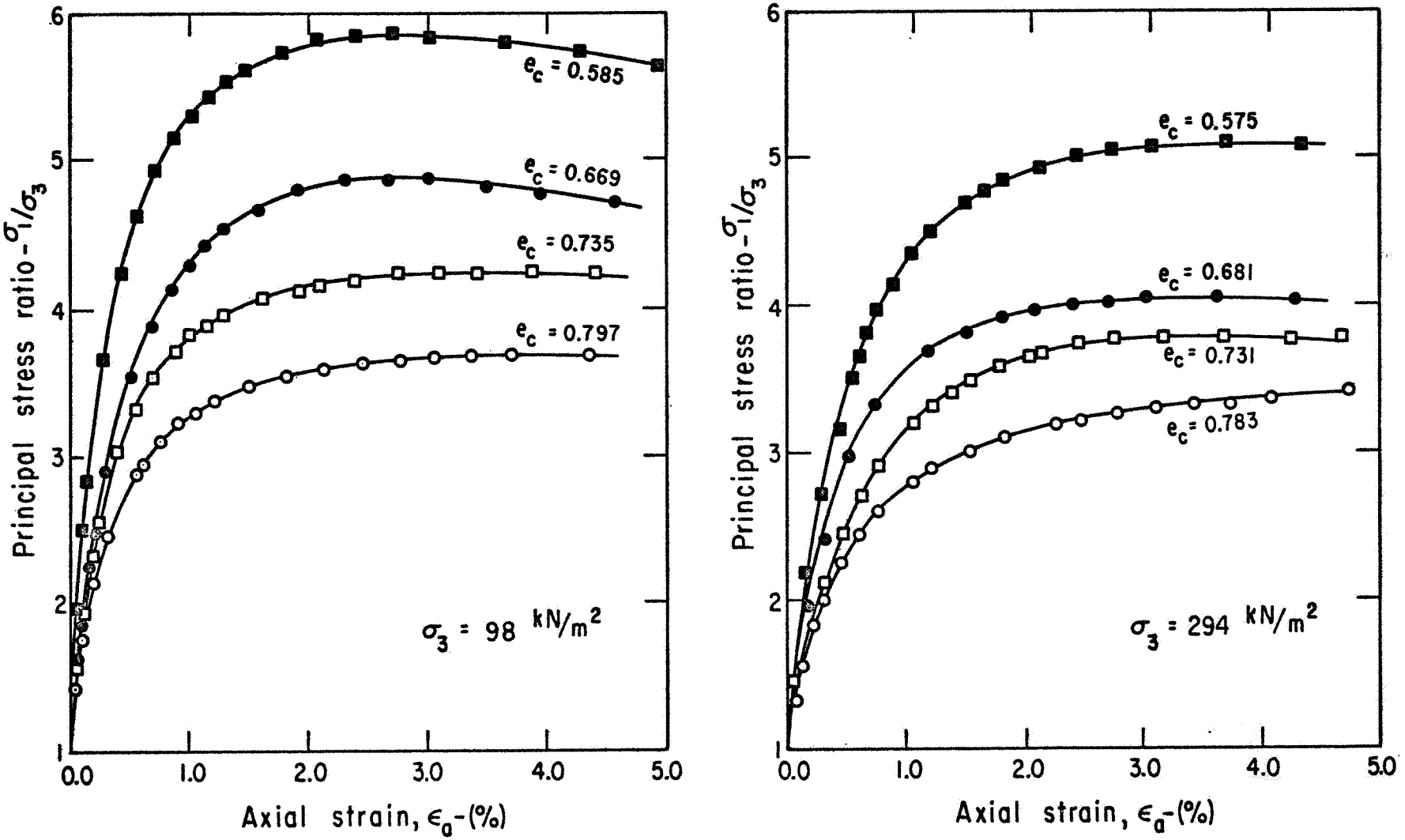

FIG. 5.3 STRESS - STRAIN RELATIONSHIPS OF AIR - DRY MONTEREY SAND No. 0 DETERMINED FROM TRIAXIAL SHEAR TESTS

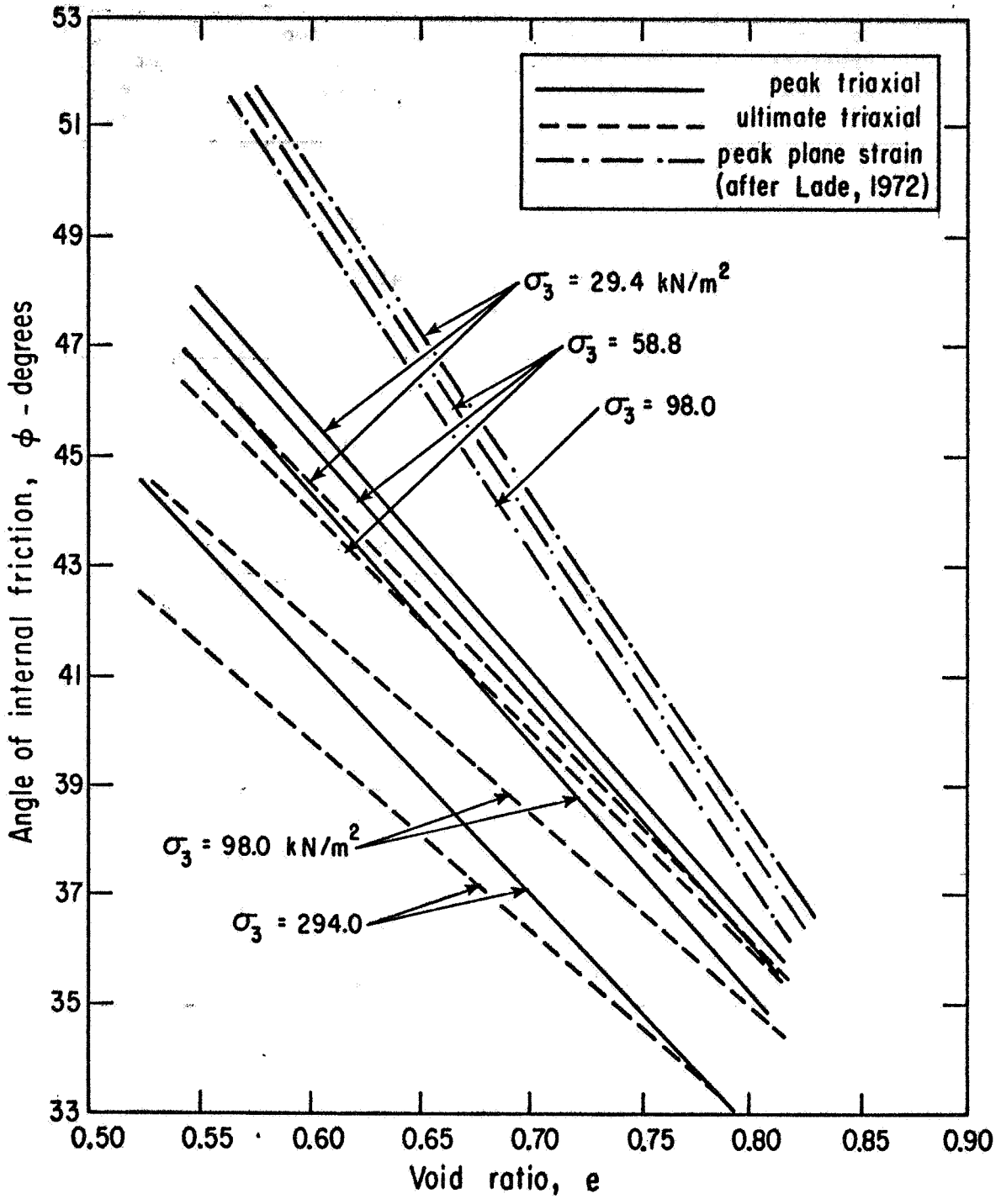

FIG. 5.4 SUMMARY OF FRICTION ANGLES FOR MONTEREY SAND No. 0

Table 5.1 SUMMARY OF TRIAXIAL PEAK AND ULTIMATE FRICTION ANGLES FOR MONTEREY SAND NO. 0

Confining Pressure σ_3-kN/m^2	Pre-shear Void Ratio e_c	Peak Friction Angle ϕ_p-deg.	Ultimate Friction Angle ϕ_r-deg.
29.4	0.802	36.4	35.9
	0.760	39.0	-
	0.692	41.2	39.8
	0.585	46.5	44.0
58.8	0.802	36.0	35.7
	0.736	39.0	-
	0.692	40.9	-
	0.585	46.5	44.5
98.0	0.797	35.1	35.0
	0.735	38.0	-
	0.669	41.2	-
	0.585	45.2	42.3
294.0	0.783	33.6	33.5
	0.731	35.8	-
	0.681	37.3	36.5
	0.575	42.1	40.6

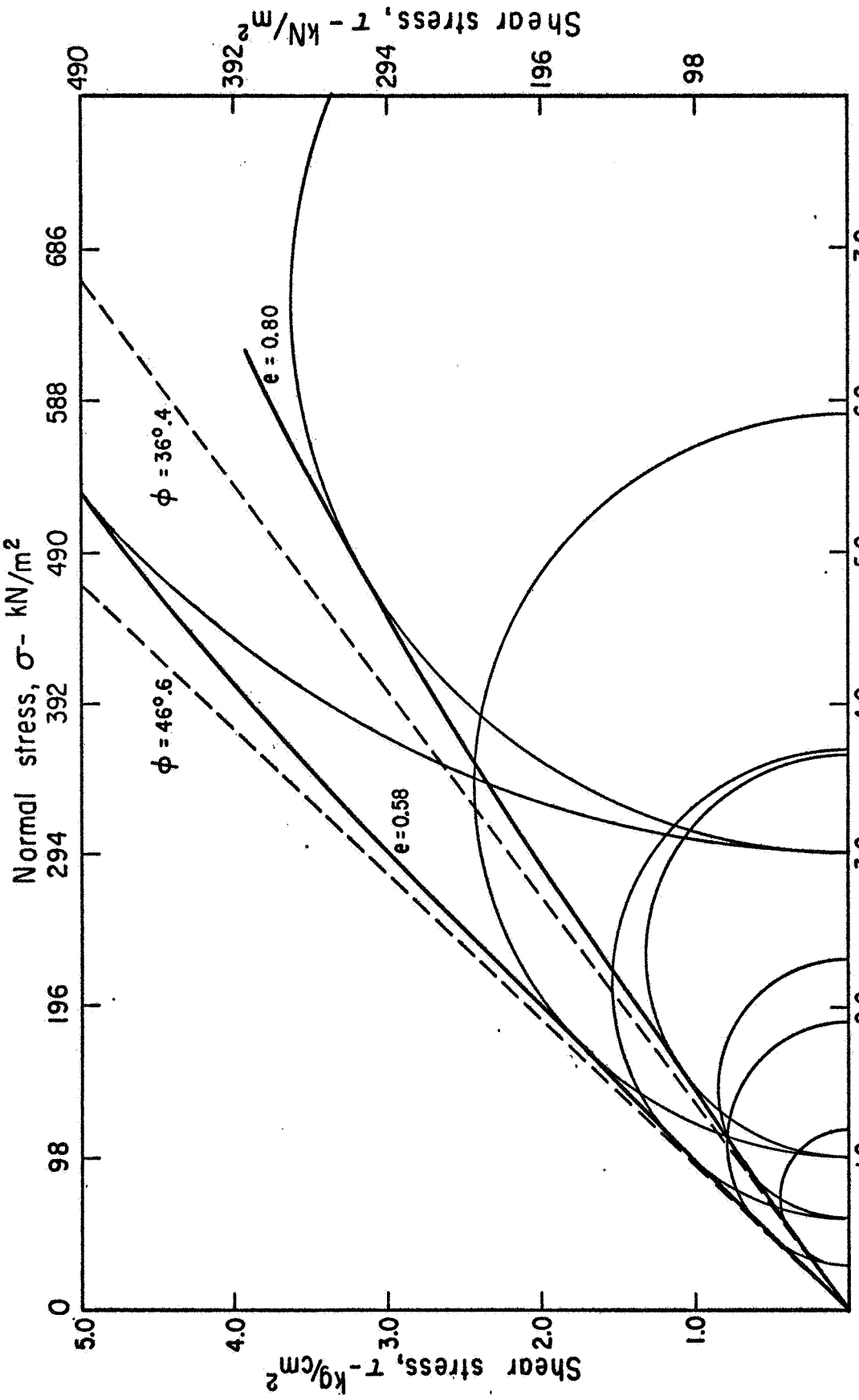

FIG. 5.5 FAILURE ENVELOPES FOR MONTEREY SAND No. 0

As suggested by Banks (1968), the triaxial ϕ values were plotted against the logarithm of confining pressure as shown in Fig. 5.6. It may be seen that the relationships can be represented by straight lines for the range of confining pressures used. This variation of ϕ with σ_3 may be expressed in the following form:

$$\phi(e_c,\sigma_3) = \phi_1(e_c) - m(e_c) \log (\sigma_3/p_a) \tag{5.2}$$

in which $\phi_1(e_c)$ is the angle of internal friction at a given pre-shear void ratio and at a confining pressure of p_a (atmospheric pressure) expressed in the same units as σ_3, and $m(e_c)$ is the reduction in ϕ per log cycle change in confining pressure. For the range of confining pressures (29.4 to 294 kN/m^2) used, m values are between 3.5 and 6.0. The triaxial friction angle of Monterey Sand No. 0 can be determined from the Figs. 5.4 and 5.6 for any value of confining pressure (or normal stress on the failure surface) and pre-shear void ratio.

STRENGTH PROPERTIES FROM DIRECT SHEAR TESTS

Penetrometer to soil friction angles (δ) were determined from the results of direct shear tests. A series of direct shear tests was also done on the sand in order to obtain values of the soil friction angle for determination of δ/ϕ.

The results of soil to soil direct shear tests are shown in Fig. 5.7 and indicate the variation of shear stress with relative shear displacements for normal stresses of 168, 353, and 535 kN/m^2. The corresponding direct shear friction angles were calcualted and are presented in Table 5.2. These values can be compared with the values obtained from triaxial tests, as shown in Fig. 5.8. Because the values are stress dependent, comparisons should be made at same normal stress values. The normal stress on the failure plane in a triaxial test is calculated from the following relationship:

$$\sigma_{mf}/\sigma_{3f} = 1 + \sin\phi \tag{5.3}$$

Fig. 5.8 shows the average ϕ versus void ratio relationship which will be used for the calculation of δ/ϕ in the following section.

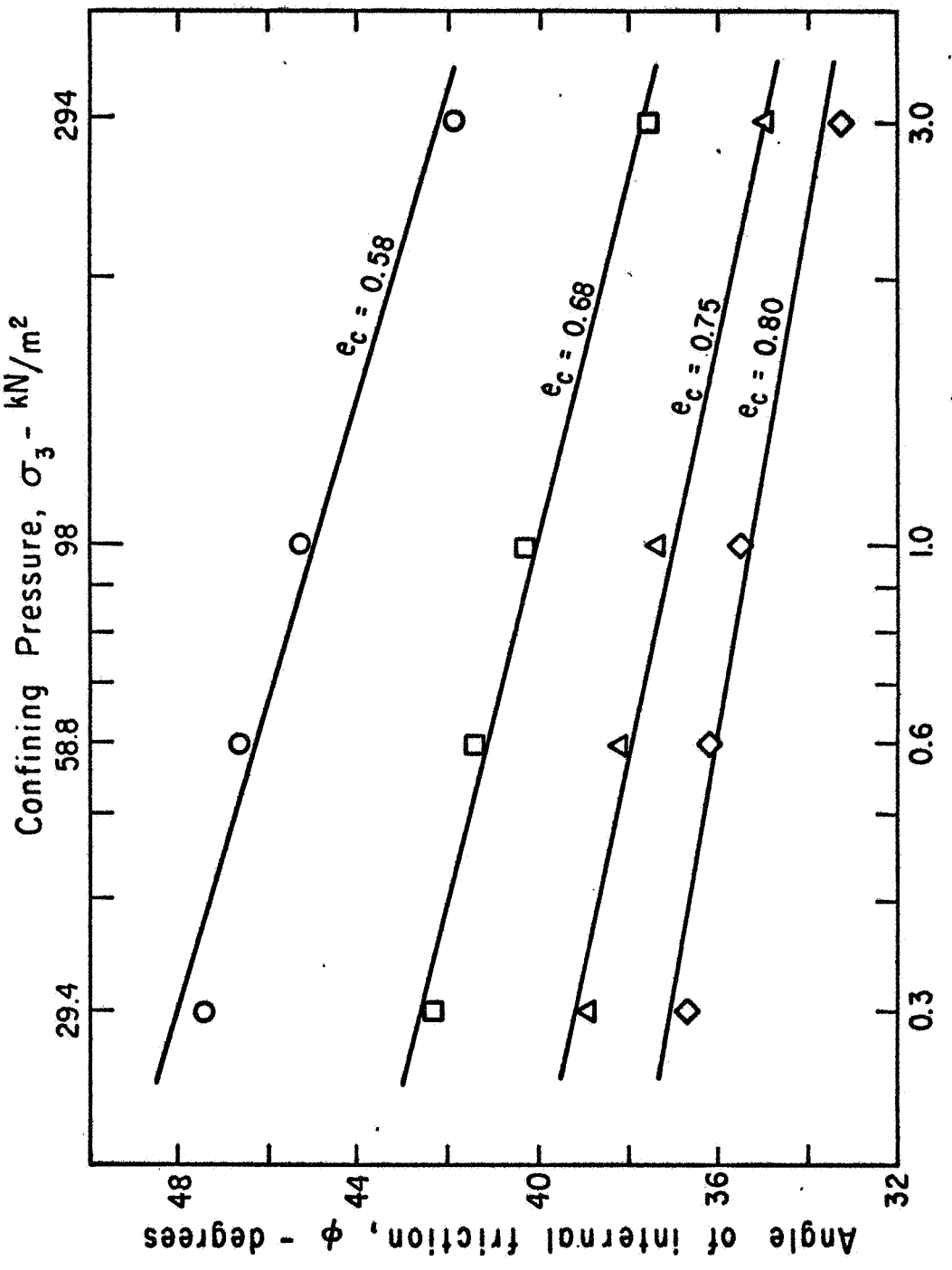

FIG. 5.6 VARIATION OF TRIAXIAL FRICTION ANGLE OF MONTEREY SAND No. 0 WITH CONFINING PRESSURE

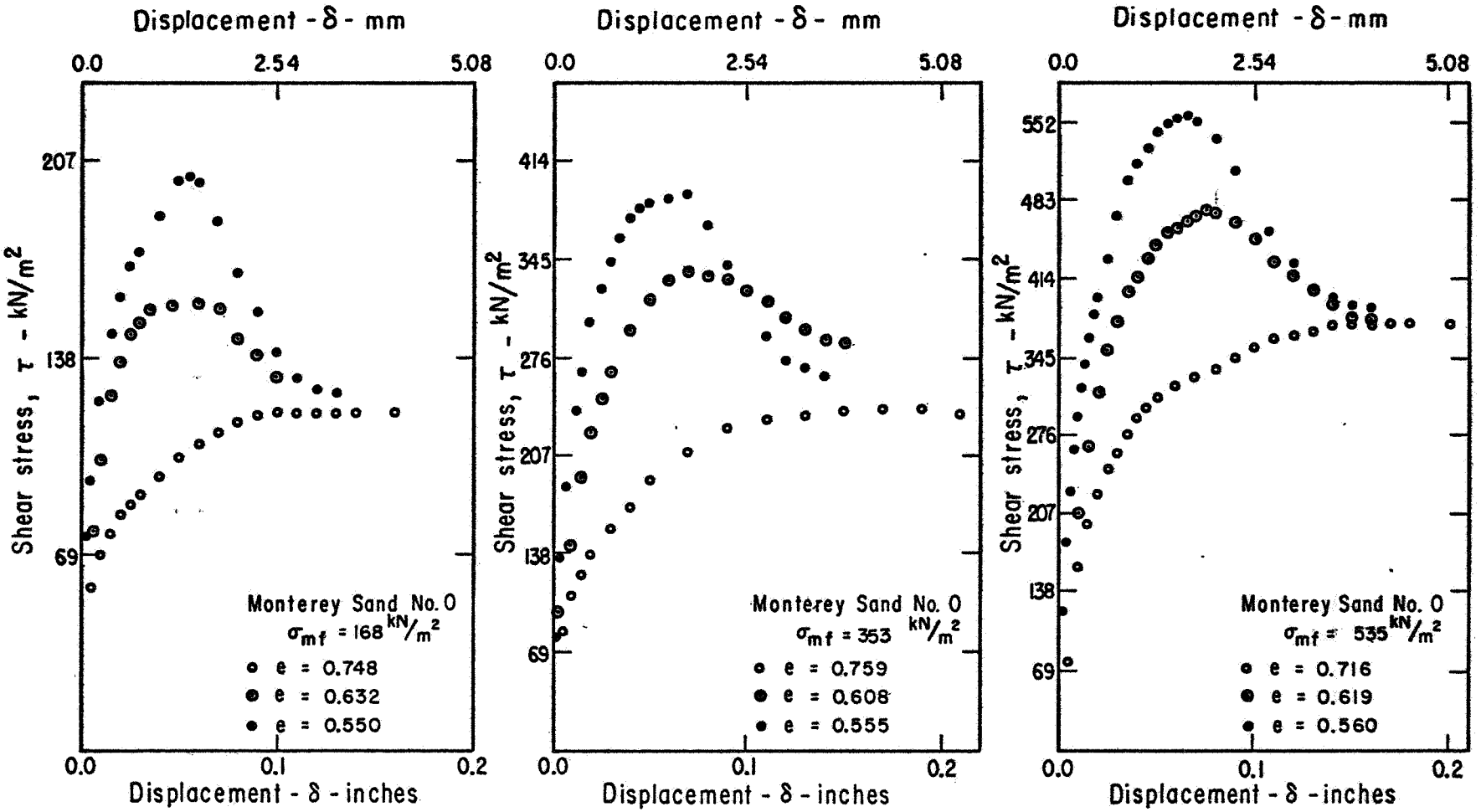

FIG. 5.7 SHEAR STRESS VERSUS SHEAR DISPLACEMENT RELATIONSHIPS OF MONTEREY SAND No. 0 DETERMINED FROM DIRECT SHEAR TESTS

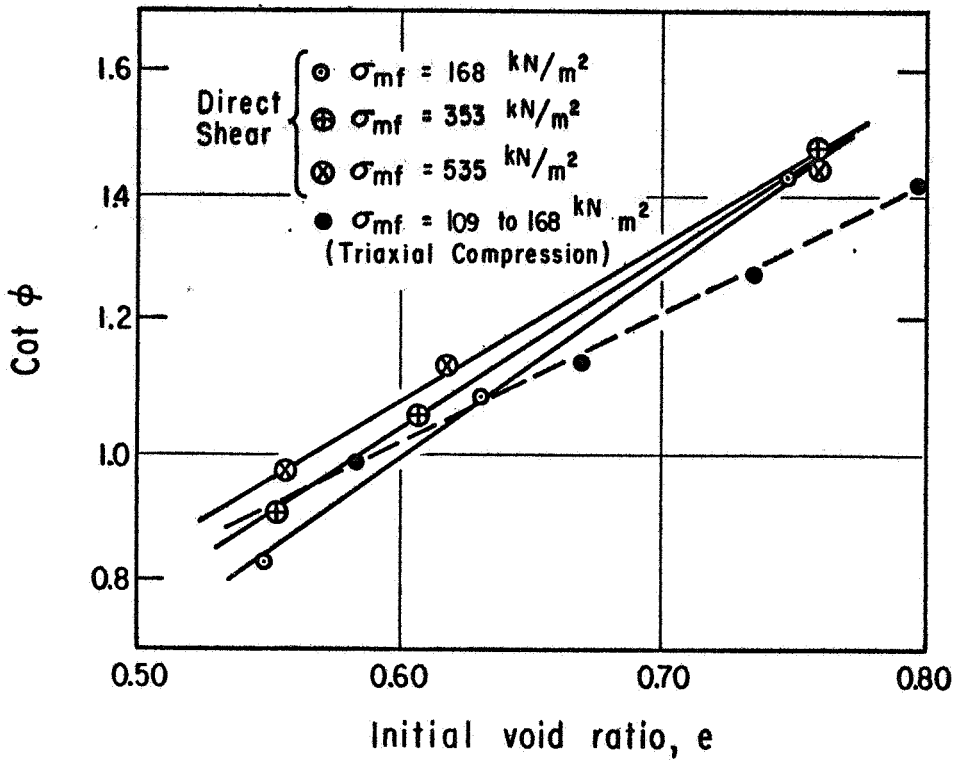

FIG. 5.8a COMPARISON OF SOIL TO SOIL TRIAXIAL AND DIRECT SHEAR FRICTION ANGLES

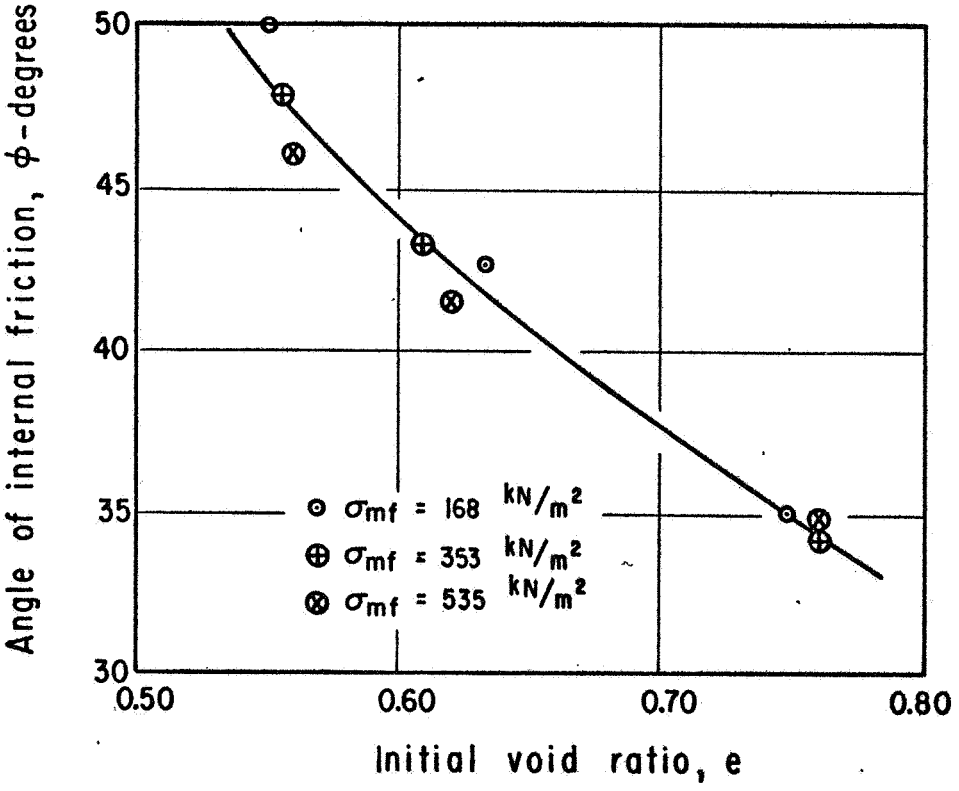

FIG. 5.8b SOIL TO SOIL FRICTION ANGLES OF MONTEREY SAND No. 0 FROM DIRECT SHEAR TESTS

Table 5.2 SUMMARY OF SOIL TO SOIL DIRECT SHEAR TESTS

Normal Stress on failure plane σ_{mf}-kN/m^2	Initial Void Ratio, e	Angle of Internal Friction ϕ-deg.
168	0.748	35.0
	0.632	42.6
	0.550	50.1
353	0.759	34.2
	0.608	43.2
	0.555	47.8
535	0.761	34.8
	0.619	41.4
	0.560	46.0

PENETROMETER TO SOIL FRICTION

To determine the friction angle between the penetrometer material and soil, and establish a basis for the variation of δ/ϕ with void ratio, tests were conducted in a similar manner to the standard direct shear test. The upper half of the shear box was filled with Monterey Sand No. 0 at a desired initial density, and the lower half of the shear box was replaced by a solid sample of penetrometer material. A section through the shear box with the samples in place is shown in Fig. 5.9. The three differenct penetrometer materials tested are listed below:

(1) Polished hard-anodized aluminum

(2) Hard-anodized aluminum

(3) Sanded aluminum (sand particles glued to aluminum).

The tests were conducted in a Karol-Warner direct shear machine connected to a variable speed motor in series with a gear reduction box so that the rate of shearing could be maintained at 0.0015 in/min (0.048 mm/min). A total of

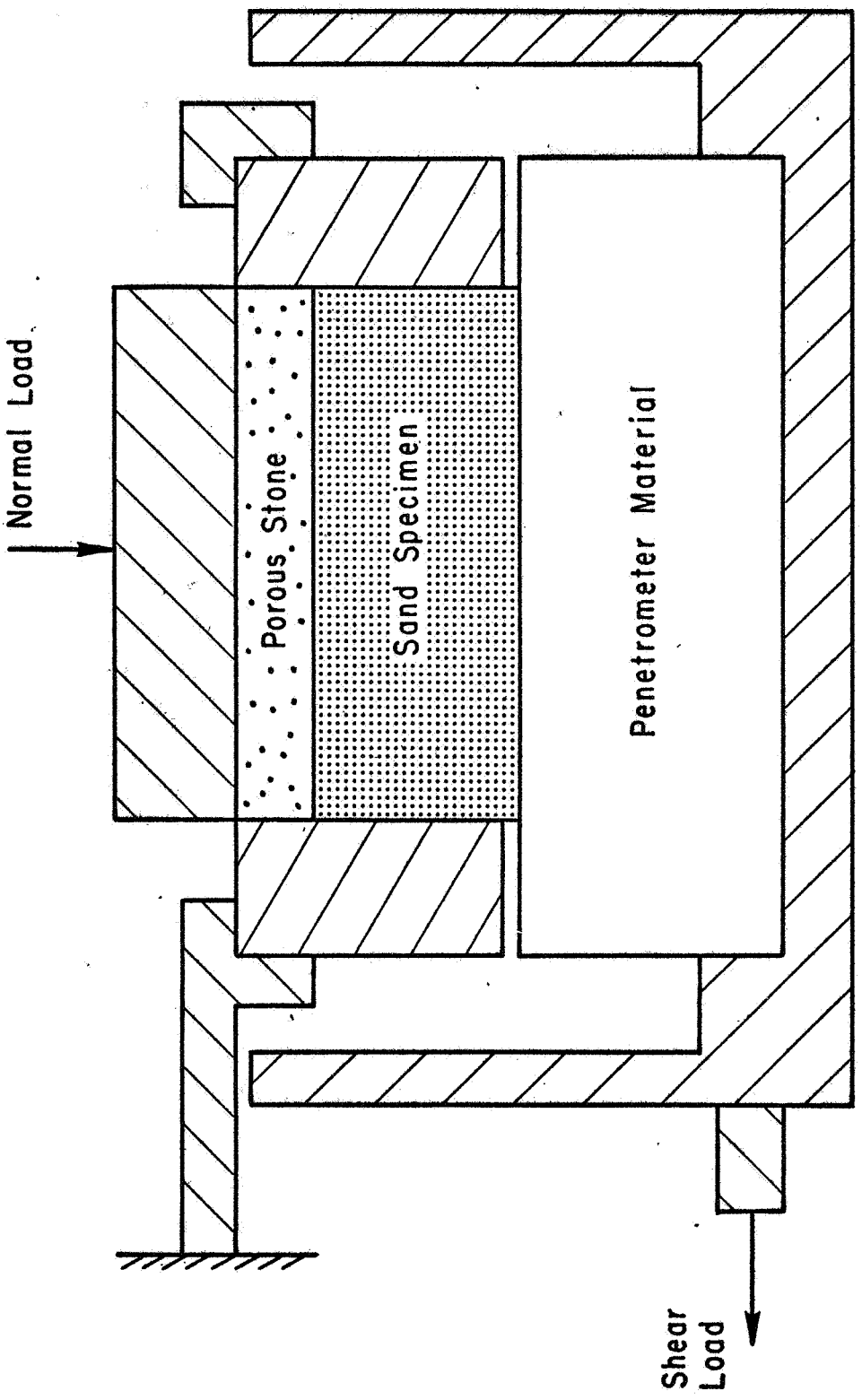

FIG. 5.9 DIRECT SHEAR TEST SETUP

15 tests at various void ratios was conducted using normal pressures of 168, 353, and 535 kN/m^2, and the results are summarized in Table 5.3 and presented graphically in Fig. 5.10. The following conclusions may be drawn based on the test results:

(1) A wide range of penetrometer to soil friction angles may be obtained depending on the penetrometer material.

(2) Penetrometer to soil friction angles are strongly affected by the initial void ratio of the soil, as are also the soil to soil friction angles.

(3) Penetrometer to soil friction angles decrease slightly with increasing values of normal stress on the failure surface as in the case of soil to soil friction tests. However, this effect can be neglected by employing an average value of (δ) for the range of normal stress values.

The friction angle δ between various penetrometer materials and the soil, as well as the angle of internal friction (ϕ) of the soil can be determined from Figs. 5.8 and 5.10 for given values of soil void ratio. Values of δ/ϕ were calculated and are presented in Table 5.4 and Fig. 5.11. It can be seen that an essentially unique value of δ/ϕ exists regardless of the soil density or soil friction angle (ϕ). Values of δ/ϕ were found to be approximately equal to 0.3, 0.5, and 0.9, respectively, for polished hard-anodized aluminum, hard-anodized aluminum, and sanded aluminum.

SUMMARY

The internal friction angle of Monterey Sand No. 0 was determined from the results of triaxial and direct shear tests. In addition, a series of direct shear interface tests has been performed to determine the penetrometer to soil friction for three different penetrometer materials. Using these results, both ϕ and δ have been formulated in terms of soil void ratio over a range of normal stresses. These results are used in the next chapter to predict the penetration resistance of Monterey Sand No. 0 in accordance with the relationships developed in Chapter Four.

Table 5.3 SUMMARY OF PENETROMETER TO SOIL FRICTION TESTS IN DIRECT SHEAR

Nature of Friction	Normal Stress on failure plane σ_{mf}-kN/m^2	Initial Void Ratio e	Friction Angle δ-deg.
Soil to polished hard-anodized aluminum	168	0.776	10.1
		0.680	11.9
		0.510	18.4
	353	0.722	9.7
		0.665	10.8
		0.551	15.4
	535	0.792	9.1
		0.672	10.5
		0.545	13.2
Soil to hard-anodized aluminum	353	0.760	16.1
		0.620	20.9
		0.555	23.8
Soil to sanded aluminum	353	0.743	31.7
		0.587	40.2
		0.535	44.2

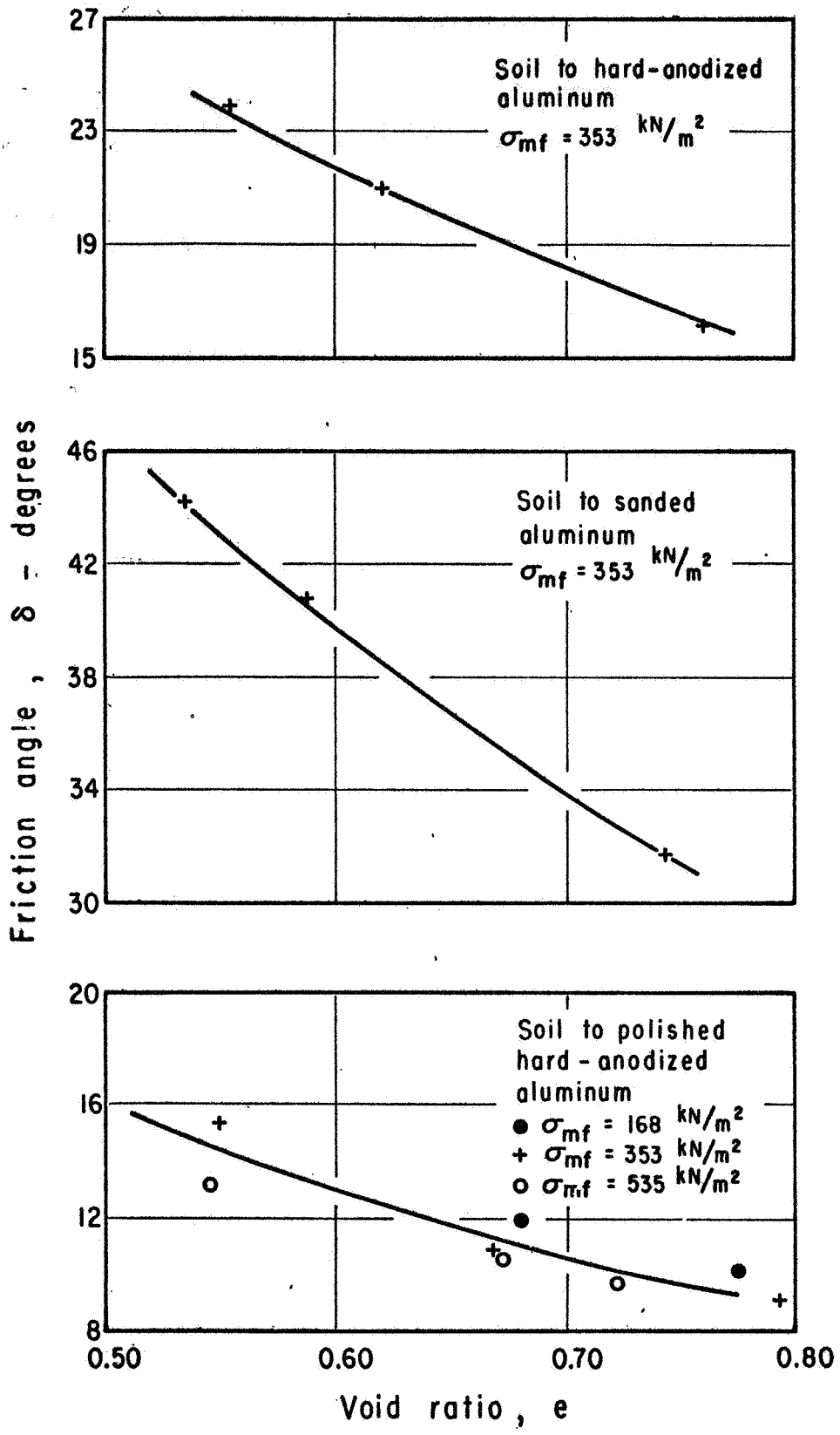

FIG. 5.10 PENETROMETER TO SOIL FRICTION ANGLES

Table 5.4 SUMMARY OF ROUGHNESS (δ/ϕ) VALUES FOR DIFFERENT PENETROMETER MATERIALS AND MONTEREY SAND NO. 0

Void Ratio e	Soil to soil friction angle ϕ-deg.	Polished hard anodized aluminum to soil friction		Hard-anodized aluminum to soil friction		Sanded aluminum to soil friction	
		δ-deg.	δ/ϕ	δ-deg.	δ/ϕ	δ-deg.	δ/ϕ
0.75	34.8	9.8	0.28	16.7	0.48	31.2	0.89
0.65	40.7	11.5	0.28	20.2	0.50	36.5	0.90
0.55	48.0	14.4	0.30	23.8	0.50	42.8	0.90

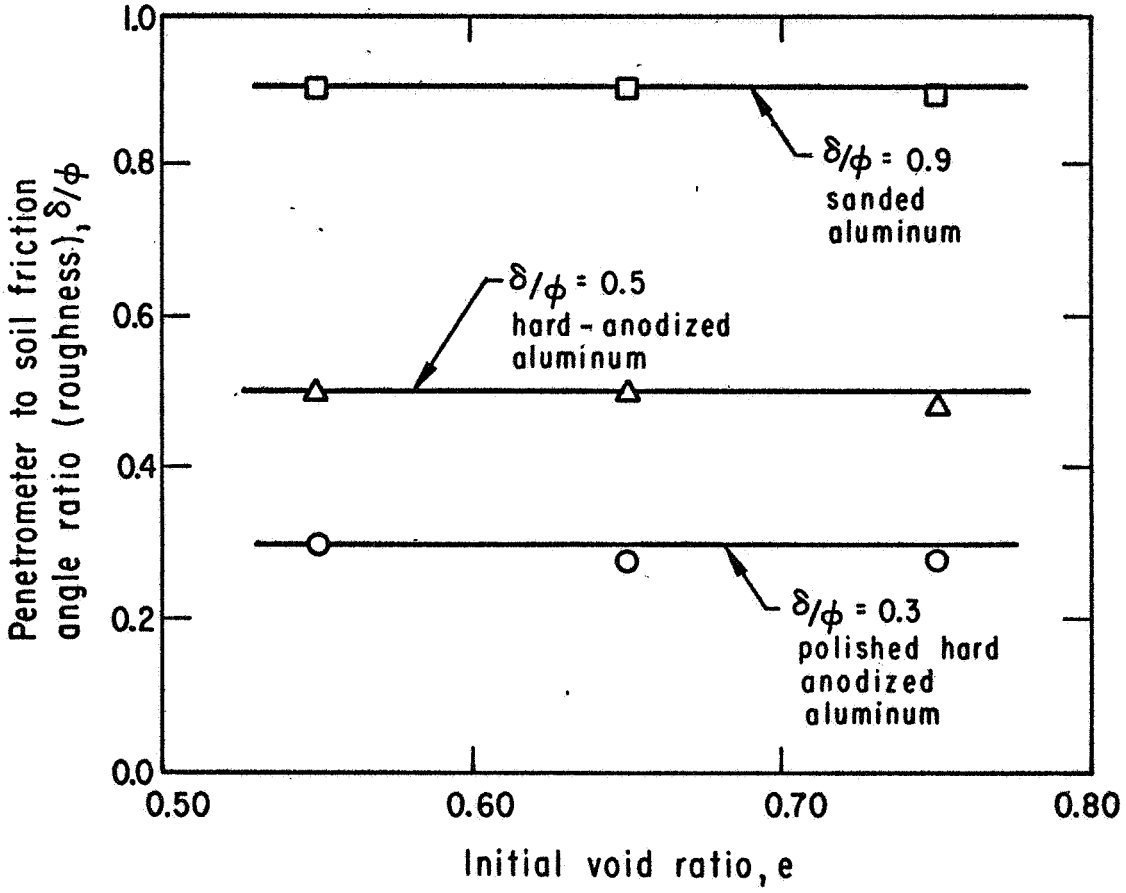

FIG. 5.11 SUMMARY OF δ/ϕ VALUES FOR VARIOUS PENETROMETER MATERIALS AND MONTEREY SAND No. 0

CHAPTER SIX

EXPERIMENTAL INVESTIGATION - LABORATORY PENETRATION TESTS

COHESIONLESS SOIL

Introduction

In order to check the accuracy of the theoretical predictions, carefully controlled laboratory tests were conducted. This section presents the results of controlled penetration tests using Monterey Sand No. 0 and comparisons of these results with predicted values.

Equipment, Facilities, and Penetrometers

Penetration tests were conducted in a test box 3.5 feet (~1.05 m) wide, 7.0 feet (~2.1 m) long, and 4.0 feet (~1.2 m) deep. The wooden test box is made up of two 2-foot high removable sections. The loading equipment included a hydraulically activated loading apparatus consisting of a 4.0 inch (102 mm) diameter double acting cylinder and a flow control system. The load was transmitted to the penetrometer by a shaft rigidly connected to the piston. The system was designed for pressures up to 150 psi (~1035 kN/m^2), and has a maximum loading capacity of 1800 pounds (~7650 N). The available piston stroke was 20.0 inches (0.508 m). (For deep penetration tests, a different cylinder with a stroke of 5 feet (~1.50 m) was used). The hydraulic system allowed application of the load either incrementally or continuously at any desired loading rate or at a constant penetration rate.

The penetration test equipment also included a supporting frame consisting of two aluminum channels spanning across the test box. The heavy supporting frame acted as a reaction for the loading piston. The supporting beam for the cylinder is connected by bolts to two channeled aluminum columns, which are individually supported on wheels and are therefore easily movable. The elevation of the supporting beam is easily adjusted to allow testing of any depth of soil deposit in the test box.

The two basic types of penetrometer tips used in the laboratory penetration tests were rectangular (strip) and circular in section. The rectangular tips had a length-to-width ratio of approximately 6 to 1. The tips were detachable from the shaft and had various semiapex angles and roughness. A complete listing of the penetrometer tips used in the tests is given in Table 6.1.

Table 6.1 SUMMARY OF PENETROMETER TIPS USED IN PENETRATION TESTS OF MONTEREY SAND NO. 0

Section Shape	Base semi-apex Angle, α	Tip Material	Roughness (δ/ϕ)
Rectangular*	15	Hard-anodized aluminum	0.5
		Sanded aluminum	0.9
	30	Hard-anodized aluminum	0.5
		Sanded aluminum	0.9
	90	Hard-anodized aluminum	0.5
Circular**	15	Polished hard anodized aluminum	0.3
		Hard-anodized aluminum	0.5
		Sanded aluminum	0.9
	30	Polished hard anodized aluminum	0.3
		Sanded aluminum	0.9
	90	Hard-anodized aluminum	0.5
		Sanded aluminum	0.9

*Tips have dimensions of 0.8" x 5.0" (20.3 mm x 127 mm), and penetrometer shaft dimensions are 0.625" x 5.0" (15.9 mm x 127 mm).

**Tips are 0.8" (20.3 mm) in base diameter, and the shaft is 0.625" (15.9 mm) in diameter.

Samples of different but uniform densities which were reproducible from test to test were required. While many sample preparation techniques are available (screen technique for loose, vibration technique for dense samples), pluvial compaction offers one of the most convenient means of preparing large uniform sand deposits at any required relative density. In pluvial compaction, air-dry sand is allowed to fall through the air in order to build up the required layer. Experiments by Kolbuszewski (1948) have shown that the factors controlling the final density are height of fall and intensity of sand rain. The method has some limitations, because it tends to produce layering in well-graded materials and it induces some cross anisotropy. The problem of layering can be eliminated by using uniformly graded materials. (The uniformity coefficient of the sand tested is around 1.5).

In addition to the ability of pluvial compaction to deposit uniform sand layers, the method also allows the deposition of large quantities of sand quickly and easily. In fact, the entire operation can be automated with a sand spreader box such as that shown in Fig. 6.1. The spreader box is similar to the device described by Walker and Whitaker (1967) and used by Silver (1970), and consists of a 1/3 cubic yard (0.26 m^3) wooden hopper sloping down to an opening at the bottom which is closed off by an aluminum roller. A rubber seal prevents sand from falling from the front of the box while the roller is stationary. The roller is driven through a chain drive by a variable speed motor. Limit switches make it possible to start and stop the roller at predetermined locations.

The spreader box is mounted on a frame that spans over the test box. The frame is chain-driven by an electric motor.

During operation, the roller rotates and sand is ejected from the box in a uniform sheet as shown in Fig. 6.1. The rate of deposition can be varied by changing the roller speed. The uniform rain of sand, the constant forward speed of frame, and the constant height drop cause uniform layers of sand to be deposited. As the soil deposit builds up, the spreader box is elevated to maintain a constant height drop.

Measurements of sand layer density showed that relative density did not vary more than 5 percent from the desired value throughout the layer (see Appendix B). For the sand used in this investigation, it was found that relative densities of from 35 to 100 percent could easily be obtained using the spreader box.

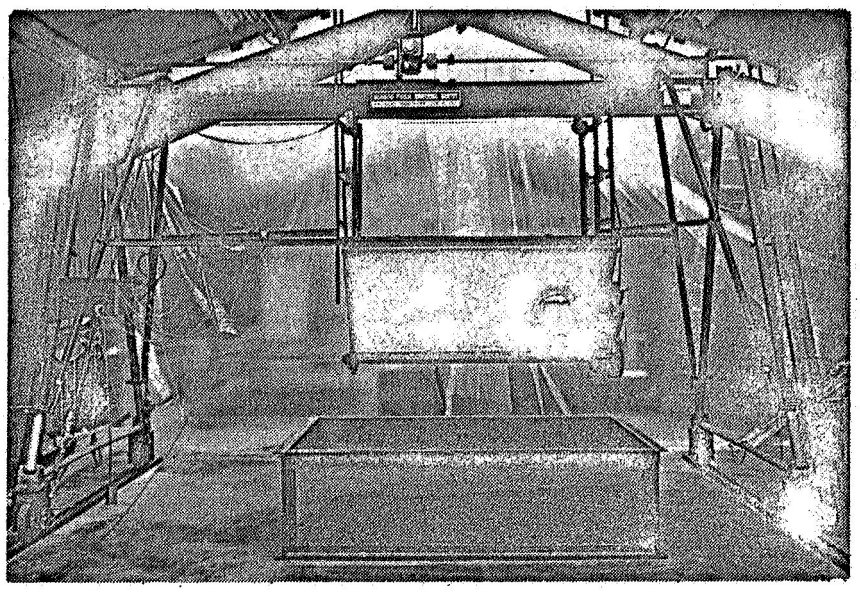

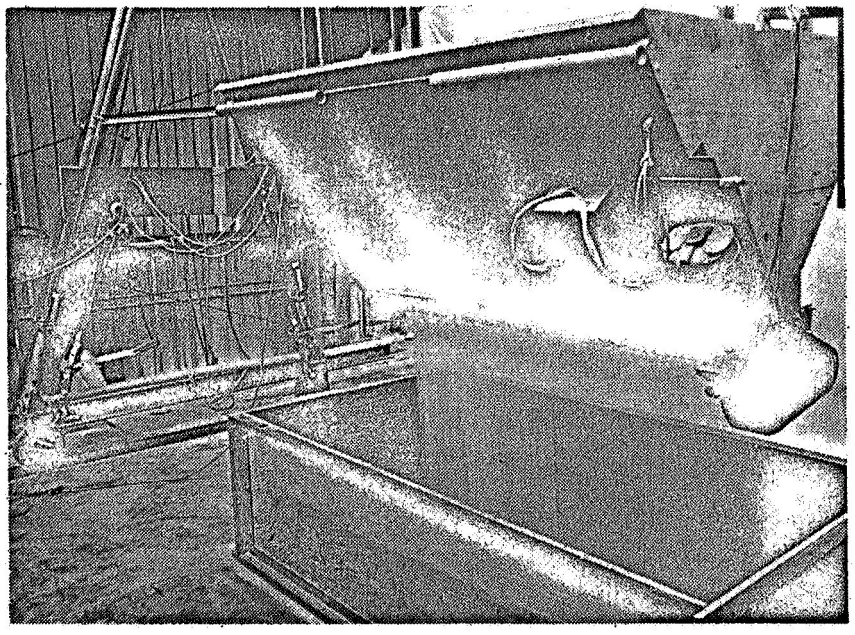

FIG. 6.1 SPREADER BOX AND SAND DEPOSITION

Test Procedure

Soil densities ranged between 35 to 100 percent relative density. The test box was large enough to allow 4 to 5 separate penetration tests on one sample. Penetrations were spaced so as to minimize test box side effects and the influence of other penetration tests. The load transfered to the penetrometer was measured with a load cell and recorded with an electronic recorder-print out system. The skin friction resistance of soil along the penetrometer shaft was insignificant due to smaller shaft diameter than the base diameter. The vertical penetration was measured by observing the relative movement of a fixed marker on a ruler.

Prediction Method

General

As described in Chapter Four, the unit penetration resistance can be determined for cohesionless soils by:

$$q_f = \gamma_s B N_{\gamma q} \xi_{\gamma q} \tag{6.1}$$

in which q_f = unit penetration resistance

γ_s = unit soil weight

$N_{\gamma q}$ = bearing capacity friction-surcharge factor

$\xi_{\gamma q}$ = shape factor

B = width of penetrometer base

In dimensionless form, Equation 6.1 may be written:

$$q_f/(\gamma_s B) = N_{\gamma q} \xi_{\gamma q} \tag{6.2}$$

Equation 6.2 indicates that, because both $N_{\gamma q}$ and ξ_{γ} are functions of relative depth, the penetration data should be presented in the form of $q_f/(\gamma_s B)$ versus D/B.

Estimation of mean normal stress

As discussed in Chapter Two, the approximate average value of mean normal stress along a failure surface can be estimated from:

$$\sigma_{g,M} = q_f/10 \tag{6.3}$$

in which $\sigma_{g,M}$ is the average mean normal stress, and q_f is the unit penetration resistance.

Determination of proper soil friction angle

The penetration problem in cohesionless soils is complicated by the fact that during the gradual load increase on the soil the shear strength is not immediately mobilized at all points of the slip surface, but at first only at the points where the shearing stresses are largest, with gradual extension to other points. This gradual progression causes modifications of the soil properties along the slip surface, especially in dense soils. In highly stressed zones, the soil begins to dilate and a decrease of density and thus a decrease in shear strength takes place. Therefore, when the state of rupture along a slip surface is reached, the shear strength corresponding to the original density is not available along the whole surface.

Further, the stress-strain characteristics of the soil must be considered in addition to the strength properties. Typical stress-strain relationships for plane strain and triaxial tests and dense and loose sands are shown in Fig. 6.2. It can be seen that if deformations at some points along the failure surface before rupture are sufficiently large to surpass the peak points of the stress-strain curves, the shear strength will drop to ultimate (residual) values. Consideration of stress-strain characteristics is most important in the case of a dense sand under plane strain conditions, because the stress-strain curve has a very distinct peak as shown in Fig. 6.2. Consequently, the use of friction angles corresponding to plane strain peak values should cause overestimation of the penetration resistance of cohesionless soils. Because the ultimate values of shear stresses control the resistance at large deformations, friction angles corresponding to ultimate values of shear stresses (ultimate friction angle) should be used in the analysis of the continuous penetration problem.

It is common practice in shear testing to obtain only peak values of the friction angle and to terminate the test before accurate ultimate values are obtained. However, as shown in Table 5.1, the triaxial peak and ultimate values for loose sands are the same and, for dense sand, the ultimate values are only slightly less than peak values. Therefore, as shown in a subsequent section, the use of peak triaxial friction angles for dense sands should cause only a small overestimation of the unit penetration resistance.

Procedure

The penetration resistance was predicted for different values of relative depth using the following procedure. For a given test, the following information is known:

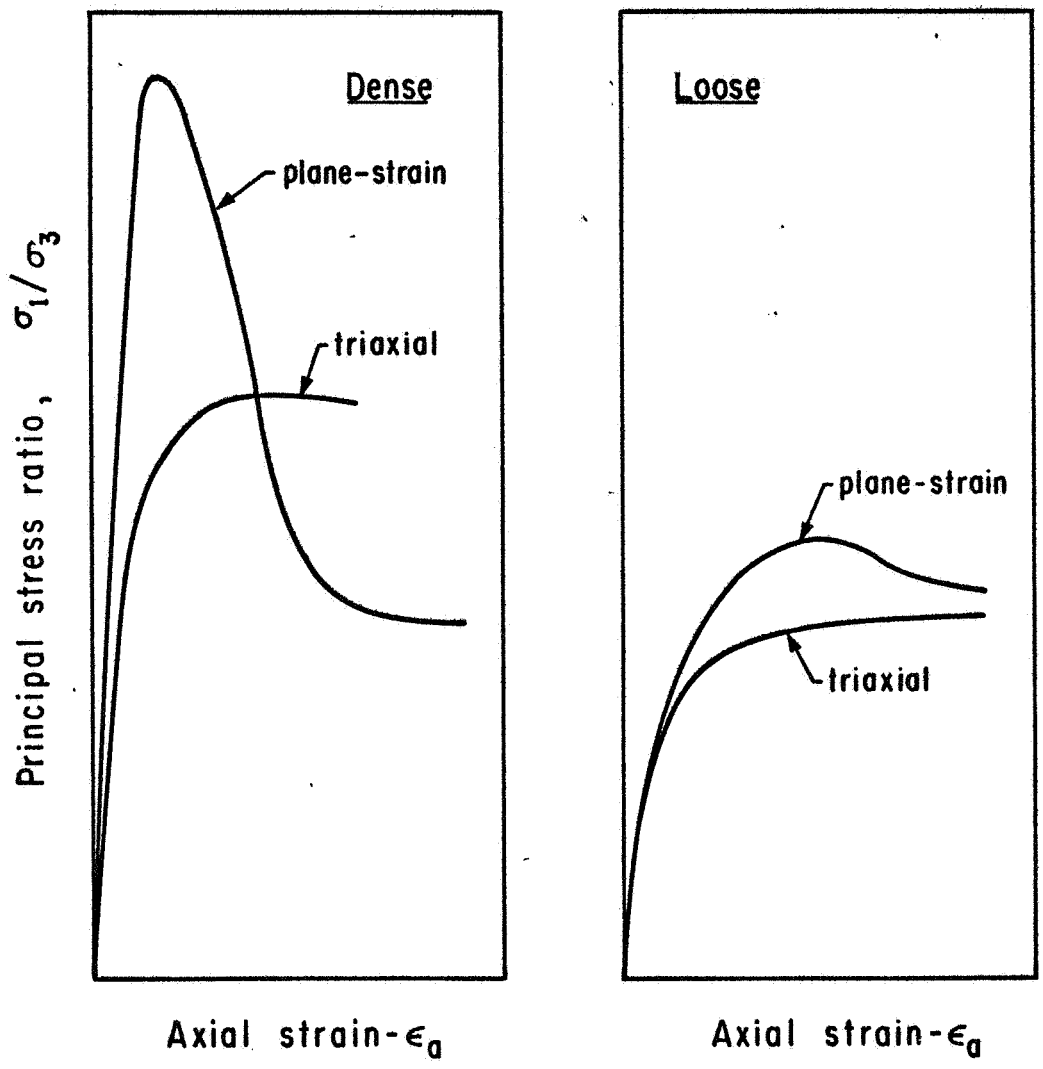

FIG. 6.2 TYPICAL STRESS-STRAIN CURVES FOR COHESIONLESS SOILS

(1) Unit weight (or void ratio) of soil deposit,

(2) Unit penetration resistance (q_f) versus penetration (D) relationship.

The following information is needed for the calculation of penetration resistance using Equation 6.1:

(1) From Equation 6.3 the average mean normal stress corresponding to a given value of relative depth (D/B),

(2) From Fig. 5.4, the angle of internal friction of the soil corresponding to given (determined) values of void ratio and normal stress,

(3) From Equation 4.9, the bearing capacity (penetration resistance) factor $N_{\gamma q}$ as a function of α, ϕ, δ/ϕ, and D/B,

(4) From Fig. 4.13 shape factor $\xi_{\gamma q}$ as a function of ϕ and D/B. (For wedges a shape factor of 1.0 is used).

Test Results and Predictions

The results of penetration tests performed using wedge-tipped penetrometers are shown in Figs. 6.3 through 6.7 in the form of unit penetration resistance versus penetration depth and also in the dimensionless form of resistance parameter $q_f/(\gamma_s B)$ versus relative depth (D/B). Predicted values using peak values of triaxial friction angles are also shown in Figs. 6.3 through 6.7.

The results of penetration tests performed using cone-tipped penetrometers are shown in Figs. 6.8 through 6.11 in the form of unit penetration resistance versus penetration depth and also in the form of the resistance parameter $q_f/(\gamma_s B)$ versus relative depth (D/B). Predicted values using peak values of triaxial friction angles and Equation 4.32 for the shape factors are also shown in Figs. 6.8 through 6.11.

It may be seen in Figs. 6.3 through 6.11 that the agreement between predicted and measured values is quite good. This suggests that the proposed analytical method may be confidently used to predict the penetration resistance of cohesionless soils, at least to the relative depths tested.

Determination of Shape Factors

The bearing capacity factors determined theoretically for strip foundations must be modified by empirically determined shape factors when computing the unit penetration resistance of circular penetrometers. Empirical formulas for the shape factor ξ_q proposed by different investigators are summarized in Table 6.2. It can be seen that the range of calculated values is quite large. However, it is possible to determine the proper shape factor for Monterey Sand No. 0 by comparing the resistance values for cones and wedges. The average values of the

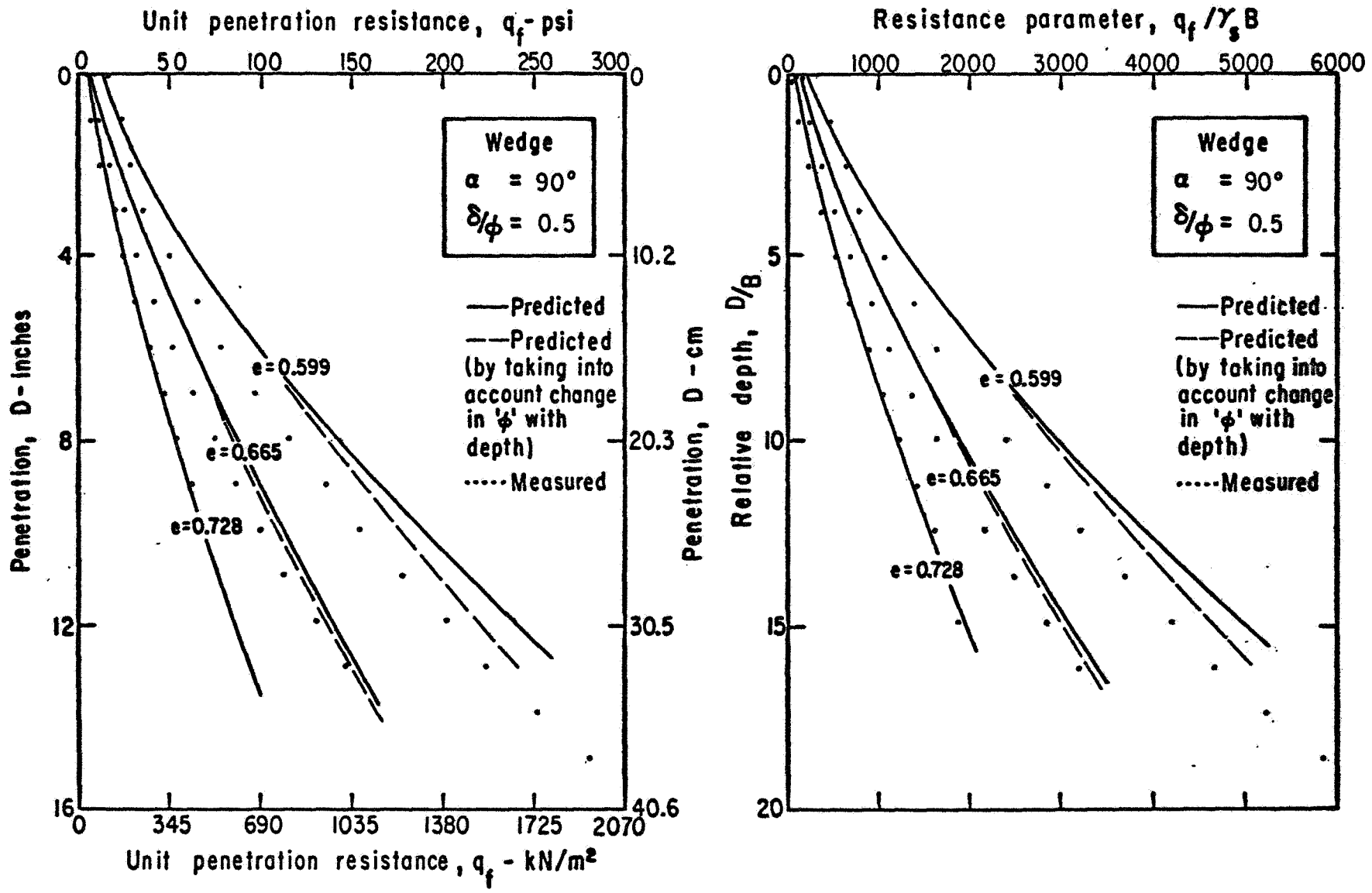

FIG. 6.3 COMPARISON OF MEASURED AND PREDICTED STATIC PENETRATION CURVES FOR MONTEREY SAND No. 0

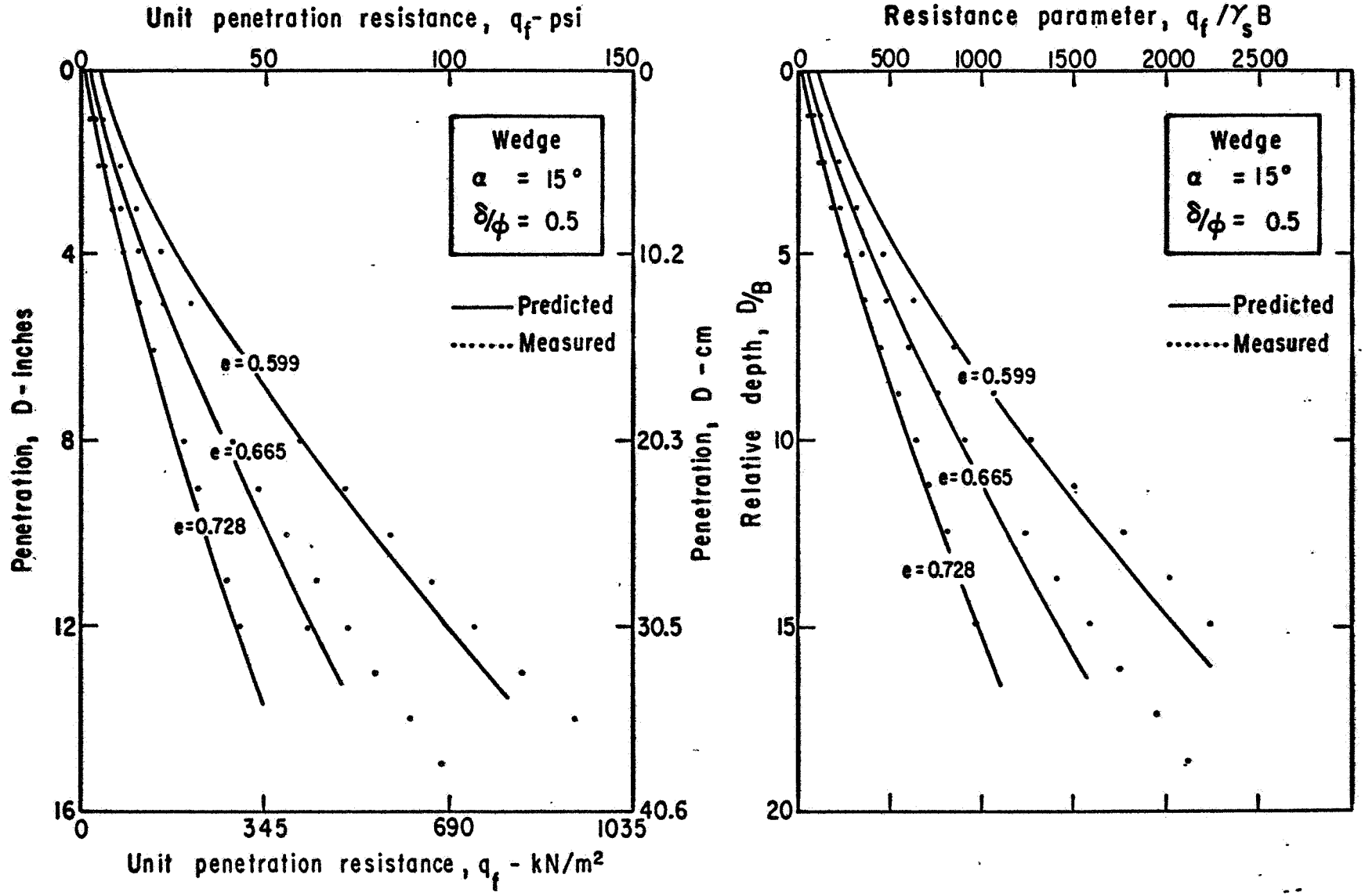

FIG. 6.4 COMPARISON OF MEASURED AND PREDICTED STATIC PENETRATION CURVES FOR MONTEREY SAND No. 0

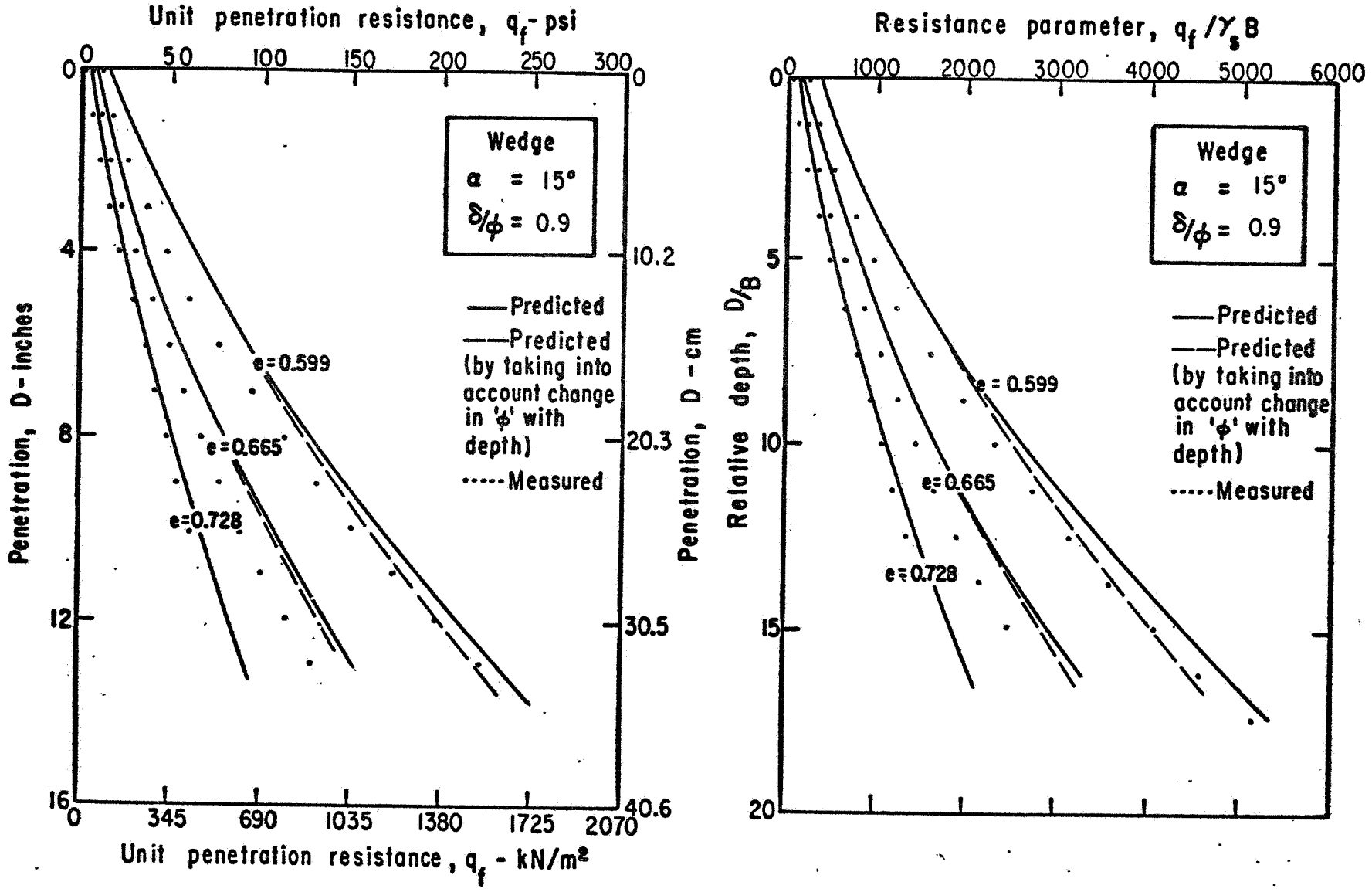

FIG. 6.5 COMPARISON OF MEASURED AND PREDICTED STATIC PENETRATION CURVES FOR MONTEREY SAND No. 0

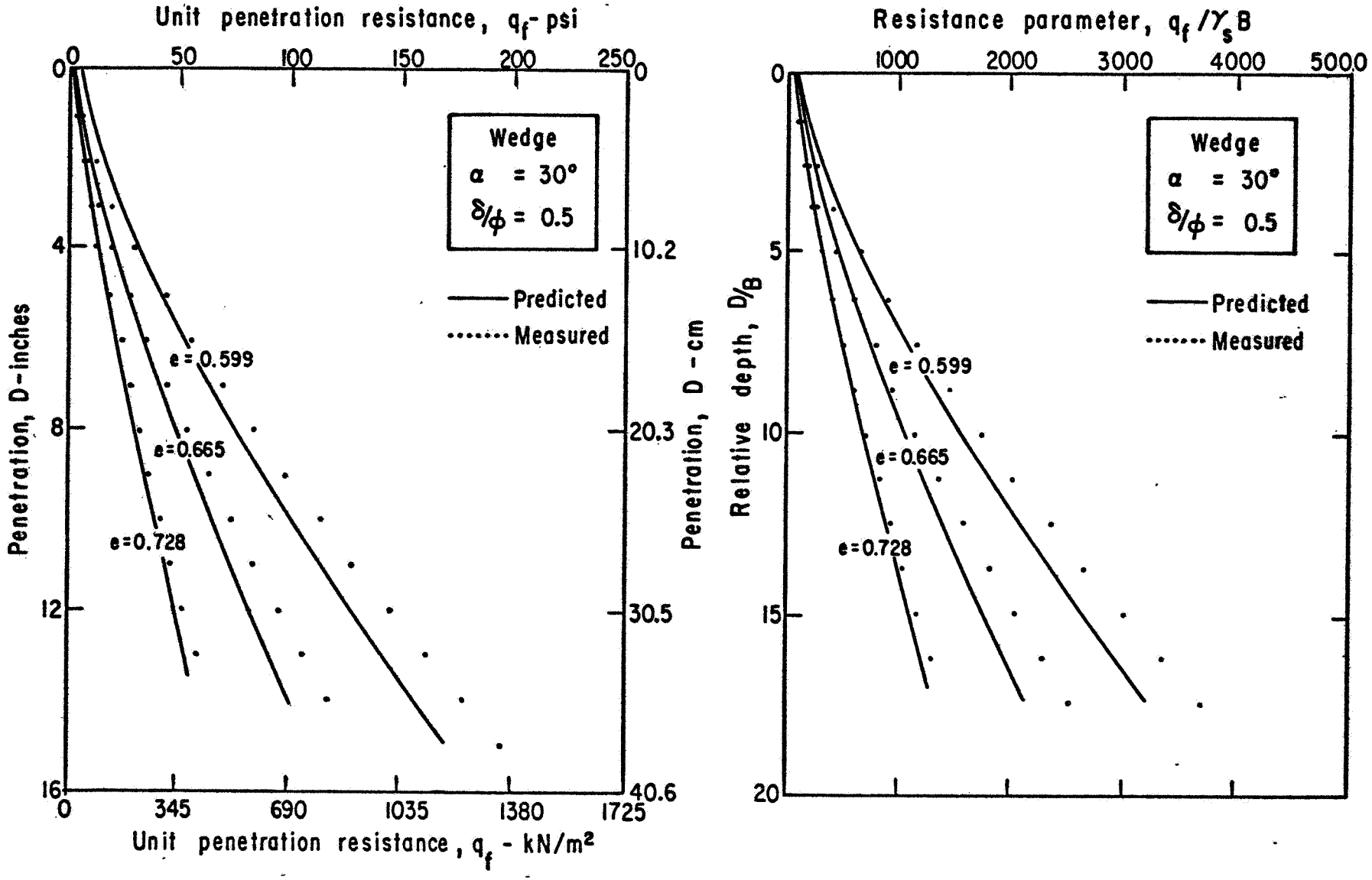

FIG. 6.6 COMPARISON OF MEASURED AND PREDICTED STATIC PENETRATION CURVES FOR MONTEREY SAND No. 0

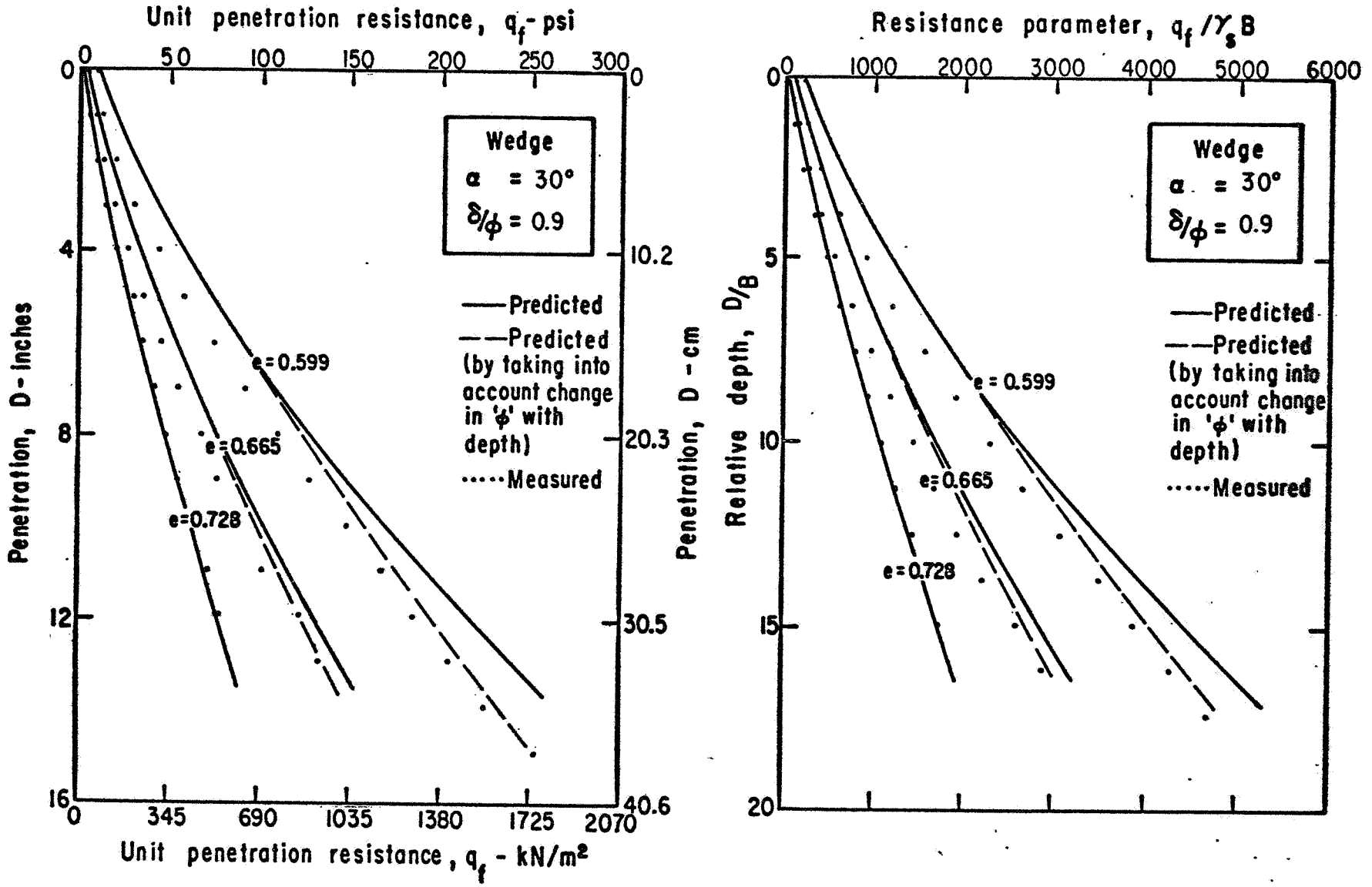

FIG. 6.7 COMPARISON OF MEASURED AND PREDICTED STATIC PENETRATION CURVES FOR MONTEREY SAND No. 0

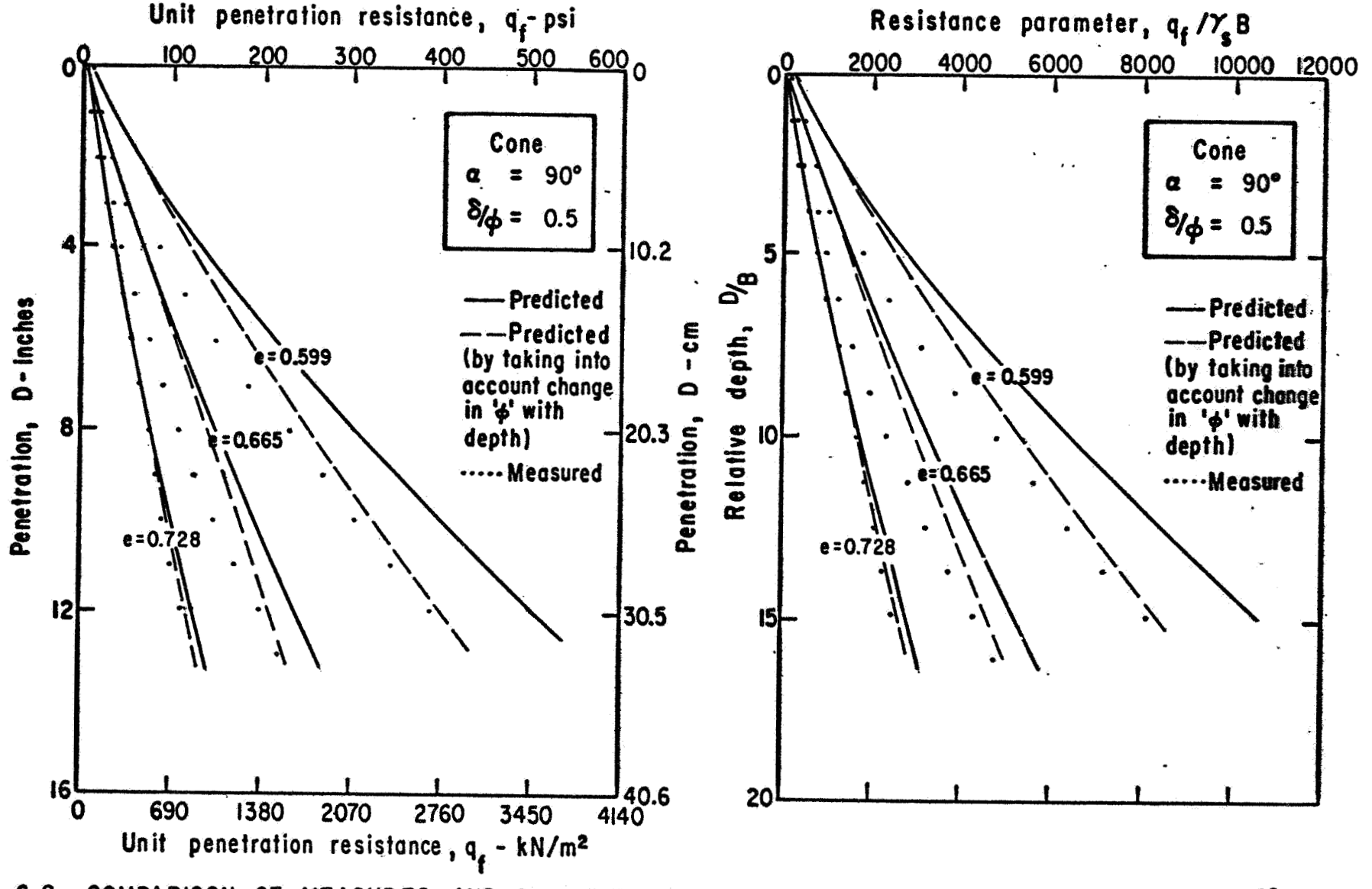

FIG. 6.8 COMPARISON OF MEASURED AND PREDICTED STATIC PENETRATION CURVES FOR MONTEREY SAND No. 0

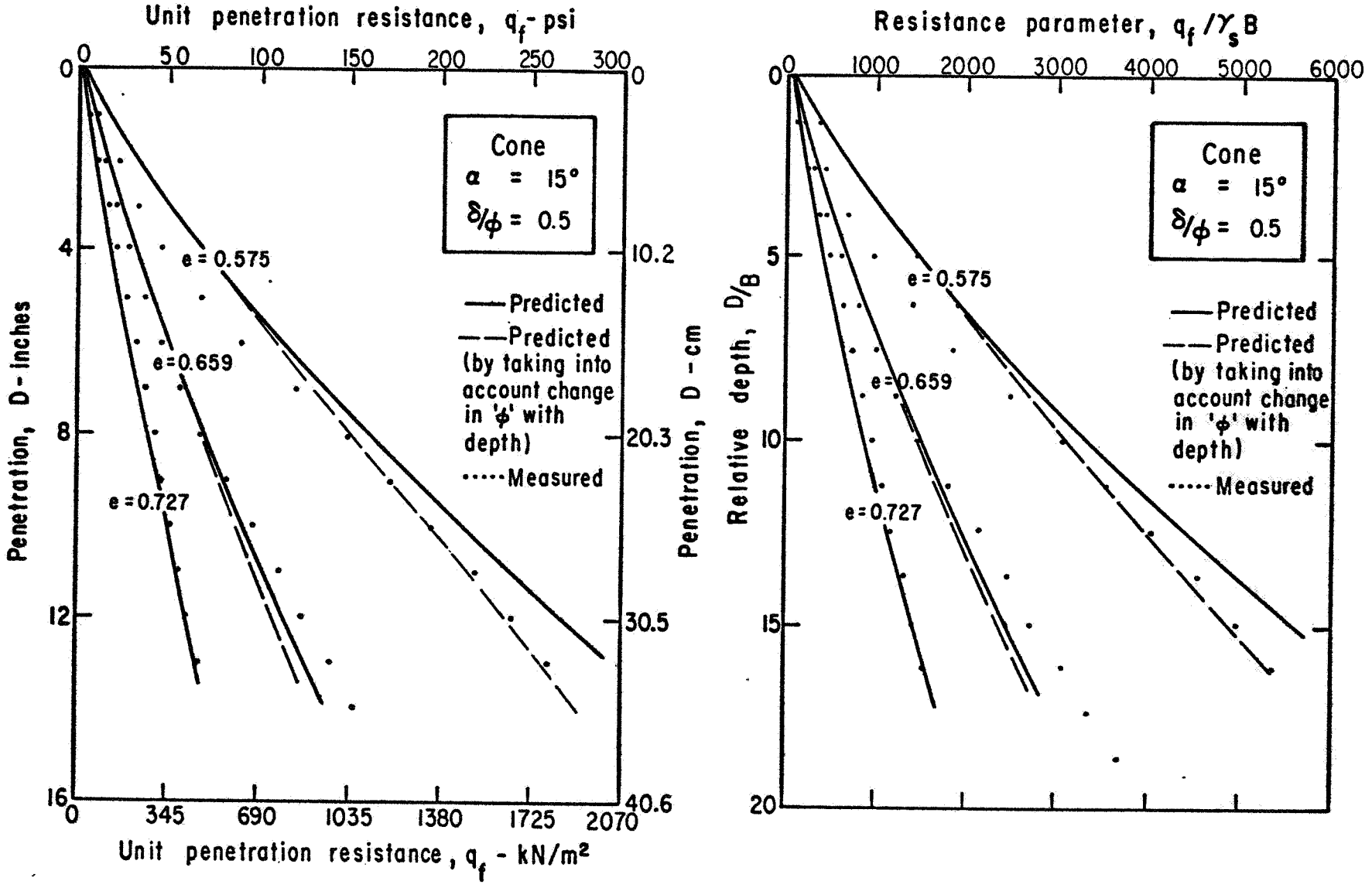

FIG. 6.9 COMPARISON OF MEASURED AND PREDICTED STATIC PENETRATION CURVES FOR MONTEREY SAND No. 0

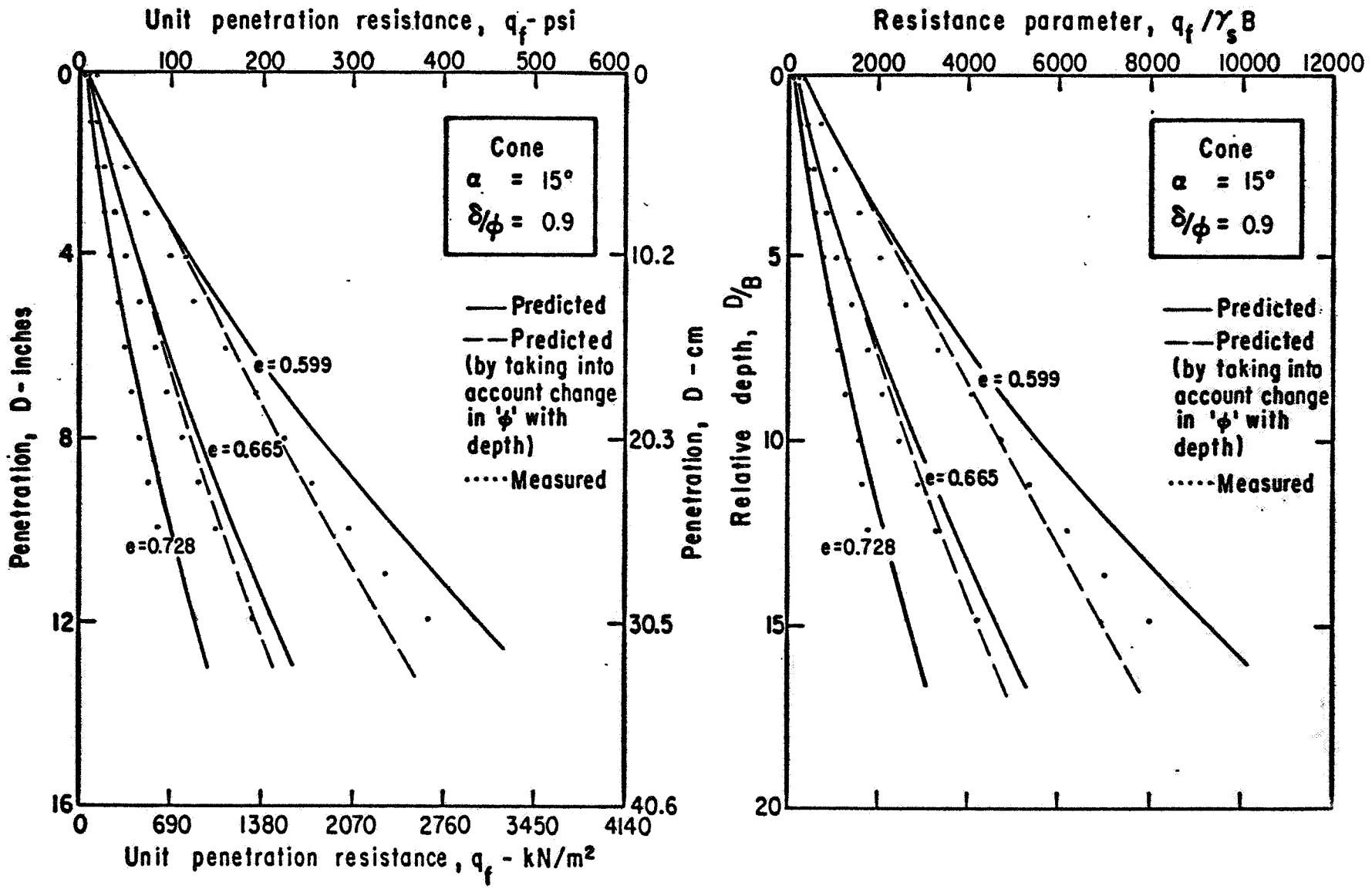

FIG. 6.10 COMPARISON OF MEASURED AND PREDICTED STATIC PENETRATION CURVES FOR MONTEREY SAND No. 0

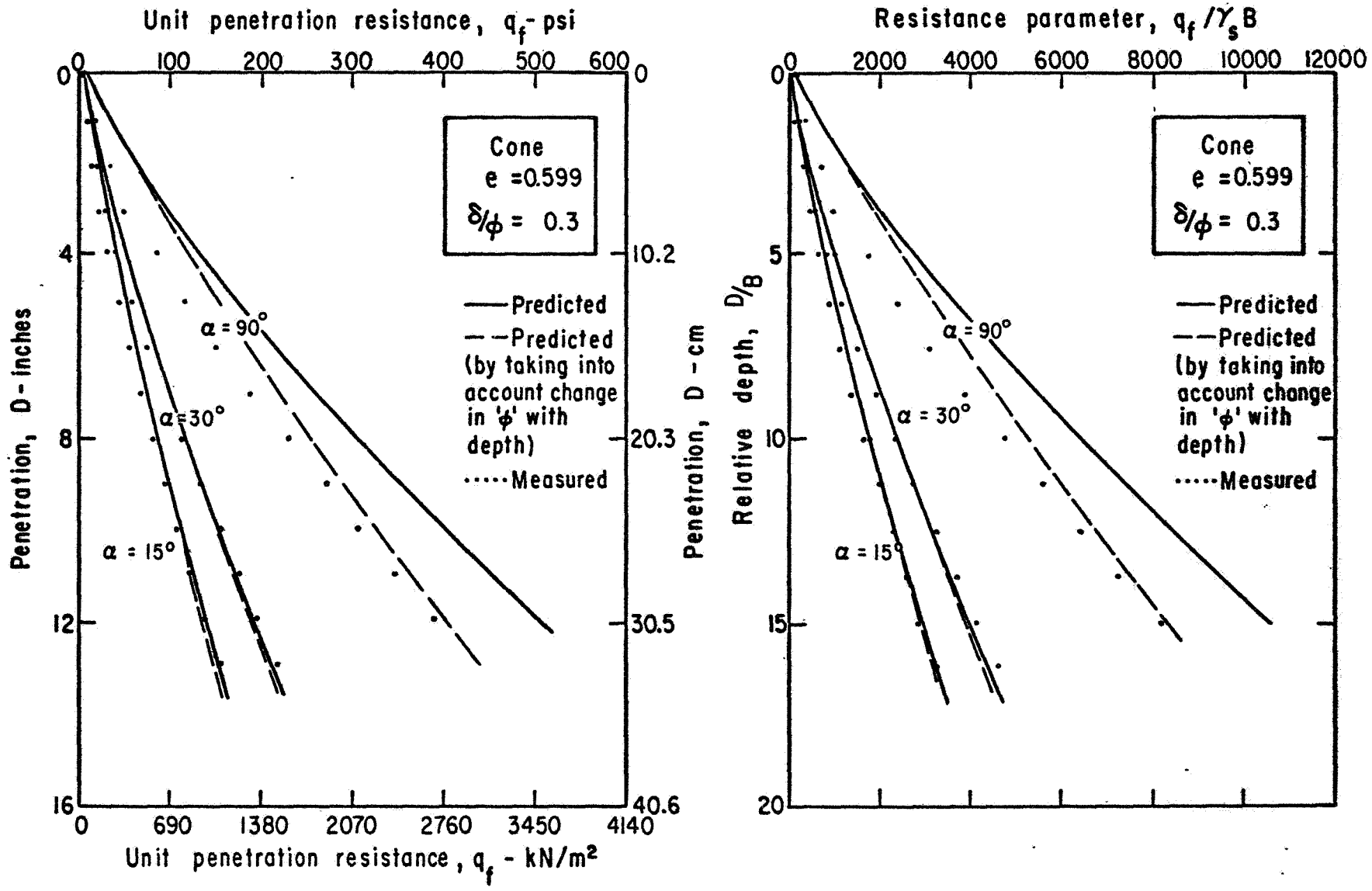

FIG. 6.11 COMPARISON OF MEASURED AND PREDICTED STATIC PENETRATION CURVES FOR MONTEREY SAND No. 0

Table 6.2 SUMMARY OF VARIOUS EMPIRICAL FORMULAS FOR SHAPE FACTOR ξ_q

Angle of internal friction ϕ-deg.	Brinch Hansen (1)	Meyerhof (2)	Vesic (3)	DeBeer (4)
25	1.21	1.25	1.67	1.42
30	1.24	1.30	1.78	1.50
35	1.32	1.37	1.90	1.57
40	1.55	1.46	2.04	1.64
45	2.20	1.59	2.20	1.71

(1) $\xi_q = 1.0 + (0.2 + \tan^6\phi)\ (B/L)$

(2) $\xi_q = 1.0 + 0.1\ \tan^2(45° + \frac{\phi}{2})\ (B/L)$

(3) $\xi_q = 1.0 + (0.2 + \tan\phi)\ (B/L)$

(4) $\xi_q = 1.0 + \sin\phi(B/L)$ for $D/B<1$

shape factor $\xi_{\gamma q}$ for the relative depth range (D/B=10 to 15) determined by this ratio procedure are shown in Fig. 6.12. The computed values of $\xi_{\gamma q}$ using Equation 4.32 which were derived from the equation (Equation 1 in Table 6.2) proposed by Brinch Hansen (1961), (see Chapter Four) are also shown in Fig. 6.12. The close agreement between the calculated and measured values of $\xi_{\gamma q}$ indicates that Equation 4.32 for shape factor $\xi_{\gamma q}$ may be used for in the prediction of cone resistance.

Some conclusions drawn from the test results may be summarized as follows:

(1) The penetration resistance is sensitive to soil density. It should therefore be possible to use the penetration resistance of cohesionless soils for estimating the in-situ soil density as well as shear strength properties.

(2) Penetration resistance increases with increasing semiapex angle for $\delta/\phi=0.3$.

(3) Penetration resistance increases with increasing penetrometer roughness (δ/ϕ).

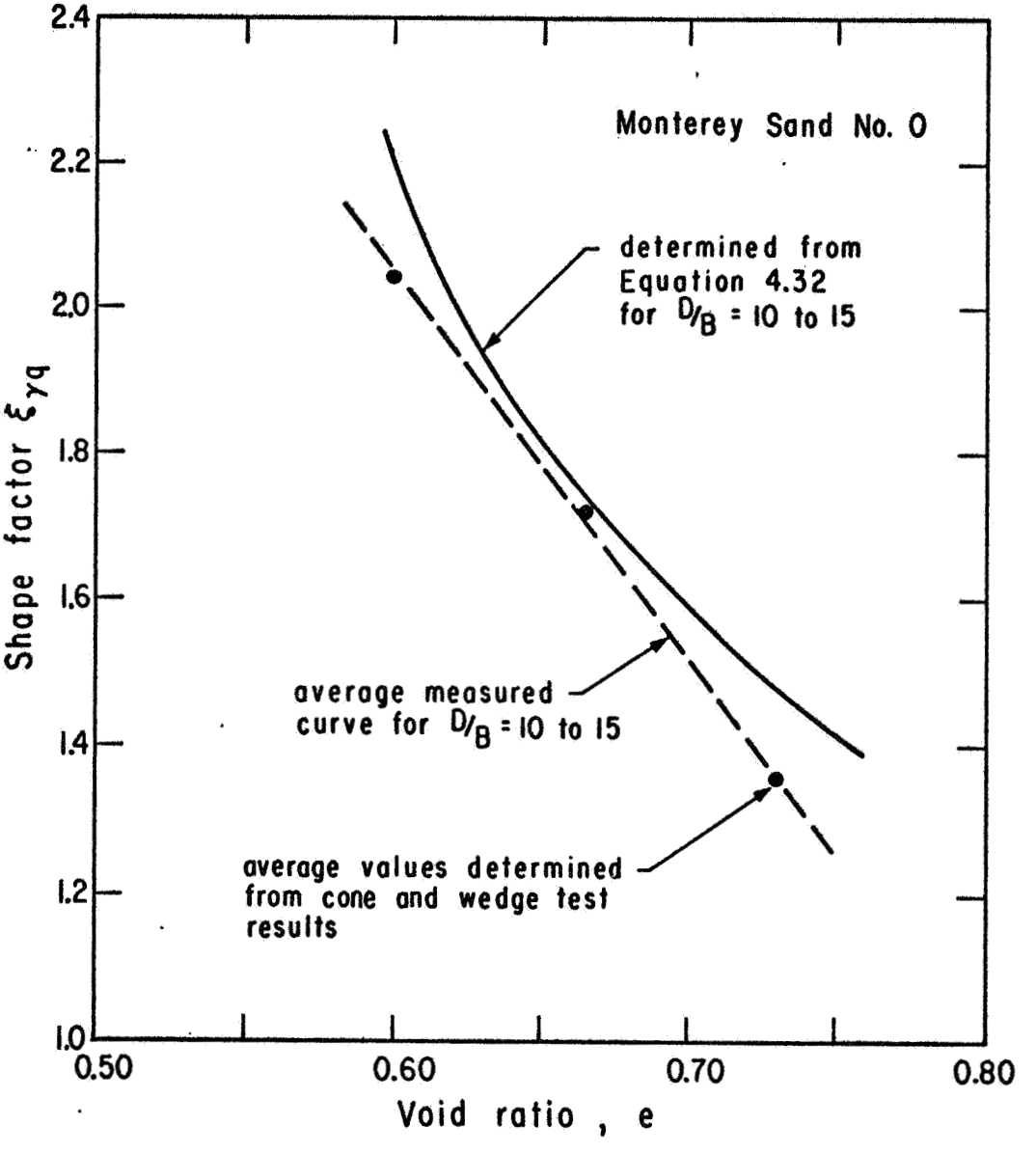

FIG. 6.12 COMPARISON OF MEASURED AND CALCULATED SHAPE FACTOR $\xi_{\gamma q}$

(4) Penetration resistance increases with increasing relative depth (D/B). There was no indication of a decrease in the rate of resistance increase with depth even for relative depths as large as D/B=20.

(5) Other factors being equal, the unit penetration resistance for cones was higher than for wedges.

Deep Penetration Tests

To establish the applicability of the proposed method and to investigate the penetration versus resistance relationships for high relative depths (D/B up to 40) a series of deep penetration tests was conducted. It was observed that there was no distinct change in resistance versus penetration relationship. The summary of the test results is given in Fig. 6.13. It can be seen that measured values of penetration resistance can be predicted reasonably well by the proposed method for relative depths as high as 40.

COHESION-FRICTION SOIL

Introduction

The close agreement between predicted and measured values of the penetration resistance of Monterey Sand No. 0 indicates the validity of Equation 4.9 for the determination of the bearing capacity factor $N_{\gamma q}$ for failure in general shear. Because lunar soil has cohesion, the validity of the proposed method must be further established for a cohesion-friction soil. The penetration tests with Lunar Soil simulant No. 2 (LSS No. 2) described in this section were performed in order to determine the validity of Equation 4.6 for the determination of the value of N_c, which is needed to apply the proposed method to such soils. At the same time the influence of soil compressibility on penetration resistance was investigated.

Equipment, Test Procedure, and Soil

Static penetration tests were conducted in a test box 2.0 feet (~0.6 m) wide, 2.0 feet (~0.6 m) long, and 3.0 feet (~0.9 m) deep. Uniform loose and medium dense deposits were prepared using the constant height of drop method; dense deposits were prepared using a vibratory technique. The loading system and test procedures used were the same as previously described for cohesionless soil.

The soil used was a crushed basalt known as Lunar Soil Simulant No. 2 having the gradational characteristics of a silty fine sand (Fig. 6.14). A comparison of the one-dimensional compression characteristics of this soil

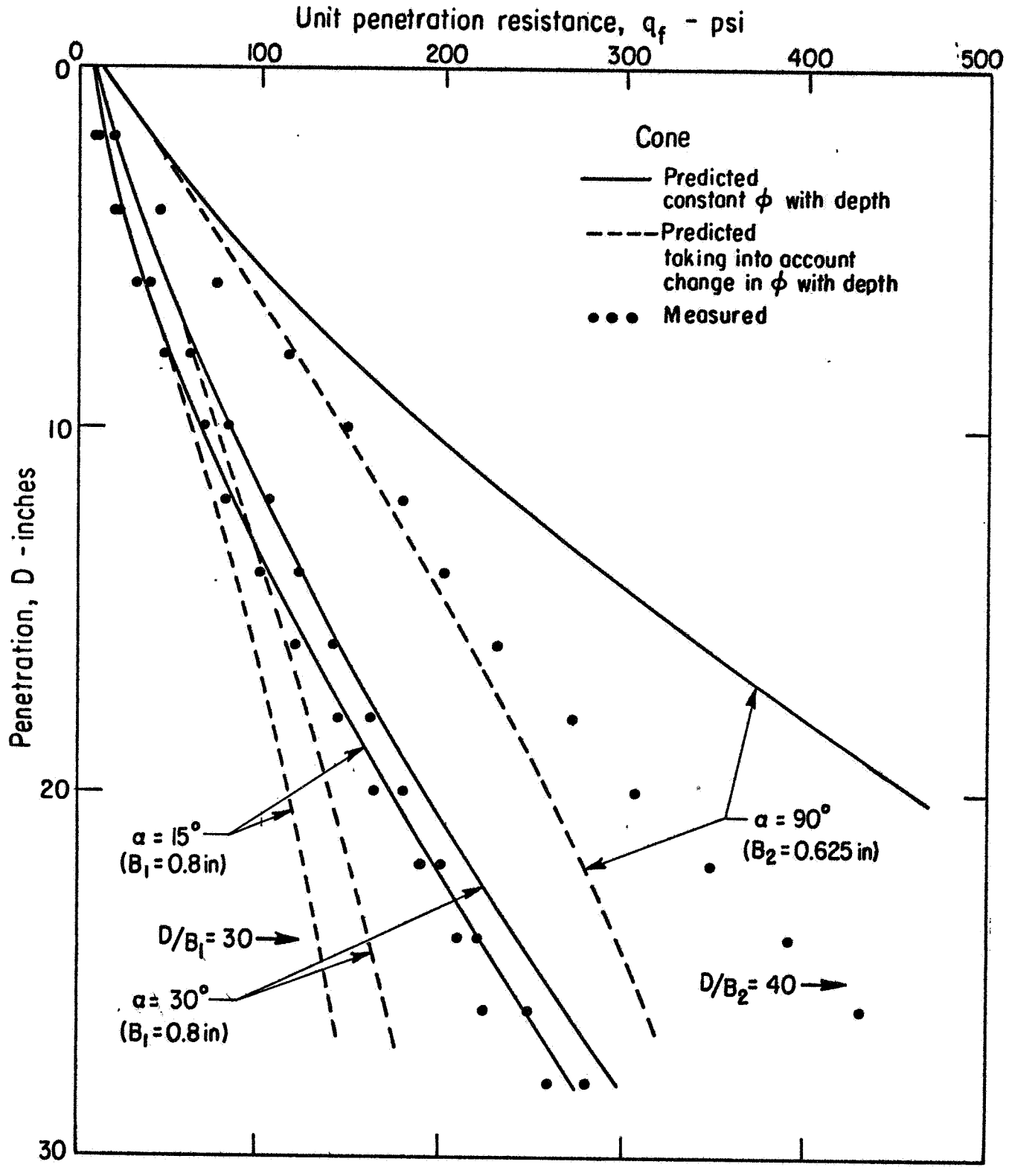

FIG. 6.13 SUMMARY OF DEEP PENETRATION TEST SERIES WITH MONTEREY SAND No. 0

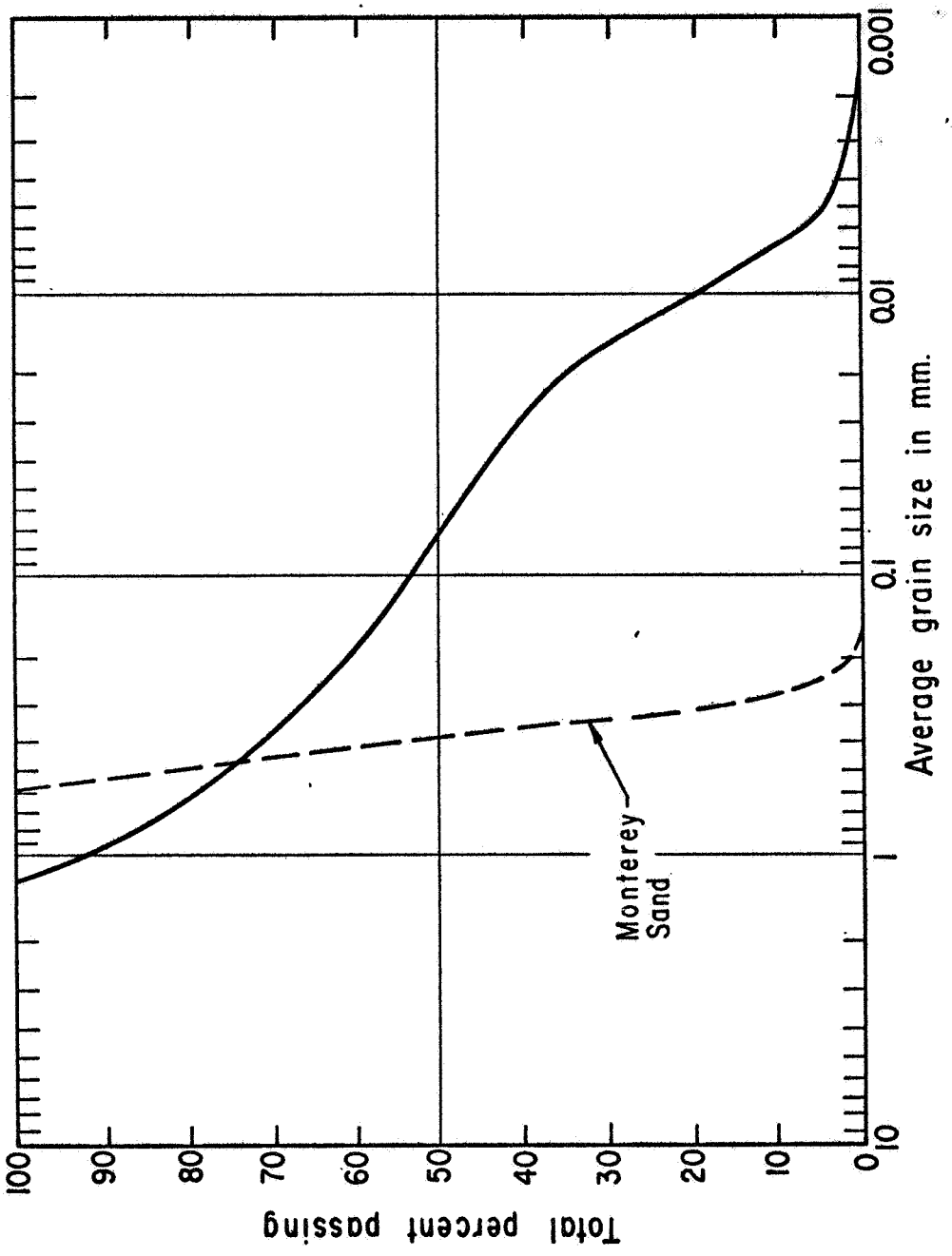

FIG. 6.14 GRADATION CURVE OF LSS No. 2 (After Mitchell et al, 1971)

and Monterey Sand No. 0 are presented in Fig. 6.15, which indicates that the simulant is much more compressible than the sand. Cohesion was obtained in the simulant by maintaining a small moisture content of about 2.0 percent. The relationship of cohesion to void ratio at various moisture contents for the simulant was determined by Mitchell et al. (1971) and is shown in Fig. 6.16.

The relationship between plane-strain friction angle of the simulant and void ratio is shown in Fig. 6.17 (Mitchell et al. 1971). These plane-strain values were converted to triaxial values according to the procedure recommended by Cornforth (1964). The estimated triaxial friction angle values for the simulant are also shown in Fig. 6.17.

Prediction Method

As discussed in Chapter Four, the unit penetration resistance can be expressed for cohesion-friction soils by:

$$q_f = cN_c\xi_c + \gamma_s BN_{\gamma q}\xi_{\gamma q} \tag{6.4}$$

or, in dimensionless form:

$$q_f/(\gamma_s B) = \frac{c}{\gamma_s B} \cdot N_c\xi_c + N_{\gamma q}\xi_{\gamma q} \tag{6.5}$$

in which q_f = unit penetration resistance
γ_s = unit weight of soil
c = cohesion
B = width of base
N_c, $N_{\gamma q}$ = bearing capacity factors f_1, $f_2(\phi, \delta/\phi, \alpha, D/B)$
ξ_c, $\xi_{\gamma q}$ = shape factors, $f_3(\phi)$, $f_4(\phi, D/B)$

The following procedure may be used to predict the ultimate penetration resistance of the simulant for known average values of void ratio and water content:

(1) Enter Fig. 6.16 with the known values of e and w, and determine the cohesion value.

(2) Enter Fig. 6.17 with the known average void ratio, and determine corresponding triaxial friction angle (ϕ) value.

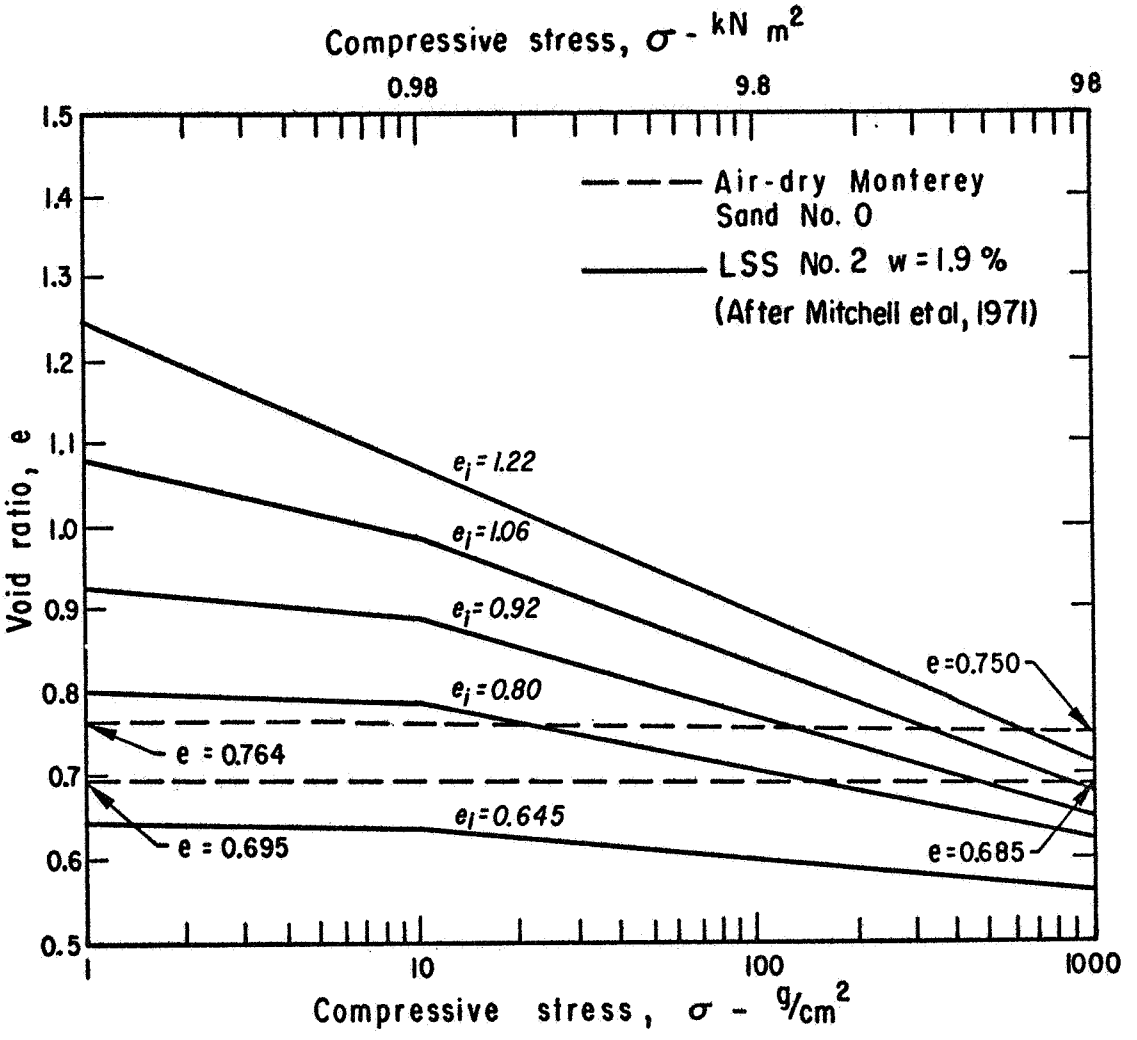

FIG. 6.15 ONE-DIMENSIONAL COMPRESSION CURVES FOR LSS No. 2 AND MONTEREY SAND No. 0

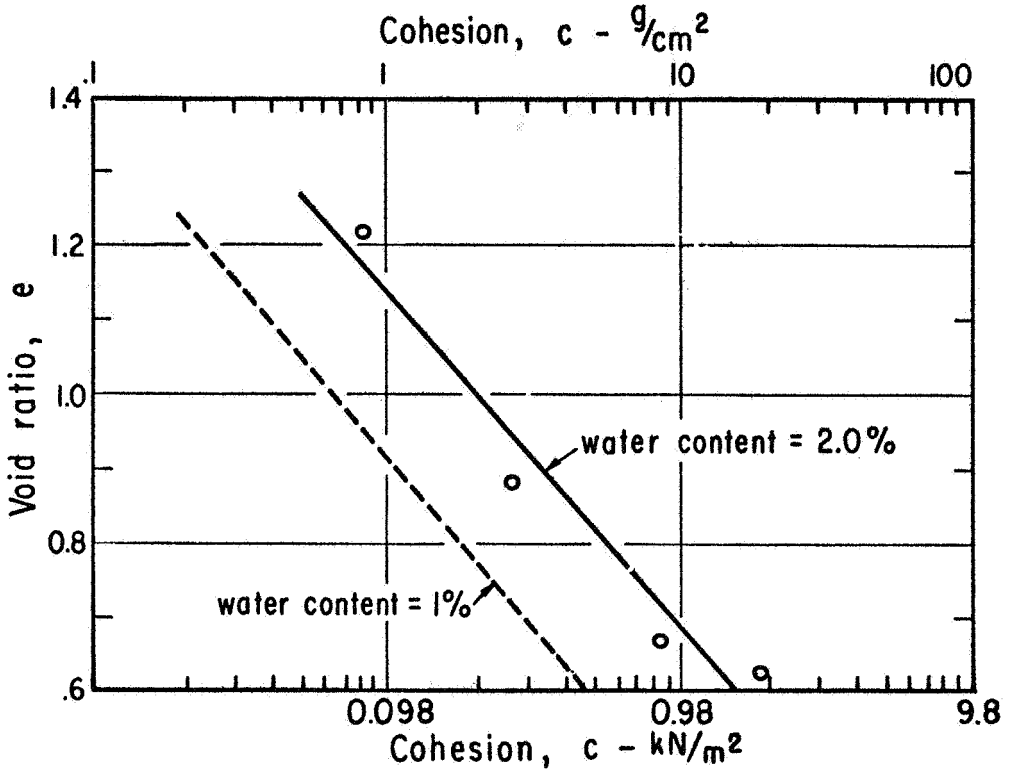

FIG. 6.16 RELATIONSHIP BETWEEN COHESION AND VOID RATIO FOR LSS No. 2

(After Mitchell et al, 1971)

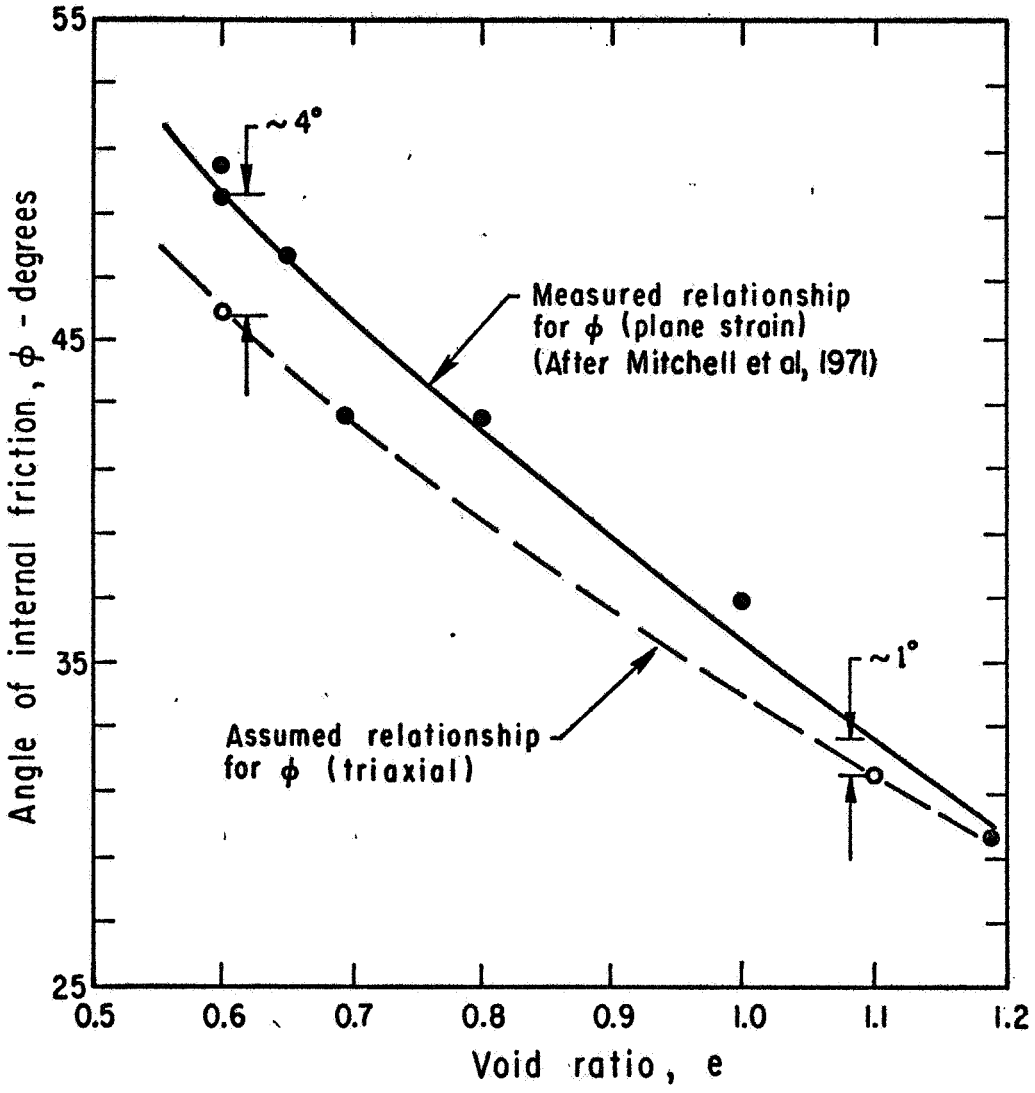

FIG. 6.17 RELATIONSHIP BETWEEN ANGLE OF INTERNAL FRICTION AND VOID RATIO FOR LSS No. 2

(3) At a given relative depth (D/B) and known values of α and δ/ϕ, enter the corresponding figures in Appendix A and determine N_c and $N_{\gamma q}$.

(4) For the ϕ value determined in step 2, use Equation 4.24a to calculate ξ_c.

(5) For the known values of ϕ and D/B use Equation 4.32 to calcualte $\xi_{\gamma q}$.

(6) Substitute the values of c, N_c, $N_{\gamma q}$, ξ_c, $\xi_{\gamma q}$, γ_s, and B into Equation 6.4 or 6.5 to determine the ultimate penetration resistance (q_f) or the dimensionless resistance parameter $q_f/(\gamma_s B)$ for the particular D/B.

(7) Repeat steps 3 through 6 for other values of D/B.

Test Results and Predictions

A series of penetration tests in the LSS No. 2 were conducted using a cone-tipped penetrometer (α=15°, B≅0.8 in., and δ/ϕ=0.5). The soil was prepared over a wide range of densities in order to evaluate the applicability of the proposed method for both dense and loose conditions.

Penetration test data are presented in Fig. 6.18 in the form of penetration resistance (q_f) versus relative depth (D/B). The ratios of predicted to measured ultimate penetration resistance are presented in Table 6.3. It may be seen from Table 6.3 and Fig. 6.19 that, for dense deposits, these ratios are close to unity, indicating the validity of the prediction procedure and the values of N_c for general shear failure conditions. However, for low densities, the ratios are larger than one, indicating the significant influence of soil compressibility on penetration resistance. This influence can be anticipated by noting in Fig. 6.15 that the simulant is much more compressible than Monterey Sand No. 0 at high void ratios. Therefore, the use of bearing capacity factors formulated for general shear failure conditions will cause overestimation of the penetration resistance of compressible deposits. As a result, of soil compressibility, the shear surface is restricted to a smaller zone around the penetrometer tip as shown in Fig. 6.20. Vesic (1963) suggested that the angle which defines the extent of the failure surface may be represented empirically by:

$$\theta = 1.9\,\phi \qquad (6.6)$$

By substituting the value of θ determined from Equation 6.6 into Equations 4.6 and 4.9, values of N_c^* and $N_{\gamma q}^*$ may be obtained for compressible

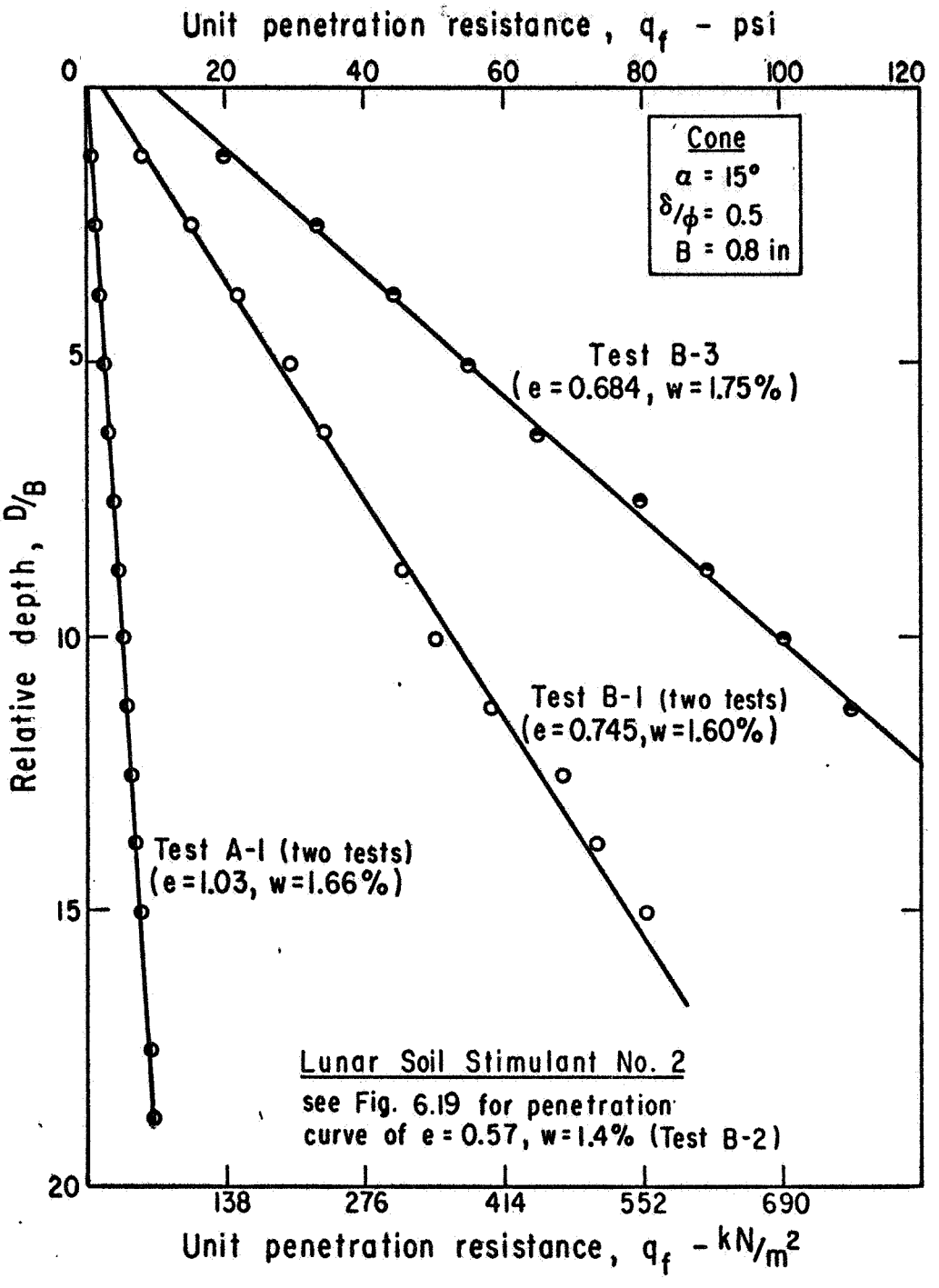

FIG. 6.18 MEASURED PENETRATION CURVES FOR LSS No.2

Table 6.3 RATIOS OF PREDICTED TO MEASURED PENETRATION RESISTANCE FOR LSS NO.2 USING GENERAL SHEAR FAILURE MECHANISM FOR ALL DENSITIES

Test No.	Void Ratio $e_{ave.}$	Water Content, w (%)	$\frac{\text{Predicted}(q_f)}{\text{Measured}(q_f)}$		
			D/B=5	D/B=10	D/B=15
A-1*	1.030	1.66	3.12	2.95	2.85
B-1*	0.745	1.60	1.25	1.43	1.30
B-3	0.684	1.75	1.15	1.20	1.25
B-2	0.570	1.40	1.03	1.02	1.02

*Average of (2) tests.

soils. However, the general validity of this semi-empirical procedure has not yet been established.

SUMMARY

Comparisons of unit penetration resistance values measured in controlled laboratory tests and predicted by the proposed analytical method have been made for both cohesionless (Monterey Sand No. 0) and cohesion-friction (Lunar Soil Simulant No. 2) soils. The agreement between measured and predicted values for the sand and dense simulant were quite good, suggesting that the proposed analytical method may be used confidently for the prediction of the static penetration resistance of relatively incompressible soils. A method has been suggested for determination of bearing capacity factors N^*_c and $N^*_{\gamma q}$ for compressible soils. However, the general validity of this method has not yet been established.

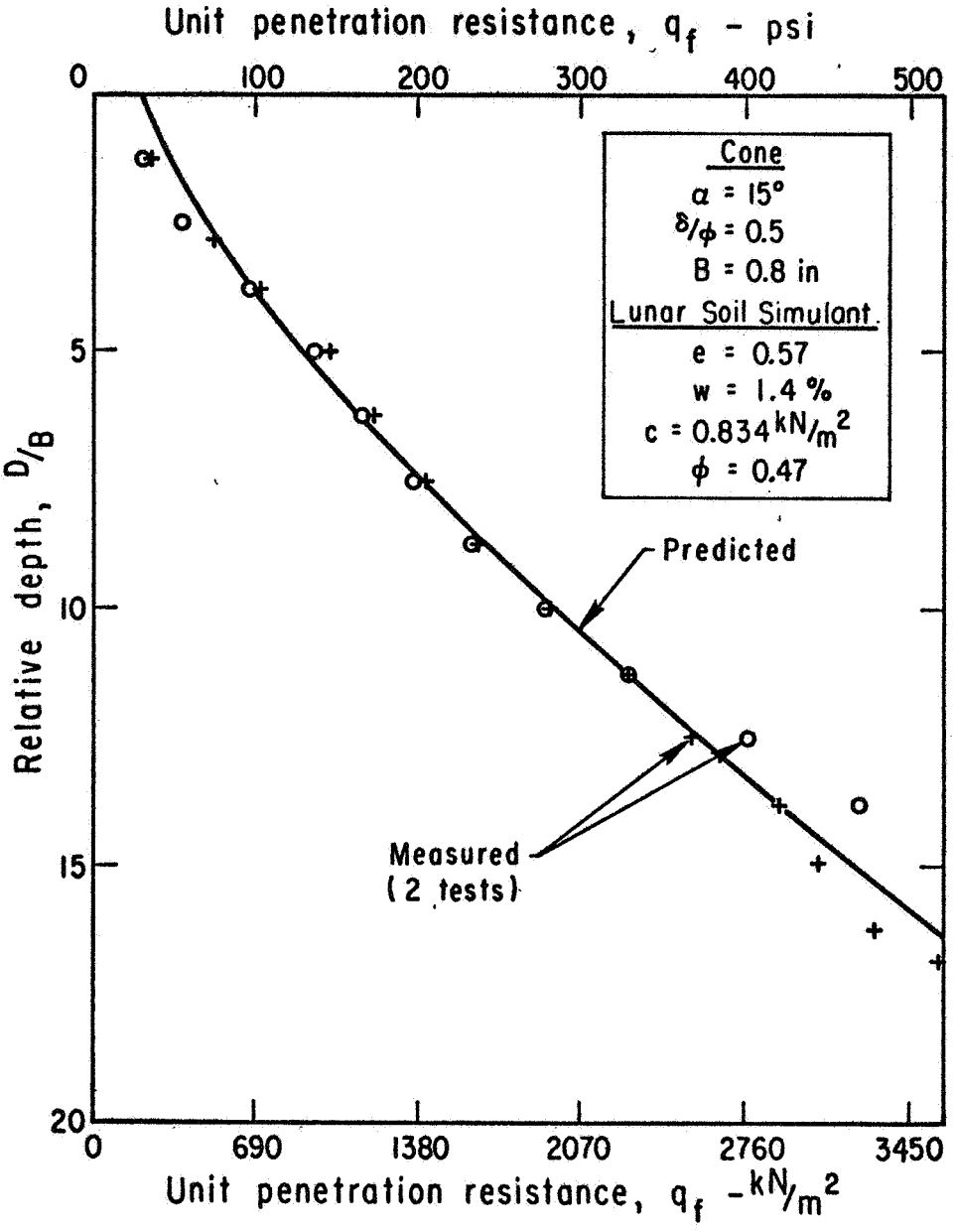

FIG. 6.19 COMPARISON OF MEASURED AND PREDICTED RESISTANCE CURVES FOR DENSE LSS No. 2

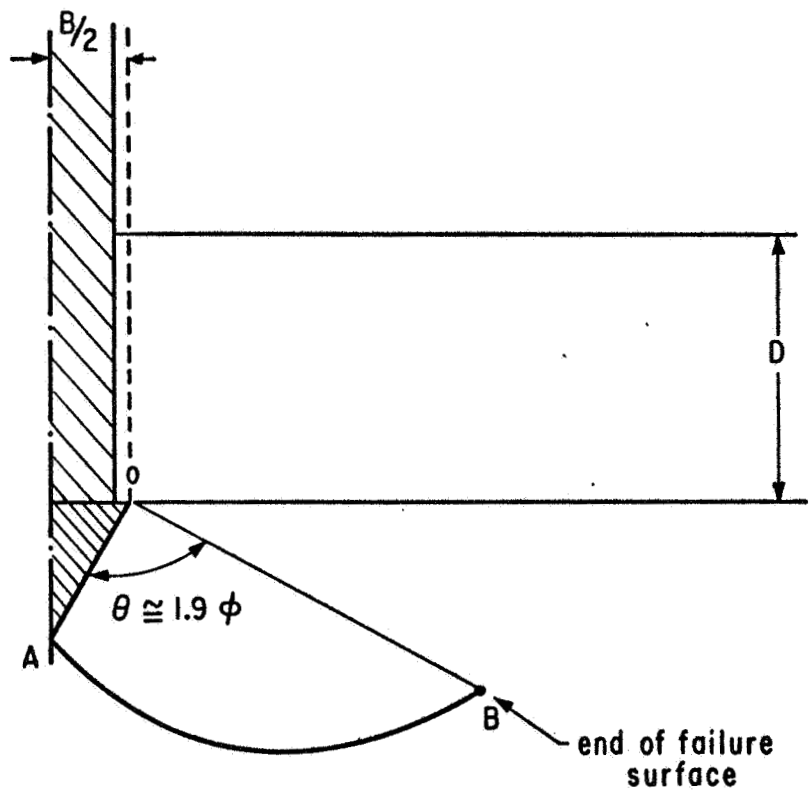

FIG. 6.20 FAILURE MECHANISM FOR COMPRESSIBLE SOILS
(After Vesic, 1963)

CHAPTER SEVEN

DETERMINATION OF IN-SITU SOIL PROPERTIES

INTRODUCTION

Because the static penetration resistance to a given penetrometer is controlled by the soil shear strength and compressibility characteristics, it should be possible to deduce the in-situ properties from the results of static penetration tests. A procedure for doing this is described in this chapter. This procedure is illustrated by application to laboratory model tests, to penetration data obtained from the literature, and to penetration data for the lunar surface obtained by the Apollo 15 self-recording penetrometer and the Soviet Lunar Rover Lunokhod-1.

PROCEDURE

As discussed in Chapter Four, the ultimate penetration resistance (q_f) may be calculated using the following equation:

$$q_f = cN_c\xi_c + \gamma_s BN_{\gamma q}\xi_{\gamma q} \tag{7.1}$$

where c = cohesion

γ_s = unit weight of soil (ρg)

B = width or diameter of penetrometer base

ξ_c, $\xi_{\gamma q}$ = shape factors

N_c, $N_{\gamma q}$ = bearing capacity or ultimate resistance factors, f_1, f_2 (ϕ, δ/ϕ, α, D/B)

ϕ = angle of internal friction (triaxial residual values)

δ = friction angle between penetrometer base and soil

α = base semiapex angle

D/B = relative depth of penetrometer base

Cohesionless Soils (c=0)

For cohesionless soils (c=0), Equation 7.1 simplifies to:

$$q_f = \gamma_s BN_{\gamma q}\xi_{\gamma q} \tag{7.2}$$

or, in dimensionless form:

$$q_f/(\gamma_s B) = N_{\gamma q}\xi_{\gamma q} \tag{7.3}$$

For a given static penetration test, the following information will be known:

(1) Cone resistance versus penetration depth or, in dimensionless form, the resistance parameter $q_f/(\gamma_s B)$ versus relative depth (D/B).

(2) Cone semiapex angle (α) and cone roughness (δ/ϕ). (Cone roughness can be approximately estimated from previous experience, from direct shear interface test results, and from the surface characteristics of the penetrometer material.

It can be shown that strength properties calculated from Equation 7.1 are not very sensitive to soil unit weight, hence any reasonable value can be assumed for the calculations. Therefore, the value of $N_{\gamma q}\xi_{\gamma q}$ can be calculated from Equation 7.3. In functional form, $N_{\gamma q}\xi_{\gamma q}$ may be expressed as follows:

$$N_{\gamma q}\xi_{\gamma q} = F(\phi,\ \delta/\phi,\ \alpha,\ D/B) \tag{7.4}$$

The only unknown in Equation 7.4 is the angle of internal friction (ϕ), and thus ϕ may be estimated from this expression for known values of α, δ/ϕ, and D/B using the following procedure:

(1) Assume a value of ϕ

(2) Enter figures in Appendix A relating $N_{\gamma q}$ to ϕ for the given parameters (α, δ/ϕ, D/B) and find corresponding value of $N_{\gamma q}$

(3) From Equation 4.32 determine the value of $\xi_{\gamma q}$ for the assumed ϕ and known relative depth

(4) Repeat steps 1 through 3 for other values of friction angle (ϕ)

(5) Prepare a plot of $N_{\gamma q}\xi_{\gamma q}$ versus ϕ (for the specific values of D/B)

(6) Having already calculated the actual value of $N_{\gamma q}\xi_{\gamma q}$ from Equation 7.3, enter the plot prepared in step 5 and determine the correct value of ϕ

This procedure may be repeated for different values of D/B to obtain the variation of ϕ with depth. Implicit in the use of the values of $N_{\gamma q}$ from Appendix A is the assumption that the at rest lateral earth pressure coefficient, $K = 1-\sin\phi$. For other values of K new values of $N_{\gamma q}$ should be determined using Equation 4.9.

Cohesive Soils (ϕ=0)

For purely cohesive soils (ϕ=0), Equation 7.1 simplifies to:

$$q_f = cN_c\xi_c + \gamma_s D \tag{7.5}$$

or, in dimensionless form:

$$q_f/c = N_c\xi_c + \left(\frac{\gamma_s B}{c}\right)\left(\frac{D}{B}\right) \tag{7.6}$$

As mentioned previously, $N_c\xi_c$ may be expressed in functional form as:

$$N_c\xi_c = F(\phi, \delta/\phi, \alpha, D/B) \tag{7.7}$$

For ϕ=0, Equation 7.7 simplifies to:

$$N_c\xi_c = F^*(\alpha, f_c, D/B) \tag{7.8}$$

where f_c is equal to c_a/c (ratio of adhesion to cohesion).

Utilizing depth factors, Equation 7.8 may be rewritten as:

$$N_c\xi_c = d_c \cdot N_c^*(\alpha, f_c)\xi_c \tag{7.9}$$

where $N_c^*(\alpha, f_c)$ = bearing capacity cohesion factor for shallow foundations obtained from Fig. 2.12a

ξ_c = shape factor for cohesion term (equal to 1.2 for ϕ=0)

d_c = depth factor for cohesion term

$$= 1.0 + \frac{0.35}{B/D + 0.6} \quad \text{(from Equation 4.19a)}$$

Thus Equation 7.5 may be rewritten as:

$$q_f = cd_c N_c^*\xi_c + \gamma_s D \tag{7.10}$$

From static penetration data, q_f is known for the range of relative depth tested. Consequently, from Equation 7.10, cohesion may be calculated directly for known values of q_f, D/B, α, and f_c. This procedure may be repeated for other values of D/B to obtain the variation of cohesion with depth.

Cohesion-Friction (c-ϕ) Soils

For cohesion-friction soils, the problem of determining in-situ soil properties from the results of static cone penetration test is more complicated for the following reasons:

(1) There are two unknowns, c and ϕ, instead of one

(2) Most c-ϕ soils are more compressible than most cohesionless soils

For c-ϕ soils, the ultimate static cone penetration resistance may be written in dimensionless form as follows:

$$q_f/(\gamma_s B) = (c/\gamma_s B)N_c\xi_c + N_{\gamma q}\xi_{\gamma q} \tag{7.11}$$

For static penetration tests performed with a given cone there are many combinations of c and ϕ which satisfy Equation 7.11 for a given value of $q_f/(\gamma_s B)$. The procedure for developing the c-ϕ relationship for given values of α, δ/ϕ, and D/B is as follows:

(1) Assume a ϕ value

(2) Enter figures in Appendix A relating N_c and $N_{\gamma q}$ to ϕ for the given parameters (α, δ/ϕ, D/B) and find the corresponding values of N_c and $N_{\gamma q}$

(3) From Equations 4.24a and 4.32 determine the values of ξ_c and $\xi_{\gamma q}$ for the assumed ϕ and known D/B

(4) Substitute the values obtained in steps 2 and 3 into Equation 7.11 and solve for cohesion

(5) Repeat steps 1 through 4 for other values of ϕ

(6) Plot the resulting c-ϕ relationship

Steps 1 through 6 may be repeated for other values of relative depth to obtain the variation of the c-ϕ relationship with depth.

It is obvious that in order to estimate c and ϕ separately, more information must be provided. The most convenient way to obtain this information is to perform an additional penetration test in the same soil deposit using a cone of a different size but having the same values of α and δ/ϕ as the first. With the penetration resistance data from two sizes of cones at the same relative depth (D/B), the following relationships may be written from Equation 7.11:

$$\left(\frac{c}{\gamma_s B}\right)_1 = \frac{(q_f/\gamma_s B)_1 - N_{\gamma q}\xi_{\gamma q}}{N_c \xi_c} \tag{7.12}$$

$$\left(\frac{c}{\gamma_s B}\right)_2 = \frac{(q_f/\gamma_s B)_2 - N_{\gamma q}\xi_{\gamma q}}{N_c \xi_c} \tag{7.13}$$

where the subscripts 1 and 2 indicate data from the small and large cones respectively ($B_2 = kB_1$). It is of interest to note in the above equations (7.12 and 7.13) that the unit penetration resistance for a large cone will be less than for a small cone at a given depth D. Assuming that there is no significant variation in cohesion over the depth range of $D=mB_1$ to kmB_1 (m=D/B) the following relationship may be obtained from Equations 7.12 and 7.13:

$$\frac{B_2}{B_1} = \frac{(q_f/\gamma_s B)_1 - N_{\gamma q}\xi_{\gamma q}}{(q_f/\gamma_s B)_2 - N_{\gamma q}\xi_{\gamma q}} \tag{7.14}$$

An expression for $N_{\gamma q}\xi_{\gamma q}$ may be obtained from Equation 7.14 as follows:

$$N_{\gamma q}\xi_{\gamma q} = \frac{B_2(q_f/\gamma_s B)_2 - B_1(q_f/\gamma_s B)_1}{B_2 - B_1} \tag{7.15}$$

The value of $N_{\gamma q}\xi_{\gamma q}$ may be calculated directly from Equation 7.15. The procedure for the determination of ϕ from a known value of $N_{\gamma q}\xi_{\gamma q}$ was given previously for the case of cohesionless soils. From Equations 7.12 and 7.13 the following relationship may be obtained for the determination of cohesion:

$$c = \frac{\gamma_s}{N_c\xi_c} \cdot \frac{\Delta(q_f/\gamma_s B)}{\Delta(1/B)} \tag{7.16}$$

or, in dimensionless form:

$$\frac{c}{\gamma_s B_1} = \frac{\left[\frac{k}{k-1}\right]\Delta(q_f/\gamma_s B)}{N_c\xi_c} \tag{7.17}$$

where k = ratio of B_2 to B_1

Δ = difference for given D/B

It should be noted that the value of cohesion obtained by two-size cone method using Equations 7.16 and 7.17 for a given relative depth represents an average value of cohesion for depths in the range of $D-mB_1$ to kmB_1.

It is also possible, if the penetration data from the two-size cone method is presented in the form of q_f versus D, to estimate the soil friction angle and cohesion at a given depth. The following relationships may be written from Equation 7.11:

$$\left(\frac{c}{\gamma_s B}\right)_1 = \frac{(q_f/\gamma_s B)_1 - (N_{\gamma q}\xi_{\gamma q})_1}{(N_c\xi_c)_1} \tag{7.18}$$

$$\left(\frac{c}{\gamma_s B}\right)_2 = \frac{(q_f/\gamma_s B)_2 - (N_{\gamma q}\xi_{\gamma q})_2}{(N_c \xi_c)_2} \tag{7.19}$$

where the subscripts 1 and 2 indicate data from the small and large cones respectively. The following relationship may be formulated from Equations 7.18 and 7.19 by noting that ξ_c is independent of relative depth:

$$\frac{B_2}{B_1} = \left[\frac{(q_f/\gamma_s B)_1 - (N_{\gamma q}\xi_{\gamma q})_1}{(q_f/\gamma_s B)_2 - (N_{\gamma q}\xi_{\gamma q})_2}\right] \frac{(N_c)_2}{(N_c)_1} \tag{7.20}$$

In order to determine ϕ from Equation 7.20, the following procedure may be used:

(1) Assume a value of ϕ.

(2) Determine values of N_c and $N_{\gamma q}$ corresponding to the assumed value of ϕ from the figures in Appendix A for the given paramenters (α, δ/ϕ, D/B). It must be remembered that the values of (D/B_1) and (D/B_2) are not the same.

(3) Determine the values of $\xi_{\gamma q}$ from Equation 4.32 corresponding to the assumed value of ϕ and known D/B.

(4) Calculate the ratio B_2/B_1.

(5) Repeat steps 1 through 4 for other assumed values of ϕ.

(6) Prepare a plot of B_2/B_1 versus ϕ.

(7) Enter plot with known value of B_2/B_1 and find the correct value of ϕ.

This procedure may be repeated for different values of D to determine the variation of ϕ with depth. It should be noted that because the contribution of cohesion relative to friction-surcharge decreases with increasing depth, the method is not expected to be a sensitive technique for determination of cohesion at large depths.

It should be noted that same method could be applied even if there are only data available for one size cone. In this case penetration resistance values (q_f) corresponding to two different penetration depths should be considered. The ratio (B_2/B_1) in Equation 7.20 will be equal to unity. Application of the method for this special case is only valid for homogeneous soil deposits.

From Equations 7.18 and 7.19, the following relationship may be obtained for the determination of cohesion:

$$c = \frac{\Delta(q_f) - \gamma_s \Delta(BN_{\gamma q} \xi_{\gamma q})}{\Delta(N_c)\ \xi_c} \tag{7.21}$$

The values of N_c, $N_{\gamma q}$, and $\xi_{\gamma q}$ obtained in order to calculate the differences (Δ) in Equation 7.21 must, of course be selected at the appropriate relative depths (D/B).

It is also possible to estimate c and ϕ separately at the same penetration depth (D) if the two cones used are not only different in size but also have different values of α and δ/ϕ. The procedure for determining ϕ is the same as described previously using Equation 7.20. However, in step 2 of the procedure, the correct values of α and δ/ϕ must be used. Cohesion may also be determined using Equation 7.21.

The procedures for determining the friction angle and cohesion of relatively homogeneous soils using penetration data obtained by the two-size cone method needs experimental verification. Also, the bearing capacity factors employed in these procedures are valid only for general shear failure conditions. For compressible soils the bearing capacity factors will be smaller than those corresponding to relatively incompressible soils. Consequently, the use of general shear bearing capacity factors in problems involving compressible soils will lead to an underestimation of shear strength parameters.

APPLICATIONS

Introduction

The procedure for cohesionless soils is illustrated by application to laboratory penetration tests data for Monterey Sand No. 0 and to data presented by Green (1970) for Yuma and Mortar sands. The procedure for cohesion-friction soils has been applied to laboratory penetration data for LSS No. 2, to lunar surface penetration data obtained during the Apollo 15 mission, and by the Soviet Lunar Rover Lunokhod-1. Where possible, comparisons are made between actual (measured) and deduced in-situ soil properties.

Cohesionless Soils

Monterey Sand No. 0

The procedure for the determination of the in-situ properties of

cohesionless soils was applied to the results (see Chapter Six) of static wedge and cone penetration tests in Monterey Sand No. 0. The results for wedges are summarized in Table 7.1 and presented in Fig. 7.1. The results for cones are summarized in Table 7.2 and presented in Fig. 7.2. As can be seen in Figs. 7.1 and 7.2, the agreement between the predicted and actual values of soil friction angle is quite good.

Yuma and Mortar Sands

The procedure was applied to measured average penetration resistance values presented (see Fig. 7.3) by Green (1970) for Yuma and Mortar sands using rough flat ended penetrometers (plates) in the range of 5.08 cm to 60.69 cm in diameter. The gradation curves for Yuma and Mortar sands are given in Fig. 7.4. Results are summarized graphically in Fig. 7.5. It can be seen that predicted and measured values of ϕ agree well.

Cohesion-Friction Soils

Lunar Soil Simulant No. 2

The procedure for the determination of the in-situ properties (cohesion and friction angle) of cohesion-friction soils was applied to the results of static cone penetration tests in dense Lunar Soil Simulant No. 2 (see Fig. 6.19). Because data were available for one-size cone only penetration resistance values (q_f) corresponding to relative depths of 5, 10, and 15 were considered. This was justified because it was known that the soil profile was homogeneous. By the application of Equations 7.20 and 7.21 and the previously described procedure, strength parameters of c=0.137 psi. (0.945 kN/m^2) and ϕ= 46.6° were obtained. Directly measured values of strength parameters for the simulant, corresponding to e=0.57 and w=1.4% were c=0.121 psi. (0.834 kN/m^2) and ϕ=47.0° (triaxial). It can be seen that agreement between predicted and measured values of both c and ϕ are excellent.

Apollo 15 Soil Mechanics Experiment

The Apollo 15 mission to Hadley Rille provided for the first time in the U. S. Lunar Program, quantitative measurement of forces of interaction between a penetrometer and the lunar soil. Quantitative analysis of the in-situ mechanical properties (c and ϕ) of the lunar soil can be made using the data obtained by the self-recording penetrometer(SRP) shown in Fig. 7.6. The SRP was used to obtain penetration versus force data in the upper part of the lunar surface. The Apollo 15 SRP could penetrate to a maximum depth of 76.0 cm (30.0 in.) and could measure penetration force to a maximum of 111 N

Table 7.1 SUMMARY OF PREDICTED FRICTION ANGLES OF MONTEREY SAND NO. 0

Depth Range	Void Ratio, e	Predicted ϕ -deg.				
		(1)	(2)	(3)	(4)	(5)
D/B≤5	0.728	39.5	39.5	39.2	39.7	39.5
	0.665	41.2	41.7	41.2	42.0	42.1
	0.599	44.5	44.3	43.8	44.2	45.3
D/B≤10	0.728	40.0	40.1	39.5	39.7	40.1
	0.665	41.7	42.7	41.5	42.0	43.7
	0.599	44.5	45.5	44.9	45.1	46.1
D/B≤15	0.728	-	40.2	-	39.7	40.1
	0.665	42.2	43.7	42.0	42.1	44.0
	0.599	44.8	46.5	45.2	44.9	46.1

(1) α = 90°, δ/ϕ= 0.5; (2) α = 15°, δ/ϕ= 0.5;
(3) α = 15°, δ/ϕ= 0.9; (4) α = 30°, δ/ϕ= 0.9;
(5) α = 30°, δ/ϕ= 0.5 (B=0.8 in. Wedges)

Void Ratio e	Predicted* ϕ-deg.	Measured**	
		ϕ_{peak} -deg.	ϕ_{ult} -deg.
0.728	39.8±0.3	39.7	39.2
0.665	42.2±0.6	42.6	41.8
0.599	45.0±0.5	45.4±0.2	44.5±0.2

* For all depths and penetrometer configurations
**Triaxial friction angles

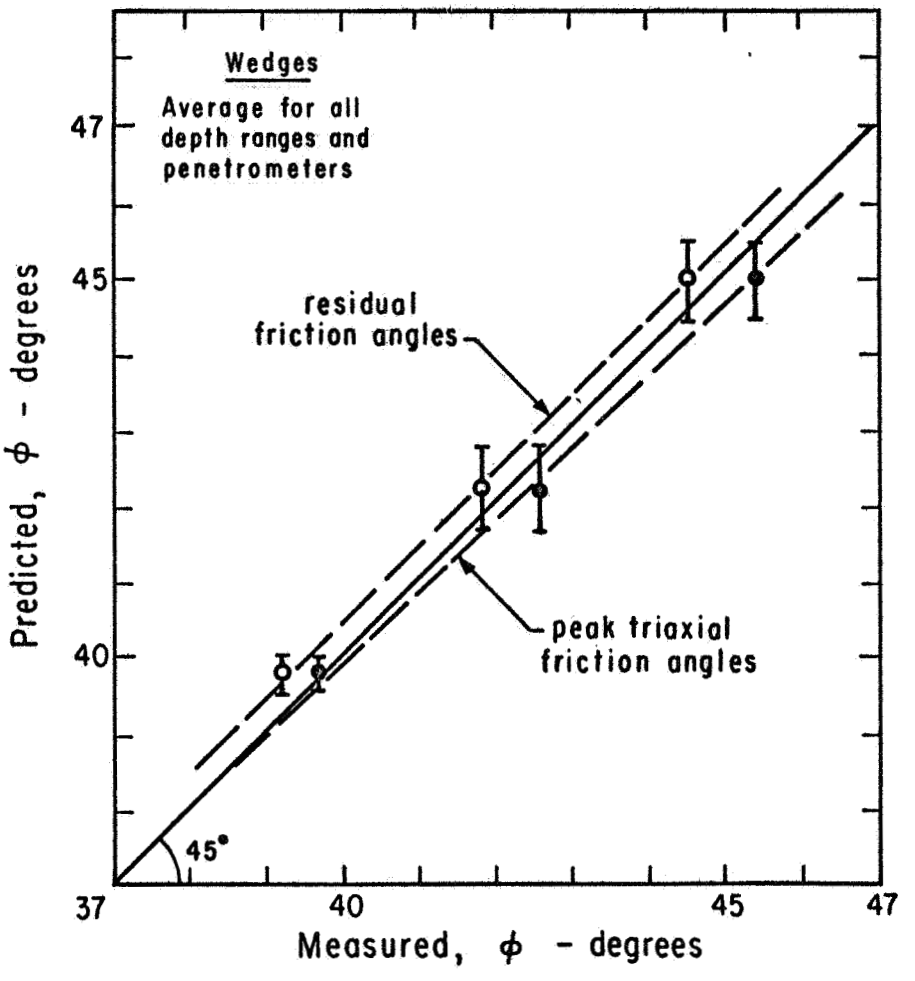

FIG. 7.1 COMPARISON OF MEASURED AND PREDICTED FRICTION ANGLES FOR MONTEREY SAND No. 0

Table 7.2 SUMMARY OF PREDICTED FRICTION ANGLES OF MONTEREY SAND NO. 0

Depth Range	Void Ratio, e	Predicted ϕ -deg.				
		(1)	(2)	(3)	(4)	(5)
D/B≤5	0.728	39.1	41.7	39.5	-	-
	0.665	40.4	-	42.0	-	-
	0.659	-	42.6	-	-	-
	0.599	43.8	-	44.9	44.8	44.8
	0.575	-	45.0	-	-	-
D/B≤10	0.728	39.1	40.2	39.1	-	-
	0.665	41.0	-	42.0	-	-
	0.659	-	42.8	-	-	-
	0.599	44.2	-	44.9	45.2	45.4
	0.575	-	46.3	-	-	-
D/B≤15	0.728	39.1	40.0	?	-	-
	0.665	41.7	-	?	-	-
	0.659	-	43.2	-	-	-
	0.599	44.5	-	45.1	45.3	45.7
	0.575	-	45.5	-	-	-

(1) $\alpha = 90°$, $\delta/\phi = 0.5$; (2) $\alpha = 15°$, $\delta/\phi = 0.5$
(3) $\alpha = 15°$, $\delta/\phi = 0.9$; (4) $\alpha = 15°$, $\delta/\phi = 0.3$
(5) $\alpha = 30°$, $\delta/\phi = 0.3$ (B = 0.8 in. Cones)

Void Ratio e	Predicted* ϕ-deg.	Measured**	
		ϕ_{peak} -deg.	ϕ_{ult} -deg.
0.728	39.7	39.7	39.2
0.665	41.5	42.6	41.8
0.659	42.9	42.9	42.0
0.599	44.9	45.6	44.7
0.575	45.6	46.8	45.6

* For all depths and penetrometer configurations
**Triaxial friction angles

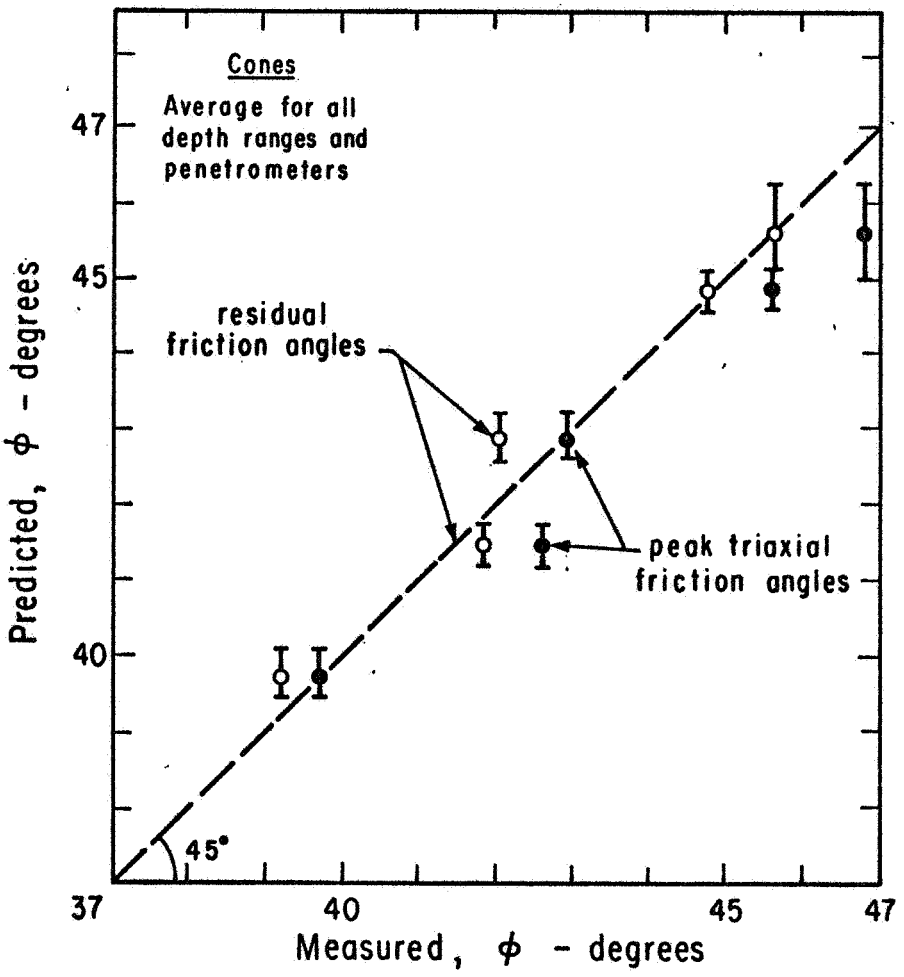

FIG. 7.2 COMPARISON OF MEASURED AND PREDICTED FRICTION ANGLES FOR MONTEREY SAND No. 0

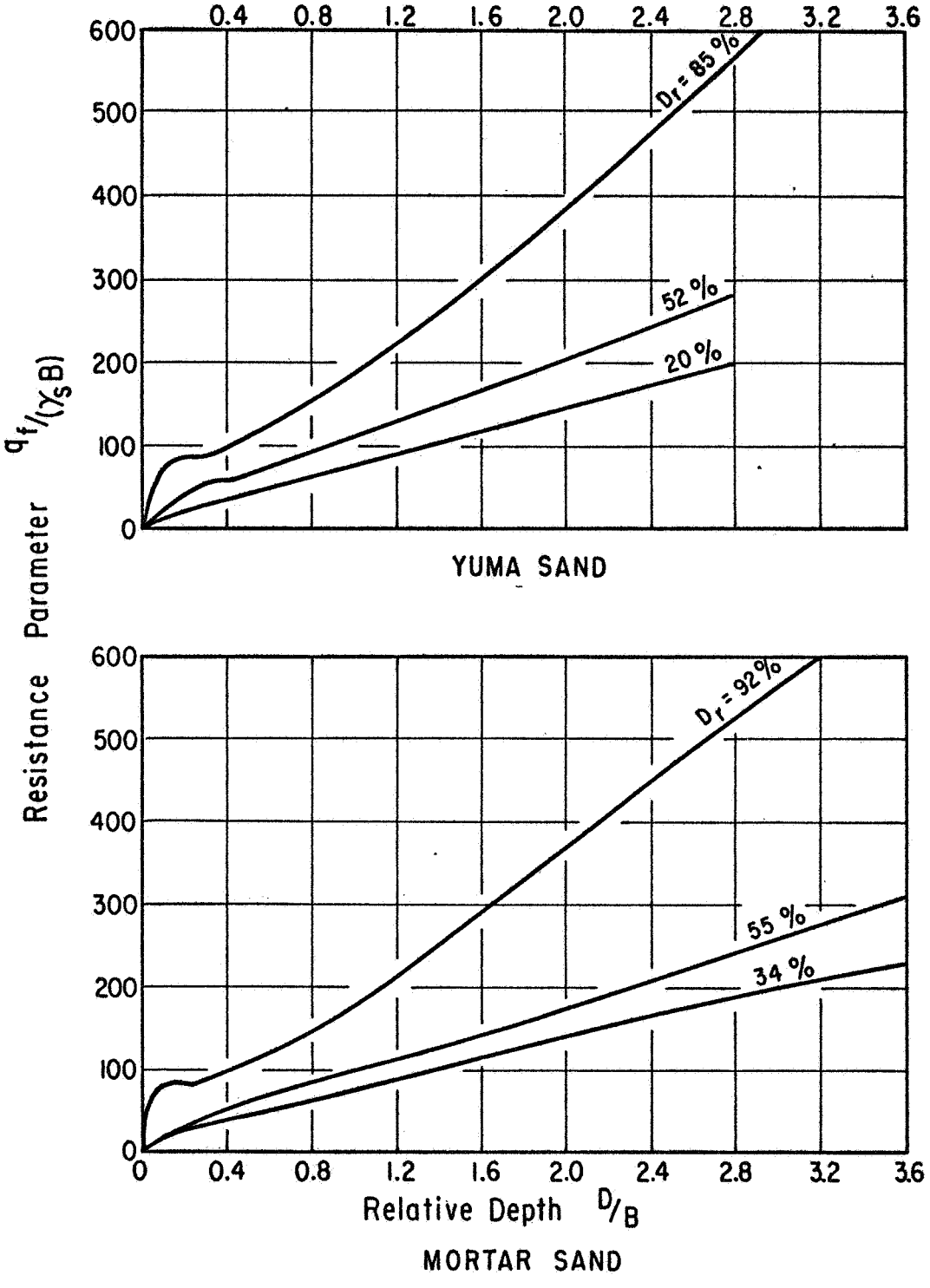

FIG. 7.3 PENETRATION CURVES FOR YUMA AND MORTAR SANDS (After Green, 1970)

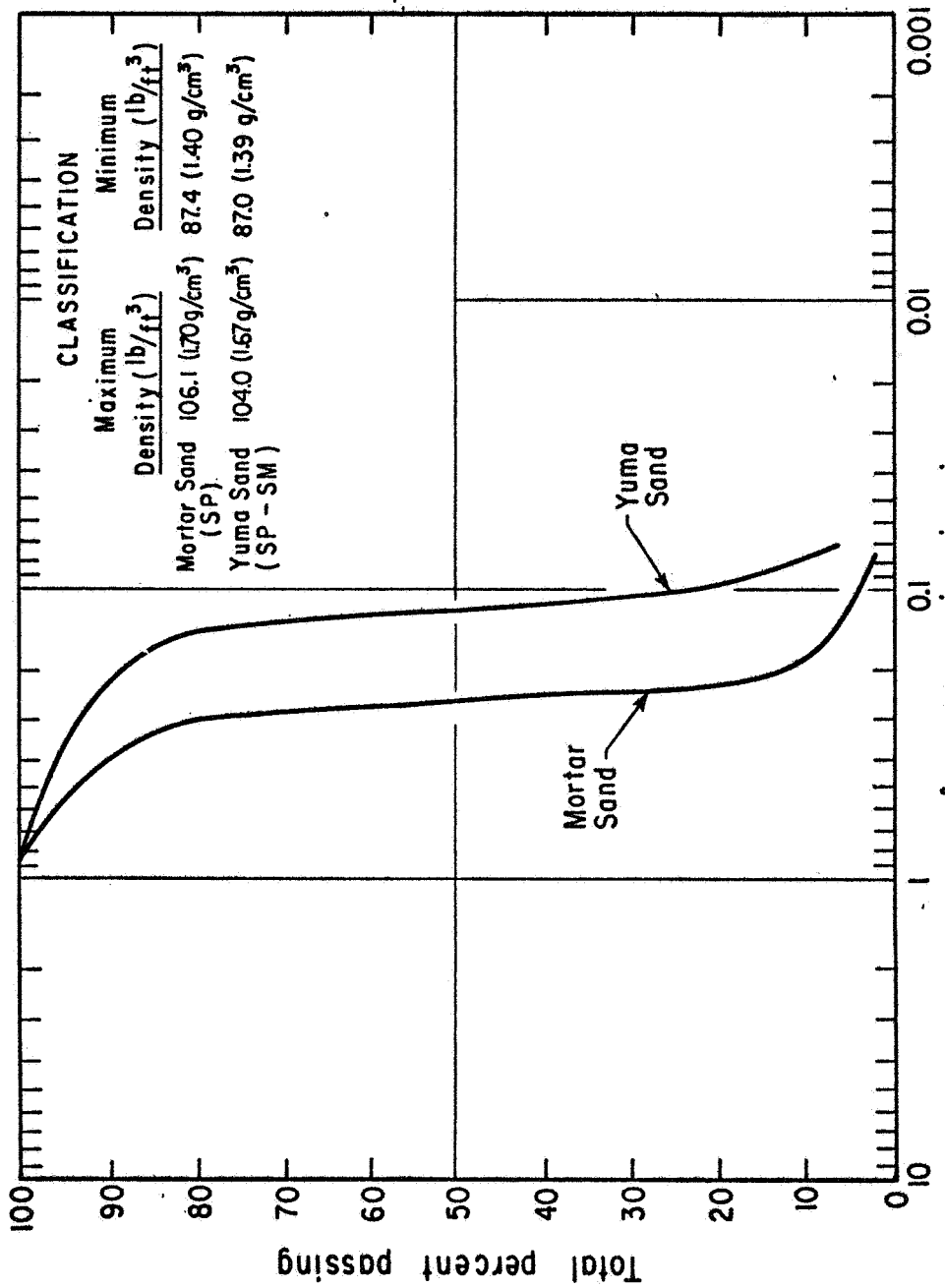

FIG. 7.4 GRADATION AND CLASSIFICATION DATA FOR YUMA AND MORTAR SANDS (After Green, 1970)

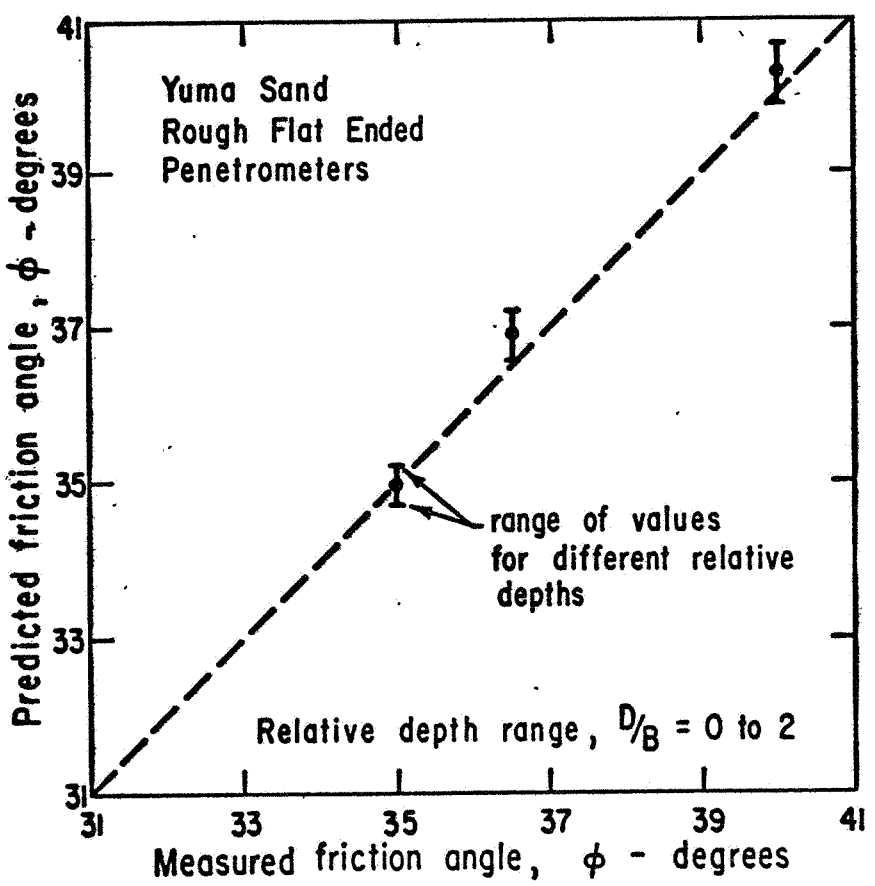

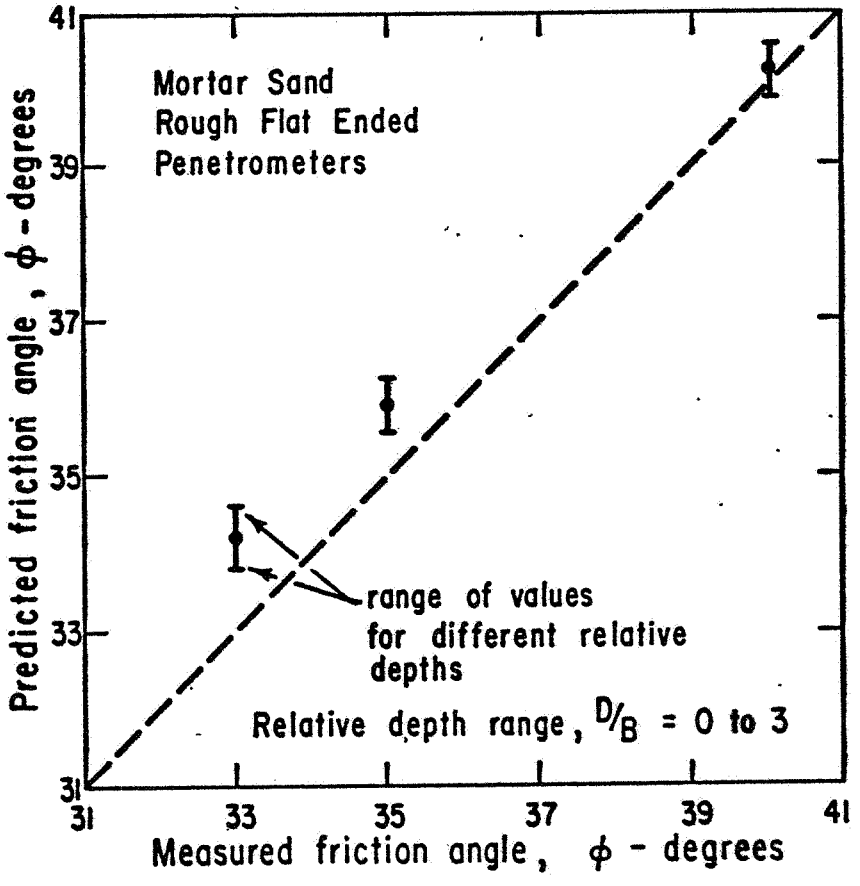

FIG. 7.5 COMPARISON OF MEASURED AND PREDICTED FRICTION ANGLES FOR YUMA AND MORTAR SANDS
(Data after Green, 1970)

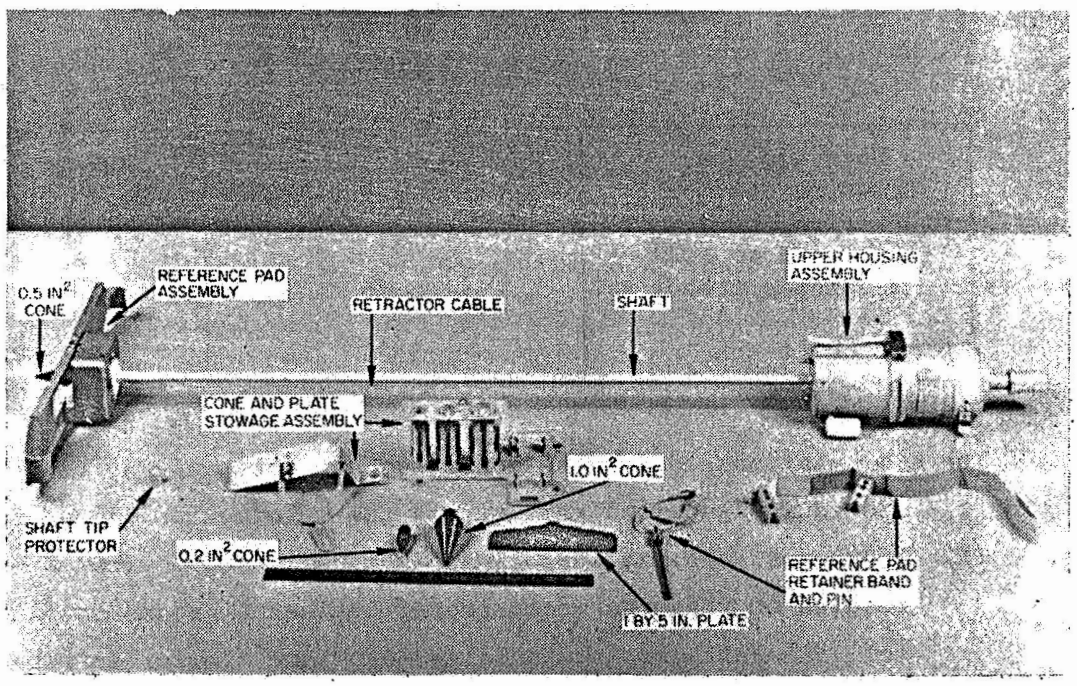

FIG. 7.6 SELF - RECORDING PENETROMETER

(25 pounds). The record of each penetration was scribed on a recording drum contained in the upper housing assembly. Detailed information about the SRP is given by Mitchell et al (1972a).

As reported by Mitchell et al, (1972a), because of the tendency of the lunar reference plane to ride up on the penetrometer shaft precise values of penetration were not known for the penetration tests on Apollo 15, and the exact shape of the force versus depth curve was not obtained. Nonetheless, estimates of the penetration were possible as indicated in Table 7.3.

Table 7.3 SUMMARY OF APOLLO 15 CONE PENETRATION TEST RESULTS FOR 0.5 SQ. IN. CONE (after Mitchell et al, 1972a)

Location Near Traverse Station 8	Penetration at q_f=50.0 psi., (cm)	Relative Depth (D/B)
Adjacent to soil mechanics trench	8.25	4.06
In LRV track	5.25	2.58

The c-ϕ relationship for the lunar surface material may be deduced by using the procedure described earlier and the information listed below:

(1) Roughness (δ/ϕ) is approximately equal to 0.5. (Based on the results of friction measurements between a ground basalt lunar soil simulant and hard-anodized aluminum similar in roughness to that used for the SRP cones).

(2) Unit weight of soil γ_s=1.8 g/cm^3 (under earth gravity).

(3) Ultimate resistance q_f=50.0 psi. (34.5 N/cm^2).

(4) Measured values of relative depth. (Table 7.3 indicates that the relative depths (D/B) for these penetration tests fall in the range of about 2.5 to 4.1). Thus the value of D/B=3 may represent the actual conditions reasonably well.

The results of these calculations are shown in Fig. 7.7. Another c-ϕ relationship was established during the Apollo 15 mission by excavating a trench and failing the wall of the trench by a known boundary loading. The c-ϕ relationship for the soil mechanics trench has also been plotted on Fig. 7.7. The intersection of this curve and the c-ϕ curve for the penetration tests provide values of c and ϕ which simultaneously satisfy the results

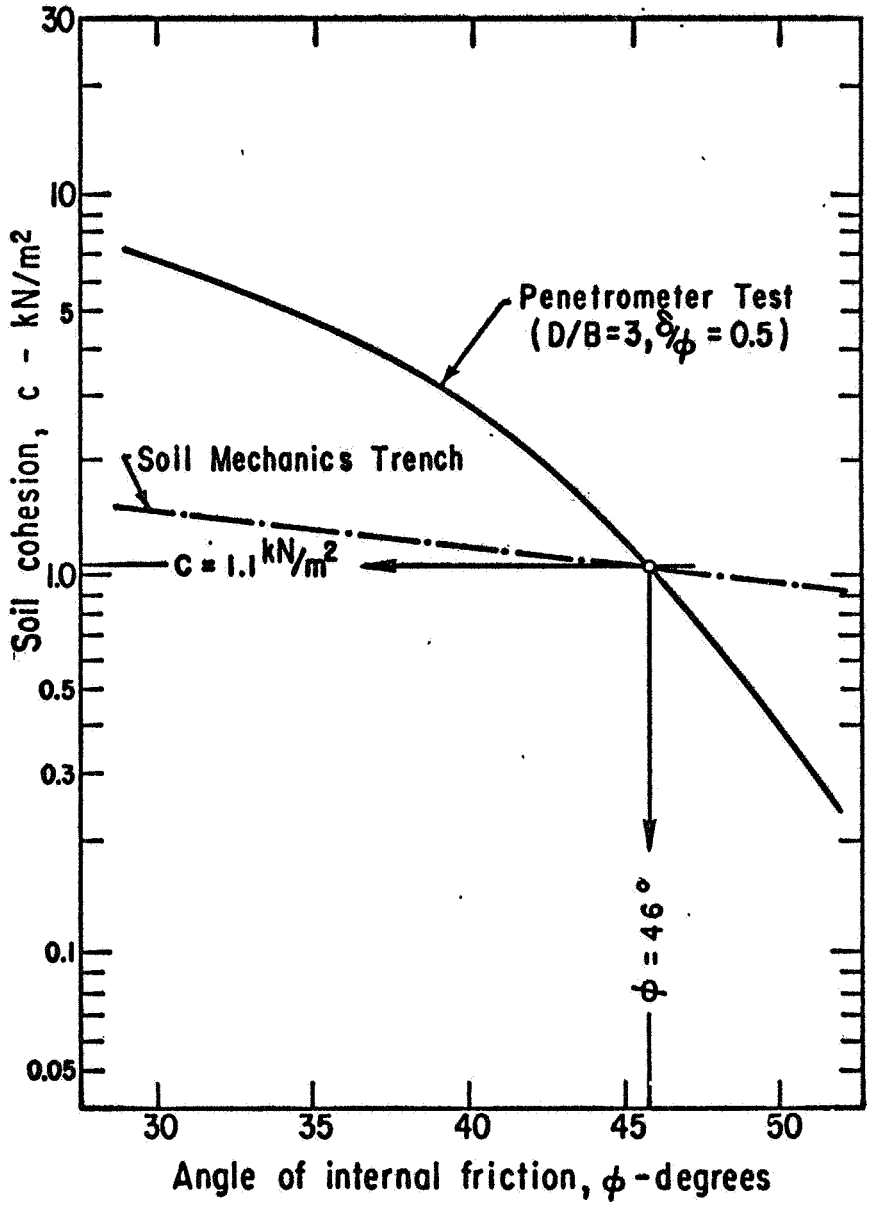

FIG. 7.7 PROPERTIES OF LUNAR SURFACE DEDUCED FROM APOLLO 15 PENETRATION TEST RESULTS

of both the trench and penetration tests. For D/B=3, the required cohesion is 1.1 kN/m^2 (0.16 psi.) and the angle of internal friction is 46.0°. It should be remembered that this value is expected to be close to the residual value of friction angle. The value obtained agrees closely with that obtained by comparison of the observed penetration behavior with that of terrestrial simulants.

Detailed analysis of Apollo penetration tests are presented in the Preliminary Science Reports for Apollo 15 and Apollo 16 (Mitchell et al, 1972a and Mitchell et al 1973).

Lunokhod-1

The procedure for deduction of cohesion and friction angle from the results of static cone penetration tests was applied to penetration resistance data for the lunar surface obtained by the Soviet Lunar Rover Lunokhod-1 which were obtained in the western side of Mare Imbrium. Data were obtained from the report of Leonovich et al (1971).

Investigations with the Lunokhod-1 were made using a special instrument by penetrating and rotating a conical-bladed punch in the ground. With the penetration of the punch it was possible to determine ground carrying capacity*, and with rotation of the vanes the resistance to rotational shear (torque resistance**) was determined. During the three months of Lunokhod operation there were 327 measurements of mechanical properties by means of penetration of the conical-bladed punch at different ground locations; e.g., craters, concentrations of rocks, horizontal and sloping surface sectors.

Summaries of the data provided by Leonovich et al (1971) are given in Tables 7.4 and 7.5. Fig. 7.8 shows a histogram and curve of the statistical distribution of ground carrying capacity and torque resistance along one of the trajectory segmants.

Analysis of vane shear tests

Usually interpretation of vane shear test results is based upon the assumption of a uniform distribution of shear resistance on the whole surface of the rotating cylinder, including the two ends. The same assumption appears to have been made by Leonovich et al (1971) leading to an estimation of the

* Ground Carrying Capacity was defined as the specific resistance on the punch for a depth of ground penetration equal to the height of the punch.

**Torque Resistance was defined as required cohesion neglecting the contribution of friction to vane resistance.

Table 7.4 SUMMARY OF TECHNICAL DATA FOR CONE-VANE PUNCH (after Leonovich et al 1971)

Maximum force on the penetrometer	196 N
Depth of penetration	50-100 mm
Angle of punch rotation	up to 90 deg.
Maximum torque on punch	0.5 kgm
Diameter of cone base	50.0 mm
Diameter of blades	70.0 mm
Height of cone-blade punch	44.0 mm
Blade thickness (square cut edge)*	1.1 to 1.6 mm
Surface roughness of cone*	0.3 to 0.5
*Estimated from the photographs	

Table 7.5 SUMMARY OF DATA FOR THE MECHANICAL PROPERTIES OF LUNAR GROUND (after Leonovich et al, 1971)

Range of Values	
Carrying capacity	19.6 to 98.0 kN/m^2
Torque resistance	1.96 to 8.82 kN/m^2
Density of soil	1.5 to 1.7 g/cm^3
Highest frequency values	
Carrying capacity	33.3 kN/m^2
Torque resistance	39.6 kN/m^2

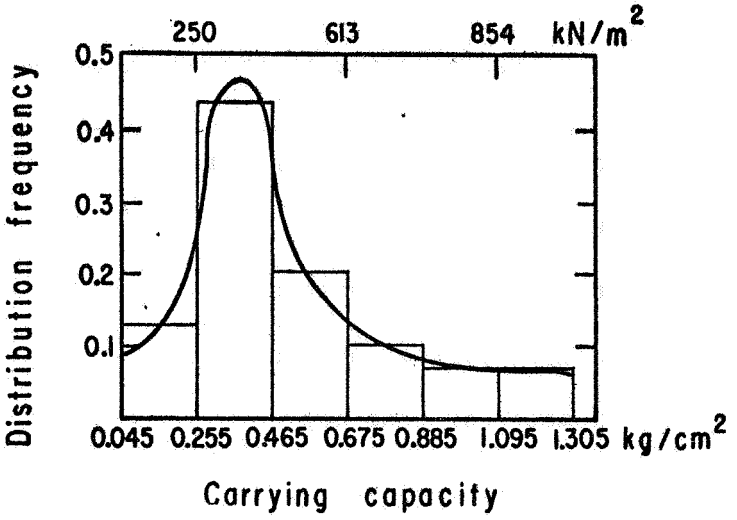

(a)

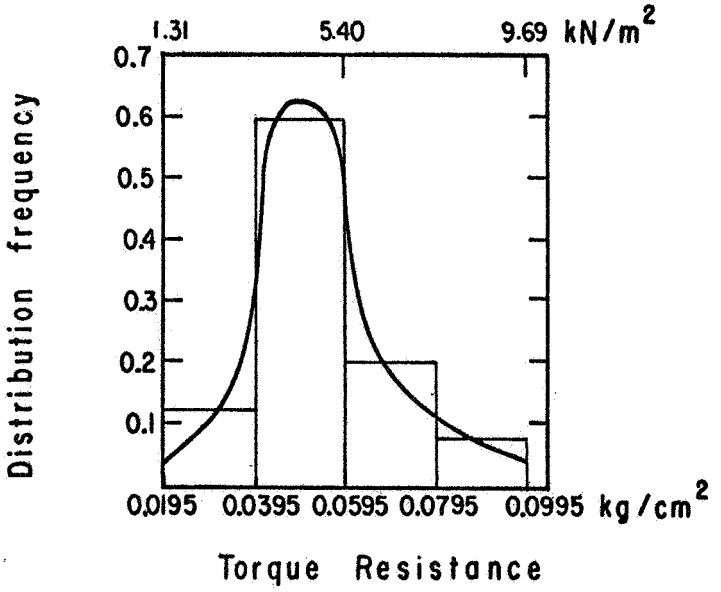

(b)

FIG. 7.8 HISTOGRAM AND CURVE REPRESENTING DISTRIBUTION OF GROUND CARRYING CAPACITY AND GROUND RESISTANCE TO TORQUE (After Leonovich et al, 1971)

highest frequency cohesion (or torque resistance) value of 39.6 kN/m^2 (0.683 psi). The estimated range of cohesion from Surveyor and Apollo data was only 0.345 to 1.38 kN/m^2. The high cohesion value estimated from the Lunokhod-1 data may be due to the fact that the contribution of friction to torque resistance was ignored by Leonovich et al, (1971). Even if it was assumed that a cylindrical failure pattern was actually obtained, the distribution of stresses around the circumference could not be uniform for soils in which there is an appreciable contribution of friction to the resistance. A uniform shear strength distribution is correct only for ϕ=0 soils, where shear strength is independent of normal stress.

Farrent (1960) derived the following expression for torque in c-ϕ soils by assuming that shear strength, s_o, develops at both ends and immediately behind the blades:

$$T = \frac{4}{3}\pi r^3 s_o + \frac{nr^2L}{2\tan\phi} s_o \left(e^{\frac{4\pi}{n}\tan\phi} - 1\right) \tag{7.22}$$

where T = torque
r = radius of vane
n = number of blades
L = length of vane
s_o = shear strength of soil
ϕ = angle of internal friction of soil

When the contribution of friction is considered, the minumum value of shear strength (s_o) can be calculated by the following relationship (after Cox, 1967):

$$s_o = c(1 + \sin\phi) \tag{7.23}$$

For the analysis of Lunokhod data (n=4 and L=1.25r) the following relationship can be written:

$$T = \frac{4}{3}\pi r^3 c(1+\sin\phi) + \frac{5r^3 c(1+\sin\phi)}{2\tan\phi}\left(e^{\pi\tan\phi} - 1\right) \tag{7.24}$$

or, in dimensionless form:

$$\frac{T}{r^3 c} = \left[\frac{4}{3}\pi + \frac{5(e^{\pi\tan\phi} - 1)}{2\tan\phi}\right](1+\sin\phi) \tag{7.25}$$

It can be shown that for $\phi=0$ soils Equation 7.25 reduces to:

$$\frac{T}{r^3c} = \frac{4}{3}\pi + \frac{5}{2}\pi = \frac{23\pi}{6} \cong 12.0 \tag{7.26}$$

The same equation can be obtained by considering the development of uniform shear strength (cohesion) on the both ends of the vane and on the cylindrical failure surface.

Values of the dimensionless parameter $T/(r^3c)$ for different values of ϕ were calculated from Equation 7.25 and are summarized in Table 7.6.

Table 7.6 VALUES OF DIMENSIONLESS PARAMETER $T/(r^3c)$ FOR DIFFERENT VALUES OF ϕ

ϕ(deg.)	20	25	30	35	40	45	50
T/r^3c	25.4	31.3	39.6	52.4	70.5	102	161

It can be seen that $T/(r^3c)$ increases with increasing ϕ for c-ϕ soils indicating that the necessary cohesion should decrease with increasing ϕ for a given T (torque) value. Consequently, the ratios of $T/(r^3c)$ corresponding to c-ϕ and $\phi=0$ analysis can be determined from the following relationships:

$$\frac{\left(\frac{T}{r^3c}\right)_{(\phi=0)}}{\left(\frac{T}{r^3c}\right)_{(c-\phi)}} = \frac{\frac{23\pi}{6}}{\left[\frac{4}{3}\pi + \frac{5(e^{\pi\tan\phi}-1)}{2\tan\phi}\right](1+\sin\phi)} \tag{7.27a}$$

or

$$\frac{(c)_{(\phi=0)}}{(c)_{(c-\phi)}} = \frac{\left[\frac{4\pi}{3} + \frac{5(e^{\pi\tan\phi}-1)}{2\tan\phi}\right](1+\sin\phi)}{\frac{23\pi}{6}} \tag{7.27b}$$

The calculated values are summarized in Table 7.7 below:

Table 7.7 THE RATIOS OF COHESION VALUES CALCULATED FROM ϕ=0 AND c-ϕ ANALYSIS

ϕ(deg.)	20	25	30	35	40	45	50
$\frac{c_{(\phi=0)}}{c_{(c-\phi)}}$	2.11	2.61	3.29	4.36	5.85	8.46	13.4

The value of cohesion c=39.6 kN/m^2 (0.683 psi) reported by Leonovich et al (1971) corresponds to a ϕ=0 analysis. Corresponding c-ϕ relationships were calculated using Table 7.7 for c-ϕ analysis, and are shown in Fig. 7.9. It can be seen that for ϕ=45° the calculated value of cohesion from c-ϕ analysis is 8.5 times smaller than the value calculated from ϕ=0 analysis.

The variation in c-ϕ relationships for different ground locations may be determined using the range of torque resistance values (1.96 to 8.82 kN/m^2) reported for these locations. The corresponding c-ϕ relationships have been calculated and are shown in Fig. 7.10. The c-ϕ relationship having the highest frequency is also plotted in Fig. 7.10. It may be concluded on the basis of these data that the mechanical properties of the lunar ground can vary over an extremely wide range.

Analysis of cone penetration tests

The cone penetration data from Lunokhod-1 also provide c-ϕ relationships for the lunar soil. The penetration resistance of the soil to the cone-vane punch has two components; (1) resistance due to end bearing of vane blades, and (2) resistance due to the cone. The largest contribution to penetration resistance comes from the cone, because its bearing area is much larger than the bearing area of the vane blades. The highest frequency value of ground carrying capacity (q_f) is 33.3 kN/m^2. If it is assumed that the contribution due to end bearing of the vane is negligible and the soil disturbance due to the penetration of the vane is insignificant, for α=30°, δ/ϕ=0.5 (assumed) and D/B=0, the calculated c-ϕ relationship is as shown in Fig. 7.11.

The effect of the end resistance of the vanes may be evaluated by considering the blades of the vane as two strip footings with a width of 1.5 mm and length of 70 mm. For a penetration of 44 mm, the relative depth (D/B) is approximately 30. For comparison, the calculated c-ϕ relationship considering both cone and vane resistance is also plotted in Fig. 7.11.

The effect of cone roughness must also be considered. Calculations for

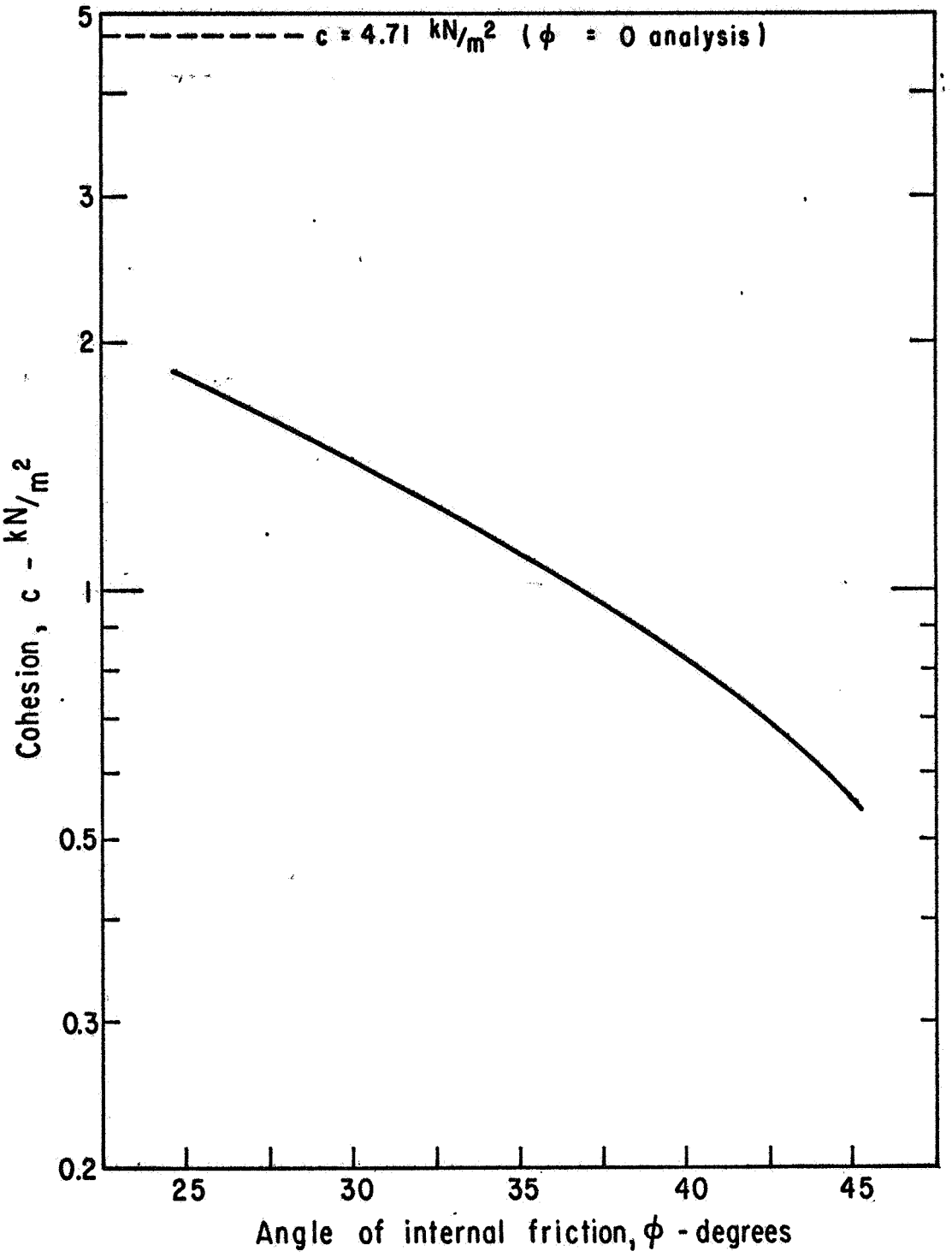

FIG. 7.9 HIGHEST FREQUENCY c - ϕ RELATIONSHIP OBTAINED FROM THE ANALYSIS OF VANE SHEAR TESTS
(Data from Leonovich et al, 1971)

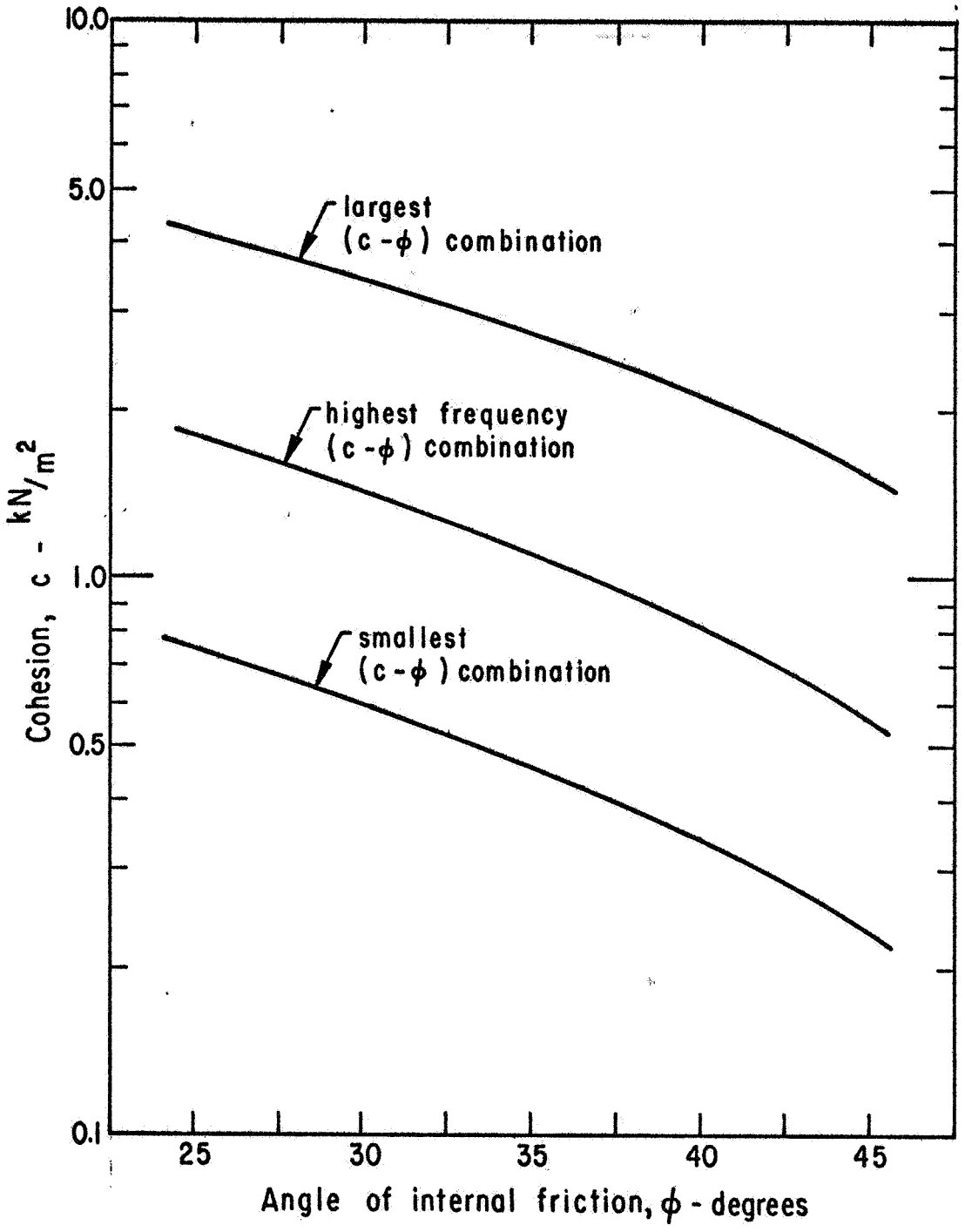

FIG. 7.10 RANGE OF c-φ RELATIONS OBTAINED FROM THE ANALYSIS OF VANE SHEAR TESTS (Data from Leonovich et al, 1971)

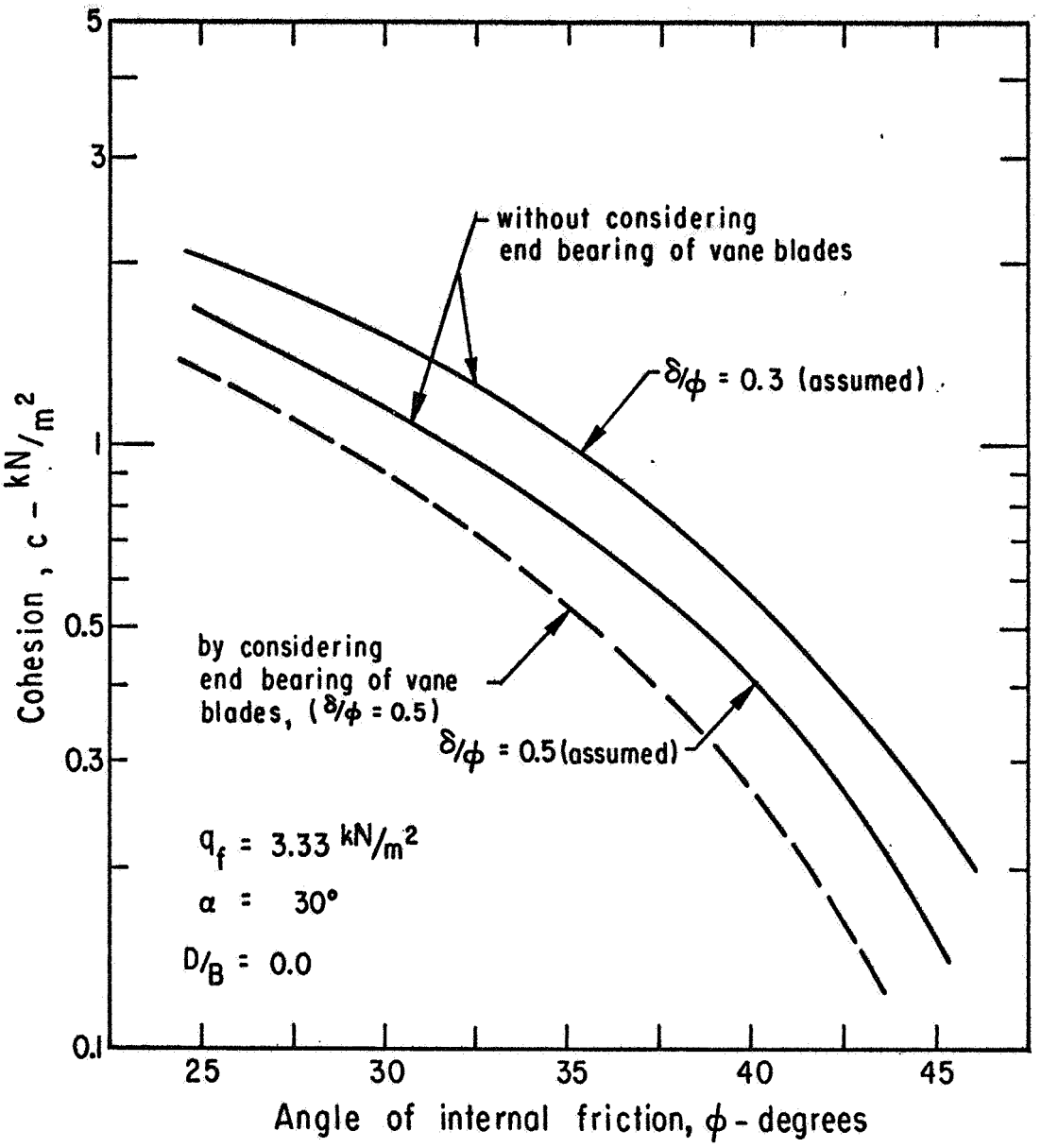

FIG. 7.11 EFFECTS OF CONE ROUGHNESS AND END BEARING OF VANE BLADES ON SHEAR STRENGTH PARAMETERS OF LUNAR SURFACE (Data from Leonovich et al, 1971)

Fig. 7.11 were based on the assumption that the cone roughness (δ/ϕ) was 0.5. For a smooth cone surface roughness will be close to 0.3. The calculated c-ϕ relationship for δ/ϕ=0.3 (neglecting end bearing of vane) is also shown in Fig. 7.11. It can be seen that the curve for δ/ϕ=0.5 with end bearing of vanes neglected represents a good average of the three alternatives considered.

The variation in c-ϕ relationships for different ground locations may be determined using the range of carrying capacity (19.6 to 98.0 kN/m^2) reported for these locations. The corresponding c-ϕ relationships have been calculated and are shown in Fig. 7.12. The c-ϕ relationship having the highest frequency (q_f = 33.3 kN/m^2) is also plotted in Fig. 7.12.

Comparison of c-ϕ relationships

A comparison of the c-ϕ relationships obtained from two different analyses (vane shear and cone penetration) is shown in Fig. 7.13. Considering the different failure mechanisms involved, the c-ϕ relationships are quite comparable. The test results for the more dense soils (higher values of ϕ) show higher values of strength parameters for the vane test results than for the penetration tests. This may be because the vane tests were done at somewhat greater depths, and also becuase the analysis of vane data may be expected to yield values of ϕ close to the peak; whereas, the cone results reflect more closely the residual strength parameters. The difference between peak and residual values for most soils generally increases with increasing density (and therefore increasing ϕ). Further, the c-ϕ relationships developed from the cone-vane penetration data reflect the assumptions made regarding appropriate value of δ/ϕ for the cone (a value of 0.5 was used for the curves shown in Fig. 7.13) and the contribution of the vane (neglected for the curves shown in Fig. 7.13).

Change in shear strength properties with depth

Leonovich et al (1971) present separate penetration data in the form of force versus penetration for different ground sectors as shown in Fig. 7.14. Separate analysis of each individual curve can be made, and the change in shear strength properties with depth can be studied. This can be done only if the change in bearing capacity factors with depth are formulated. As discussed in detail in Chapter Four, bearing capacity factors can be calculated from Equations 4.6 and 4.9 as functions of relative depth (D/B). As an example, the penetration data for horizontal ground sector (curve 1 in Fig. 7.14) were analyzed. The penetration data obtained from Fig. 7.14

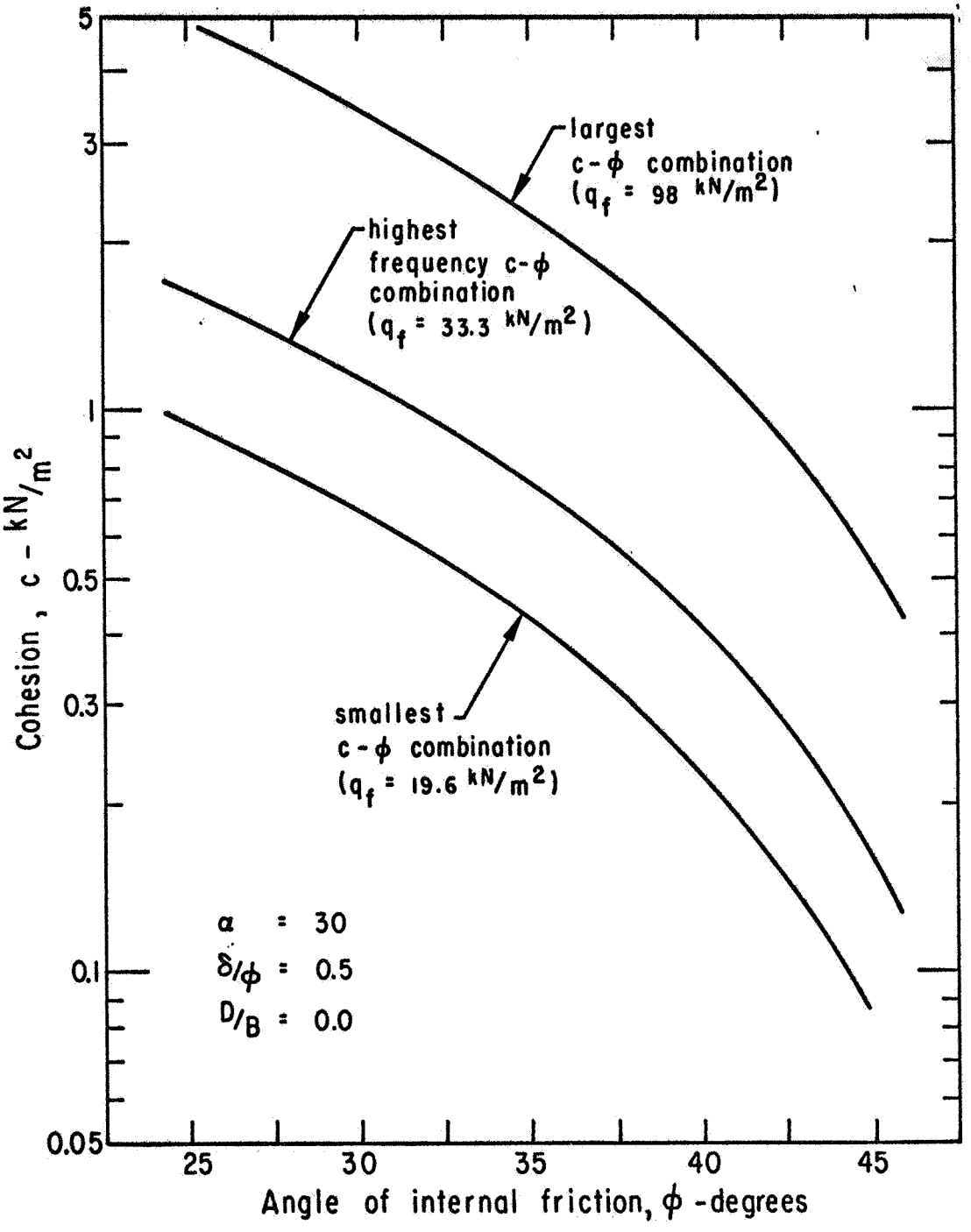

FIG. 7.12 RANGE OF SHEAR STRENGTH PARAMETERS OBTAINED FOR LUNAR SURFACE FROM CONE PENETRATION TEST RESULTS (Data from Leonovich et al, 1971)

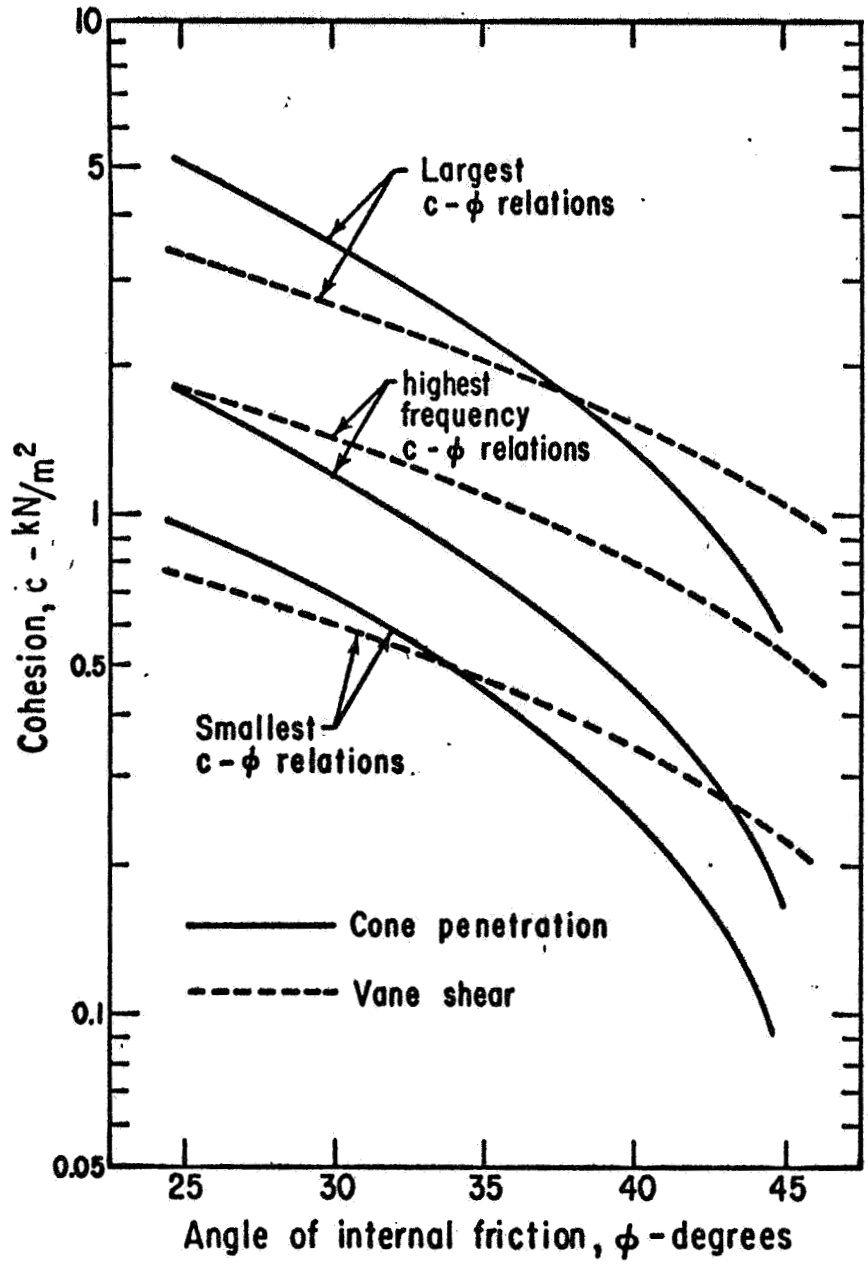

FIG. 7.13 COMPARISON OF c-ϕ RELATIONS OBTAINED FROM CONE PENETRATION AND VANE SHEAR TESTS

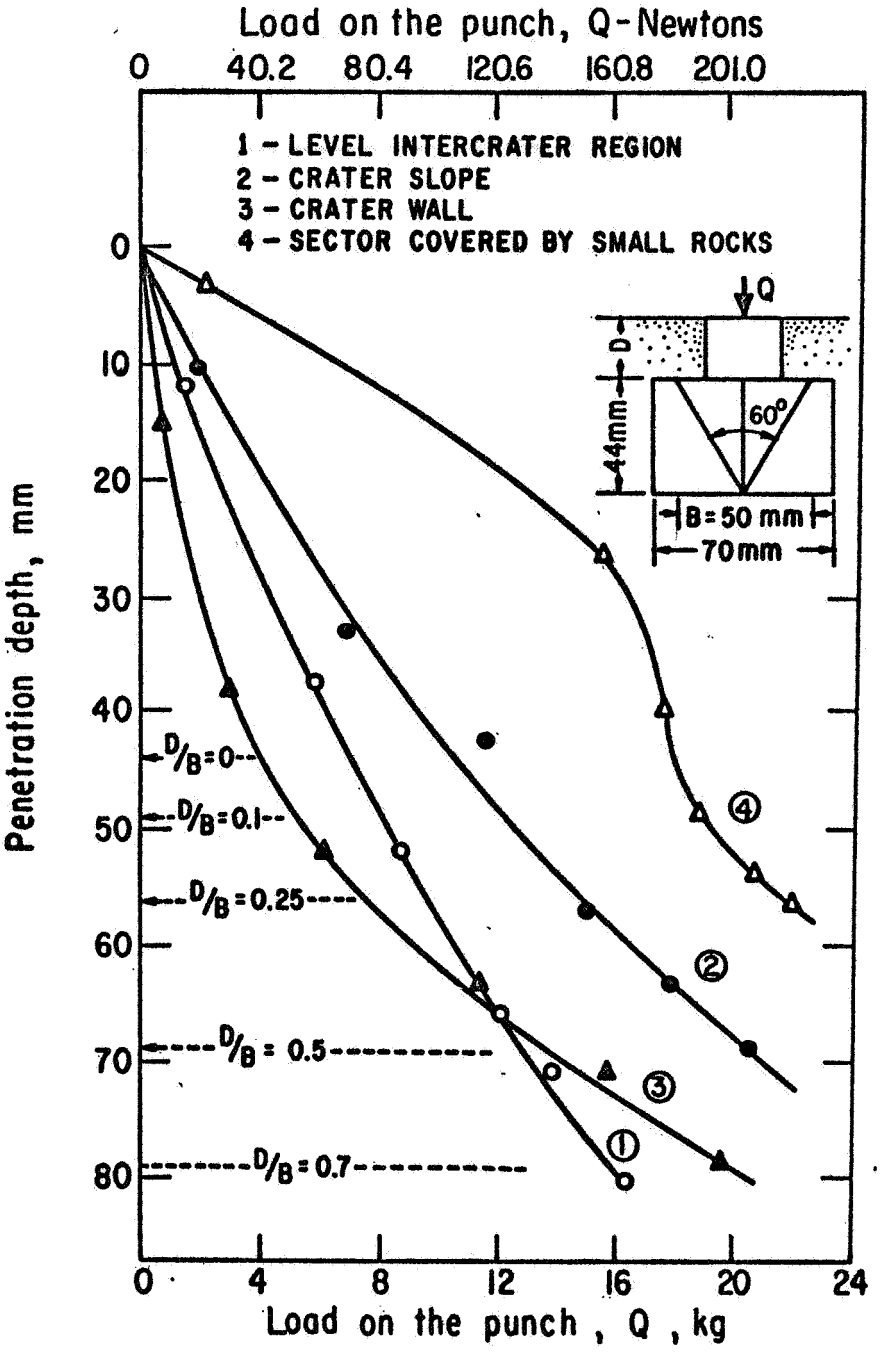

FIG. 7.14 PENETRATION DATA OBTAINED BY LUNOKHOD-1 FOR FOUR CONDITIONS IN THE WESTERN PART OF MARE IMBRIUM

(Data from Leonovich, et al. 1971)

are summarized in Table 7.8 for different relative depths.

Table 7.8 PENETRATION DATA FOR LUNAR SURFACE AT A HORIZONTAL GROUND SECTOR (after Leonovich et al, 1971)

Relative Depth (D/B)	Force Q (kg)	Unit Penetration Resistance, q_f	
		kg/cm^2	kN/m^2
0.00	7.2	0.367	36.0
0.10	8.0	0.408	40.0
0.25	9.8	0.500	49.0
0.50	12.8	0.653	64.0
0.70	15.8	0.806	79.0

For a given relative depth (D/B) using the procedure outlined in this chapter, corresponding c-ϕ relationships were calculated. The calculated relationships are shown in Fig. 7.15. It can be seen that there is a slight increase in shear strength parameters with depth. This may be an indication of an increase in soil density with depth.

SUMMARY

Procedures for the determination of in-situ soil strength parameters from the results of static penetration tests in cohesionless, purely cohesive, and cohesion-friction soils have been presented. These procedures have also been illustrated by application to laboratory test results, to penetration data obtained from the literature, and to penetration data for the lunar surface obtained by the Apollo 15 self-recording penetrometer and the Soviet Lunar Rover Lunokhod-1. Comparisons of measured and predicted strength parameters have been made where possible. These comparisons indicate very good agreement between measured and predicted values.

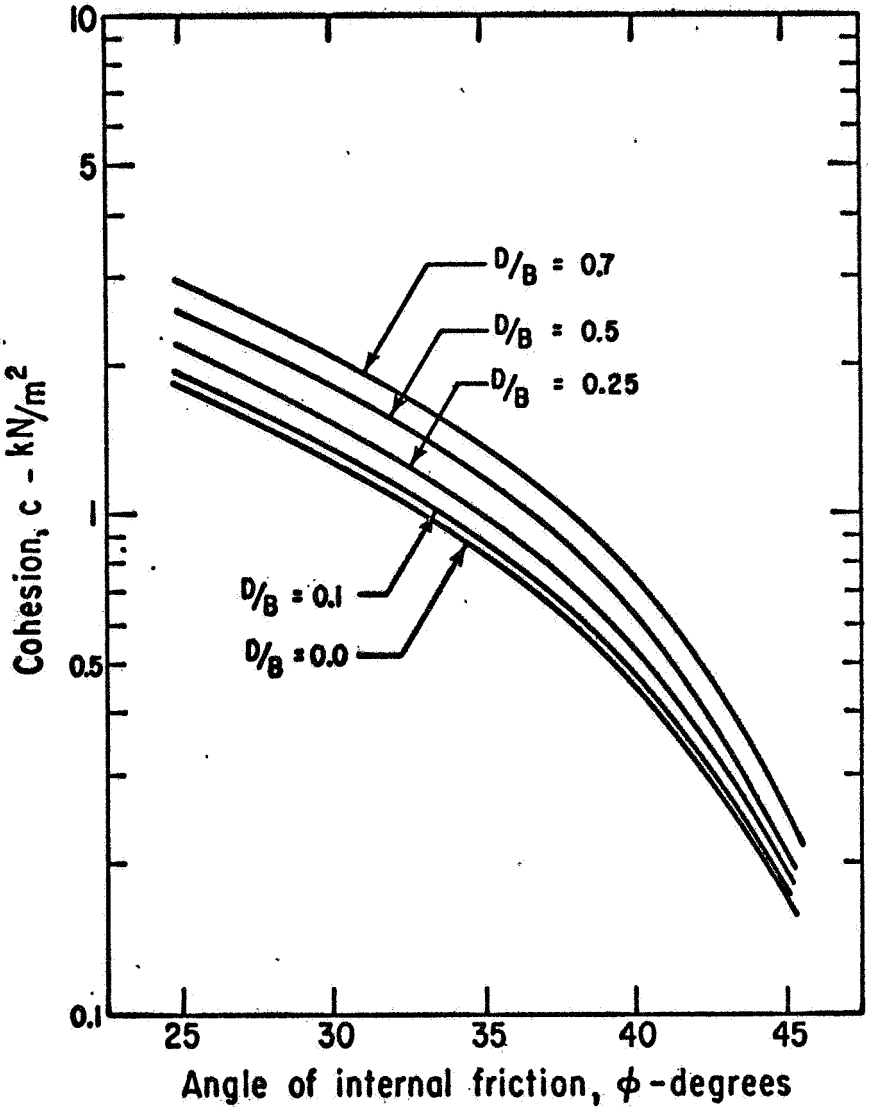

FIG. 7.15 CHANGE IN SHEAR STRENGTH PROPERTIES WITH DEPTH, LEVEL INTERCRATER REGION (Data from Leonovich, et al 1971)

CHAPTER EIGHT

SUMMARY AND CONCLUSIONS

GENERAL

This study was undertaken to develop practical analytical procedures which would provide a theoretical basis for the understanding and utilization of the results of static penetration tests for the determination of in-situ lunar soil properties in support of the Lunar Soil Mechanics Experiment. Model tests were used to establish a rational basis for theoretical developments and to improve the understanding of penetrometer-soil interaction. The effects of penetrometer to soil friction, soil friction angle, base apex angle, and relative depth (ratio of penetrometer base depth to the base width) on the failure mechanism were investigated. A failure mechanism has been proposed based on the interpretation of features observed in the models and the results of previous studies. Knowledge of the failure mechanism has permitted the development of new relationships for determining the ultimate base resistance which account explicitly for such important parameters as base apex angle, base roughness, soil friction angle, and relative depth.

Values of input variables (soil friction angle and penetrometer to soil friction angle) for a fine sand (Monterey Sand No. 0) and a silty fine sand (LSS No. 2) were determined in order to experimentally evaluate the proposed relationships. Carefully controlled laboratory penetration tests were conducted on both of these soils. The measured values of input variables were used to predict the penetration resistance of these soils in accordance with the theory presented. Comparisons were made of the measured and predicted penetration resistance values, and agreement was found to be very good.

Analytical procedures for the determination of in-situ soil strength parameters from the results of static penetration tests in cohesionless, purely cohesive and cohesion-friction soils have been presented. These procedures have been illustrated by application to (1) laboratory test results, (2) penetration resistance data obtained from the literature, and (3) penetration resistance data for the lunar surface obtained by the Apollo 15 self-recording penetrometer and the Soviet Lunar Rover Lunokhod-1. Comparisons of measured and predicted strength parameters have indicated very good agreement.

FAILURE MECHANISM

From the results of model tests it was found that a failure surface as shown in Fig. 3.11 represents closely the actual failure surface associated with wedge penetration. A plane shear zone exists adjacent to the base of the penetrometer. The dimensions of this plane shear zone depend on both the penetrometer to soil friction angle (δ) and soil friction angle (ϕ), as described by Equation 3.9.

A logarithmic spiral bounds a radial shear zone to a point of vertical tangency, above which the failure surface rises vertically to the ground surface for large depths of penetration. For shallow penetration depths, the logarithmic spiral breaks out at ground surface before vertical tangency is reached. This failure mechanism associated with the penetration of wedges is consistent with those suggested also by Biarez et al (1961) and Hu (1965).

THEORY

Equations 4.3, 4.6 and 4.9 describe the resistance to penetration of wedge shaped penetrometers in terms of soil friction angle, cohesion, and density and base apex angle (2α), base roughness (δ/ϕ), and relative depth of penetrometer base (D/B). This solution to the static penetration problem provides a generality not previously available.

For determination of penetration resistance of cones, bearing capacity factors corresponding to strip loading must be modified by proper shape factors. Equations 4.26 and 4.32 can be used for calculation of these shape factors.

It has been shown that the use of bearing capacity factors formulated for general shear failure conditions will cause overestimation of the penetration resistance of compressible soils, such as loose to medium-dense silty fine sands. As a result of soil compressibility, the shear surface is restricted to a smaller zone around the penetrometer tip. A procedure has been suggested for determination of bearing capacity factors for compressible soils. However the general validity of this procedure has not yet been established.

For resistance of wedge and cone shaped penetrometers the following conclusions can be drawn from the theory:

(1) For rough wedges and cones with obtuse base apex angles, the bearing capacity factors are nearly equal to those for plane and horizontal contact areas.

(2) The bearing capacity factors for rough bases increase with decreasing values of base semi-apex angle (α) below approximately 15°.

(3) For perfectly smooth wedges and cones, the bearing capacity factors increase with increasing base apex angle.

(4) The bearing capacity factors for a given roughness should not be estimated by linear interpolation between perfectly smooth and perfectly rough values.

(5) Base roughness has little or no influence on the penetration resistance encountered by plane and horizontal contact areas in cohesive soils. However, at the surface of a cohesionless soil, a smooth flat-ended penetrometer will encounter less penetration resistance than one having a rough base.

(6) For relative depths greater than a critical relative depth dependent on the particular angle of internal friction, base apex angle, and base roughness:

   (a) There will be no change in the bearing capacity cohesion factor N_c with further penetration.

   (b) The increase in bearing capacity friction-surcharge factor $N_{\gamma q}$ with further penetration will be proportional to the increase in depth.

DETERMINATION OF STRENGTH PARAMETERS

From the results of direct shear interface tests, it is concluded that the roughness (δ/ϕ) has almost an unique value for a given soil and penetrometer. In other words, δ/ϕ is not sensitive to soil density. It has also been shown that $\delta/\phi \cong 0.3 - 0.5$ for a smooth cone and $\delta/\phi \cong 0.9$ for rough surfaced cones.

The use of friction angles corresponding to plane strain peak values will cause overestimation of the penetration resistance of soils. Because the ultimate values of shear stresses control the resistance at large deformations, friction angles corresponding to ultimate (residual) values of shear stresses should be used in the analysis of the continuous static penetration problem. It is common practice, in shear testing, however, to obtain only peak values of the friction angle and to terminate the test before accurate ultimate values are obtained. It has been shown that the use of peak triaxial friction angles could cause approximately 20 to 30 percent overestimation of the penetration resistance for dense sands. Further, the

use of peak values of friction angle for less dense sands will yield correct values of penetration resistance, because peak and ultimate values of friction angles agree closely for such soils.

Several examples have been presented to show that predicted and measured shear strength parameters of both cohesionless and cohesion-friction soils agree well. Therefore, it is concluded that the proposed analytical method (Equations 7.1 through 7.21) with the aid of the developed theory can satisfactorily be used for the determination of in-situ shear strength properties of soils which fail in general shear.

RECOMMENDATIONS

It is recommended that further efforts be directed to:

(1) Verification of the proposed analytical method for a greater variety of cohesionless and cohesion-friction soils,

(2) Further investigation of the effect of soil compressibility, and development of an analytical method for determination of penetration resistance of compressible soils,

(3) Development of a method for analysis of the penetration resistance of layered soils (in which properties differ greatly among layers).

REFERENCES

Abdul-Baki, A. and Lewis, A. B. (1970), "Bearing Capacity of Foundations on Sand," Journal of Soil Mechanics and Foundations Division, ASCE, Vol. 96, No. SM2, March, 1970, pp. 545-559.

Bachelier, M. and Parez, L. (1965), "Contribution a l'etude de la compressibilite des sols a l'aide du penetrometre a cone," Proceedings, Sixth International Conference on Soil Mechanics and Foundation Engineering, Vol. 2, pp. 3-7.

Balla, A. (1962), "Bearing Capacity of Foundations," Journal of Soil Mechanics and Foundations Division, ASCE, Oct., 1962, No. SM5, pp. 13-34.

Banks, D. C. (1968), "Selected Methods for Analyzing the Stability of Crater Slopes," U. S. Army Engineer Waterways Experiment Station, Vicksburg, Mississippi, Miscellaneous Paper S-68-8, July, 1968.

Begemann, H. K. S. (1965), "The Friction Jacket Cone as Aid in Determining the Soil Profile," Proceedings, Sixth International Conference on Soil Mechanics and Foundation Engineering, Vol. 1, 1965, pp. 17-20.

Begemann, H. K. S. (1969), "The Dutch Static Penetration Test with the Adhesion Jacket Cone," L. G. M. Mededelingen, Publications Delft Laboratory for Soil Mechanics, Vol. 12, No. 4, April, 1969 and Vol. 13, No. 1, July, 1969.

Berezantsev, V. G. and Kovalev, I. V. (1968), "Consideration of the Curvilinearity of the Shear Graph when Conducting Tests on Model Foundations," Translated from Osnovaniya, Fundamenty i Mekhanika Gruntov, No. 1, Jan.-Feb., 1968, pp. 1-4.

Biarez, J., Burel, M. and Wack, B. (1961), "Contribution a l'etude de la force portante des Fondations," Proceedings, Fifth International Conference on Soil Mechanics and Foundation Engineering, Vol. 1, 1961, pp. 603-609.

Brinch Hansen, J. (1961), "A General Formula for Bearing Capacity," Bulletin No. 11, 1961, Danish Geotechnical Institute, Copenhagen, pp. 38-46.

Brinch Hansen, J. (1966), "Note Concerning GI Bulletin No. 11." Bulletin No. 21, 1966, Danish Geotechnical Institute, Copenhagen, p. 13.

Chan, C. K. and Duncan, J. M. (1967), "A New Device for Measuring Volume Changes and Pressures in Triaxial Tests on Soils," Materials Research and Standards, Vol. 7, No. 7, pp. 312-314.

Cornforth, D. H. (1964), "Some Experiments on the Influence of Strain Conditions on the Strength of Sand," Geotechnique, Vol. 14, No. 2, 1964, pp. 143-167.

Cox, A. D., Eason, G. and Hopkins, H. G. (1961), "Axially Symmetric Plastic Deformations in Soils," Transactions, Royal Society of London, Vol. 254A, 1961.

Cox, A. D. (1962), "Axially Symmetric Plastic Deformation in Soils-II, Indention of Ponderable Soils," International Journal of Mech. Sci., Vol. 4, 1962, p. 371.

Cox, M. E. (1967), "A Review of the Vane Test," Civil Engineering Transactions, April, 1967, The Institution of Engineers-Australia, pp. 19-29.

D'Appolonia, D., Whitman, R. and D'Appolonia, E. (1969), "Sand Compaction with Vibratory Rollers," Journal of the Soil Mechanics and Foundations Division, ASCE, Vol. 95, No. SM1, pp. 263-284.

DeBeer, E. E. (1967), "Bearing Capacity and Settlement of Shallow Foundations on Sand," Proceedings, Symposium on Bearing Capacity an d Settlement of Foundations, Duke University, 1965, pp. 15-34.

DeBeer, E. E. (1970), "Experimental Determination of the Shape Factors and the Bearing Capacity Factors of Sand," Geotechnique, Vol. 20, No. 4, pp. 387-411.

DeRuiter, J. (1971), "Electric Penetrometer for Site Investigations," Journal of the Soil Mechanics and Foundations Division, ASCE, Vol. 97, No. SM2, February, 1971, pp. 457-472.

Farrent, T. A. (1960), "The Interpretation of Vane Tests in Soils Having Friction," Proceedings, Third Aust.-New Zealand Conf., Soil Mechanics and Foundation Engineering, Sydney, Institution of Civil Engineers, pp. 81-86.

Gawith, A. H. (1952), "The Use of In-Situ Shear Tests in the Design of Flexible Pavements," Proceedings, First Aust.-New Zealand Conference on Soil Mechanics and Foundation Engineering, pp. 233-240.

Gorbunov-Possadov, M. I. (1965), "Calculations for the Stability of Sand Bed by a Solution Combining the Theories of Ela-ticity and Plasticity," Proceedings, Sixth International Conference on Soil Mechanics and Foundation Engineering, Vol. 2, 1965, pp. 51-55.

Graham, J. (1968), "Plastic Failure in Cohesionless Soils," Geotechnique, Vol. 18, No. 3, 1968, pp. 301-316.

Graham, J. and Stuart, J. G. (1971), "Scale and Boundary Effects in Foundation Analysis," Journal of the Soil Mechanics and Foundations Division, ASCE, Vol. 97, No. SM11, November, 1971, pp. 1533-1548.

Green, A. J. (1970), "Penetration Resistance of Soils, Report-1, Tests with Circular Footings in Air-Dry Sands," Technical Report M-70-14, U. S. Army Engineer Waterways Experiment Station, Vicksburg, Mississippi.

Hansen, B. and Christensen, N. H. (1969), discussion on "Theoretical Bearing Capacity of Very Shallow Footings," by Larkin, L. A., Journal of the Soil Mechanics and Foundations Division, ASCE, Vol. 95, No. SM6, November, 1969, pp. 1568-1572.

Hu, G. (1964), "Variable Factors Theory of Bearing Capacity," Journal of the Soil Mechanics and Foundations Division, ASCE, July, 1964, pp. 85-93.

Hu, G. (1965), "Bearing Capacity of Foundations with Overburden Shear," Sols-Soils, No. 13, June, 1965, pp. 11-18.

Hu, G. (1970), discussion of "Bearing Capacity of Foundations on Sand," by Abdul-Baki and Lewis, Journal of Soil Mechanics and Foundations Division, ASCE, Vol. 96, No. SM6, November, 1970, p. 2151.

Hvorslev, M. J. (1970), "The Basic Sinkage Equations and Bearing Capacity Theories," Technical Report M-70-1, U. S. Army Engineer Waterways Experiment Station, Vicksburg, Mississippi.

Jumikis, (1961), "The Shape of Rapture Surface in Dry Sand," Proceedings of Fifth International Conference on Soil Mechanics and Foundation Engineering, Vol. 1, p. 693, and Vol. 3, p. 227.

Kingston, M. R. and Spencer, A. J. M. (1970), "General Yield Considerations in Plane Deformations of Granular Media," J. Mech, Phys, Solids, Vol. 18, 1970, pp. 233-243.

Kolbuszewski, J. J. (1948), "An Experimental Study of the Maximum and Minimum Porosities of Sands," Proceedings, Second International Conference on Soil Mechanics and Foundation Engineering, Vol. 1, 1948, pp. 158-165.

Lade, P. (1972), "The Drained Stress-Strain and Strength Characteristics of Cohesionless Soils," Dissertation presented to the University of California, Berkeley, in 1972, in partial fulfillment of the requirements for the degree of Doctor of Philosophy.

Larkin, L. A. (1968), "Theoretical Bearing Capacity of Very Shallow Footings," Journal of the Soil Mechanics and Foundations Division, ASCE, Vol. 94, No. SM6, November, 1968, pp. 1347-1357.

Leonovich, A. K., Gromov, V. V., Rybakov, A. V., Petrov, V. K., Pavlov, P. S., Cherkasov, I. I. and Shvavav, V. V. (1971), "Studies of Lunar Ground Mechanical Properties with the Self-Propelled 'Lunokhod-1' Chapt. 8 of Peredvizhnaya Laboratoriya na Luna-Lunokhod-1, pp. 120-135.

Lundgren, H. and Mortensen, K. (1953), "Determination by the Theory of Plasticity of the Bearing Capacity of Continuous Footings on Sand," Proceedings, Third International Conference on Soil Mechanics and Foundation Engineering, Vol. 1, p. 409.

Lundgren, H. (1957), "Dimensional Analysis in Soil Mechanics," Acta Polytechnica 237, Civil Engineering and Building Construction Series, Vol. 4, No. 10, 1957, Copenhagen, Denmark.

Meyerhof, G. G. (1951), "The Ultimate Bearing Capacity of Foundations," Geotechnique, Vol. 2, No. 4, 1951, pp. 301-332.

Meyerhof, G. G. (1955), "Influence of Roughness of Base and Ground Water Conditions on the Ultimate Bearing Capacity of Foundations," Geotechnique, Vol. 5, September, 1955, pp. 227-242.

Meyerhof, G. G. (1961a), "The Ultimate Bearing Capacity of Wedge-Shaped Foundations," Proceedings, Fifth International Conference on Soil Mechanics and Foundation Engineering, Vol. 2, 1961, pp. 105-109.

Meyerhof, G. G. (1961b), discussion of "Shallow Foundations: Influence of the Dimensions and the Shape of the Foundations," Proceedings, Fifth International Conference on Soil Mechanics and Foundation Engineering, Vol. 3, 1961, pp. 193-195.

Meyerhof, G. G. (1963), "Some Recent Research on the Bearing Capacity of Foundations," Canadian Geotechnical Journal, Vol. 1, No. 1, 1963, pp. 16-26.

Mitchell, J. K., Houston, W. N., Vinson, T. S., Durgunoglu, T., Namiq, L. I., Thompson, J. B. and Treadwell, D. D. (1971), "Lunar Surface Engineering Properties Experiment Definition," Prepared for George C. Marshall Space Flight Center, Huntsville, Alabama, under NASA Contract NAS 8-21432.

Mitchell, J. K., Bromwell, L. G., Carrier, W. D., III, Costes, N. C., Houston, W. N., and Scott, R. F. (1972), "Soil-Mechanics Experiment," Apollo 15 Preliminary Science Report, NASA SP-289.

Mitchell, J. K., Carrier, W. D., III, Houston, W. N., Scott, R. F., Bromwell, L. G., Durgunoglu, H. T., Hovland, H. J., Treadwell, D. D., and Costes, N. C. (1973), "Soil-Mechanics Experiment," Apollo 16 Preliminary Science Report, NASA SP-315.

Muhs, E. (1963), "Ueber die zulassige Belastung nicht bindigen Boden-Mitteilungen der Degebo," Berlin, Helft 16.

Nowatzki, E. A. (1971), "A Theoretical Assessment of the SPT," Proceedings, Fourth Pan American Conference on Soil Mechanics and Foundation Engineering, June, 1971, Vol. 2, pp. 45-61.

Nowatzki, E. A. and Karafiath, L. L. (1972), "The Effect of Cone Angle on Penetration Resistance," Presented at the 51st Annual Meeting of the Highway Research Board.

Prandtl, L. (1921), "Uber die Eindringungsfestigkeit (Harte) plastischer Baustoffe und die Festigkeit von Schneiden," Zeit.angew. Math. Mech., 1, No. 1, pp. 15-20.

Reissner, H. (1924), "Zum Erddruckproblem," Proceedings, First International Congress of Applied Mechanics, Delft, pp. 295-311.

Schmertmann, J. H. (1967), "Static Cone Penetrometers for Soil Exploration," Civil Eng., 37, June, 1967.

Schmertmann, J. H. (1970), "Static Cone to Compute Static Settlement Over Sand," Journal of the Soil Mechanics and Foundations Division, ASCE, Vol. 96, No. SM3, May, 1970, pp. 1011-1043.

Silver, M. L. (1969), "The Behavior of Sands Under Seismic Loading Conditions," Dissertation presented to the University of California, Berkeley, in 1969, in partial fulfillment of the requirements for the degree of Doctor of Philosophy.

Skempton, A. W. (1951), "The Bearing Capacity of Clays," Proceedings, Building Research Congress, London, Vol. 1, 1951, pp. 180-189.

Terzaghi, K. (1925), "Principles on Soil Mechanics VII-Friction in Sand and Clay," Engineering News Record, Vol. 95, No. 26, p. 1026.

Terzaghi, K. (1943), "Theoretical Soil Mechanics," Wiley, New York, 1943.

Vermeiden, J. (1948), "Improved Sounding Apparatus as Developed in Holland since 1936," Proceedings, Second International Conference on Soil Mechanics and Foundation Engineering, Vol. 1, 1948, pp. 280-287.

Vesic, A. S. (1963), "Bearing Capacity of Deep Foundations in Sand," Stresses in Soils and Layered Systems, Highway Research Board Record No. 39, 1963, pp. 112-153.

Vesic A. S. (1967), "Ultimate Loads and Settlements of Deep Foundations in Sand," Proceedings, Symposium on Bearing Capacity and Settlement of Foundations, Duke University, 1965, pp. 53-68.

Walker, B. P. and Whitaker, T. (1967), "An Apparatus for Forming Uniform Beds of Sand for Model Foundation Tests," Geotechnique, Vol. 17, pp. 161-167.

Yaroshenko, V. A. (1964), "Interpretation of the Results of Static Penetration of Sands," Fundamenty Proekt., No. 3, 1964.

APPENDIX A

DERIVATION OF FORMULAS FOR BEARING CAPACITY FACTORS

DETERMINATION OF BEARING CAPACITY FACTOR N_c

The failure mechanism and associated free body diagram are given in Fig. A.1. According to solutions of equilibrium equations for a weightless body, the radial shear zone is defined by a logarithmic spiral and any radial plane is a failure plane. Therefore OC is a plane where full mobilization of shear strength takes place, consequently stresses σ_b and τ_b can be represented by point B on Mohr's envelope. Stresses σ_o and τ_o are stresses on plane OD. Stress σ_b can be written in terms of σ_o as follows:

$$\sigma_b = \sigma_o + \frac{\tau_b}{\cos\phi}\,[\sin(2\varepsilon+\phi)-\sin\phi] \tag{A.1}$$

where

$$\tau_b = c+\sigma_b\tan\phi \tag{A.2a}$$

By substituting Equation A.2a into Equation A.1:

$$\sigma_b = \sigma_o + \frac{(c+\sigma_b\tan\phi)}{\cos\phi}\cdot[\sin(2\varepsilon+\phi)-\sin\phi] \tag{A.2b}$$

By rewriting Equation A.2b:

$$\sigma_b = \frac{\cos\phi\ \sigma_o+[\sin(2\varepsilon+\phi)-\sin\phi]c}{[\cos\phi-\tan\phi[\sin(2\varepsilon+\phi)-\sin\phi]]} \tag{A.2c}$$

From equilibrium of the logarithmic spiral bounded by OBC:

$$\Sigma M_o = 0 \tag{A.3a}$$

$$\sigma_b\cdot\frac{r_2^2}{2} - \sigma_c\,\frac{r_1^2}{2} + \int_0^\theta cr^2 d\theta = 0 \tag{A.3b}$$

From the general equation of a logarithmic spiral $\left(r=r\ e^{\theta\tan\phi}\right)$ and by substituting

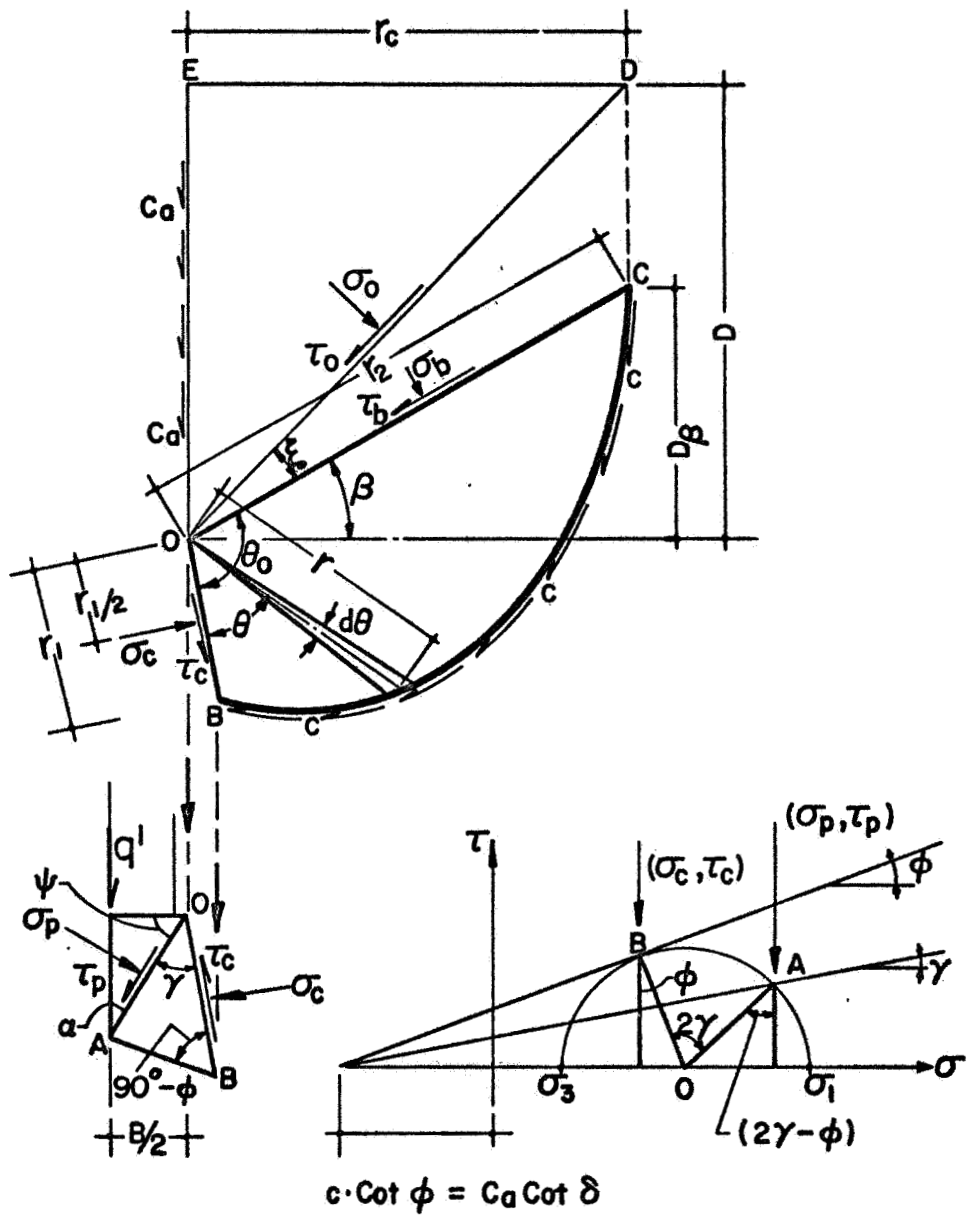

FIG. A.1 FREE BODY DIAGRAM FOR DETERMINATION OF BEARING CAPACITY FACTOR N_c

into Equation A.3b and solving for σ_c, the following relationship can be obtained:

$$\sigma_c = e^{2\theta_o \tan\phi}\ \sigma_b + \frac{c}{\tan\phi}(e^{2\theta_o \tan\phi} - 1) \tag{A.4}$$

Since OB is a slip plane:

$$\tau_c = c + \sigma_c \tan\phi \tag{A.5a}$$

Substituting Equation A.4 into Equation A.5a:

$$\tau_c = (c + \sigma_b \tan\phi)e^{2\theta_o \tan\phi} \tag{A.5b}$$

Substituting the value of σ_b from Equation A.2c into Equations A.4 and A.5b:

$$\tau_c = \frac{[1+\tan\phi(\sin(2\xi+\phi)-\sin\phi)]e^{2\theta_o \tan\phi}\ c+\sin\phi\ e^{2\theta_o \tan\phi}\ \sigma_o}{[\cos\phi-\tan\phi(\sin(2\xi+\phi)-\sin\phi)]} \tag{A.6a}$$

$$\sigma_c = \frac{[\sin(2\xi+\phi)-\sin\phi]\ c + \cos\phi\ \sigma_o}{[\cos\phi-\tan\phi(\sin(2\xi+\phi)-\sin\phi)]}\ e^{2\theta_o \tan\phi}$$

$$+ c\ \cot\phi(e^{2\theta_o \tan\phi} - 1) \tag{A.6b}$$

From Fig. A.1 stresses σ_p and τ_p can be written in terms of σ_c and τ_c as follows:

$$\sigma_p = [\frac{1}{\sin\phi}+\sin(2\gamma-\phi)]\ \frac{\tau_c}{\cos\phi} - \frac{c}{\tan\phi} \tag{A.7a}$$

and

$$\tau_p = \tau_c \cdot \frac{\cos(2\gamma-\phi)}{\cos\phi} \tag{A.7b}$$

By substituting Equation A.6a into Equations A.7a and A.7b the following expressions can be obtained for σ_p and τ_p:

$$\sigma_p = \frac{[1+\sin\phi\ \sin(2\gamma-\phi)]c\ e^{2\theta_o\tan\phi}}{\sin\phi\ \cos\phi} - \frac{c}{\tan\phi}$$

$$+ \frac{[(\sin(2\xi+\phi)-\sin\phi)\ \cos\phi\ c + \sigma_o]\cdot[1+\sin\phi\ \sin(2\gamma-\phi)]e^{2\theta_o\tan\phi}}{\cos^2\phi[\cos\phi-\tan\phi\ (\sin(2\xi+\phi)-\sin\phi)]} \qquad \text{(A.8a)}$$

$$\tau_p = \frac{[(\sin(2\xi+\phi)-\sin\phi)c\cdot\cos\phi+\sigma_o]\ \tan\phi\ \cos(2\gamma-\phi)e^{2\theta_o\tan\phi}}{\cos\phi[\cos\phi-\tan\phi\ (\sin(2\xi+\phi)-\sin\phi)]}$$

$$+ \frac{\cos(2\gamma-\phi)e^{2\theta_o\tan\phi}\ c}{\cos\phi} \qquad \text{(A.8b)}$$

From equilibrium of wedge 00'A:

$$q' = \sigma_p + \tau_p\ \tan\Psi \qquad \text{(A.9)}$$

By substituting values of σ_p and τ_p into Equation A.9 and recalling that N_c is the constant corresponding to cohesion(c), the following relationship is obtained:

$$N_c = \frac{[1+\sin\phi\sin(2\gamma-\phi)]e^{2\theta_o\tan\phi}}{\sin\phi\ \cos\phi} + \frac{\cos(2\gamma-\phi)\cdot\tan\Psi\cdot e^{2\theta_o\tan\phi}}{\cos\phi}$$

$$- \frac{1}{\tan\phi} + \frac{[\sin(2\xi+\phi)-\sin\phi]\ [1+\sin\phi\ \sin(2\gamma-\phi)]e^{2\theta_o\tan\phi}}{\cos^2\phi[\cos\phi-\tan\phi(\sin(2\xi+\phi)-\sin\phi)]}$$

$$+ \frac{\tan\phi\ \tan\Psi\ \cos(2\gamma-\phi)\ [\sin(2\gamma+\phi)-\sin\phi]e^{2\theta_o\tan\phi}}{\cos\phi\cdot[\cos\phi-\tan\phi\ (\sin(2\xi+\phi)-\sin\phi)]} \qquad \text{(A.10)}$$

However, because it is assumed that no shear stress develops on vertical plane CD, angle ξ can be taken equal to zero, and Equation A.10 simplifies to:

$$N_c = \frac{[1+\sin\phi\ \sin(2\gamma-\phi)]\cdot e^{2\theta_o\tan\phi}}{\sin\phi\cdot\cos\phi} - \frac{1}{\tan\phi}$$

$$+ \frac{\cos(2\gamma-\phi)\cdot\tan\Psi\cdot e^{2\theta_o\tan\phi}}{\cos\phi} \qquad \text{(A.11)}$$

DETERMINATION OF BEARING CAPACITY FACTOR $N_{\gamma q}$

The failure mechanism and associated free body diagram is given in Fig. A.2. From static equilibrium of the body OCEFG, the sum of the moments about point 0 must be zero:

$$\Sigma M_o = 0 \tag{A.12a}$$

or

$$F_b \cdot L_b + P_{s1} \cdot L_{s1} = P_{s2} \cdot L_{s2} + P_1 \cdot L_{p1} + P_2 \cdot L_p 2 + W_1 \cdot L_{w1} \tag{A.12b}$$

Note that moments of F forces are zero because they pass through point 0.

Determination of W_1 L_{w1}

Refering to Fig. A.2, the area of logarithmic spiral segment OL_1L_2 is:

$$dA = 1/2\ r^2 d\theta \tag{A.13a}$$

where

$$r = r_1\ e^{\theta \tan\phi} \tag{A.13b}$$

By substitution, the previous two equations yield the following relationships:

$$dA = 1/2\ r_1^2\ e^{2\theta \tan\phi}\ d\theta \tag{A.13c}$$

and

$$dW = 1/2 \cdot \gamma_s \cdot r_1^2\ e^{2\theta \tan\phi} \cdot d\theta \tag{A.13d}$$

The moment around point 0 becomes

$$dM = dW \cdot L_w \tag{A.14a}$$

where

$$L_w = 2/3 \cdot\ r_1 \cdot e^{\theta \tan\phi}\ \cos(\theta_o - \beta - \theta) \tag{A.14b}$$

and by substituting Equation A.14b and Equation A.13d into Equation A.14a:

$$dM = 1/3 \cdot \gamma_s \cdot r_1^3\ e^{3\theta \tan\phi}\ \cos(\theta_o - \beta - \theta)\ d\theta \tag{A.15}$$

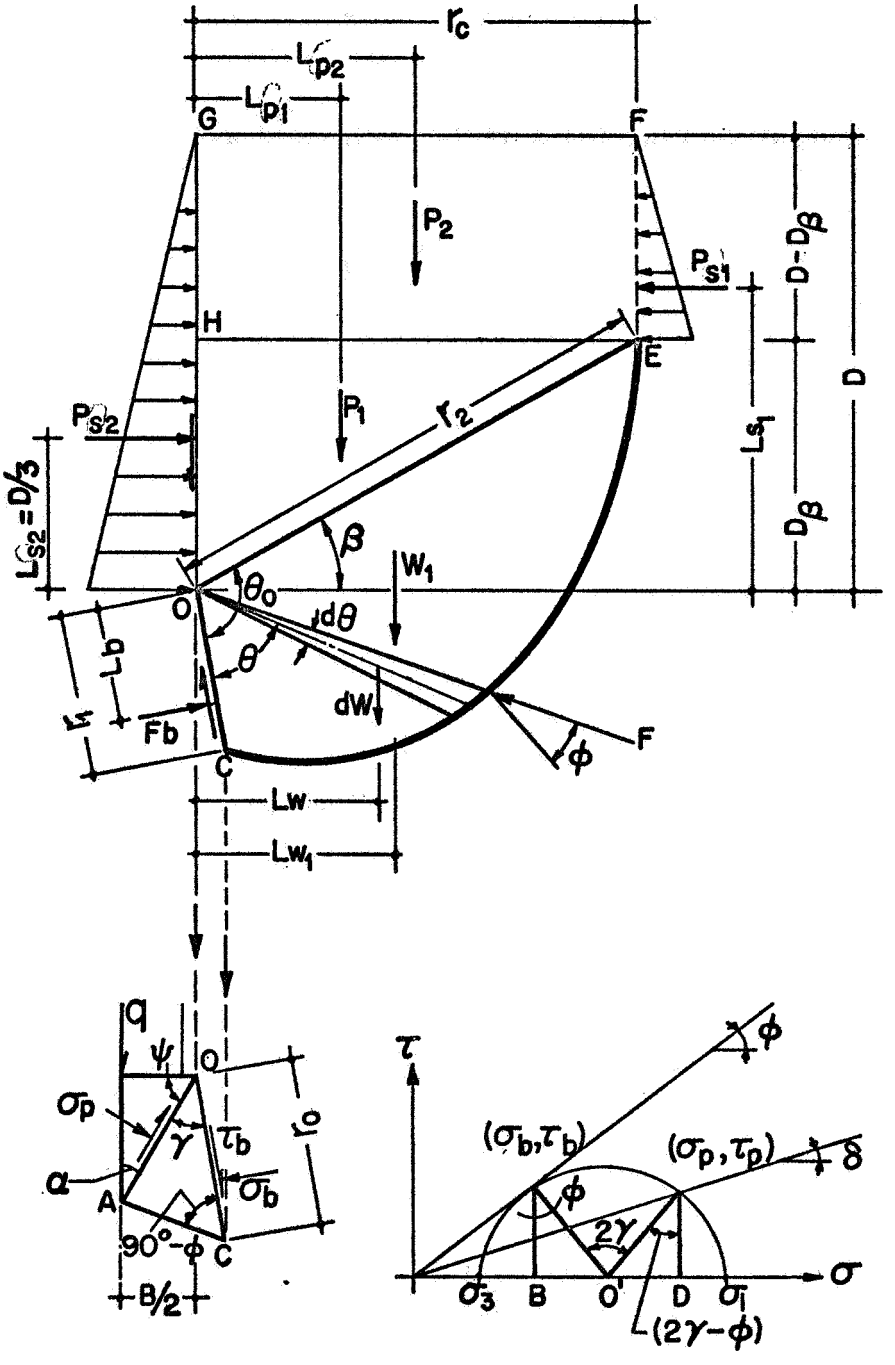

FIG. A.2 FREE BODY DIAGRAM FOR DETERMINATION OF BEARING CAPACITY FACTOR $N_{\gamma q}$

thus,

$$W_1 L_{w1} = \int_0^{\theta_o} dM = 1/3 \cdot \gamma_s \cdot r_1^3 \int_0^{\theta_o} e^{3\theta\tan\phi} \cos(\theta_o - \beta - \theta)\, d\theta \qquad (A.16)$$

If the integral in Equation A.16 is designated as

$$I_\theta = \int_0^{\theta_o} e^{3\theta\tan\phi} \cos(\theta_o - \beta - \theta)\, d\theta \qquad (A.17)$$

then the following relationship is obtained:

$$W_1 L_{w1} = 1/3 \cdot \gamma_s \cdot r_1^3 \cdot I_\theta \qquad (A.18)$$

Determination of I_θ

By partial integration:

$$I_\theta = \frac{1}{3\tan\phi} e^{3\theta\tan\phi} \cos(\theta_o - \beta - \theta) \Big|_o^{\theta_o} - \frac{1}{3\tan\phi} \int_0^{\theta_o} e^{3\theta\tan\phi} \sin(\theta_o - \beta - \theta) d\theta \qquad (A.19a)$$

Similarly the second term may be partially integrated:

$$I_\theta = \frac{1}{3\tan\phi} e^{3\theta\tan\phi} \cos(\theta_o - \beta - \theta) \Big|_0^{\theta_o} - \frac{1}{9\tan^2\phi} e^{3\theta\tan\phi}$$

$$\sin(\theta_o - \beta - \theta) \Big|_0^{\theta_o} - \frac{1}{9\tan^2\phi} \int_0^{\theta_o} e^{3\theta\tan\phi} \cos(\theta_o - \beta - \theta)\, d\theta \qquad (A.19b)$$

It can be seen that the last term in Equation A.19b is the same as I_θ; therefore, the equation may be rewritten as:

$$(1 + \frac{1}{9\tan^2\phi})\ I_\theta = \left\{ \frac{1}{3\tan\phi}\, e^{3\theta\tan\phi}\, \cos(\theta_o - \beta - \theta) - \right.$$

$$\left. \frac{1}{9\tan^2\phi}\, e^{3\theta\tan\phi}\, \sin(\theta_o - \beta - \theta) \right\} \Bigg|_0^{\theta_o} \qquad \text{(A.19c)}$$

Considering the boundary values, the following expression for I_θ is obtained:

$$I_\theta = \frac{1}{1+9\tan^2\phi} \left\{ 3\tan\phi [e^{3\theta_o\tan\phi}\cos\beta - \cos(\theta_o - \beta)] + \right.$$

$$\left. [e^{3\theta_o\tan\phi}\sin\beta + \sin(\theta_o - \beta)] \right\} \qquad \text{(A.20)}$$

Determination of $P_1 L_{p1}$

From Fig. A.2 the following relationships can be written:

$$OE = r_2 = r_1 e^{\theta\tan\phi} \qquad \text{(A.21a)}$$

$$OH = OE\ \sin\beta = r_1 e^{\theta_o\tan\phi}\sin\beta \qquad \text{(A.21b)}$$

$$HE = OE\ \cos\beta = r_1 e^{\theta_o\tan\phi}\cos\beta \qquad \text{(A.21c)}$$

and

$$P_1 = 1/2\gamma_s \cdot OH \cdot HE \qquad \text{(A.22a)}$$

It is readily apparent that

$$P_1 = 1/2\ \gamma_s r_i^2\ \sin\beta\ \cos\beta\ e^{2\theta_o\tan\phi} \qquad \text{(A.22b)}$$

and

$$L_{p1} = HE/3 = 1/3\ r_1 e^{\theta_o \tan\phi} \cos\beta \qquad (A.22c)$$

and thus,

$$P_1 L_{p1} = 1/6\ \gamma_s\ r_1^3\ \sin\beta\ \cos^2\beta\ e^{3\theta_o \tan\phi} \qquad (A.23)$$

Determination of $P_2 L_{p2}$

From Fig. A.2:

$$EF = OG - OH = D - r_1 \sin\beta\ e^{\theta_o \tan\phi} \qquad (A.24a)$$

By introducing, m = D/B, Equation A.24a may be written as

$$EF = mB - r_1 \sin\beta\ e^{\theta_o \tan\phi} \qquad (A.24b)$$

The force P_2 is given by:

$$P_2 = \gamma_s \cdot EF \cdot HE \qquad (A.24c)$$

By substituting Equations A.21c and A.24b into Equation A.24c:

$$P_2 = \gamma_s \cdot r_1 \cos\beta\ e^{\theta_o \tan\phi} (mB - r_1 \sin\beta\ e^{\theta_o \tan\phi}) \qquad (A.24d)$$

From Fig. A.2:

$$L_{p2} = HE/2 = 1/2\ r_1 \cos\beta e^{\theta_o \tan\phi} \qquad (A.24e)$$

From Equations A.24d and A.24e:

$$P_2 L_{p2} = 1/2\ \gamma_s r_1^2 \cos^2\beta e^{\theta_o \tan\phi} (mB - r_1 \sin\beta e^{\theta_o \tan\phi}) \qquad (A.25)$$

Determination of $P_{s1} L_{s1}$

The average value of earth pressure on vertical plane EF is given by:

$$P^*_{s1} = 1/2\ K_o \cdot \gamma_s \cdot (D - D_\beta) \qquad (A.26a)$$

The force P_{s1} may be written as follows:

$$P_{s1} = 1/2\ K_o \cdot \gamma_s \cdot (D - D_\beta)^2 \qquad \text{(A.26b)}$$

The moment arm L_{s1} is given by:

$$L_{s1} = 1/3\ (D + 2D_\beta) \qquad \text{(A.26c)}$$

Combining Equations A.26b and A.26c and making the substitutions $D = mB$ and $D_\beta = m'B$ yields the following expression:

$$P_{s1}L_{s1} = 1/6\ \gamma_s\ B^3\ K_o\ (m - m')^2(m + 2m') \qquad \text{(A.27)}$$

Determination of $P_{s2}L_{s2}$

The average value of earth pressure on the vertical plane OG is given by:

$$P^*_{s2} = 1/2\ K \cdot \gamma_s \cdot D \qquad \text{(A.28a)}$$

The force P_{s2} may be written as:

$$P_{s2} = 1/2\ K \cdot \gamma_s \cdot D \qquad \text{(A.28b)}$$

The moment arm $L_{s2} = D/3$, consequently;

$$P_{s2}L_{s2} = 1/6\ K \cdot \gamma_s \cdot D^3 \qquad \text{(A.28c)}$$

or by substituting $D = mB$:

$$P_{s2}L_{s2} = 1/6\ K\ \gamma_s\ B^3m^3 \qquad \text{(A.29)}$$

It should be noted that the coefficients K_o and K which appear in Equations A.27 and A.29, respectively, are lateral earth pressure coefficients. In computing the $N_{\gamma q}$ values presented later in this appendix, they are assigned the value $K_o = K = 1-\sin\phi$.

Solution of Moment Equation

The moment equation (Equation A.12b) may now be resolved by taking $L_b = \frac{2}{3} r_1$ and by substituting the expressions given in Equations A.18, A.23, A.25, A.27, and A.29:

$$F_b = \frac{1}{2} \gamma_s r_1^2 I_\theta$$

$$+ \frac{1}{4} \gamma_s r_1^2 \sin\beta \cos^2\beta \, e^{\theta_o \tan\phi}$$

$$+ \frac{3}{4} \gamma_s r_1 \cos^2\beta \, e^{2\theta_o \tan\phi} (mB - r_1 \sin\beta \, e^{\theta_o \tan\phi})$$

$$+ \frac{1}{4} K \gamma_s (B^3/r_1) m^3$$

$$- \frac{1}{4} K_o \gamma_s (B^3/r_1) (m-m')^2 (m+2m') \qquad \text{(A.30)}$$

Development of Expression for $N_{\gamma q}$

Because OC is a slip plane, stresses on plane OC can be represented by point A on Mohr's diagram. The plane OA is not a slip plane; however, stresses on this plane can be determined by the intersection of envelope $\tau = \sigma\tan\delta$ and the Mohr's circle at point C. From the geometry of Mohr's circle, the following relationships can be written:

$$OD = \sigma_p = 00' + 0'D \qquad \text{(A.31a)}$$

where $00' = (0'A/\sin\phi)$ and $0'A = (AB/\cos\phi)$, and

$$00' = \frac{AB}{\cos\phi \sin\phi} \qquad \text{(A.31b)}$$

$$0'D = 0'C \sin(2\gamma - \phi) \qquad \text{(A.31c)}$$

where $0'C = 0'A = (AB/\cos\phi)$

and $$0'D = \frac{AB \sin(2\gamma - \phi)}{\cos\phi} \qquad \text{(A.31d)}$$

Recognizing that $AB = \tau_b$, and substituting Equations A.31b and A.31d into Equation A.31a:

$$\sigma_p = \frac{\tau_b}{\cos\phi} \left[\frac{1}{\sin\phi} + \sin(2\gamma - \phi) \right] \qquad \text{(A.32a)}$$

By substituting $\tau_b = \sigma_b \tan\phi$ into Equation A.32a:

$$\sigma_p = \sigma_b \cdot \frac{[1+\sin\phi \sin(2\gamma-\phi)]}{\cos^2\phi} \tag{A.32b}$$

Normal forces on planes OC and OA are given by:

$$F_p = \sigma_p r_o \text{ and } F_b = \sigma_b r_1 \tag{A.33a}$$

or

$$F_p/F_b = (\sigma_p/\sigma_b)(r_o/r_1) \tag{A.33b}$$

Recalling the identity $\sin\alpha = \cos(90°-\alpha)$, the following relationship may be written:

$$r_1 = r_o \frac{\cos(\gamma-\phi)}{\cos\phi} \tag{A.33c}$$

By substituting Equations A.32b and A.33c into Equation A.33b

$$F_p = F_b \frac{1 + \sin\phi \sin(2\gamma-\phi)}{\cos\phi \cos(\gamma-\phi)} \tag{A.34}$$

By substituting F_b from Equation A.30 into Equation A.34, the following relationship is obtained:

$$\begin{aligned} F_p = \left[\frac{1 + \sin\phi \sin(2\gamma-\phi)}{\cos\phi \cos(\gamma-\phi)}\right] \Bigg[& \frac{1}{2} \gamma_s r_1^2 I_\theta \\ & + \frac{1}{4} \gamma_s r_1^2 \sin\beta \cos^2\beta \, e^{3\theta_o \tan\phi} \\ & + \frac{3}{4} \gamma_s r_1 \cos^2\beta \, e^{2\theta_o \tan\phi} (mB - r_1 \sin\beta e^{\theta_o \tan\phi}) \\ & + \frac{1}{4} K \gamma_s (B^3/r_1) m^3 \\ & - \frac{1}{4} K_o \gamma_s (B^3/r_1) (m-m')^2 (m+2m') \Bigg] \end{aligned} \tag{A.35}$$

Denoting the vertical component of F_p as F_{pv} where $F_{pv} = F_p/\cos\delta$ and considering the vertical equilibrium of the force qB/2 exerted downward on the penetrometer and the resisting force, the following relationships are obtained:

$$qB = 2\ F_{pv}\ \cos(\psi-\delta) \tag{A.36a}$$

and

$$qB = 2\ F_{p}\ \frac{\cos(\psi-\delta)}{\cos\delta} \tag{A.36b}$$

Considering the weight (W) of the soil wedge for flat-ended penetrometers, Equation A.36b is modified as follows:

$$q = \frac{2\ F_p}{B}\ \frac{\cos(\psi-\delta)}{\cos\delta} - \frac{W}{B} \tag{A.36c}$$

Also, the following relationship should be applied to the expression for F_p:

$$r_1 = \frac{B\ \cos(\gamma-\phi)}{2\ \cos\psi\ \cos\phi} \tag{A.36d}$$

Then substitution of Equation A.36d into Equation A.35 yields the following:

$$\begin{aligned} F_p = &\left[\frac{1 + \sin\phi\ \sin(2\gamma-\phi)}{\cos\phi\ \cos(\gamma-\phi)}\right] \cdot \\ &\left[\frac{1}{8}\gamma_s B^2\ \frac{\cos^2(\gamma-\phi)}{\cos^2\psi\ \cos^2\phi}\ I_\theta\right. \\ &+ \frac{1}{16}\gamma_s B^2\ \frac{\cos^2(\gamma-\phi)}{\cos^2\psi\ \cos^2\phi}\ \sin\beta\ \cos^2\beta e^{\ 3\theta_o\tan\phi} \\ &+ \frac{3}{8}\gamma_s B\ \frac{\cos(\gamma-\phi)}{\cos\psi\ \cos\phi}\ \cos^2\beta e^{\ 2\theta_o\tan\phi}\left(mB - \frac{B}{2}\right. \\ &\left.\left.\frac{\cos(\gamma-\phi)}{\cos\psi\ \cos\phi}\ \sin\beta\ e^{\ \theta_o\tan\phi}\right)\right. \\ &+ \frac{1}{2} K \gamma_s B^2\ \frac{\cos\psi\ \cos\phi}{\cos(\gamma-\phi)}\ m^3 \\ &\left. - \frac{1}{2} K_o \gamma_s B^2\ \frac{\cos\psi\ \cos\phi}{\cos(\gamma-\phi)}\ (m-m')^2\ \ (m+2m')\right] \end{aligned} \tag{A.36e}$$

Utilizing the relationship

$$m' = \frac{\cos(\gamma-\phi)}{2\ \cos\psi\ \cos\phi}\ \sin\beta\ e^{\theta_o\tan\phi}\ ,$$

Equation A.36e may be further simplified and combined:

$$F_p = \left[\frac{1 + \sin\phi \sin(2\gamma-\phi)}{\cos \cos(\gamma-\phi)}\right] \cdot$$

$$\left[\frac{1}{8}\gamma_s B^2 \frac{\cos^2(\gamma-\phi)}{\cos^2\psi \cos^2\phi} I_\theta\right.$$

$$+ \frac{3}{8}\gamma_s B^2 \frac{\cos(\gamma-\phi)}{\cos\psi \cos\phi} \cos^2\beta \, e^{2\theta_o \tan\phi} (m - \frac{2}{3}m')$$

$$+ \frac{1}{2} K \gamma_s B^2 \frac{\cos\psi \cos\phi}{\cos(\gamma-\phi)} m^3$$

$$\left. - \frac{1}{2} K_o \gamma_s B^2 \frac{\cos\psi \cos\phi}{\cos(\gamma-\phi)} (m-m')^2 (m+2m')\right] \qquad (A.36f)$$

Substituting the expression for F_p given in Equation A.36f into Equation A.36c the following relationship is obtained:

$$q = (\gamma_s B) \cdot \left[\frac{\cos(\psi-\delta)}{\cos\delta}\right] \cdot \left[\frac{1 + \sin\phi \sin(2\gamma-\phi)}{\cos\phi \cos(\gamma-\phi)}\right] \cdot$$

$$\left[\frac{1}{4} \frac{\cos^2(\gamma-\phi)}{\cos^2\psi \cos^2\phi} I_\theta\right.$$

$$+ \frac{3}{4} \frac{\cos(\gamma-\phi)}{\cos\psi \cos\phi} \cos^2\beta \, e^{2\theta_o \tan\phi} (m - \frac{2}{3}m')$$

$$+ K \frac{\cos\psi \cos\phi}{\cos(\gamma-\phi)} m^3$$

$$\left. - K_o \frac{\cos\psi \cos\phi}{\cos(\gamma-\phi)} (m-m')^2 (m+2m')\right]$$

$$- \frac{\gamma_s B \tan\psi}{4} \qquad (A.37)$$

Considering that $q_f = cN_c + \gamma_s B N_{\gamma q}$, the following expression is obtained for the $N_{\gamma q}$ factor:

$$N_{\gamma q} = \left[\frac{\cos(\psi-\delta)}{\cos\delta}\right]\cdot\left[\frac{1+\sin\phi\,\sin(2\gamma-\phi)}{\cos\phi\,\cos(\gamma-\phi)}\right]\cdot$$

$$\left[\frac{1}{4}\frac{\cos^2(\gamma-\phi)}{\cos^2\psi\,\cos^2\phi}\;I_\theta\right.$$

$$+\;\frac{3}{4}\frac{\cos(\gamma-\phi)}{\cos\psi\,\cos\phi}\cos^2\beta\;e^{2\theta_o\tan\phi}\left(m-\frac{2}{3}m'\right)$$

$$+\;K\frac{\cos\psi\,\cos\phi}{\cos(\gamma-\phi)}\,m^3$$

$$\left.-\;K_o\frac{\cos\psi\,\cos\phi}{\cos(\gamma-\phi)}(m-m')^2\,(m+2m')\right]-\frac{\tan\psi}{4} \qquad \text{(A.38)}$$

where I_θ is given by Equation A.20.

CURVES FOR BEARING CAPACITY FACTORS

FOR DIFFERENT VALUES OF ANGLE OF INTERNAL

FRICTION (ϕ), BASE SEMIAPEX ANGLE (α),

BASE ROUGHNESS (δ/ϕ), AND RELATIVE DEPTH OF BASE (D/B)

Note: In computing values of $N_{\gamma q}$, the lateral earth pressure coefficients, K and K_o (see Equation A.38) were assumed as $K=K_o=1-\sin\phi$.

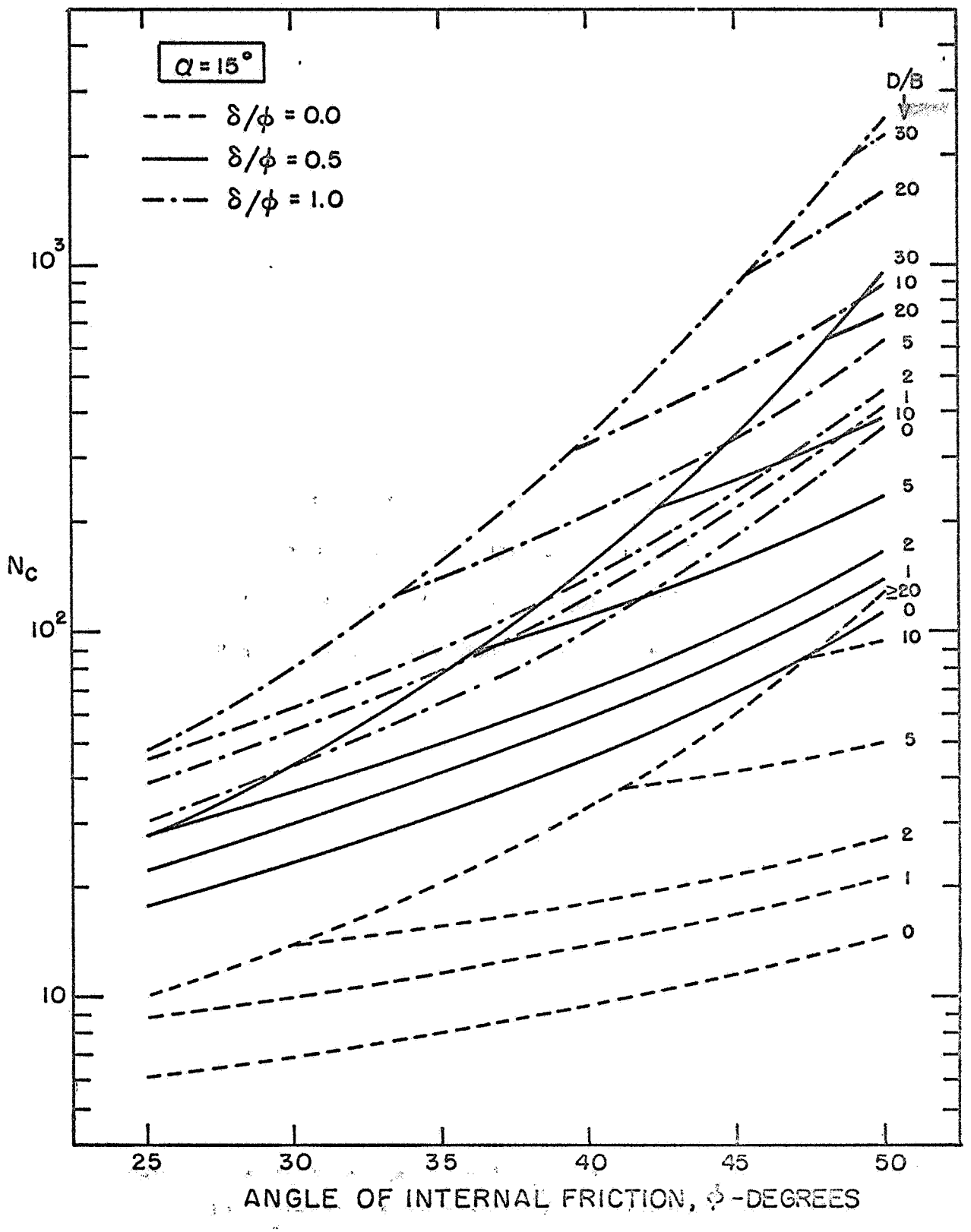

FIG. A.3 BEARING CAPACITY FACTOR N_c FOR WEDGES (GENERAL SHEAR

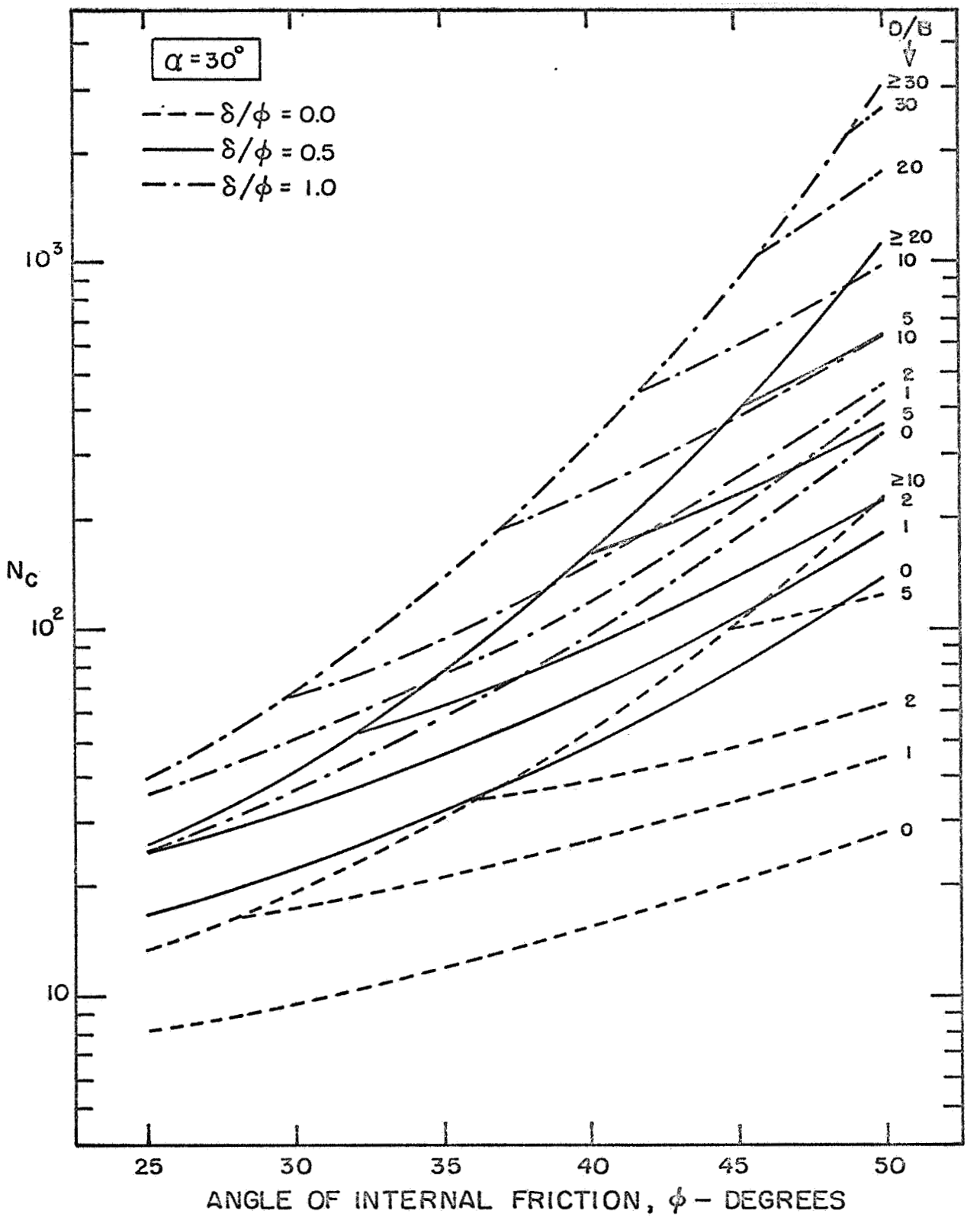

FIG. A.4 BEARING CAPACITY FACTOR N_c FOR WEDGES (GENERAL SHEAR)

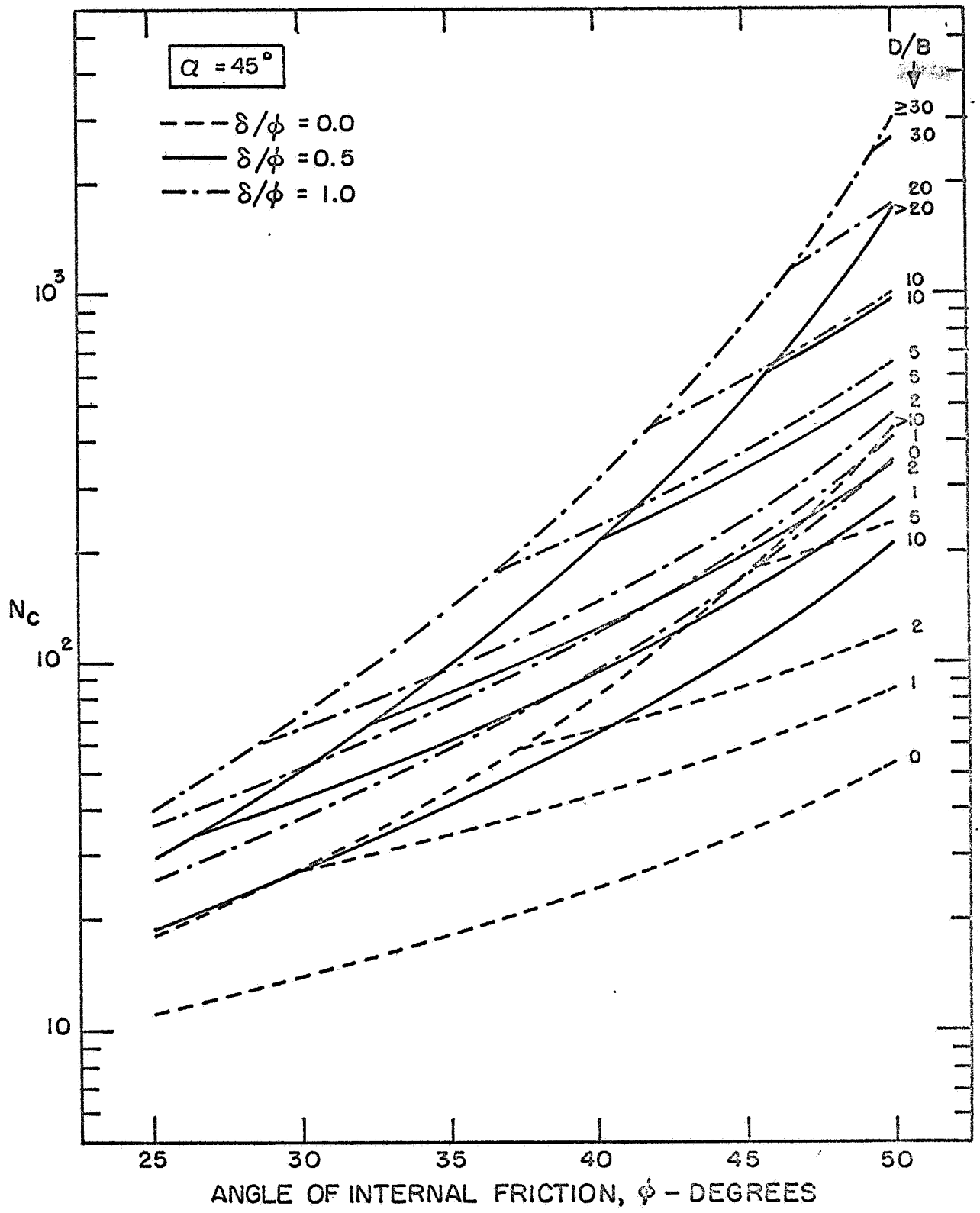

FIG. A.5 BEARING CAPACITY FACTOR N_c FOR WEDGES (GENERAL SHEA

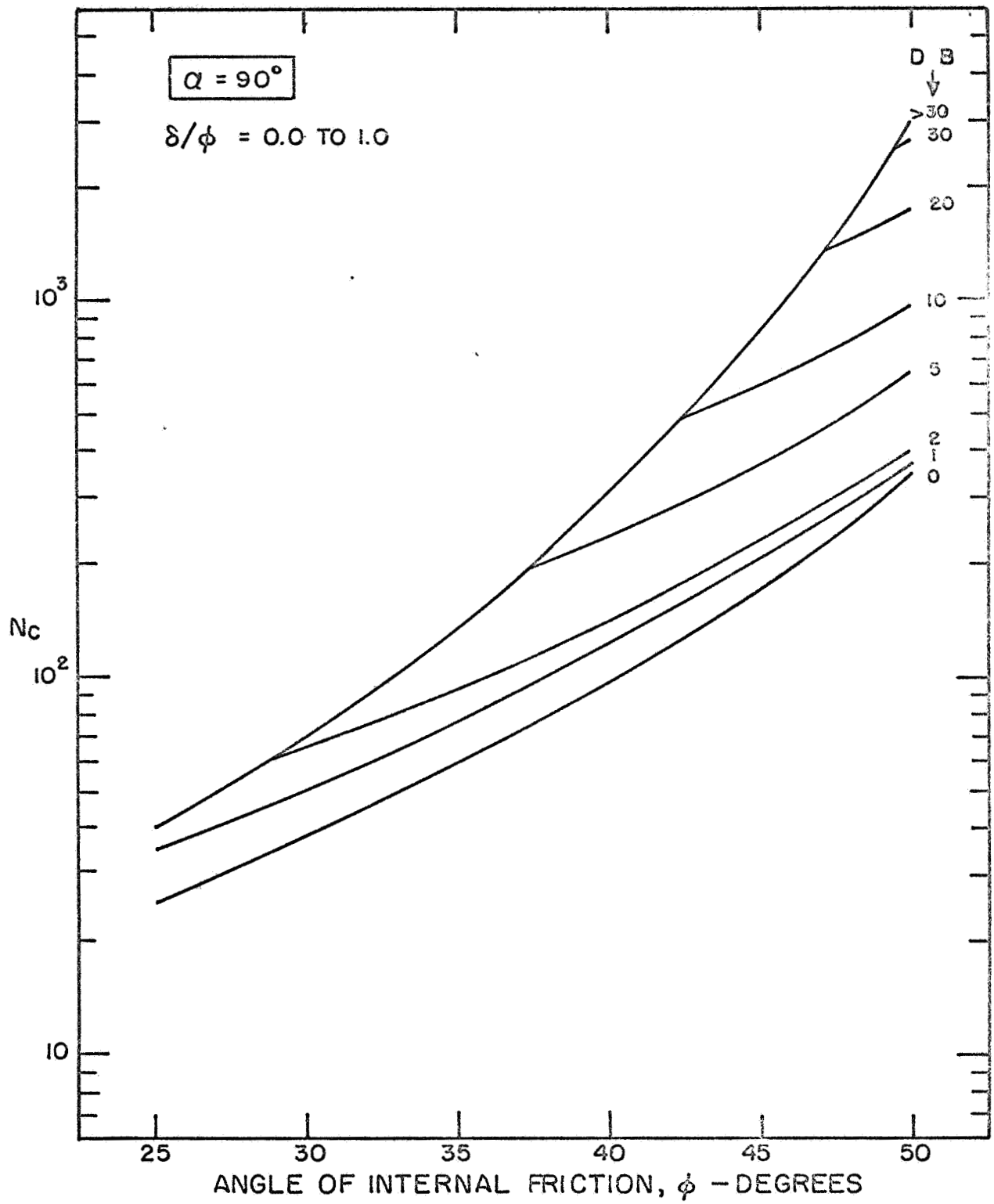

FIG. A.6 BEARING CAPACITY FACTOR N_c FOR WEDGES (GENERAL SHEAR)

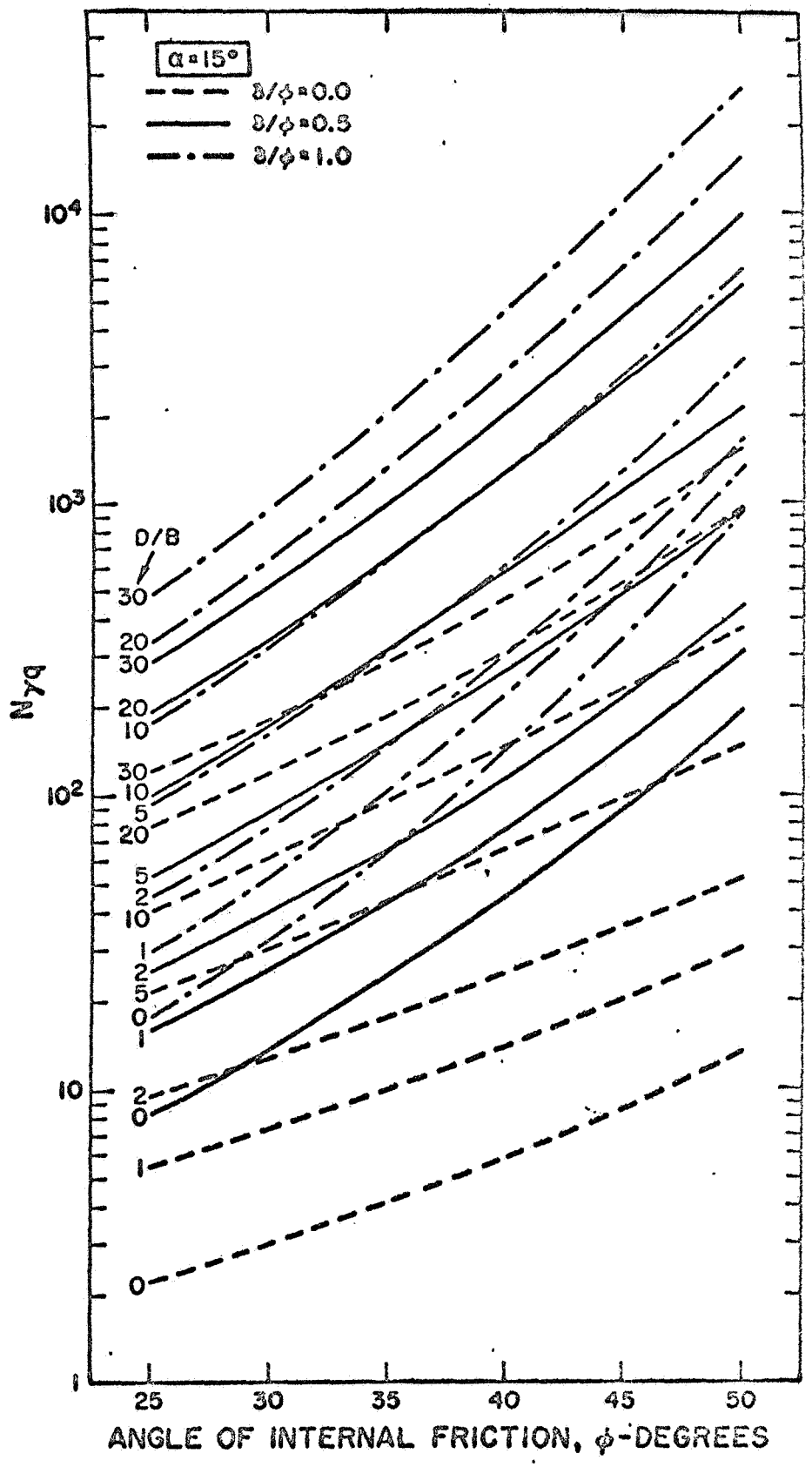

FIG. A.7 BEARING CAPACITY FACTOR $N_{\gamma q}$ FOR WEDGES (GENERAL SHEAR)

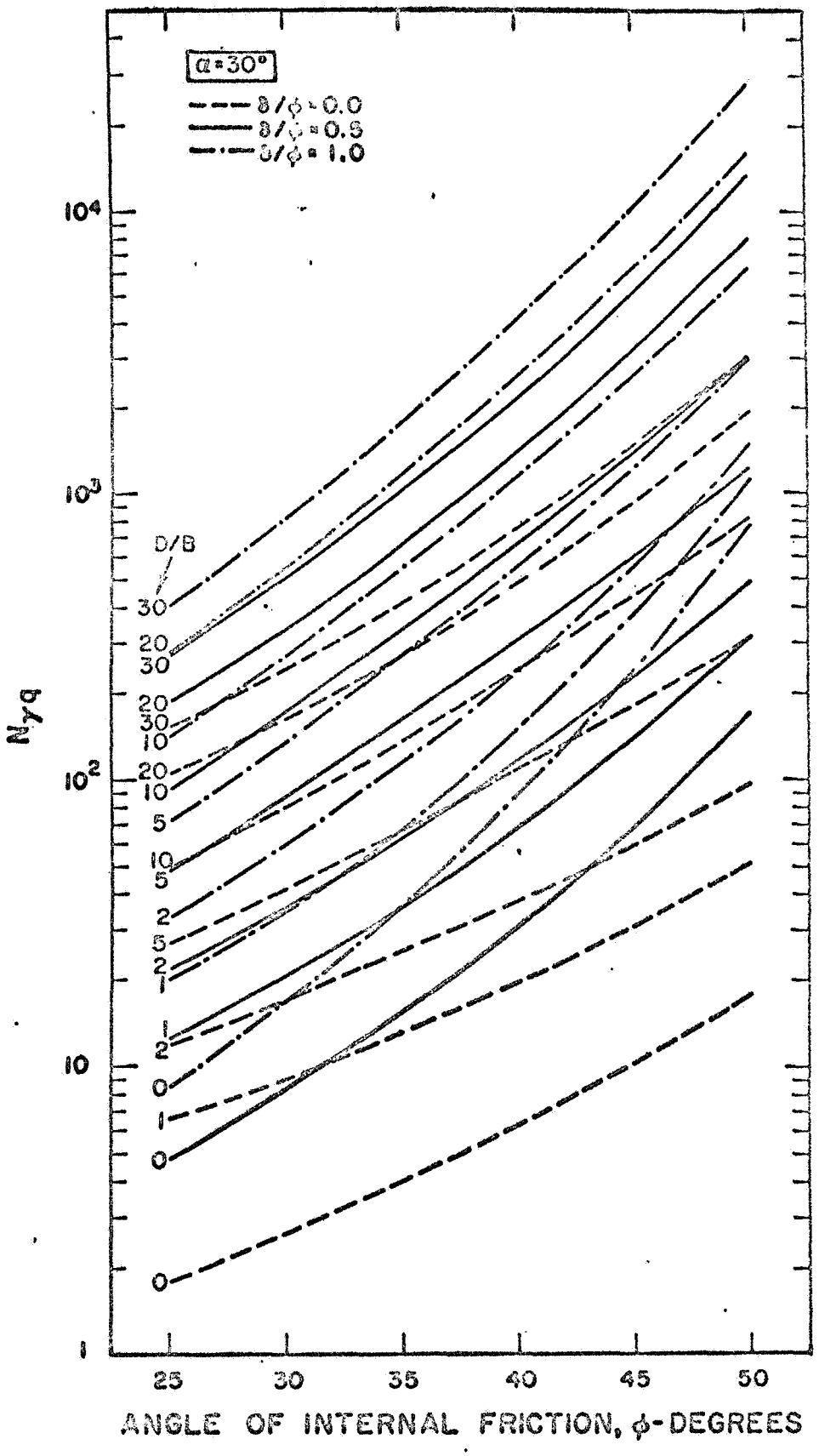

FIG. A.8 BEARING CAPACITY FACTOR $N_{\gamma q}$ FOR WEDGES (GENERAL SHEAR)

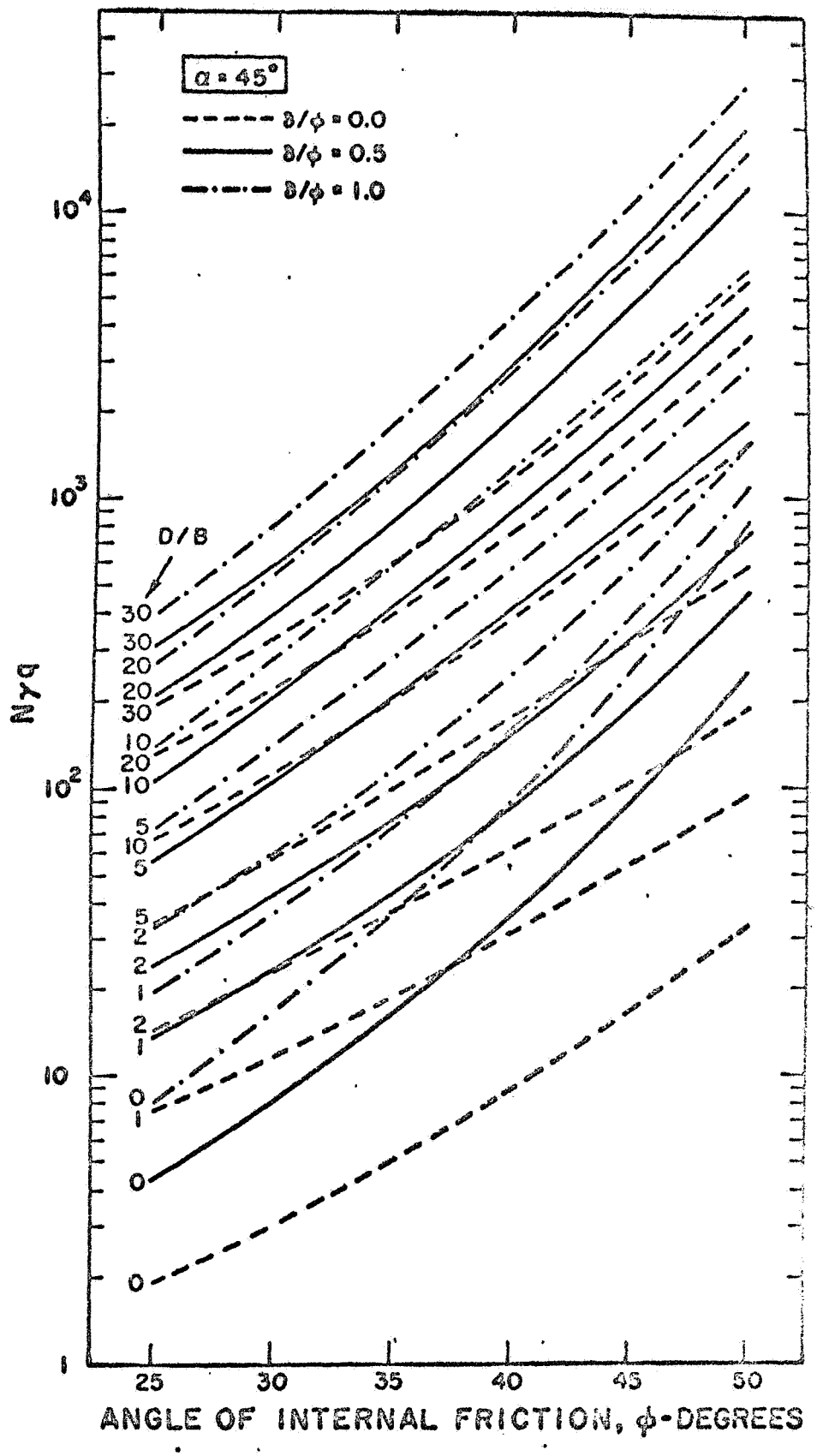

FIG. A.9 BEARING CAPACITY FACTOR $N_{\gamma q}$ FOR WEDGES (GENERAL SHEAR)

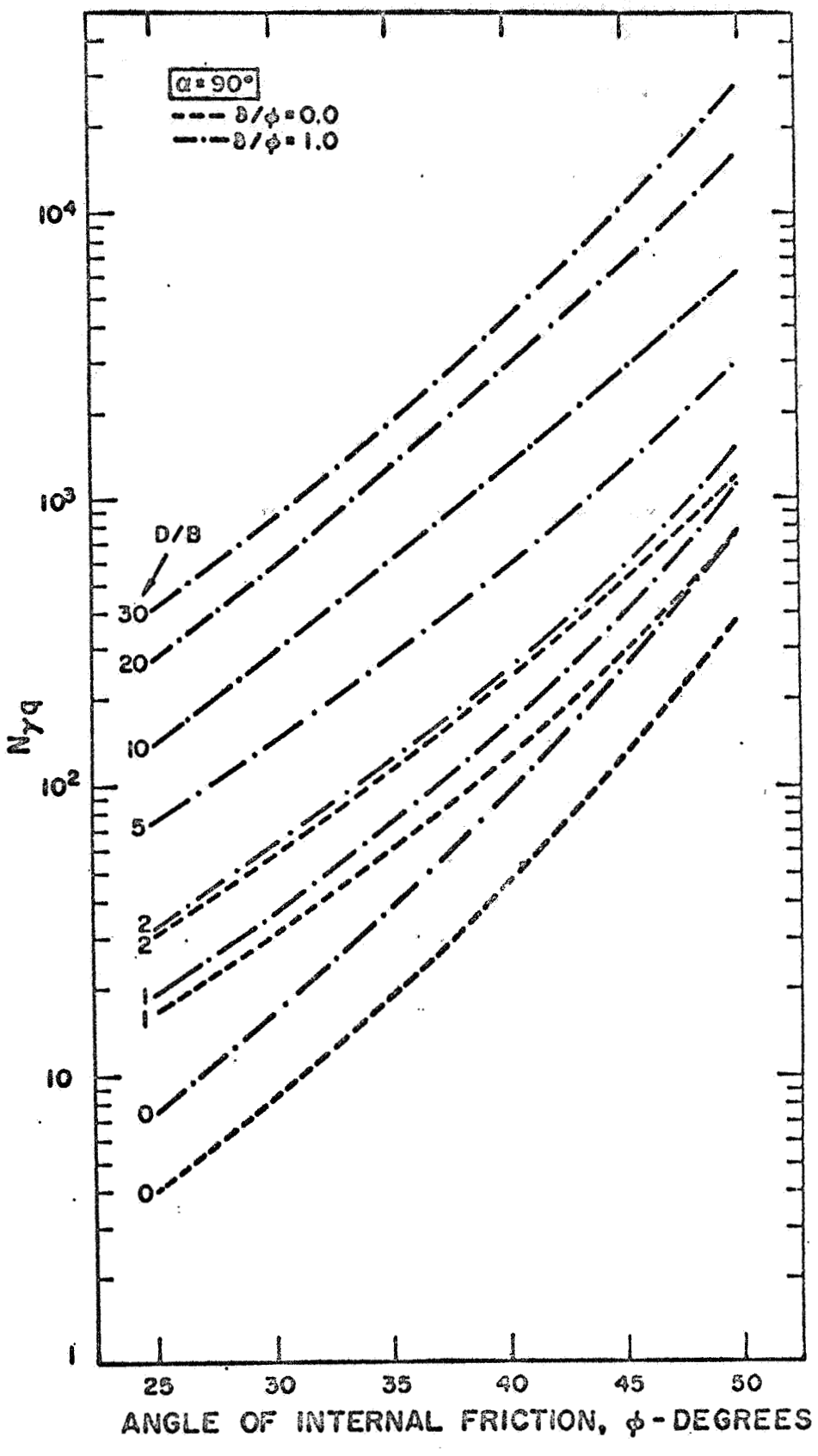

FIG. A.10 BEARING CAPACITY FACTOR $N_{\gamma q}$ FOR WEDGES (GENERAL SHEAR)

A COMPUTER PROGRAM FOR THE DETERMINATION OF BEARING BEARING CAPACITY FACTORS OF WEDGES AND CONES

The following computer program which consists of a main program (NC or NGQ) and one subroutine (ANG) was written for the determination of bearing capacity factors N_c and $N_{\gamma q}$ of wedges and cones.

Subroutine ANG calculates angle γ (the topmost angle of the plane shear zone) from Equation 3.27. Programs NC and NGQ calculate bearing capacity factors N_c and $N_{\gamma q}$ from Equations 4.5 and 4.9 respectively. Angle β is calculated in the main program and Equations 4.26 and 4.32 were used for the shape factors in the calculation of cone bearing capacity factors.

Data Input

Control Card (I 10)

Columns 1-10 Number of factors to be determined (N)

Note: Each set of α, δ/ϕ and D/B corresponds to a single bearing capacity factor to be determined.

Penetrometer Property Card (3 F10.0)

Columns 1-10 Semi-apex angle of penetrometer (α-ALFA)

Columns 11-20 Roughness of penetrometer (δ/ϕ-FAS)

Columns 21-30 Relative depth of penetrometer (D/B-DPT)

N number of cards are required

Notes: (1) Bearing capacity factors for both wedges and cones are calculated for $20° < \phi < 50°$ with increments of 5°.

(2) Separate Input Data should be prepared for program NC and program NGQ.

LISTING OF THE COMPUTER PROGRAM FOR THE DETERMINATION OF BEARING CAPACITY FACTORS OF WEDGES AND CONES

```
      PROGRAM NC (INPUT,OUTPUT)
C     PROGRAM CONE RESISTANCE NC FACTORS
C         N= NUMBER OF DATA SETS
C      ALFA= HALF APEX ANGLE
C       FAS= ROUGHNESS
C       DPT= DEPTH TO DIAMETER RATIO
C        FI= ANGLE OF INTERNAL FRICTION
C      ATAR= SHAPE FACTOR
C     DELTA= PENETROMETER TO SOIL FRICTION ANGLE
      READ 1 , N
    1 FORMAT(I10)
C***** READ AND PRINT WEDGE ANGLE, ROUGHNESS, REL. DEPTH ************
      DO 30  K=1,N
      READ 10,ALFA,FAS,DPT
   10 FORMAT(3F10.0)
      PRINT 21,ALFA,FAS,DPT
   21 FORMAT(1H1,4X,5HALFA=,F10.2,//
     1           5X,10HROUGHNESS=,F5.2,//
     2           5X,10HREL.DEPTH=,F5.2,//)
      ALFAR=ALFA/57.28
      FI=20.
      PRINT 24
   24 FORMAT(//,10X,2HFI,15X,3HPSI,1 X,4HGAMA,14X,4HTETA,9X,5HDELTA,5X,
     1HWEDGE FACTORS,5X,12HCONE FACTORS,/)
      DO 25  J=1,10
      FIR=FI/57.28
      ATAR=1.0+0.2+(TAN(FIR)**6)
C*****CALCULATION OF ANGLE GAMA*************************************
      CALL ANG(FI,FAS,GAMA)
      V6=SIN(FIR)/COS(FIR)
      DELTA= FAS*FI
      DELTAR=DELTA/57.28
      IF (FAS-1.0)   33,32,33
   32 FIS=45.-FI/2.
      IF (ALFA-FIS)  15,15,16
   16 PSI=FIS+FI
      GO TO 17
   15 CONTINUE
   33 PSI=90.-ALFA
   17 PSIR=PSI/57.28
C**** CALCULATE BETA BY ITERATION  ***********************************
      BETA=1.*FI
      BETAR=BETA/57.28
      GAMAR=GAMA/57.28
      TETA= 180.-PSI+BETA-GAMA
      TETAR=TETA/57.28
      DEDPT=0.5*(COS(GAMAR-FIR))*(SIN(BETAR))*EXP((TETAR*SIN(FIR))/
     1COS(FIR))/(COS(FIR)*COS(PSIR))
      PRINT 44,DEDPT
   44 FORMAT (/,5X,4HDC.=,F10.2,/)
      IF (DEDPT-DPT)  11,11,12
   12 ETA=180.-PSI-GAMA
      SOTA=0.
      ETAR= ETA/57.28
      T1=2.*DPT*COS(FIR)*COS(PSIR)/(COS(GAMAR-FIR)*(EXP(ETAR*V6)))
      BOR=ATAN(T1)
      BO= BOR*57.28
```

```
      IF(BO-FI)  310,310,311
  311  BO=FI
  310 CONTINUE
      DO 101  I=1,20
      T2=2.*DPT*COS(FIR)*COS(PSIR)/(COS(GAMAR-FIR)*(EXP(((180.-PSI
     1-GAMA+BO)/57.28)*V6)))
      T3=T2/(SQRT(1.-T2**2))
      BNR=ATAN(T3)
      BN=BNR*57.28
      IF(ABS(BN-BO)-0.1)  501,501,502
  501 GO TO 102
  502 BO=(BN+BO)/2.
  101 CONTINUE
  102 BETA= BN
      BETAR= BETA/57.28
      PRINT 668,I
  668 FORMAT(4X,10HITERATION=,I2,/)
      PRINT 669, BETA
  669 FORMAT(4X,5HBETA=,F7.1,/)
C**** CALCULATE WEDGE AND CONE FACTORS ***********************************
      TETA= 180.-PSI+BETA-GAMA
      TETAR= TETA/57.28
      GO TO 70
   11 CONTINUE
      B1=(2.*COS(FIR)*COS(PSIR)*DPT)/(COS(GAMAR-FIR)*COS(BETAR)*EXP(TE
     1R*V6))
      QSIR=ATAN(B1)
      QSI=QSIR*57.28
      SOTA=0.
   70 SOTAR=SOTA/57.28
      C1=SIN(FIR)
      C2=COS(FIR)
      C3=SIN(2.*GAMAR-FIR)
      C4=EXP(2.*TETAR*V6)
      C5=SIN(2.*SOTAR+FIR)
      C6=COS(2.*GAMAR-FIR)
      C7=SIN(PSIR)/COS(PSIR)
      C8=((1.+C1*C3)/(C1*C2))*C4+(((C5-C1)*(1.+C1*C2))/((C2**2)*(C2-V6*
     1(C5-C1))))*C4-1./V6+(C6*C7*C4)/C2
      C9=(V6*C7*C6*(C5-C1)*C4)/(C2*(C2-V6*(C5-C1)))
      ENC=C8+C9
      ENCO=ATAR*ENC
      PRINT 26,FI,PSI,GAMA,TETA,DELTA,ENC,ENCO
   26 FORMAT(4X,F10.1,7X,F10.1,3X,F10.1,9X,F10.1,3X,F10.2,6X,F10.1,9X,F
     110.1)
   71 FI=FI+5.
   25 CONTINUE
   30 CONTINUE
      END
```

```
      SUBROUTINE ANG(FI,FAS,QNEW)
C     CALCULATION OF GAMA ANGLE
      DELTA=FAS*FI
      DELTAR=DELTA/57.28
      IF(FAS.EQ.1.) GO TO 2
      IF(FAS.EQ.0.) GO TO 3
      QSI=(1.-FAS)*(45.+FI/2.)
      QSIR=QSI/57.28
      FIR=FI/57.28
      VALO=(SIN(DELTAR)/COS(DELTAR))*(1.+SIN(FIR)*SIN(2.*QSIR-FIR))
     1-SIN(FIR)*COS(2.*QSIR-FIR)
      DO 81  K=1,150
      QSI=QSI+0.1
      QSIR=QSI/57.28
      VALN=(SIN(DELTAR)/COS(DELTAR))*(1.+SIN(FIR)*SIN(2.*QSIR-FIR))
     1-SIN(FIR)*COS(2.*QSIR-FIR)
      VAL=VALN*VALO
      IF (VAL)  12,13,11
   11 VALO=VALN
   81 CONTINUE
   13 QNEW=QSI
      GO TO 4
   12 DQSI=(VALN/(VALN-VALO))*0.1
      QNEW=QSI-DQSI
      GO TO 4
    3 QNEW=45.+FI/2.
      GO TO 4
    2 QNEW=0.
    4 CONTINUE
      RETURN
      END
```

```
      PROGRAM NGO (INPUT,OUTPUT)
C     CONE AND WEDGE RESISTANCE NGO FACTORS
C         N= NUMBER OF DATA SETS
C      ALFA= HALF APEX ANGLE
C       FAS= ROUGHNESS
C       DPT= DEPTH TO DIAMETER RATIO
C        FI= ANGLE OF INTERNAL FRICTION
C      ALEM= SHAPE FACTOR
C     DELTA= PENETROMETER TO SOIL FRICTION ANGLE
      READ 1 , N
    1 FORMAT(I10)
C***** READ AND PRINT WEDGE ANGLE, ROUGHNESS, REL. DEPTH **************
      DO 30  K=1,N
      READ 10, ALFA,FAS,DPT
   10 FORMAT(3F10.0)
      PRINT 21, ALFA,FAS,DPT
   21 FORMAT(1H1,4X,5HALFA=,F10.2,//
     1           5X,10HROUGHNESS=,F5.2,//
     2           5X,10HREL.DEPTH=,F5.2,//)
      ALFAR=ALFA/57.28
      PRINT 24
   24 FORMAT(/,10X,2HFI,15X,3HPSI,1 X,4HGAMA,14X,4HBETA,9X,5HDELTA,5X,1
     1HWEDGE FACTORS,5X,12HCONE FACTORS,/)
      FI=20.
      DO 25  J=1,7
      FIR=FI/57.28
      ALEM=0.6+(1.5/(1./DPT+(1.5/( .6+(TAN(FIR)**6)))))
C*****CALCULATION OF ANGLE GAMA**************************************
      CALL ANG(FI,FAS,GAMA)
      V6=SIN(FIR)/COS(FIR)
      DELTA= FAS*FI
      DELTAR=DELTA/57.28
      IF (FAS-1.0)   33,32,33
   32 FIS=45.-FI/2.
      IF (ALFA-FIS)  15,15,16
   16 PSI=FIS+FI
      GO TO 17
   15 CONTINUE
   33 PSI=90.-ALFA
   17 PSIR=PSI/57.28
C*****CALCULATION OF ANGLE BETA BY ITERATION**************************
      BETA=FI
      BETAR=BETA/57.28
      GAMAR=GAMA/57.28
      TETA= 180.-PSI+BETA-GAMA
      TETAR=TETA/57.28
      DEDPT=(0.5*COS(GAMAR-FIR)*SIN(BETAR)*EXP(TETAR*V6))/(COS(FIR)*COS
     1(PSIR))
      PRINT 44,DEDPT
   44 FORMAT (/,5X,4HDC/=,F10.2,/)
      IF(DEDPT-DPT) 11,11,12
   12 DEDPT=DPT
      ETA=180.-PSI-GAMA
      ETAR= ETA/57.28
      T1=(2.*DPT*COS(FIR)*COS(PSIR))/(COS(GAMAR-FIR)*(EXP(ETAR*V6)))
      BOR=ATAN(T1)
      BO= BOR*57.28
```

```
      IF (BO-FI)    310,310,311
  311  BO=FI
  310 CONTINUE
      DO 101   I=1,20
      T2=(2.*DPT*COS(FIR)*COS(PSIR))/(COS(GAMAR-FIR)*(EXP(((180.-PSI-G
     1A+BO)/57.28)*V6)))
      T3=T2/(SQRT(1.-T2**2))
      BNR=ATAN(T3)
      BN=BNR*57.28
      IF(ABS(BN-BO)-0.1)     501,501,502
  501 GO TO 102
  502 BO=(BN+BO)/2.
  101 CONTINUE
  102 BETA= BN
      BETAR= BETA/57.28
      PRINT 668, I
  668 FORMAT(4X,10HITERATION=,I2,/)
      PRINT 669, BETA
  669 FORMAT(4X,5HBETA=,F7.1,/)
      TETA=180.-PSI-GAMA+BETA
      TETAR= TETA/57.28
   11 CONTINUE
      RADIS=DEDPT/TAN(BETAR)
      PRINT 45,RADIS
   45 FORMAT(/,6X,4HRD.=,F10.2,/)
C*****CALCULATION OF NGQ FACTORS**********************************
      WEIGH=SIN(PSIR)/(4.*COS(PSIR))
      IF   (ALFA-90.)     13,14,13
   13 WEIGH=0.
   14 CONTINUE
      V1=EXP(3.*TETAR*V6)
      V2=V1*COS(BETAR)-COS(TETAR-BETAR)
      V3=V1*SIN(BETAR)+SIN(TETAR-BETAR)
      V4=3.*V6*V2+V3
      V5=V4/(1.+9.*(V6**2))
      U1=COS(GAMAR-FIR)
      U2=COS(FIR)
      U3=COS(PSIR)
      U4=COS(BETAR)
      U5=(1./4.)*(U1**2)*V5/((U3**2)*(U2**2))
      U7=EXP(2.*TETAR*V6)
      U8=U1*(U4**2)/(U3*U2)
      U9=(3./4.)*U8*U7*(DPT-(2./3.)*DEDPT)
      D6=1.-SIN(FIR)
      D2=((D6*U3*U2)/(U1))*((DPT-DEDPT)**2)*(DPT+2.*DEDPT)
      D4=((D6*U3*U2)*(DPT**3))/U1
      P1=(U5+U9-D2+D4)*(COS(PSIR-DELTAR)/COS(DELTAR))
      P2=((1.+SIN(FIR)*SIN(2.*GAMAR-FIR))/(U2*U1))*P1
      ENGAQ=P2-WEIGH
      ENGAC=ALEM*ENGAQ
      PRINT 26,FI,PSI,GAMA,TETA,DELTA,ENGAQ,ENGAC
   26 FORMAT(4X,F10.1,7X,F10.1,3X,F10.1,9X,F10.1,3X,F10.2,6X,F10.1,9X,
     1F10.1)
      FI=FI+5.0
   25 CONTINUE
   30 CONTINUE
      END
```

```
      SUBROUTINE ANG(FI,FAS,QNEW)
C     CALCULATION OF GAMA ANGLE
      DELTA=FAS*FI
      DELTAR=DELTA/57.29
      IF(FAS.EQ.1.) GO TO 2
      IF(FAS.EQ.0.) GO TO 3
      QSI=(1.-FAS)*(45.+FI/2.)
      QSIR=QSI/57.28
      FIR=FI/57.28
      VALO=(SIN(DELTAR)/COS(DELTAR))*(1.+SIN(FIR)*SIN(2.*QSIR-FIR))
     1-SIN(FIR)*COS(2.*QSIR-FIR)
      DO 81  K=1,150
      QSI=QSI+0.1
      QSIR=QSI/57.28
      VALN=(SIN(DELTAR)/COS(DELTAR))*(1.+SIN(FIR)*SIN(2.*QSIR-FIR))
     1-SIN(FIR)*COS(2.*QSIR-FIR)
      VAL=VALN*VALO
      IF (VAL)  12,13,11
   11 VALO=VALN
   81 CONTINUE
   13 QNEW=QSI
      GO TO 4
   12 DQSI=(VALN/(VALN-VALO))*0.1
      QNEW=QSI-DQSI
      GO TO 4
    3 QNEW=45.+FI/2.
      GO TO 4
    2 QNEW=0.
    4 CONTINUE
      RETURN
      END
```

APPENDIX B

SPREADER BOX CALIBRATION

Pluvial compaction, the deposition of air-dry sand by allowing it to fall as a rain to build up a bed, was used to produce a large range of densities. Sand was stored in 55 gallon (~0.22m^3) drums between tests. Prior to deposition, the frame travel micro-switches were adjusted and the spreader box was filled with sand using a barrel turner attached to a fork lift truck. Motion of the frame was iniated one foot from where the roller started to eject sand to ensure that the frame reached its required speed and that transient vibrations had died out. A second micro-switch started the deposition which continued until a third switch was contacted stopping the rain of sand. A fourth micro-switch reversed the direction of travel allowing the frame to move back and forth spreading out about a 1.0 in. (25.4 mm) thick sand layer. The spreader box was intermittently elevated to maintain a constant height drop. The procedure was repeated until the required sample height was attained.

In order to determine the uniformity of the sand layer deposited by the spreader box, the sand density at various locations in the layer was measured by weighing the quantity of sand deposited into volume calibrated cylinders. Cylinders of 3.0 in. (76.2 mm) diameter and 3.0 in. (76.2 mm) height were used as recommended by Kolbuzewski (1948). In several tests, cylinders were placed along the transverse and longitudinal direction of the box motion. Figs. B.1 and B.2 show the variation of sand density along these directions of the box. In several tests, cylinders were placed at different elevations to check if there was any density change due to additional sand deposition. It was found that the variation in density was negligible, even for loose sand deposits. The overall average density was determined by weighing the quantity of sand deposited into the test box.

The density of sand deposited using the spreader box is related to roller speed for a given gap width and height of fall so that once calibrated, it is possible to reproduce any required density by properly adjusting the roller speed. The calibration curve obtained for Monterey Sand No. 0 is shown in Fig. 8.3. It may be seen from Fig. B.3 that obtainable relative density range is quite large, 34 to 100 percent.

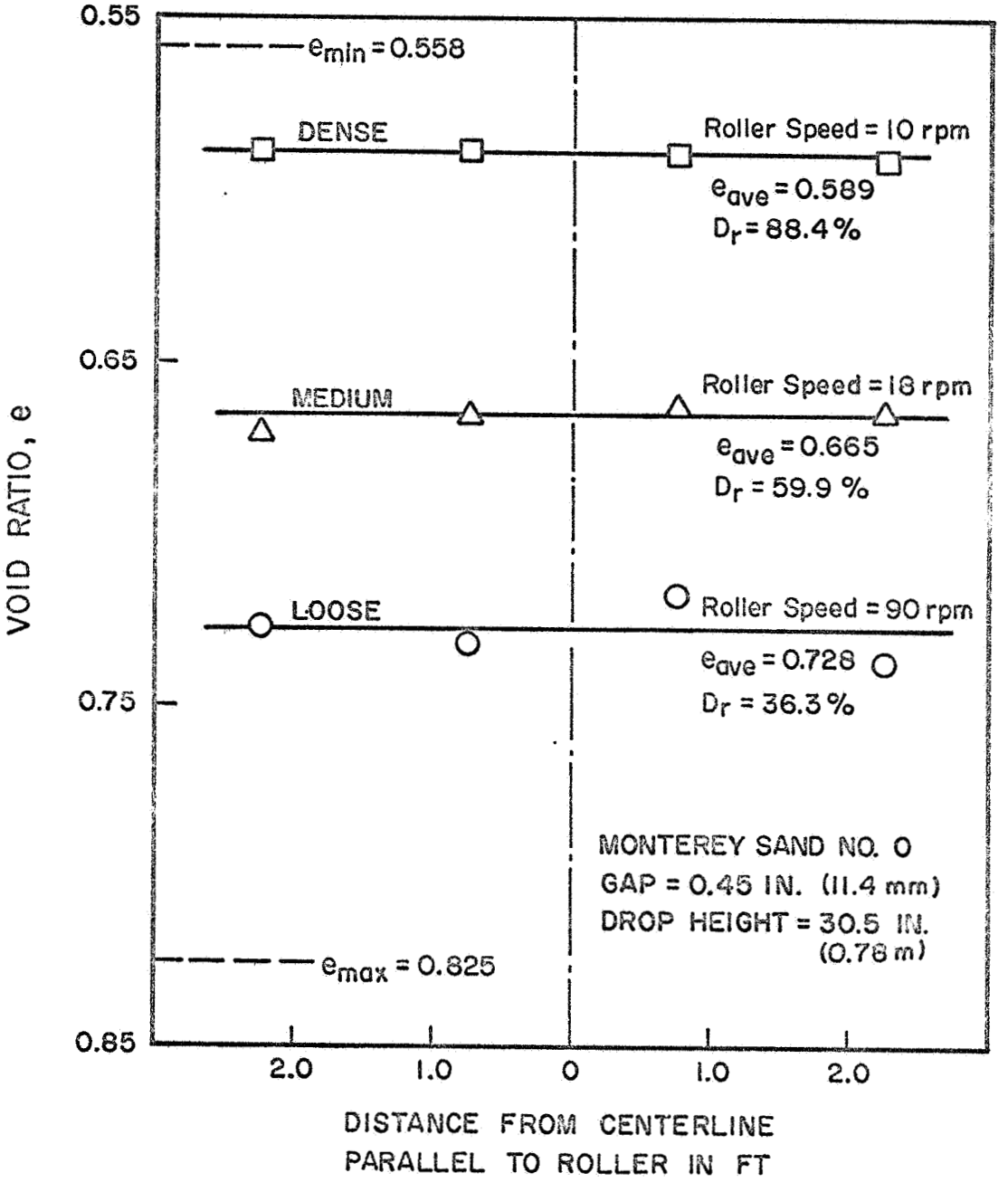

FIG. B.1 DENSITY VARIATION IN THE BOX PARALLEL TO ROLLER

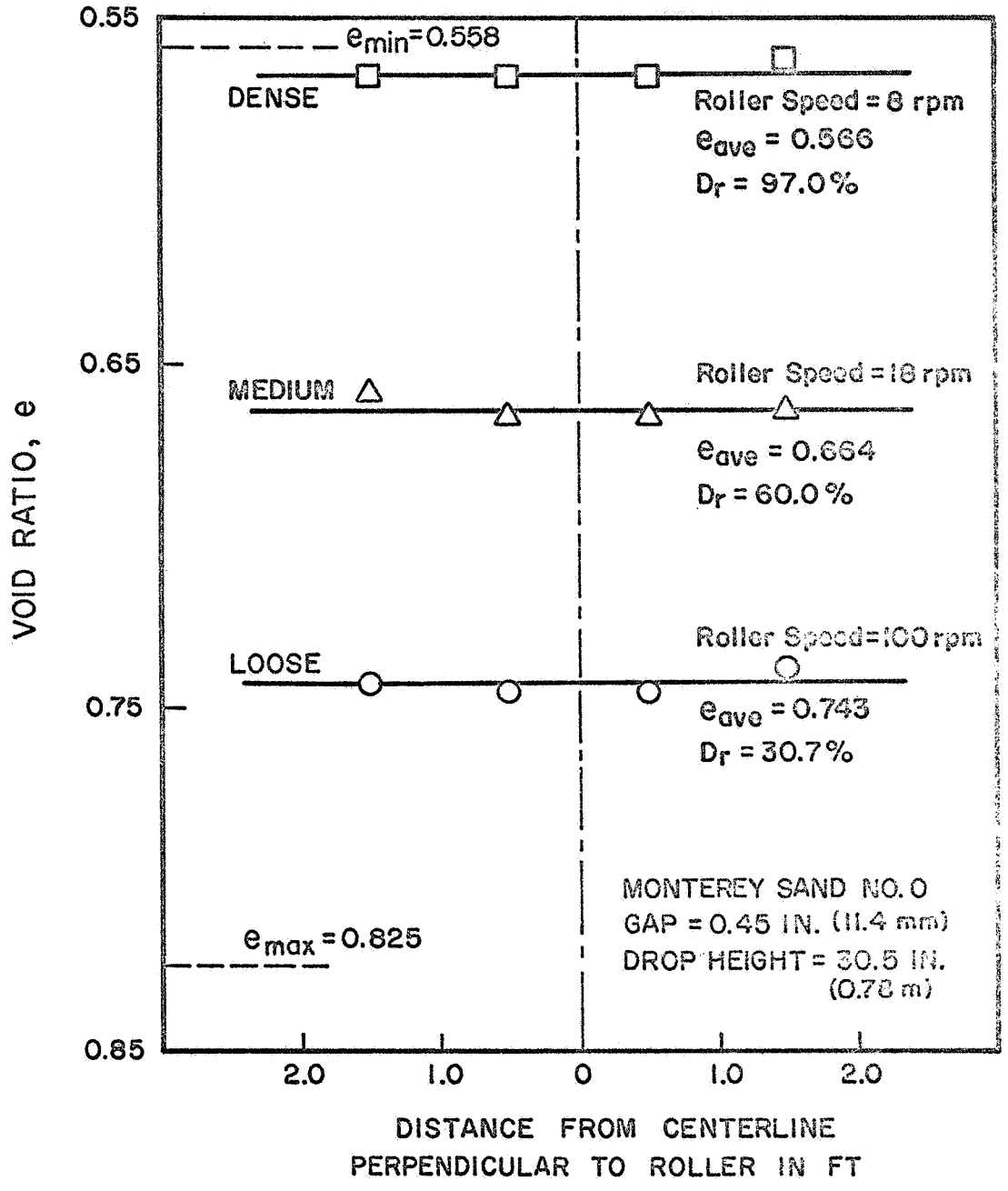

FIG. B.2 DENSITY VARIATION IN THE BOX PERPENDICULAR TO ROLLER

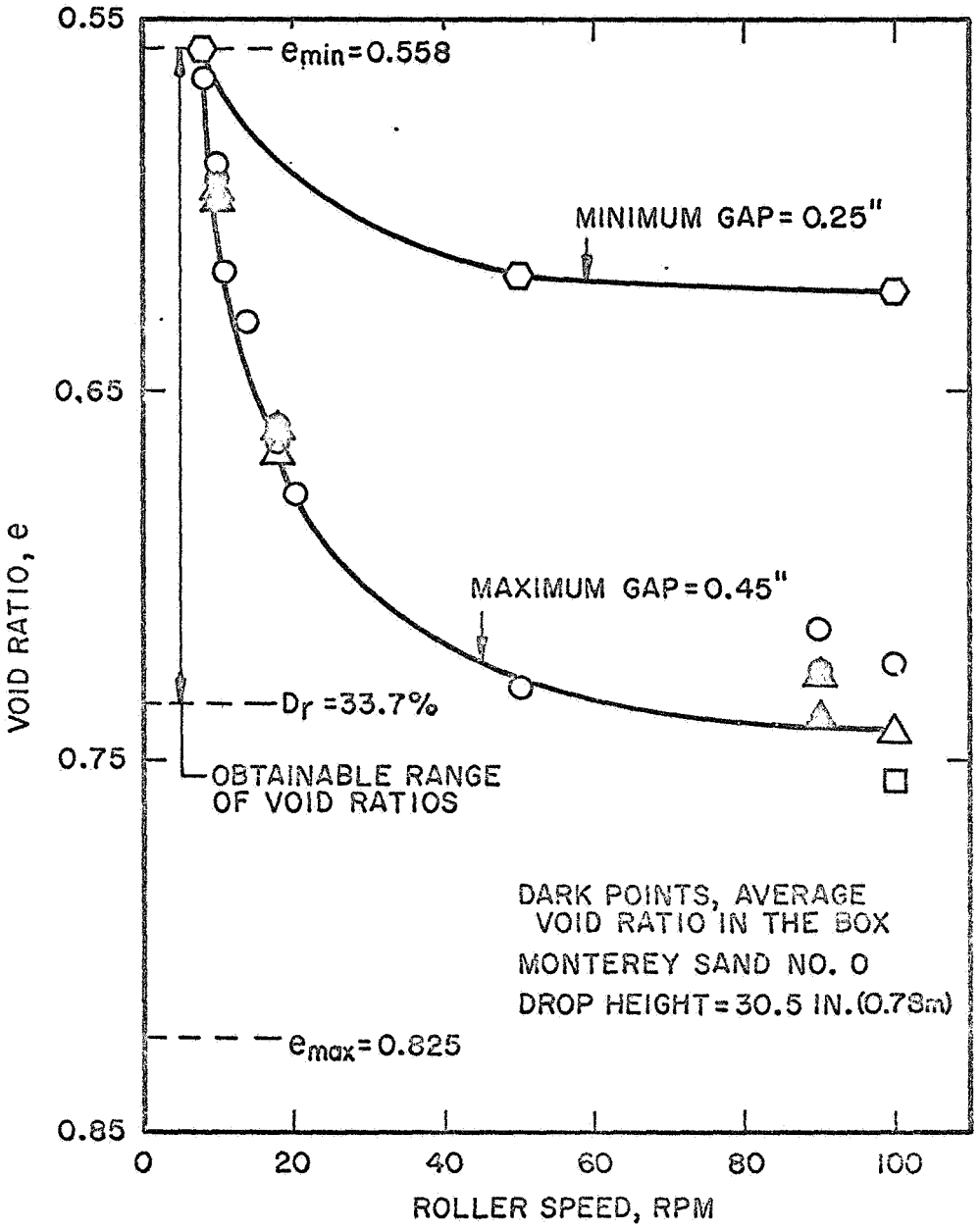

FIG. B.3 CALIBRATION OF SPREADER BOX FOR MONTEREY SAND NO. 0